université
PARIS-SACLAY

Formulation of anisotropic damage in quasi-brittle materials and structures based on discrete element simulation

Formulation de l'endommagement anisotrope des matériaux et stuctures quasi-fragiles basée sur la simulation discrète de la fissuration

Thèse de doctorat de l'université Paris-Saclay

École doctorale n°579, Sciences mécaniques et énergétiques, matériaux et géosciences (SMEMaG)
Spécialité de doctorat : Mécanique des matériaux
Graduate School : Sciences de l'ingénierie et des systèmes.
Référent : ENS Paris-Saclay

Thèse préparée dans l'unité de recherche **LMPS - Laboratoire de Mécanique Paris-Saclay (Université Paris-Saclay, CentraleSupélec, ENS Paris-Saclay, CNRS)**, sous la direction de **Rodrigue DESMORAT**, Professeur des Universités, et la co-supervision de **Cécile OLIVER-LEBLOND**, Maîtresse de conférences

Thèse soutenue à Paris-Saclay, le 12 décembre 2023, par

Flavien LOISEAU

Composition du jury
Membres du jury avec voix délibérative

Gilles PIJAUDIER-CABOT	Président
Professeur des Universités, Université de Pau et des Pays de l'Adour	
Milan JIRÁSEK	Rapporteur & Examinateur
Professeur, Czech Technical University in Prague	
Claude STOLZ	Rapporteur & Examinateur
Directeur de Recherche, Institut des Sciences de la mécanique et Applications industrielles	
Arnaud DELAPLACE	Examinateur
Ingénieur de Recherche Senior HDR, Holcim	

Titre : Formulation de l'endommagement anisotrope des matériaux et stuctures quasi-fragiles basée sur la simulation discrète de la fissuration

Mots clés : Anisotropie, Élasticité, Endommagement, Éléments Discrets, Matériaux quasi-fragiles, Micro-fissuration.

Résumé : Les matériaux quasi-fragiles, couramment utilisés pour les structures du génie civil, ont tendance à se dégrader lorsqu'ils sont soumis à des chargements mécaniques. Cette dégradation induit une perte de propriété mécanique et peut induire une anisotropie du comportement qui dépend de la direction du chargement. La prédiction de cette dégradation et de son impact sur le matériau est un enjeu important pour garantir l'intégrité des structures et la sécurité des usagers. Cette problématique est au cœur de ce travail qui vise à formuler un modèle d'endommagement anisotrope (macroscopique) pour les matériaux quasi-fragiles en 2D. Pour ce faire, une base de donnée de tenseurs d'élasticité est générée par essais "virtuels". Un élément d'aire (mésoscopique) du matériau est représentée par un modèle discret *beam-particle* fournissant une description explicite de la micro-fissuration. L'évolution du tenseur d'élasticité effectif de l'élément est mesurée pour différents chargements (dont certains multiaxiaux et non proportionnels). L'analyse des tenseurs par le calcul des distances aux classes de symétrie montre qu'une variable tensorielle d'ordre au moins deux est nécessaire pour décrire la micro-fissuration. Afin de faciliter la construction du modèle d'état, une formule de reconstruction du tenseur d'élasticité par ses covariants ainsi qu'une variable d'endommagement sous-jacente, toutes deux issues de travaux précédents, sont rappelées. En se basant sur ces outils ainsi que sur la base de donnée générée, un modèle du tenseur d'élasticité effectif en fonction de la variable d'endommagement, *i.e.* un modèle d'état, est proposé puis évalué. Concernant la modélisation de l'évolution, la fonction critère de l'élément d'aire est déterminée puis calibrée par essais "virtuels". Enfin, après une analyse de l'évolution de l'endommagement dans la base de donnée, un modèle (préliminaire) non-standard de l'évolution de l'endommagement est proposé.

Title : Formulation of anisotropic damage in quasi-brittle materials and structures based on discrete element simulation

Keywords : Anisotropy, Damage, Discrete Elements, Elasticity, Microcracking, Quasi-brittle Materials.

Abstract : Quasi-brittle materials, commonly found in civil engineering structures, tend to degrade when submitted to mechanical loadings. This degradation leads to a loss in mechanical properties and can induce anisotropy of the material behavior, which depends on the loading direction. Predicting this degradation and its impact on the material is essential to guarantee the integrity of structures and the safety of users. This problem is at the heart of this work, which aims to formulate a (macroscopic) anisotropic damage model for quasi-brittle materials in 2D. To this end, a dataset of effective elasticity tensors is generated by "virtual" testing. A (mesoscopic) area element of the material is represented by a discrete beam-particle model, which provides an explicit description of micro-cracking. The evolution of the element's effective elasticity tensor is measured for various loadings (some of which are multiaxial and non-proportional). The analysis of the measured tensors by calculating distances to symmetry classes shows that a tensor variable of order two or higher is needed to describe micro-cracking. To facilitate the formulation of the state model, a formula for reconstructing the elasticity tensor from its covariants and an associated damage variable, both derived from previous work, are recalled. Based on these tools and the generated dataset, a model of the effective elasticity tensor as a function of the damage variable, *i.e.* a state model, is proposed and evaluated. For evolution modeling, the criterion function of the area element is determined and calibrated by "virtual" testing. Finally, a (preliminary) non-standard evolution model is proposed after an analysis of the damage evolution in the dataset.

Acknowledgements

First and foremost, I would like to thank Mr. Gilles Pijaudier-Cabot, who did me the honor of chairing my thesis jury, and Mr. Milan Jirásek and Mr. Claude Stolz, who took the time to examine my manuscript and give it their informed opinion. I would also like to thank Mr. Arnaud Delaplace for his interest in my work. Finally, I would like to thank the jury for the enriching questions and discussions that followed my defense.

Then, I would like to thank my supervisors for giving me the opportunity to carry out this thesis and supervised me during these three years. I want to start by thanking my thesis director, Rodrigue Desmorat, who has taught me a lot scientifically, particularly in damage mechanics and mathematics, but also about research in general. You also taught me a certain rigor and attention to detail. Thanks also to Cécile Oliver-Leblond for her guidance and all the interesting discussions, whether scientific or not. You also guided me through my first supervision experience. I learned a lot from both of you and really enjoyed working with both of you during those three years.

Next, I would like to thank several people at LMPS who helped and supported me during those three years. I will start by thanking the "Centre de Simulation" team for their technical assistance. In particular, I would like to thank Thomas Verbeke for his help with DEAP and our many discussions. I also thank the "Centre de Gestion" team, specifically Charlène Marche, for their help with all the administrative formalities.

This thesis also marks the end of my training at ENS Paris-Saclay. I want to take this opportunity to thank all the teachers who accompanied me during my training years (and some of whom continued to accompany us during our breaks). I would also like to thank the permanent members of LMPS with whom I've been able to interact and from whom I've also learned a lot: Boris Kolev (who taught me a lot of maths), Amélie Fau, Federica Daghia, Emmanuel Baranger, Yoann Guilhem and the members of the COMMET team. I would also like to take this opportunity to thank Antoine and Louis, whom I supervised during their project/internship and with whom it was enjoyable and instructive to work.

I would also like to thank the LMPS Ph.D. students with whom I've had a great time and who have made my three years at LMPS so enjoyable: Julien, Claire, Yannick, Victor, Quentin, Pierre-Elliot, Clément, Théodore, Marie, Héloïse, Mamhoud. There are a few people I wanted to thank, more specifically, starting with Breno I enjoyed the discussions and the time we spent together. Then, I would also like to thank Aurélia, Floriane, and Alexandre for all the great times we've had together. It was really great to be by your side during the thesis. So I wanted to thank you for all the daily exchanges and support, but above all, for all the fun times we've had together.

My last thanks go to Laura, who supported and helped me enormously over those years.

Contents

Bibliography   159

List of Symbols

Spaces

$\mathbb{R}$	Real space
$O(n)$	Orthogonal group of dimension d
$\mathbb{H}^n(\mathbb{R}^2)$	Space of nth-order harmonic tensors in $\mathbb{R}^2$
$\mathbb{E}la(\mathbb{R}^2)$	Space of bi-dimensional elasticity tensors in $\mathbb{R}^2$

Operators

$\bullet^{\mathrm{T}}$	Transposition
$\bullet^{\mathrm{S}}$	Symmetrization ($\bullet^{\mathrm{S}} = \frac{1}{2}(\bullet + \bullet^{\mathrm{T}})$)
$\mathrm{tr}(\bullet)$	Trace of second-order tensor $\bullet$
$\mathrm{tr}_{ij}(\bullet)$	Trace ij of fourth-order tensor $\bullet$
$\bullet'$	Deviatoric part of second-order tensor $\bullet$
$\det(\bullet)$	Determinant of second-order tensor $\bullet$
$\|\bullet\|$	Norm of $\bullet$ (Frobenius norm by default)
$\otimes$	Tensor product
$\odot$	Symmetric tensor product
$*$	Harmonic product
$\langle\bullet\rangle_+$	Positive part of $\bullet$

Constants

$\mathbf{0}$	Null tensor
$\mathbf{1}$	Second-order identity tensor
$\mathbf{I}$	Fourth-order identity tensor
$\mathbf{J}$	Deviatoric projector (4th-order tensor)

Continuous variables

$\boldsymbol{e}_1, \boldsymbol{e}_2$	Basis vectors of $\mathbb{R}^2$
$\boldsymbol{x}$	Coordinate
$\boldsymbol{u}$	Displacement
$\boldsymbol{\varepsilon}$	Strain tensor
$\boldsymbol{\sigma}$	Stress tensor
$\mathbf{D}$	Damage tensor
$\mathbf{Y}$	Thermodynamic force associated with damage
$\mathbf{E}$	Elasticity tensor
$\mathbf{E}_0$	Initial elasticity tensor
$\tilde{\mathbf{E}}(\mathbf{D})$	Effective elasticity tensor
$\rho\psi$	State potential (Helmholtz specific free energy)
$\mathscr{D}$	Intrinsic dissipation
f	Damaging criterion function
ε_D	Damage yield strain
$\dot{\lambda}_{\mathbf{D}}$	Damage multiplier
$\mathbf{P_D}$	Damaging direction
$\boldsymbol{\Delta}$	Evolution variable
$\dot{\lambda}$	Multiplier associated with the evolution variable
$\mathbf{P}$	Evolution of the evolution variable
$\varepsilon_{\mathrm{eq}}$	Generic equivalent strain
$\varepsilon_{\mathrm{vM}}$	von Mises equivalent strain
$\varepsilon_{\mathrm{DP}}$	Drucker-Prager equivalent strain
$[\bullet]$	Kelvin notation of the tensor $\bullet$
$\bullet_{\mathrm{vM}}$	von Mises equivalent tensor
$I_i(\bullet)$	Invariants of the second-order tensor $\bullet$ ($I_n\bullet = \mathrm{tr}(\bullet^n)$)
m	Non-linear shear-damage coupling parameter
h	Harmonic pre-factor parameter

Harmonic decomposition

μ	Shear modulus
κ	Bulk modulus
$\mathbf{d}$	Dilatation tensor
$\mathbf{v}$	Voigt tensor

Iso	Isotropic part
Dil	Dilatation part
H	Harmonic part

Symmetry analysis

| d_Σ | Distance to the symmetry class Σ |
| Δ_Σ | Relative distance to the symmetry class Σ |

Discrete model variables

$\bullet_b$	Quantity associated to the beam b
$\bullet_{pq}$	Quantity associated to the beam linking particle p and q
$\boldsymbol{x}_p$	Position of particle center of particle p
$\boldsymbol{u}_p$	Displacement of particle p
$u_{i,p}$	Displacement of particle p along e_i axis
θ_p	Rotation of particle p
$\bar{l}_b$	Average beam length
l_b	Beam length of the beam b
f_b	Value of the failure criterion function of the beam b
ε_b	Extension of the beam b
$\varepsilon_b^{\mathrm{cr}}$	Critical extension of the beam b
$\Delta\theta_b$	Difference of rotation associated to the beam b
$\Delta\theta_b^{\mathrm{cr}}$	Critical difference of rotation associated to the beam b
$\lambda_{\varepsilon,\mathrm{cr}}$	Scale factor of the Weibull distribution for extension failure thresholds
$\lambda_{\theta,\mathrm{cr}}$	Scale factor of the Weibull distribution for rotation failure thresholds
k	Shape factor of the Weibull distributions both failure thresholds
KUBC	Kinematically Uniform Boundary Conditions
SUBC	Statically Uniform Boundary Conditions
PBC	Periodic Boundary Conditions
EXPE	Boundary Conditions with imposed displacement on faces of the specimen

Introduction

1   General context

One of today main challenges is to have a sustainable production and use of energy and materials. This challenge drives the necessity for research on materials, to ensure their sustainable usage in structures while guaranteeing that they fulfill their function over time. This dissertation focuses on studying quasi-brittle materials, such as concrete, ceramics and ice. These materials are widely employed across various domains like infrastructures, transportation, and energy. In particular, concrete is the most used material in the world. According to the Chatham House Report, it is responsible for around 8% of global CO2 emissions (Lehne & Preston, 2018). Therefore, we must employ such materials more efficiently (for instance, by reducing safety margins in structure design) to reduce their usage and production impact.

Accurately describing the (complex) behavior of quasi-brittle materials up to failure is necessary to achieve this objective. In particular, it is essential to understand how a material subjected to various loads (mechanical, thermal, etc.) behave during its life cycle. These loads can change the material state and degrade its properties. Depending on this change, the structure ability to fulfill its intended function may be compromised, putting equipment and even lives at risk. The mechanical degradation of quasi-brittle materials, usually due to the nucleation of micro-cracks, have a strong influence on their mechanical behavior. In particular, it causes a loss of stiffness and, potentially, variations in material properties based on its orientation. Such a degradation occurs when the material is subjected to high mechanical loads. Accounting for this behavior change is of utmost importance for accurately simulating and efficiently designing structures.

2   Scientific approach

This dissertation aims to model the degradation, *i.e.* micro-cracking, of quasi-brittle materials. To this end, the first step consists of gathering reference data on the behavior of quasi-brittle materials. The gathered data must then be analyzed to identify the different phenomena occurring during their degradation process. From such a dataset, a mathematical model of their degradation can be developed. This last task is generally divided into two sub-tasks: (1) modeling how the degradation affects the overall behavior of the material, and (2) modeling when and how the degradation evolves when a mechanical loading is applied.

Formulating a multiaxial damage model requires first gathering data on the material degradation. It means understanding how the degradation changes over time and affects the material behavior under different multi-axial and non-proportional loads. This process requires precise measurement of how the material effective elastic properties change during each loading. Moreover, each experiment must be repeated sufficiently to gather a statistically significant amount of results. However, conducting such an extensive experimental campaign would be difficult, if not impossible. Indeed, it would mean carrying out highly accurate material characterization tests on significant number of specimens, some of them severely damaged. Therefore, this work employs virtual testing as an alternative and complementary approach to experiments. Virtual testing involves using a model, estimated to be sufficiently accurate, of the material response at a meso-scale to simulate and study its macroscopic behavior. The meso-scale model is chosen to be a discrete beam-particle model in this work as it provides an explicit representation of micro-cracking. Furthermore, it accurately considers how the micro-cracks affect the macroscopic behavior of the material. Yet, we chose to neglect the crack closure effect for this study. The results from virtual testing in 2D will serve to constitute a dataset of bi-dimensional effective elasticity tensors. This dataset will be our reference to formulate the multi-axial damage model.

This dissertation pays particular attention to the rigorous analysis of anisotropy induced by micro-cracking, the so-called anisotropic damage. To this end, mathematical notions related to material symmetries in 2D are recalled and used. In particular, the distances of an elasticity tensor to a symmetry class are employed to justify the necessity of anisotropic damage models. The notion of invariants and covariants (a tensorial generalization of invariants) are also used to analyze the tensors without any reference to a particular basis. After those first analyses, we aim to formulate a model that captures how micro-cracking affects the bi-dimensional effective elasticity tensor. We rely on a tensorial (equivariant) reconstruction formula for elasticity tensors to simplify the modeling process. This formula gives an expression of the elasticity tensor from its invariants and (tensorial) covariants. Based on this formula, previous works have introduced a (tensorial) damage variable, a covariant of the effective elasticity tensor, to represent the degradation state of the material. It has the particularity to offer explicit expressions for certain parts of the effective elasticity tensor as functions of the damage variable. The remaining parts are modeled based on the reference dataset. In particular, a sparse and interpretable data-driven approach is employed to formulate one of the parts of the model. To complete the model, we need to model the evolution of the degradation, *i.e.* of damage, when a mechanical load is applied to the material. First, we must establish a criterion to identify when damage occurs based on data from discrete simulations. Then, we will formulate a damage evolution model to describe how degradation evolves during mechanical loading.

To summarize, this study proposes to use a virtual testing approach as a foundation to formulate a model of the mechanical degradation of quasi-brittle material. The virtual experiments are performed by simulating area elements using a discrete beam-particle model. The resulting evolutions of the area element effective elasticity tensors are stored in a dataset. By analyzing the dataset, we highlight the need for an anisotropic damage model to describe their behavior accurately. The dataset then serves as a reference for the anisotropic damage model formulation. First, the impact of damage, *i.e.* micro-cracking, on

the effective elasticity tensor is modeled, leading to the formulation of the state potential. Then, a (non-standard) damage evolution law is proposed to complete the model. Non-local damage is then discussed to introduce the application of the model to structure simulations.

3 Outline

This dissertation is organized into two parts and six chapters. The first part is mainly dedicated to analyzing existing works from the literature. It places this work in the context of existing literature, justifies the research methodology, and introduces the notions and (existing) tools employed in the second part. This part is composed of three chapters.

- **Chapter 1** provides the reasons for studying quasi-brittle materials by showcasing their behavior during mechanical degradation through experiments from the literature. It emphasizes the key phenomena that need to be considered for accurate modeling. This chapter then covers the modeling of material degradation and damage, covering discrete and continuous models. Special attention is given to the structure and formulation of damage models.

- **Chapter 2** offers an overview of the literature on the mathematical study of elasticity tensors. It introduces key definitions to study the anisotropy of elasticity tensors (elasticity tensors, symmetry classes, invariants, covariants, etc.). This chapter then presents the harmonic decomposition, representing 2D elasticity tensors from four (covariant) harmonic components. Based on this decomposition, it presents formulas to reconstruct an elasticity tensor from its covariants that will be used to formulate the state model in subsequent chapters. Finally, it introduces the concept of distance of an elasticity tensor to a symmetry class, providing a rigorous basis for justifying modeling choices related to anisotropy.

- **Chapter 3** focuses on determining the effective elasticity tensor of a discrete area element. It starts by introducing the beam-particle model used and then addresses fundamental homogenization questions. First, the average stress and strain definition in an area element are discussed, as well as the appropriate boundary conditions to apply to the area element in the measurement procedure. After addressing those questions, a procedure to measure the effective elasticity tensor of an area element is described and discussed.

The second part is dedicated to the main contributions of this work and is composed of three chapters:

- **Chapter 4** is dedicated to generating and analyzing the dataset of effective elasticity tensors. This dataset will serve as the reference for the 2D anisotropic damage model formulation. Area elements are submitted to both proportional and non-proportional loadings, and their effective elasticity tensors are measured at each load step. This chapter also illustrates the measurements by analyzing a particular elasticity tensor evolution during a non-proportional loading. Additionally, a validity check is conducted by assessing errors in the measurement process and checking for inconsistencies in

the dataset, such as losses of positive definiteness or increases in stiffness. Finally, a quantified anisotropy analysis is performed.

- **Chapter 5** develops an anisotropic damage state model based on the reconstruction by covariants. The goal is to express each harmonic component of the effective elasticity tensor as a function of damage. An anisotropic damage variable from the literature, based on a second-order covariant of the effective elasticity tensor, is introduced. This damage variable, coupled with the reconstruction formula, provides an exact modeling of two (out of four in 2D) harmonic components. The two remaining harmonic components are then modeled based on the reference dataset and using a sparse data-driven approach for one of them. The resulting model expresses the bi-dimensional effective elasticity tensor in terms of the initial elastic properties, a new parameter called the harmonic pre-factor, and the damage variable. Finally, the model accuracy is assessed by comparing it with results obtained from the discrete model.

- **Chapter 6** is dedicated to the development of a non-standard damage evolution law. This development is performed in three steps. Firstly, the initial yield surface of multiple area elements is efficiently measured using a method proposed in this work. The equivalent strain is then defined by fitting a polynomial of strain invariants to this measured yield surface. Secondly, the chapter analyzes the damage evolution by applying various strain loadings to (discrete) area elements. This investigation identifies crucial phenomena during the degradation process, which must be incorporated into the model. Based on the discrete results, a preliminary non-standard damage evolution law is then proposed. Extension of the model to non-local damage is discussed.

Part I

Generalities for the analysis of quasi-brittle materials

1

Mechanical degradation/damage of quasi-brittle materials

This chapter motivates the study of quasi-brittle materials. It begins with a presentation of different experiments to illustrate the behavior of quasi-brittle materials during their mechanical degradation. It highlights various phenomena that must be accounted for to model those materials. Then, the focus is shifted on the modeling of material degradation/damage. First, an overview of the discrete models is provided. Then, the continuous damage models are discussed. In particular, an emphasis is put on the structure and formulation of damage models.

Quasi-brittle materials, such are concrete or mortar, are highly used in civil engineering structures. Ensuring their integrity is of crucial importance to guarantee its safe use. The best way to guarantee the integrity of a structure would be to make a full-scale prototype of the structure. Due to the scale of civil engineering structure, this method is usually impossible. Yet, the size effect (Bažant, 1984; Bažant & Planas, 2019) makes the use of small scale prototypes difficult.

It motivates the need of means to accurately simulate structures. To simulate the mechanical behavior of structures, different steps are required. The first step is to characterize the materials of the structure. The characterization consists in measuring the response of a material when submitted to different loadings to gather information on the material behavior. It enables to put forward different phenomena that must be accounted for to correctly model the material. Once enough information is acquired, it can be used to formulate models. In material science, a model is a mathematical description of the observed phenomena valid under certain assumptions. Using numerical (or analytical) tools, the model can be applied to analyze the response of a whole structure to different loadings.

1   Experimental observations

This section aims at introducing and presenting the behavior of quasi-brittle material based on experimental evidence. For most of the studies presented here, the material used in the experiments are concrete or mortar. Bones, some composites, wood, amongst others are

other example of quasi-brittle materials.

1.1   Macroscopic behavior

In general, the behavior of a material is first characterized through macroscopic mechanical experiments. In this subsection, different tests are reviewed to showcase particularities of the behavior of quasi-brittle material.

Cyclic behavior in tension.   Different uni-axial cyclic experiments on concrete have been carried out to characterize its behavior under a tensile loading (Terrien, 1980; Reinhardt & Cornelissen, 1984; Reinhardt et al., 1986; Mazars & Berthaud, 1989; Mazars et al., 1990; Nouailletas et al., 2015). For instance, results from Terrien (1980) are reported in Figure 1.1. At the beginning of the tensile loading, the relation between strain and stress is linear which corresponds to an elastic behavior. When the loading reaches a specific threshold called the yield strength, the relation become non-linear. It is one of the manifestation of the damage growth at macroscopic scale. After reaching a peak stress, the stress starts to decrease with the strain. This part is called the softening phase which appears as the material further continues to damage. Terrien (1980) also unloaded the material during the softening phase. Different observations are important to mention:

1. A permanent strain still persists even if the stress goes back to 0.

2. Stress decreases almost linearly with strain during unloading.

3. The further in the softening phase, the smaller the slope during unloading.

The unloading is almost linear; thus, it can be considered as elastic. The slope of the unloading corresponds to the effective rigidity of the material. The successive unloadings show a gradual decrease of the effective rigidity. Those observations will be explained from local phenomena in Section 1.3.
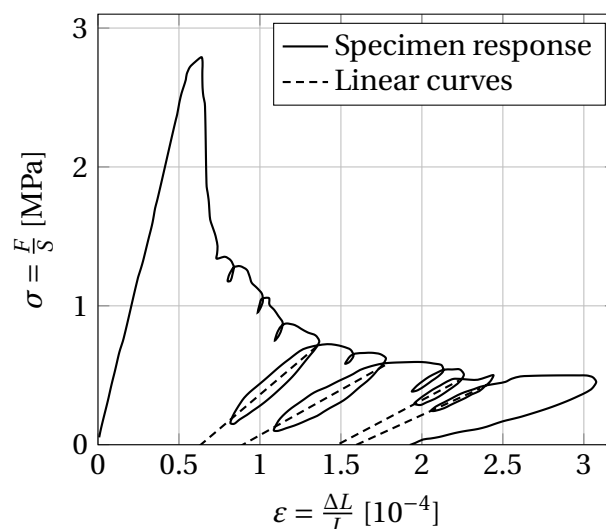
Figure 1.1 • Stress strain cyclic tensile curve (adapted from Terrien (1980)).

Unilateral effect. In its experiment, Terrien (1980) stopped to unload when the stress returned to 0. In a similar experiment, Mazars et al. (1990) unloaded the specimen and then applied compressive loading to it. Figure 1.2 displays stress-strain curve from the experiment. Note that the studies of Reinhardt and Cornelissen (1984), Reinhardt et al. (1986), and Nouailletas et al. (2015) show similar results. The curve in Figure 1.2 displays different phases. The phase 1 is the elastic loading and the beginning of the softening phase. During phase 2, the specimen is unloaded to almost null strain. When the stress becomes null, a permanent strain remains. Then, the specimen is reloaded. Once again, the unloading and the loading are almost linear with a decreased slope, corresponding to a degraded macroscopic rigidity. Phase 3 is the end of the softening phase. During phase 4, the material is unloaded and shows a linear stress evolution with strain. In phase 5, the stress-strain relationship is still linear, with an increased slope compared to phase 4. Note that the slope is close to the one in phase 1, meaning that the rigidity is close its initial value (in the elastic phase). This stiffness recovery is the so-called unilateral effect. It also seems important to point out that, in the range of the compressive loading, the softening in compression is not reached. It means that the stiffness of the material is now higher in compression than in tension.
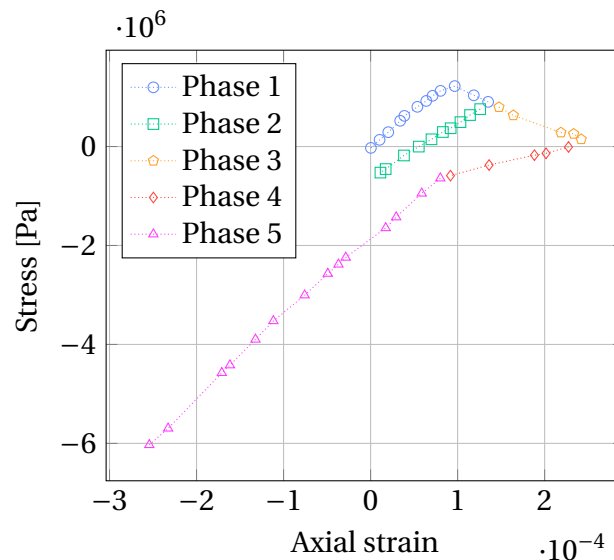
Figure 1.2 • Stress-strain curve of an alternating tension-compression loading applied to a concrete cylinder (adapted from Mazars et al. (1990)).

Damage-induced anisotropy. After being subjected to a damaging loading, an initially isotropic material can become anisotropic. It means that is degraded mechanical properties vary with the measurement direction. This phenomenon is called damage-induced anisotropy. For instance, Berthaud (1991) subjected a square concrete specimen to uniaxial compression in the direction $\mathbf{e}_1$. The evolution of Young's modulus in directions $\mathbf{e}_1$ and $\mathbf{e}_3$ are measured and reported in Figure 1.3a. Moreover, the evolution of Poisson ratios ν_{12} and ν_{23} are also measured and reported in Figure 1.3b. As shown on those figures, the specimen is initially isotropic as the elastic moduli $E_1 = E_3$, and the Poisson coefficients $\nu_{12} = \nu_{32}$. During the compressive loading, E_1 stays approximately constant and equal to E_0 whereas

(a) Young modulus.

(b) Evolution of Poisson ratios.
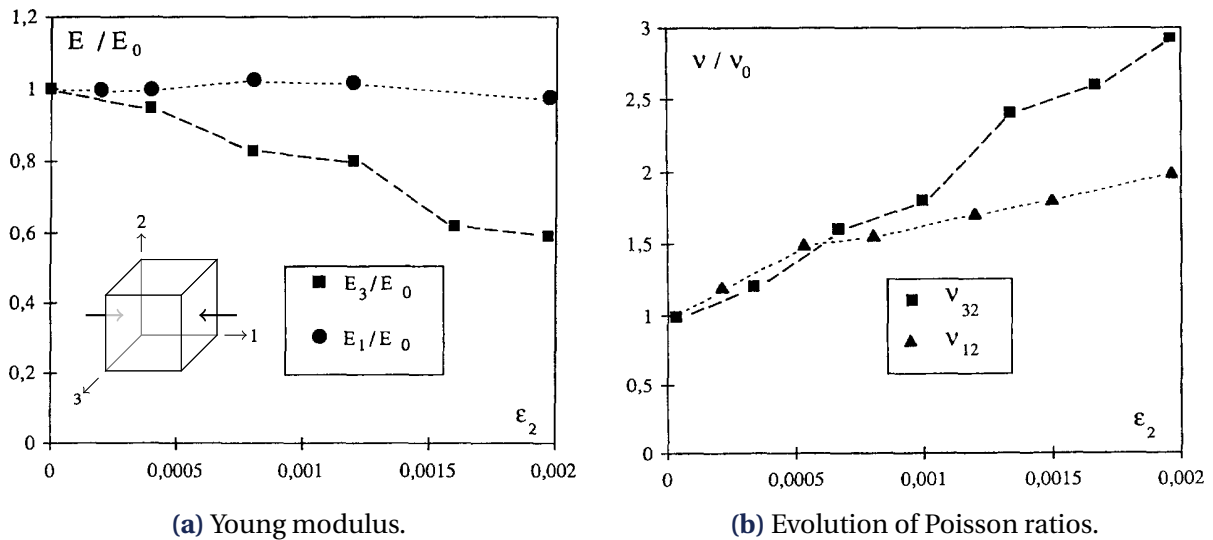
Figure 1.3 • Evolution of the mechanical properties during a compressive loading by Berthaud (1991).

E_3 strongly decreases. In addition, the Poisson ratios become different. It shows that the degradation can make a material mechanically anisotropic.

📝 **Conclusion – Macroscopic behavior of quasi-brittle material**

During tensile experiments on quasi-brittle structures, we observe

- an elastic phase at the beginning of the loading;

- a damaging phase when a specific threshold is reached (the yield strength);

- a softening phase (inside the damaging phase) when the tensile strength is reached;

- a nearly elastic response when unloading the specimen during the softening, with a degraded rigidity;

- a permanent strain when going back to zero stress after softening;

- a rigidity recovery when compressing the specimen after softening.

An anisotropy of the behavior induced by the degradation, itself caused by the mechanical loading, is also observed.

1.2   Yield surface – When does the damage growth begins ?

The softening phase starts at a specific point of the loading, which corresponds to the beginning of the mechanical degradation. This part aims at presenting experimental observations of the transition between the elastic phase and the damaging phase. For instance, Kupfer et al. (1969), Nelissen (1972), and Lee et al. (2004) investigate the behavior of concrete under biaxial loading. In particular, Lee et al. (2004) examine square plate concrete specimens, $200 \times 200 \times 60 \text{ mm}^3$. Two types of concrete used in Korean nuclear containment buildings are studied. The specimens are subjected to loadings with different stress ratios ($\alpha = f_1 / f_2$), where f_1 and
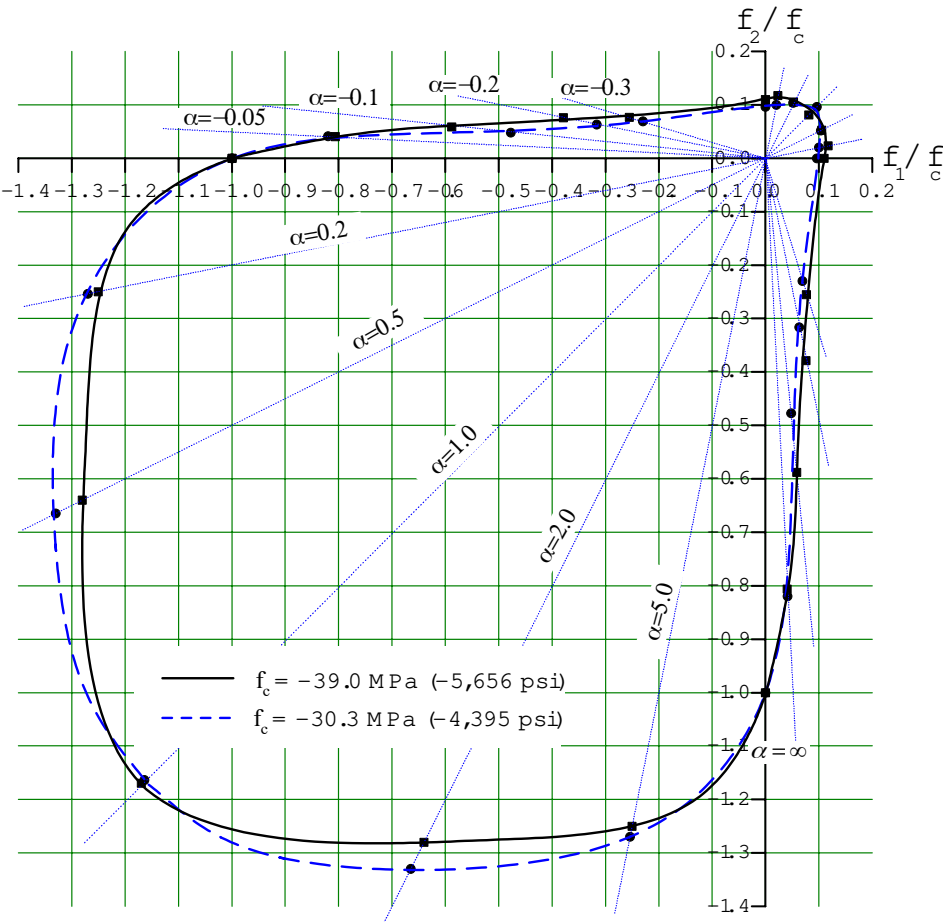
Figure 1.4 • Biaxial strength envelops for two different types of concrete under biaxial stress (Lee et al., 2004). f_c is the compressive strength of the specimen.

f_2 are principal stresses. The results of this study are represented in Figure 1.4. It shows that the strength of the material varies with the loading direction. In particular, the strength in compression is around ten times higher than in tension. It means that the specimen is more resistant to damage from compressive loads than from tensile loads.

1.3 A zoom on the fracture process

To explain the macroscopic behavior of quasi-brittle materials, a look at smaller scales is necessary. Different techniques provide means to investigate the "local" material behavior. Mindess (1991) proposes a review of such techniques. Here, experimental results using an Acoustic Emission Technique are presented. Based on those results, different macroscopic phenomena (such as the unilateral effect and the damage induced anisotropy) are explained.

Acoustic Emission Techniques.   The book of Grosse et al. (2022) —especially the chapter "AE in Concrete"— provides an overview of different AE techniques. Ohtsu (1996) also gives a historical review of early developments and applications of those techniques. Acoustic emissions techniques are based on the release of elastic energy due to an acoustic event which generates the propagation of an acoustic wave in the specimen. Different phenomena can generate an acoustic event: the creation of a micro-crack, inter-granular friction, amongst others. By placing piezoelectric transducers at different locations on the specimen surface, the acoustic source intensity and location can be measured. Since the end of the 80s, numerous acoustic emissions studies have been carried out to study concrete failure, see for instance the works of Maji and Shah (1988), Rossi et al. (1990), Ouyang et al. (1991), Landis (1999), and Saliba et al. (2016), amongst others. The work of Landis (1999) provides an analysis of the fracture process during a 3-point bending test. Figure 1.5 shows the results from a three-point bending test applied to a coarse mortar specimen. In those results, each acoustic event is considered to be the creation of a micro-crack. Different phases are observed. The first phase, from the beginning of the loading until 80% of peak load, displays few diffuse acoustic events. This phase contains the elastic part of the loading and the beginning of the micro-cracking. Note that the micro-cracks appear diffusely in the most loaded region of the specimen. The second phase ranges from 80% of peak load until the peak load. This phase starts with an increase in event rate, corresponding to an acceleration of the micro-cracking. In this phase, bridges between existing micro-cracks appear, leading to micro-cracking localization. At the macroscopic scale, a significant loss of rigidity is observed. The last two phases are softening phases. During those phases, acoustic events propagate in the bulk of the material in a localized manner. It corresponds to the propagation of a macroscopic crack in the specimen. A conclusion of this experiment is that the mechanical degradation of quasi-brittle materials is mainly caused by the nucleation and propagation of micro-cracks in the material. In the next paragraphs, this observation is used to explain most of the observed macroscopic phenomena.

Loss of stiffness.   The nucleation and growth of micro-cracks create a loss of cohesion in the material, inducing a macroscopic reduction of the stiffness. This leads to the decrease of the observed Young modulus observed in Terrien (1980) results in Figure 1.1.

(a) Load and intensity of acoustic events.

(b) Acoustic events location and crack paths.
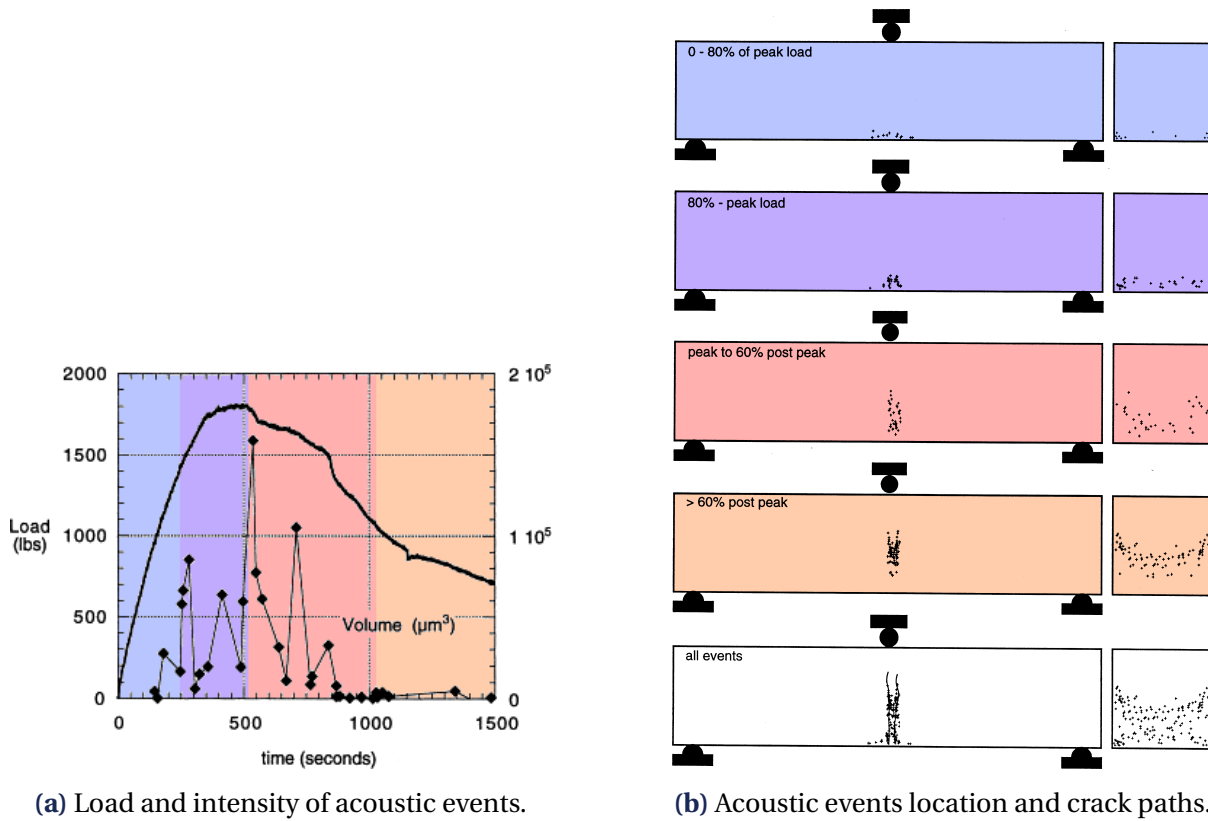
Figure 1.5 • Acoustic Emission applied to a coarse mortar subjected to three-point bending (Landis, 1999).

Unilateral effect. The unilateral effect is also explained by those micro-cracks. A tensile loading leads to the nucleation of micro-crack in directions orthogonal to the loading direction (Mazars, 1984; Lemaitre & Mazars, 1982). Then, if a compressive loading is applied in the same direction, the micro-cracks will close and the load will be transmitted by contact between crack faces. It leads to an apparent recovery of stiffness observed in Figure 1.2. In practice, each individual micro-crack can be either open or close, depending on the loading. When a crack closes, it leads to a gain of stiffness (without any change of the micro-cracking).

Permanent strain at unloading. Yet, Figure 1.1 also displays permanent strains. It is due to the friction between the crack faces which induces irreversible strains (Andrieux et al., 1986).
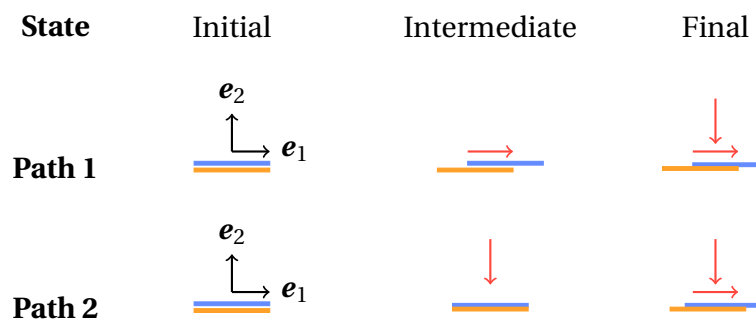
Figure 1.6 • Different loading paths applied to a crack (adapted from Kachanov (1982)).

For illustration purposes, the Figure 1.6 shows two loading paths applied to a crack. In the first one, the crack is first sheared, leading to a sliding δ_1, and then, a normal stress is applied to it. In the second one, a normal stress is first applied to the crack. Due to friction, this normal stress induces a rise of the sliding resistance; thus, it acts as a "lock" of the crack.

If the friction between crack faces is accounted for, there are different possible cases:

- **Adherence.** The crack surfaces adhere to each other ($\delta_2 = 0$), leading to a complete regain of stiffness.

- **Friction.** The crack surfaces slide with friction ($0 < \delta_2 < \delta_1$); thus, the crack can still transmit partially stress in the plane of the crack, leading to a partial regain of stiffness.

- **Gliding.** The crack surfaces perfectly slide (without friction) ($\delta_2 = \delta_1$); thus, the crack cannot transmit stress in the plane of the crack, leading to a recovery of stiffness in the direction normal to the crack.

Also note that, in most cases, the crack has a certain roughness, leading to additional contact effects (which may be, at least partially, accounted for with friction).

Damage-induced anisotropy. The damage-induced anisotropy is due to micro-cracks orientations and positions. For a uni-axial loading, micro-cracks nucleates such that the crack plane is normal to the loading direction. Thus, the perceived loss of stiffness will depend on the relative orientation between the crack and the direction in which the stiffness is measured.

1.4 Conclusion on the mechanical degradation of quasi-brittle materials

To conclude this first section, let us highlight the phenomena occurring when a quasi-brittle material is damaging and discuss which phenomena will be accounted for in the proposed model. The model needs to represent the initial elastic phase up until the yield surface is reached. During the damaging phase, it should also incorporate the stiffness loss due to micro-cracking. In order to accurately represent the softening phase under multi-axial loads, the model must additionally account for the damage-induced anisotropy. However, to ease the modeling process, the crack closure effects, such as the stiffness recovery and the permanent strain at unloading, will be omitted for now and left to future works.

2 Discrete models

This section aims at presenting discrete models for the modeling of quasi-brittle materials. Three types of models – lattice, particular, and hybrid – are presented separately. A more complete review of discrete model is provided by Bolander et al. (2021).

2.1 Lattice models

In lattice models, the material is represented by a network of 1D elements such as springs or beams. According to Capecchi et al. (2010), lattice models were introduced through the work

of French mechanicians in the early 1800s to make a molecular model of matter. Poisson (1828) establishes the basis of the molecular theory of elasticity. However, this theory suffered a critical flaw: the constitutive law of an isotropic body is characterized by only one parameter, in so-called rari-constant elasticity theory (Love, 1892). The solution proposed by Voigt (1887) is to modify the molecular model to define interaction through potentials, thus deviating from a lattice model. The first lattice model to solve this issue is proposed by Hrennikoff
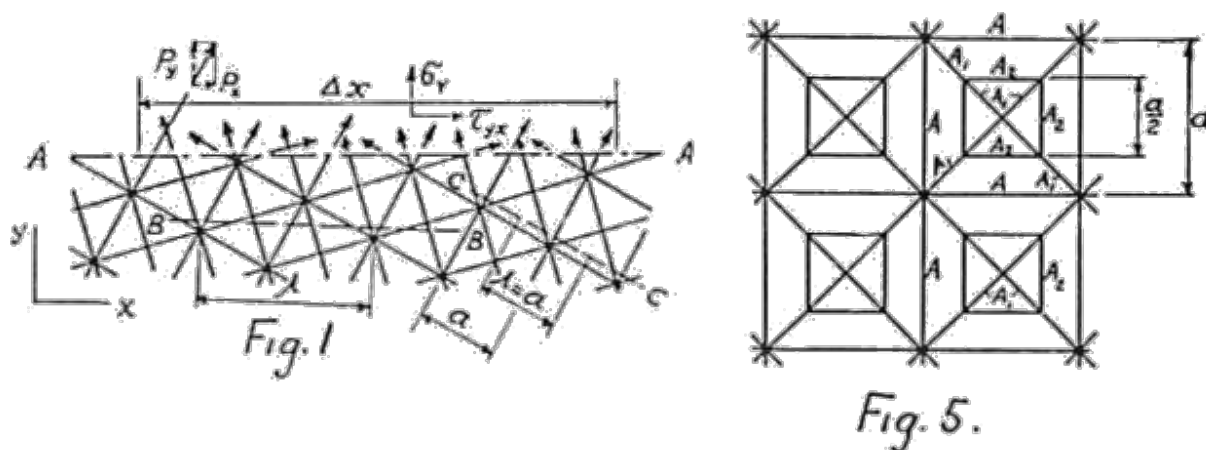
Figure 1.7 • Lattice patterns proposed by Hrennikoff (1941) to represent .

(1941). The principle consists of choosing specific periodic lattice patterns that capture the correct elastic behavior of the structure. Some patterns proposed by Hrennikoff (1941) are shown on Figure 1.7. Note that patterns such as the number 1 has a Poisson ratio close to the one of metals. By changing the geometric parameters in the pattern number 5, Hrennikoff (1941) states that any arbitrary Poisson ratio can be obtained. One of the first attempts to model the fracture of elastic materials with a lattice model is made by Roux and Guyon (1985) and Herrmann et al. (1989). These works use a periodic network of beams with a square pattern. Beams are given random brittle failure thresholds in tension and bending. This discrete model shows different cracking regimes during a loading: a first "controlled regime dominated by disorder" corresponding to the diffuse micro-cracking phase, then after reaching the brittle threshold (the peak stress is reached), a catastrophic failure happens. Inspired by particular models, Bažant et al. (1990) proposed a lattice model which accounts for the material heterogeneous meso-structure through random particle generation. This model correctly reproduces micro-cracking and its localization. It also displays the size effect observed in quasi-brittle materials. Based on the work of Herrmann et al. (1989) and Herrmann and Roux (1990), Schlangen and van Mier (1992) used a network of brittle beams with a triangular pattern to model concrete specimens. The authors compare two means to introduce heterogeneities: assigning random failure to the beam and assigning different mechanical properties to the aggregates, matrix, and bond zones. The authors found that both approaches accurately predict the fracture pattern. The results of Schlangen and van Mier (1992) using random bar strength are represented on Figure 1.8 along with experimental results.
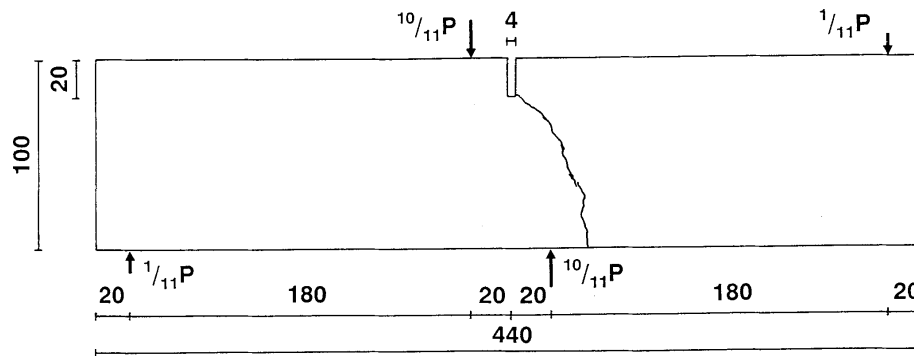
(a) Experiment
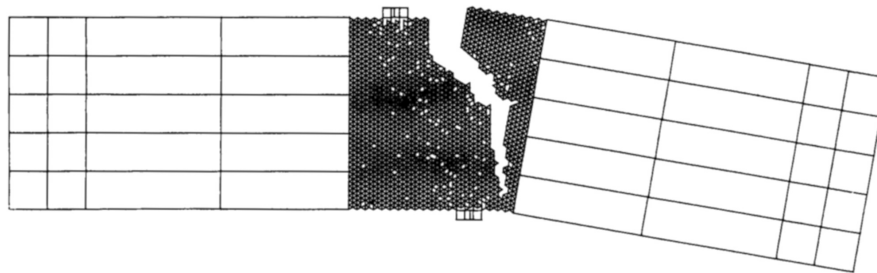
(b) Lattice model

Figure 1.8 • Comparison of the lattice model with experiments during a four-point shear test (adapted from Schlangen and van Mier (1992)).

2.2   Particulate models

The particulate discrete models are mostly based on the Distinct Element Method proposed by Cundall and Strack (1979). This method considers an assembly of rigid discs in 2D and spheres in 3D. Each particle has a mass and is subjected to inertial effect; thus, the Distinct Element Method is a dynamic model. As shown on Figure 1.9, the only interactions between the particles are the contacts. The motion of each particle are tracked individually. In order to model an elastic material with this method, Kawai (1978) proposed to introduce cohesion between rigid bodies. Instead of considering the contact between the rigid bodies, the authors consider that they are linked with spring in the contact zone. Even if this model is based on an assembly of rigid bodies, it is closer to a lattice method in its implementation. Meguro and Hakuno (1989) also modified the Distinct Element Method with the objective to model concrete structure. In their model, particles are linked with normal and tangential springs at their interface. Moreover, the springs can fail in tension to represent the creation of a crack. However, a failed spring keeps its stiffness when subjected to compression to model crack closure effects. Some bi-dimensional results on the compression of a concrete specimen are presented in Figure 1.10.

2.3   Hybrid models

Even if the boundary between particulate and lattice models is often thin, the model that combines both approach to model quasi-brittle material is proposed by D'Addetta et al.
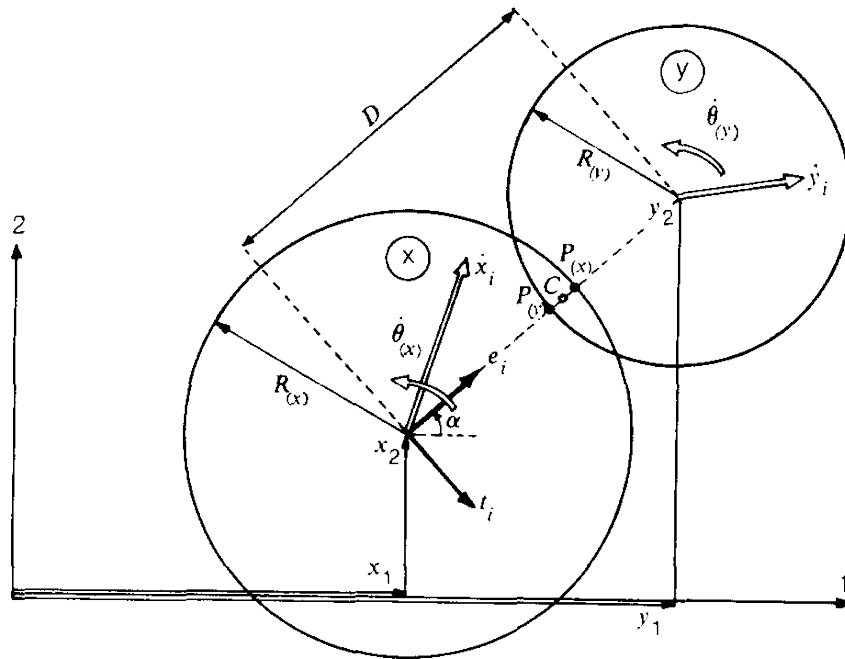
Figure 1.9 • Particle interactions in the discrete model of Cundall and Strack (1979).

Upper Row : Particle distribution
Middle Row : Mortar-spring distribution
Bottom Row : Velocity distribution
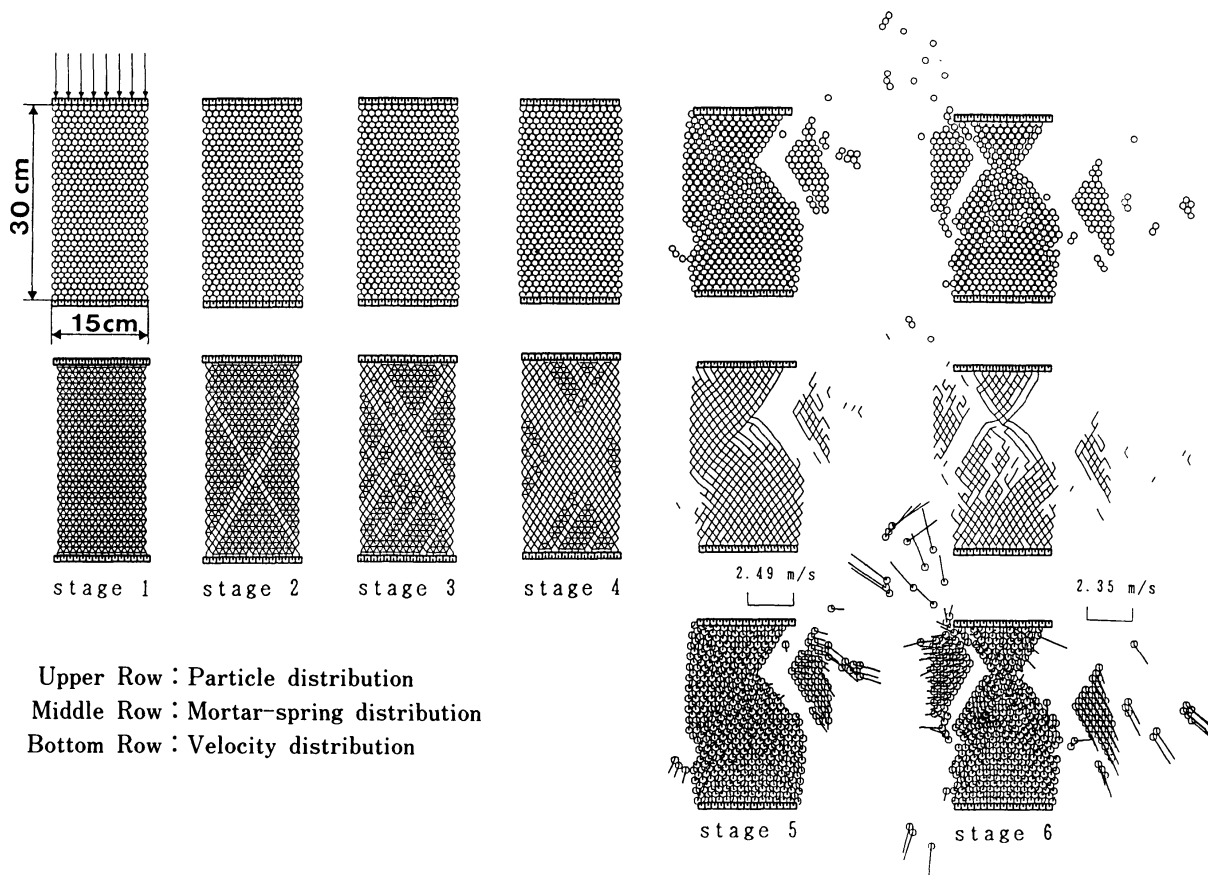
Figure 1.10 • Fracture process during a compression test using a particulate method (Meguro & Hakuno, 1989).
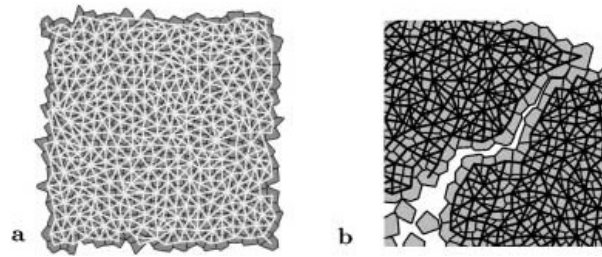
Figure 1.11 • Hybrid model where rigid polygonal particles are linked by beam (D'Addetta et al., 2002).

(2002). This discrete model is an assembly of rigid particles linked by a network of beams to obtain cohesion. Beam failure is governed by a combination of the beam elongation and the rotations of its particles and his parametrized by two constant thresholds. Instead of considering the particle elastic, D'Addetta et al. (2002) choose to let particles virtually interpenetrate. Contact forces are applied to the particles when an interpenetration occurs and directly relate to the surface/volume of interpenetration. The authors concluded that hybrid models are promising to model and understand the failure processes of concrete or ceramics. Since then, the hybrid models continue to be developed in particular through the works of Delaplace (2008), Grassl and Jirásek (2010), Cusatis et al. (2011b, 2011a), Vassaux et al. (2016), and Pathirage et al. (2023).

3 Continuous damage models

Continuous models are another category of models used to represent the behavior of quasi-brittle materials. They account for the material mechanical degradation during loading, including damage initiation (Lemaitre, 1992; Krajcinovic, 1996; Lemaitre & Desmorat, 2005; Murakami, 2012). Unlike discrete models, continuous models provides a continuous description of the material. They do not explicitly account for the micro-scale phenomena but provides their averaged representation at the macroscopic scale.

Section 3.1 gives an overview of the different progress in the formulation of damage models. Then, Section 3.2 explains the formulation of a damage model in the framework in the thermodynamics of irreversible process. Section 3.3 discuss the transition to structure by focusing on non-local damage. Finally, a brief overview on the formulation of material models using a data-driven approach is presented in Section 3.4.

3.1 An overview on the formulation of damage models

This subsection gives an overview of the growth and evolution of continuum damage mechanics. More details on continuum damage mechanics are available in classical references (Kachanov, 1986; Krajcinovic & Lemaitre, 1987; Lemaitre, 1996; Lemaitre & Desmorat, 2005; Murakami, 2012).

The first occurrence of a variable to describe the material mechanical degradation is in the work of Kachanov (1958) where a scalar damage variable is used to account for the degradation of the material during a creep loading. As explained by Lemaitre (1984), the

damage variable has been used in the seventies to formulate constitutive equation in the framework of thermodynamics for different phenomena: low-cycle fatigue (Lemaitre, 1971), coupling between damage and creep (Leckie & Hayhurst, 1974; Hult, 1974), high-cycle fatigue (Chaboche, 1974), creep-fatigue interaction (Lemaitre & Chaboche, 1975), and ductile plastic damage (Lemaitre & Dufailly, 1977). This representation of mechanical degradation has been applied to model quasi-brittle materials such as concrete (Mazars, 1986; Lubliner et al., 1989; Mazars & Pijaudier-Cabot, 1989; Grassl & Jirásek, 2006).

Effective stress.   Rabotnov (1969) introduced the notion of effective stress $\tilde{\sigma}$ to discuss tertiary creep. Lemaitre (1971) and Chaboche (1978, 1979) extended it to the coupling with elasticity and with plasticity. Let us introduce the area unaffected by damage noted $\tilde{S} = S - S_D$, where S is an elementary area and S_D is the damaged part of S. The effective stress is the stress acting on the area $\tilde{S}$ which carry the load. Thus, applying the force equilibrium

$$\tilde{\sigma}\tilde{S} = \sigma S \implies \tilde{\sigma} = \frac{\sigma}{1 - D}, \qquad \text{where } D = 1 - \frac{\tilde{S}}{S}. \tag{1.1}$$

The variable D is the damage variable and represents the degradation state of the material. As specified by Cordebois and Sidoroff (1982), the definition of the effective stress can be extended to anisotropic damage

$$\tilde{\sigma} = \mathbf{M}(\mathbf{D}) : \sigma = \sigma : \mathbf{M}(\mathbf{D}), \tag{1.2}$$

where $\mathbf{M}$ is a fourth-order tensor with the minor and major index symmetries. The original definition is recovered for $\mathbf{M}(D) = (1 - D)\mathbf{I}$, where $\mathbf{I}$ is the fourth-order identity.

Principle of strain equivalence.   Lemaitre (1971, 1985) proposed the principle of strain equivalence. According to Lemaitre et al. (2009), "it states that the strain constitutive equations of a damaged material is derived from the same formalism as for a non-damaged material except that the stress is replaced by the effective stress". It means that the deformation of the undamaged material is equal to the deformation of the damaged material,

$$\tilde{\sigma} = \mathbf{E}_0 : \varepsilon \iff \sigma = \tilde{\mathbf{E}} : \varepsilon. \tag{1.3}$$

Note that the strain equivalence in used as the basis to build most of the models presented in the remainder of this section. However, the direct generalization of this principle (combined with the effective stress) is not straightforward as it does not lead to a correct elastic potential (Cordebois & Sidoroff, 1982). There is also a principle of stress equivalence proposed by Simo and Ju (1987) and a principle of energy equivalence (Cordebois & Sidoroff, 1982). The latter have been applied in the works of Chow and Wang (1987) and Ju (1989), amongst others, and extended by Saanouni et al. (1994).

Normality rule.   In parallel, developments have been made on the side of the evolution law. Hill (1967) proposed the use of a normality rule for the evolution of internal variables. For plasticity, applying the normality rule to the yield function is equivalent to applying the principle of maximum plastic work (Hill, 1948). This work was further formalized in the

framework of Standard Generalized Materials by Halphen and Son Nguyen (1975). In this framework, the evolution of each internal variable is obtained by applying the normality rule to a pseudo-dissipation potential (Germain et al., 1983).

Damage evolution laws. The normality rule has been applied to construct various associated evolution law for isotropic damage (Marigo, 1981) and anisotropic damage (Halm & Dragon, 1996, 1998; Murakami & Kamiya, 1997). Yet, there is no principle of maximum dissipation in damage mechanics: the damage is not necessarily normal to the damage yield surface. Thus, various models use non-associated models (Lemaitre et al., 2000). To go even further, other models are non-standard, meaning that the evolution law does not derive from a potential. Examples of such models are the isotropic damage models of Mazars (1984) and Fichant et al. (1999) or the anisotropic one of Desmorat (2016).

Unilateral effect. In addition to the development of the framework of continuum damage mechanics, research efforts also concentrate on other phenomena. For quasi-brittle materials, we have seen that the unilateral effect is important (see Figure 1.2). One of the first attempt to model this phenomenon is the work of Ladevèze (1983b) and Ladeveze and Lemaitre (1984) as well as the one of Horii and Nemat-Nasser (1983), followed by Ortiz (1985). Yet, the modeling of the unilateral effect is complicated, and several early studies have inconsistencies (see the works of Chaboche (1992), Carol and Willam (1996), Cormery and Welemane (2002), and Challamel et al. (2006)). In order to be consistent with thermodynamics, Lemaitre and Desmorat (2005) and Desmorat et al. (2007) proposed two modeling constraints

- do not introduce any new damage variable to specifically model crack closure effects (since a thermodynamics damage variable represents the state of micro-cracking, whatever the loading sign), and

- the damage variable must influence differently the behavior in tension and in compression.

Most of existing models are based on a decomposition of strain or stress into a positive part and a negative part. The modeling of this phenomenon is still at the core of recent contributions (Cormery & Welemane, 2010; Goidescu et al., 2013; Desmorat & Desmorat, 2016). The crack closure effect has also been studied using micro-mechanics in the early works of Walsh (1965a, 1965b), Kachanov (1980), and Kachanov (1982), and more recently by Pensée et al. (2002), Cormery and Welemane (2010), and Goidescu et al. (2013)). For instance, Desmorat and Desmorat (2016) proposed a general framework to account for crack closure effect with open and closed cracks in 2D. The authors show that a single second-order tensor is sufficient to represent the effect of both open and closed frictionless cracks (also called "lubricated cracks"). In the previous presented works, the closed cracks are often supposed to be frictionless. Yet, we have recalled that friction between crack faces induces permanent strains (Andrieux et al., 1986). This effect is often accounted for through plasticity (Lubliner et al., 1989; Jason et al., 2006; Ragueneau et al., 2006; Richard et al., 2010; Richard & Ragueneau, 2013; Benelfellah, 2013).

Following the work of Willam et al. (1989), Angrand (2016) proposed a method based on non-proportional loadings to check whether there is any inconsistency regarding unilateral effect. The idea consists in applying square loadings in the space of strain eigenvalues to a material point. Any discontinuity in the stress response (in the strain-stress curves) indicates an inconsistency in the model.

3.2 Formulating a damage model in the framework of thermodynamics

Most continuous models can be written in the framework of the thermodynamics of irreversible processes. It enables to formulate a damage model in three main steps (Lemaitre & Chaboche, 1985),

1. the definition of the state variables, which represents the physical state of the material,

2. the definition of the state potential, which describes the relation between each state variable and their associated thermodynamic forces,

3. the definition of the dissipation potential, which describes the evolution laws for each state variable through their dissipation mechanisms[1].

The goal of the following sections is to detail each step of this process.

3.2.1 State variables

The first step to formulate a model in the thermodynamics framework consists in choosing mathematical variables to describe the state of the system. To model elasticity, the first (observable) state variable is the strain tensor ε which represents the deformation of the material. The degradation of the material is another change of state, which is accounted for by introducing a damage variable **D**. The damage variable is an internal state variable associated with a dissipative phenomenon, whereas strain is an observable state variable.

The choice of the damage variable is important as the model is only able to account for the information given by this variable. In particular, the model will only be able to account for the change of symmetry that the variable can represent. Thus, the tensorial nature of the damage variable is widely discussed in classical literature (Vakulenko & Kachanov, 1971; Chaboche, 1979; Leckie & Onat, 1981; Chaboche, 1984; Lemaitre & Chaboche, 1985; Murakami, 1988; Ramtani et al., 1992) and is still discussed in recent works (Cormery & Welemane, 2010; Desmorat & Desmorat, 2016; Dormieux & Kondo, 2016; Fassin et al., 2019; Oliver-Leblond et al., 2021). The main question is whether the mechanical degradation of the material can be represented

- by a scalar variable, as in most classical damage models (Kachanov, 1958; Rabotnov, 1969; Lemaitre, 1984),

- by a single second-order tensor (Murakami & Ohno, 1978; Cordebois & Sidoroff, 1980, 1982; Murakami, 1988; Ramtani et al., 1992; Kachanov, 1993; Halm & Dragon, 1996;

---

[1]Note that the second principle of thermodynamics constrains the choice of the dissipation potential, *i.e.* the evolution laws, as it must be positive.

Papa & Taliercio, 1996; Lemaitre et al., 2000; Lemaitre & Desmorat, 2005; Desmorat et al., 2018),

- by two second-order tensors (Ladevèze, 1983b, 1995; Desmorat & Desmorat, 2016), or

- by a fourth-order tensor (Chaboche, 1978, 1979; Krajcinovic, 1985; Kachanov, 1993).

The definition of the damage variable is addressed through Chapter 2, Chapter 4, and, to a lesser extent, in Chapter 5.

In the modeling of quasi-brittle materials, the simplest choice is to use a single scalar damage variable. As it cannot account for any orientation of the micro-cracking, a model using such a variable is called an isotropic damage model. Thanks to their simplicity, isotropic damage models are often used to compute the degradation of concrete structures (Mazars, 1984; Grassl & Jirásek, 2006; Richard & Ragueneau, 2013). These models assume that the material behavior remains isotropic when damaging. In accordance with damage measurements (Ramtani et al., 1992; Lemaitre et al., 2000), micro-mechanics studies of micro-cracked media, such as the ones of Chaboche (1984), Lubarda and Krajcinovic (1993), and Kachanov (1993), show indeed that damage is not isotropic and has to be represented by a damage tensor physically linked to the crack density:

- a fourth-order tensor in the 3D case,

- a second-order tensor in the simpler 2D case with lubricated non-interacting cracks.

3.2.2 State potential

The second step to formulate a damage model in the framework of thermodynamics consists in defining the state potential. Let us take the Helmholtz specific free energy as the state potential. In general, the state potential writes

$$\rho\psi(\varepsilon, \mathbf{D}) = \frac{1}{2}\varepsilon : \tilde{\mathbf{E}}(\mathbf{D}) : \varepsilon. \tag{1.4}$$

The state model is derived from the state potential (see the books of Lemaitre and Desmorat (2005) and Lemaitre et al. (2009))

$$\boldsymbol{\sigma} = \rho\frac{\partial\psi}{\partial\varepsilon} \implies \boldsymbol{\sigma} = \tilde{\mathbf{E}}(\mathbf{D}) : \varepsilon, \qquad -\mathbf{Y} = \rho\frac{\partial\psi}{\partial\mathbf{D}} \implies \mathbf{Y} = -\frac{1}{2}\varepsilon : \frac{\partial\tilde{\mathbf{E}}(\mathbf{D})}{\partial\mathbf{D}} : \varepsilon, \tag{1.5}$$

where the stress $\boldsymbol{\sigma}$ is the thermodynamic force associated with strain ε and relates to it through the Hooke's law (with the effective elasticity $\tilde{\mathbf{E}}(\mathbf{D})$ affected by damage), and the energy density release rate $\mathbf{Y}$ is thermodynamic force associated with damage. In the state model, the effective elasticity tensor $\tilde{\mathbf{E}}(\mathbf{D})$ is introduced. To formulate a state model, this tensorial function of damage has to be defined and identified based on experimental data. It is the main objective of Chapter 5.

Examples of state potentials. The most classic choice for the state potential is

$$\rho\psi(\boldsymbol{\varepsilon}, D) = \frac{1}{2}\boldsymbol{\varepsilon} : (1-D)\mathbf{E}_0 : \boldsymbol{\varepsilon}, \qquad \mathbf{E}(D) = (1-D)\mathbf{E}_0 \tag{1.6}$$

As specified, this type of model does not enable to account for damage-induced anisotropy. Dragon et al. (1994) proposed, also detailed by Halm and Dragon (1996), to define the state potential as a polynomial of (joint) invariants of the state variable

$$\rho\psi = \frac{1}{2}\lambda(\operatorname{tr}\boldsymbol{\varepsilon})^2 + \mu\boldsymbol{\varepsilon} : \boldsymbol{\varepsilon} + g\boldsymbol{\varepsilon} : \mathbf{D} + \alpha(\operatorname{tr}\boldsymbol{\varepsilon})\boldsymbol{\varepsilon} : \mathbf{D} + 2\beta\operatorname{tr}(\boldsymbol{\varepsilon}\boldsymbol{\varepsilon}\mathbf{D}) \tag{1.7}$$

where λ and μ are the Lamé constants, α, β and g are supplementary constants to describe the coupling between strain and damage.

Examples with unilateral effect. Until now, the presented state models neglected the unilateral effect. In this paragraph, different state potential accounting for it are presented. For a unidirectional isotropic model, a first approach consists in splitting the strain into a positive and a negative part

$$\rho\psi = \frac{1}{2}(1-D)E\langle\varepsilon\rangle_+^2 + \frac{1}{2}(1-hD)E : \langle\varepsilon\rangle_-^2 \tag{1.8}$$

where E is the Young modulus, and ε is the 1D strain, and $h \in [0,1]$ is a parameter to control the total or partial stiffness recovery in compression. The stiffness recovery in compression is either total (unilateral effect) when $h = 0$, or partial (quasi-unilateral effect) when $h > 0$. This type of decomposition cannot be directly generalized to the 2D and 3D cases. In those cases, one must also rely on the hydrostatic/deviatoric split of the strain tensor

$$\rho\psi = \frac{1}{2}\left(2\mu(1-D)\boldsymbol{\varepsilon}' : \boldsymbol{\varepsilon}' + \kappa(1-D)\langle\operatorname{tr}\boldsymbol{\varepsilon}\rangle_+^2 - \kappa(1-hD)\langle-\operatorname{tr}\boldsymbol{\varepsilon}\rangle_+^2\right) \tag{1.9}$$

where μ is the shear modulus and κ is the bulk modulus. In this case, the crack opening or closure does not impact the deviatoric part of stress. This method can also be extended to anisotropic damage model. For instance, the state model of Desmorat (2016), based on the work of Ladevèze (1983b), in 3D is defined as

$$\rho\psi = \frac{1}{2}\left(2\mu\left((\mathbf{H}^{-1}\boldsymbol{\varepsilon}) : (\mathbf{H}^{-1}\boldsymbol{\varepsilon}) - \frac{(\mathbf{H}^{-2} : \boldsymbol{\varepsilon})^2}{\operatorname{tr}\mathbf{H}^{-2}}\right) + \kappa\left(\frac{3\langle\operatorname{tr}\boldsymbol{\varepsilon}\rangle_+^2}{\operatorname{tr}\mathbf{H}^2} - \langle-\operatorname{tr}\boldsymbol{\varepsilon}\rangle_+^2\right)\right) \tag{1.10}$$

where $\mathbf{H} = (\mathbf{1}-\mathbf{D})^{-\frac{1}{2}}$. Another example of anisotropic damage model accounting for the unilateral effect the work of Badel et al. (2007). There is still an issue in this kind of model: the derivative of stress with respect to strain is discontinuous when going from the open cracks to close cracks and conversely. More recently, Jefferson and Mihai (2015) proposed a regularized version of this technique and Zafati and Richard (2019) applied it to model the behavior of concrete (based on the work of Desmorat (2016)). Globally, the idea consists in using a regularized positive part function.

3.2.3 Damage criterion

The damage criterion, also called the damage growth criterion, is the component of the model which tells whether the material is currently damaging. The damage criterion function, denoted $f(\varepsilon, \mathbf{D})$, is such that

$$f(\varepsilon, \mathbf{D}) < 0 \implies \text{damage stays constant, and } f(\varepsilon, \mathbf{D}) = 0 \implies \text{damage grows.} \qquad (1.11)$$

It describes whether the damage grows for any value of the state variables. Here, we will focus on criteria based on the strains. In most work on quasi-brittle materials, the damage criterion function has the form

$$f(\varepsilon, \mathbf{D}) = \varepsilon_{\text{eq}} - C(\mathbf{D}) \qquad (1.12)$$

where ε_{eq} is an equivalent strain and $C(\mathbf{D})$ is the consolidation function[2], which accounts for evolution of the damage threshold with damage, *i.e.* the evolution of the damage yield surface. This type of criterion function cannot account for an anisotropic growth of the yield surface. As the consolidation is a scalar, the yield surface will keep the same form and the growth of damage only acts as a homothety on this form. Here, we only cover the definition of equivalent strain ε_{eq} as the choice of $C(\mathbf{D})$ directly relates to the evolution law. It means that we concentrate on the definition of the initial damage criterion (and not how the criterion is affected by damage).

Examples of damage criteria for quasi-brittle materials are presented in the following paragraphs. Most of those yield criteria are based on invariants of the stress or the strain

$$I_1(\varepsilon) = \text{tr}(\varepsilon) = \varepsilon : \mathbf{1}, \qquad I_2(\varepsilon) = \text{tr}(\varepsilon^2) = \varepsilon : \varepsilon. \qquad (1.13)$$

de Vree. Let us start by introducing de Vree criterion (de Vree et al., 1995), which is a modification of the von Mises criterion

$$\varepsilon_{\text{dV}} = \frac{\gamma - 1}{2\gamma(1 - 2\nu)} I_1(\varepsilon) + \frac{1}{2\gamma} \sqrt{\left(\frac{\gamma - 1}{1 - 2\nu} I_1(\varepsilon) \right)^2 + \frac{12\gamma}{(1 + \nu)^2} I_2(\varepsilon')} \qquad (1.14)$$

where γ is the ratio of the tensile and compressive strength.

Mazars. Mazars (1984) considered that the damage in concrete is purely due to local extension of the material. Thus, Mazars (1984) defined another equivalent strain as

$$\varepsilon_{\text{Maz}} = \sqrt{\langle \varepsilon \rangle_+ : \langle \varepsilon \rangle_+}, \qquad \langle \varepsilon \rangle_+ = \sum_{i=1}^{d} \langle \varepsilon_i \rangle_+ \boldsymbol{v}_i \otimes \boldsymbol{v}_i, \qquad \langle \varepsilon_i \rangle_+ = \max(\varepsilon_i, 0), \qquad (1.15)$$

where $\langle \varepsilon \rangle_+$ is the positive part of the strain tensor, d is the dimension, ε_i is i-th eigenvalue of strain, and $\boldsymbol{v}_i$ is i-th eigenvector of strain.

---

[2]The consolidation function is often denoted $\kappa(\mathbf{D})$ in the classical literature. Here, κ will be used to define the bulk modulus.

Drucker-Prager. Another criterion based on invariants —that has been used for soils, rocks, concrete, amongst others— is the Drucker-Prager criterion (Drucker & Prager, 1952). It is defined such that

$$f(\varepsilon, \mathbf{0}) = 0 \iff \sqrt{I_2(\varepsilon')} = \varepsilon_y + k' I_1(\varepsilon), \tag{1.16}$$

where k' is a parameter of the equivalent strain. It leads to

$$\varepsilon_{\mathrm{DP}} = \varepsilon_{\mathrm{vM}} + k I_1(\varepsilon) \tag{1.17}$$

where $\varepsilon_{\mathrm{vM}} = \sqrt{2 I_2(\varepsilon')}$ is the von Mises equivalent strain (in 2D), and k is a coefficient associated to the hydrostatic strain. Various extension of the Drucker-Prager criterion exists and some a presented in the work of Alejano and Bobet (2012).

Other criteria. The early work of Ottosen (1977) introduces a four-parameter criterion for concrete. Chow and Wang (1987) proposed a damage criterion function based on the energy release rate **Y**. More recently, François (2008) presents other two-parameter criteria and compares them to the experimental data from Kupfer et al. (1969). Ragueneau et al. (2008) also compared several damage criteria function based on Mazars equivalent strain to the same experimental data. Furthermore, Mattiello and Desmorat (2021) presents different functions that can be used as yield criterion, with a particular focus on a specific invariant: the Lode angle. Kolupaev (2018) provides numerous equivalent stresses that can be adapted into equivalent strain definition.

3.2.4 Dissipation potential and damage evolution

The evolution of each internal state variable must be described as a function of the other state variables. The evolution laws are constrained by the second principle of thermodynamics. According to the second principle, the evolution law must be such that the intrinsic dissipation $\mathscr{D}$ is always positive. Thus,

$$\mathscr{D} = -\rho \frac{\partial \psi}{\partial \mathbf{D}} : \dot{\mathbf{D}} = \mathbf{Y} : \dot{\mathbf{D}} \geqslant 0, \qquad \mathbf{Y} = -\rho \frac{\partial \psi}{\partial \mathbf{D}}, \tag{1.18}$$

where $\dot{\mathbf{D}}$ is the temporal derivative of damage.

Associated damage evolution. The framework of Generalized Standard Materials (Halphen & Son Nguyen, 1975) provides generic structure of evolution law ensuring that the second principle is satisfied. In this framework, a dissipation potential is used to define the evolution law. For associated damage models, the dissipation potential is supposed to be a characteristic function of the damage criterion function $f(\varepsilon, \mathbf{D})$. In practice, the damage evolution law, is supposed to derive from the normality rule applied to the damage criterion function (Ladevèze, 1983b),

$$\dot{\mathbf{D}} = \dot{\lambda}_{\mathbf{D}} \frac{\partial f}{\partial \mathbf{Y}} \tag{1.19}$$

where $\dot{\lambda}_{\mathbf{D}}$ is the damage multiplier satisfying the following Kuhn-Tucker conditions

$$f(\varepsilon, \mathbf{D}) \leqslant 0, \qquad \dot{\lambda}_{\mathbf{D}} \geqslant 0, \qquad f(\varepsilon, \mathbf{D}) \dot{\lambda}_{\mathbf{D}} = 0. \tag{1.20}$$

This kind of damage evolution law is called associated damage model. While this framework clearly facilitates the formulation of an evolution law, it is restrictive as there is a unique evolution law per damage criterion function.

Non-associated damage evolution. A less restrictive framework is provided by the non-associated damage framework. The damage evolution is no longer normal to the yield surface but to an arbitrary evolution potential denoted $\mathscr{F}$. In this case, the damage evolution law is given by

$$\dot{\mathbf{D}} = \dot{\lambda}_{\mathbf{D}} \frac{\partial \mathscr{F}}{\partial \mathbf{Y}}, \qquad \mathbf{Y} = -\rho \frac{\partial \psi}{\partial \mathbf{D}}, \tag{1.21}$$

where $\dot{\lambda}_{\mathbf{D}}$ is still obtained from the Kuhn-Tucker conditions in Equation (1.20) which gives the expression of the damage multiplier as a function of the damage criterion function. Using the evolution potential corresponds to the most general case handled by the framework of Generalized Standard Materials (Halphen & Son Nguyen, 1975). In order to satisfy the second principle, the evolution potential depends on the state variables $\mathscr{F}(\varepsilon, \mathbf{D}, ...)$. It must contain the origin $\mathscr{F}(\mathbf{0}, \mathbf{0}, ...) = 0$, be positive $\mathscr{F}(\varepsilon, \mathbf{D}, ...) \geqslant 0$, and be convex in the thermodynamic forces.

Non-standard damage evolution. For further flexibility, the damage evolution might not derive from an evolution potential. In this case, the damage evolution law is defined as an arbitrary function of the state variables and thermodynamic forces

$$\dot{\mathbf{D}}(\varepsilon, \mathbf{D}) = ... \tag{1.22}$$

Usually, the damage evolution law is given as

$$\dot{\mathbf{D}} = \dot{\lambda}_{\mathbf{D}} \mathbf{P}_{\mathbf{D}}, \tag{1.23}$$

where $\dot{\lambda}_{\mathbf{D}}$ is the damage multiplier, which still verifies the Khun-Tucker conditions in Equation (1.20), and $\mathbf{P}_{\mathbf{D}}$ is the damage direction which depends on strain and may also depend on damage. For instance, the first anisotropic damage model studied by Desmorat (2016) uses the damaging direction $\mathbf{P}_{\mathbf{D}} = \langle \varepsilon \rangle_+$ as proposed by Ramtani et al. (1992). However, the normality assumption is lifted, so it is important to note that the positivity of the dissipation, *i.e.* the second principle, is not ensured anymore and must be proved.

3.2.5 Summary: Structure of a damage model

To summarize, a damage model is assembled from several components. The first one is the definition of a set of state variables $\mathcal{V} = \{\varepsilon, \mathbf{D}, ...\}$. Then, at least two scalar functions are required

- a state potential $\rho\psi(\varepsilon, \mathbf{D})$ from which the associated thermodynamic force are computed ($\sigma = \rho \frac{\partial \psi}{\partial \varepsilon}$, $\mathbf{Y} = -\rho \frac{\partial \psi}{\partial \mathbf{D}}$, ...),

- a damage criterion function $f(\varepsilon, \mathbf{D})$, also called yield surface,

For the evolution of each internal variables, only damage **D** in the simplest case, there are three possibilities.

- In the associated case, a dissipation potential $\mathscr{F}$ is defined as the criterion function $f(\varepsilon, \mathbf{D})$. It gives the damage evolution law, or damage flow rule, as $\dot{\mathbf{D}} = \dot{\lambda}\frac{\partial f}{\partial \mathbf{Y}}$.

- In the non-associated case, an arbitrary evolution potential $\mathscr{F}$ that is positive and convex in the thermodynamic forces is defined. It gives the damage evolution law, or damage flow rule, as $\dot{\mathbf{D}} = \dot{\lambda}\frac{\partial \mathscr{F}}{\partial \mathbf{Y}}$.

- In the non-standard case, an arbitrary damage evolution law $\dot{\mathbf{D}}$ is directly defined as a function of the state variables (and thermodynamic forces). In this case, the second principle, *i.e.* the positivity of the dissipation, must be checked.

3.3   Non-local damage

Until now, the discussion was centered on the behavior of a material point. However, those models are usually applied at the scale of a whole structure. This brings a new issue with strain-softening material: there is a loss of ellipticity of the boundary value problem making the problem ill-posed (Hadamard, 1903; Rudnicki & Rice, 1975; Benallal et al., 1989; Borré & Maier, 1989; Benallal et al., 1993). For applications to concrete, we refer to the work of Jirásek (2002, 2007) and Masseron et al. (2022).

This issue manifests itself in the numerical resolution of a mechanical problem with local damage model (Bažant, 1976). For a uni-dimensional problem, the damage variable is defined for each element of the spatial discretization. When damage occurs, it is the whole volume of the element that is affected by damage, *i.e.* which dissipate energy. Once an element starts to damage, the remaining of the domain is gradually unloaded and the strain localizes in this element. Thus, for any discretization, the damage will always localize in one element. The global dissipated energy, which is equal to the energy dissipated during the damaging of the element, will change with the discretization size. It makes the mechanical response dependent on numerical parameters.

To solve this issue, non-local damage models have been proposed (Bažant & Jirásek, 2002; Jirásek, 2004; Pijaudier-Cabot & Grégoire, 2014). The principle consists in limiting the damage localization by replacing the damage driving mechanical quantity, often the local equivalent strain $\varepsilon_{\mathrm{eq}}(\boldsymbol{x})$, by its non-local counterpart $\bar{\varepsilon}_{\mathrm{eq}}(\boldsymbol{x})$. The non-local damage driving quantity is, in general, a spatially averaged version of the local damage driving quantity. It prevents the localization of damage in an infinitely thin region; thus, keeping the problem well-posed during the softening phase. From a numerical point of view, the results should be independent of the numerical discretization and parameters (or at-least have convergence properties). For instance, changing the spatial discretization should not affect the resulting damage field. Another important criterion is that the solution must be consistent with experimental results (in particular with the size effect (Le Bellégo et al., 2003)).

Non-local integral.   The non-local integral approach, proposed by Pijaudier-Cabot and Bažant (1987), is a first mean to solve this issue. To achieve that, Pijaudier-Cabot and Bažant

(1987), inspired by the work of (Eringen & Edelen, 1972), proposed to replace the equivalent strain ε_{eq} in the evolution law by its non-local counterpart

$$\bar{\varepsilon}_{\text{eq}}(\boldsymbol{x}) = \frac{1}{V_{\Omega}(\boldsymbol{x})} \int_{\Omega} w(\|\boldsymbol{x} - \boldsymbol{y}\| / \ell_c) \varepsilon_{\text{eq}}(\boldsymbol{y}) \mathrm{d}\boldsymbol{y}, \qquad V_{\Omega}(\boldsymbol{x}) = \int_{\Omega} w(\|\boldsymbol{x} - \boldsymbol{y}\| / \ell_c) \mathrm{d}\boldsymbol{y} \qquad (1.24)$$

where Ω denotes the spatial domain of the structure, w is the weight function, and ℓ_c is a characteristic length parameter. The weight function w is usually taken as the Gauss distribution function

$$w(\|\boldsymbol{x} - \boldsymbol{y}\| / \ell_c) = \exp\left(-\frac{4\|\boldsymbol{x} - \boldsymbol{y}\|^2}{\ell_c^2}\right). \qquad (1.25)$$

Non-local gradient. Non-local gradient models are another type of localization limiters (Peerlings et al., 1996). The equivalent strain in the damage evolution law is still replaced by its non-local counterpart. In this case, the non-local equivalent strain $\bar{\varepsilon}_{\text{eq}}$ is given by a partial differential equation

$$\bar{\varepsilon}_{\text{eq}}(\boldsymbol{x}) - c\nabla^2 \bar{\varepsilon}_{\text{eq}}(\boldsymbol{x}) = \varepsilon_{\text{eq}}(\boldsymbol{x}), \qquad \forall \boldsymbol{x} \in \Omega, \qquad (1.26)$$

$$\nabla \bar{\varepsilon}_{\text{eq}}(\boldsymbol{x}) \cdot \boldsymbol{n}(\boldsymbol{x}) = 0, \qquad \forall \boldsymbol{x} \in \partial\Omega, \qquad (1.27)$$

where c is homogeneous to a square length and can be related to the characteristic length ℓ_c, $\partial\Omega$ is the boundary of the domain Ω, and $\boldsymbol{n}$ is the outward-pointing normal to the boundary. Note that the boundary conditions, in Equation (1.27), is an arbitrary choice as discussed by Krayani et al. (2009). Note that Peerlings et al. (2001) shows that the non-local gradient models relates to the non-local integral models through the Green function of the partial differential equation.
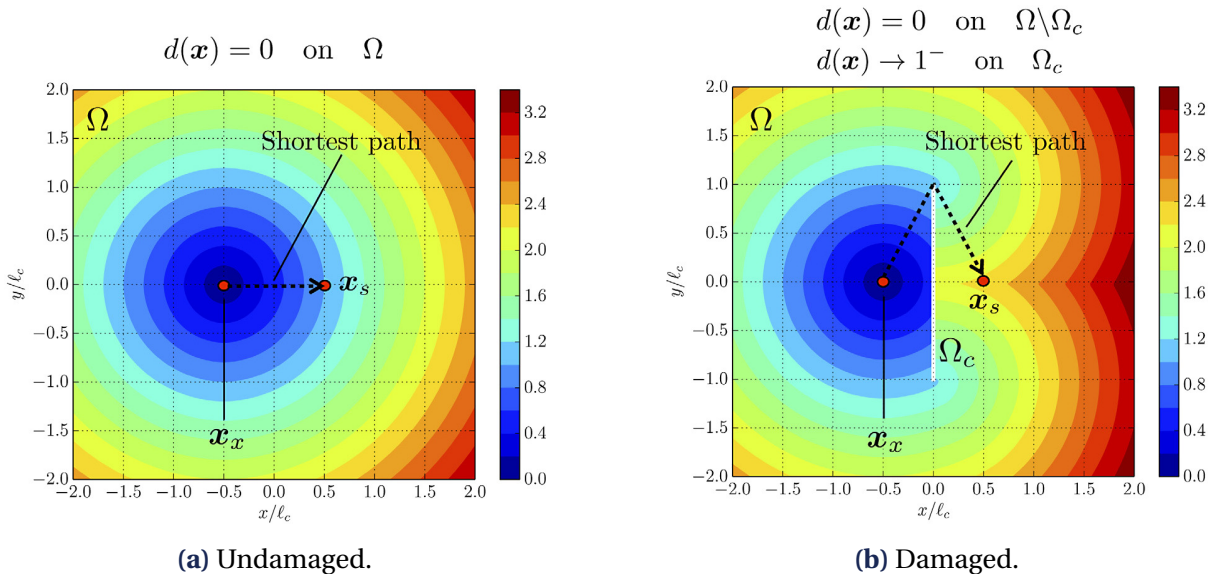

(a) Undamaged.

(b) Damaged.

Figure 1.12 • Illustration of the interaction length obtained with the non-local Eikonal approach. (Rastiello et al., 2018)

Evolving interaction length. For both integral and gradient non-local models, recent works focus on the introduction of an evolving characteristic length. In order to understand the

reason why, let us consider two points A and B geometrically close to each other and separated by a crack. An illustration of an evolving interaction length, from the Eikonal approach (Rastiello et al., 2018), is given in the Figure 1.12. This figure represents the effective distance between the red dotted point and any other point of the domain, in two configuration. The first configuration (Figure 1.12a) is the case where the material is undamaged. In this case, the effective distance between two points is given by the shortest path using the Euclidian distance. For the second configuration (Figure 1.12b), a notch is added. The strain at point x_s should not contribute much to the degradation of point at the red dot as the crack prevents the transmission of cohesive forces, *i.e.* it prevents interactions. In classic non-local models, this interaction is not prevented. Various models with an interaction length evolving with mechanical fields have been proposed in the literature to solve this issue (Geers et al., 1998; Pijaudier-Cabot et al., 2004; Simone et al., 2003; Giry et al., 2011; Desmorat et al., 2015; Poh & Sun, 2017; Rastiello et al., 2018).

Regularization of the damage field. Another method consists in directly regularizing the damage field. This is the case of the phase-field method (Francfort & Marigo, 1998; Bourdin et al., 2000; Bourdin et al., 2008). The phase-field method is based on the balance between the elastic energy and the energy dissipated by damage. Moreover, the localization of damage is constrained by a penalization of the damage gradient. Note that a related approach, called the Lip-field approach, has been recently proposed by Moës and Chevaugeon (2021) and Chevaugeon and Moës (2022) It relies on the same type of functional, yet instead of penalizing the damage gradient, the Lipschitz regularity constraint is applied to the internal variable provoking the softening. Other methods based on the regularization of the damage field are, amongst others, the Thick Level Set method (Moës et al., 2011; Bernard et al., 2012) and the more recent graded damage (Stolz, 2019; Valoroso & Stolz, 2022).

3.4 Data-driven models

During the last decade, data-driven (constitutive) models have seen a rise in popularity. These models aim to reduce the number of arbitrary modeling choices while emphasizing using (reliable) experimental data. In practice, the idea is to reconstruct the Constitutive Manifold (Ibañez et al., 2016; Ibañez et al., 2017) from the set of strain-strain couples from experimental data. This set is composed of discrete points of the Constitutive Manifold (σ_i, ε_i) and is usually called the Experimental Constitutive Manifold (ECM).

In the original data-driven approach (Kirchdoerfer & Ortiz, 2016, 2017; Carrara et al., 2020), the Constitutive Manifold is directly replaced with the Experimental Constitutive Manifold. The idea consists in finding the point of the Experimental Constitutive Manifold that best verifies the equilibrium (including the boundary conditions). This method has been formalized by Ladevèze et al. (2019) as finding the intersection between the Experimental Constitutive Manifold and the admissibility manifold $\mathscr{A}_d$, which is the manifold of the stress-strain couple verifying the equilibrium. This formalization is represented in the Figure 1.13. One of the main advantage of this method is that it is model-free. Even if this may be a promising method in some cases (Eggersmann et al., 2019), it is not capable of extrapolating outside the provided dataset as the raw data points are used. Additionally, for behavior depending
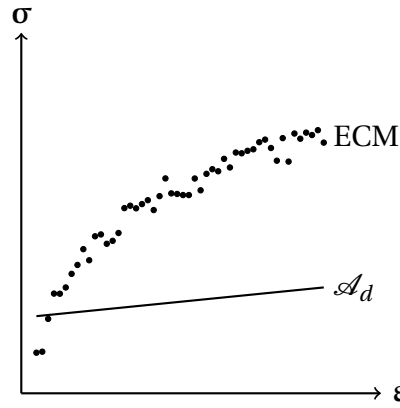
Figure 1.13 • Representation of the data-driven approach problem proposed by Kirchdoerfer and Ortiz (2016) (figure adapted from Ladevèze et al. (2019)).

on internal variables, the knowledge of the stress and strain is not sufficient to fully define the behavior and internal variables are required. Instead of directly using the Experimental Constitutive Manifold, Ibañez et al. (2017) proposed to approximate the Experimental Constitutive Manifold, using polynomials for instance. The goal is to reconstruct a continuous version of the Experimental Constitutive Manifold to obtain a less biased[3] relation between stress and strain, with possible hidden variables. Recently, there is also a strong focus on the reconstruction of the Experimental Constitutive Manifold while accounting for physical constraint (As'ad et al., 2022; Bonatti & Mohr, 2022), or even thermodynamic principles (Masi et al., 2021; Masi & Stefanou, 2023).

Let us cite the work of Ladevèze et al. (2019), Gerbaud et al. (2022), and Ladevèze et al. (2022) who concentrate on the automatic detection of hidden/internal variables for history-dependent material. Their method is based on the notion of univocity. For instance, if the data contains two times the same strain ε but associated to different stresses σ_1 and σ_2, it means that an internal state variable is necessary to correctly describe the relations

$$\sigma(\varepsilon, v_1) = \sigma_1, \qquad \sigma(\varepsilon, v_2) = \sigma_2 \qquad (1.28)$$

Most of the data-driven modeling approaches presented until now gives a black-box constitutive model. This issue is addressed by the notion of interpretable machine learning (Molnar, 2022). This subfield of machine learning aims at providing tools to obtain human-friendly explanations of the those black-box models. To go even further, some machine learning methods even enables to obtain "simple" analytical model. For instance, the sparse regression method (Tibshirani, 1996) can fit a generic polynomial to data while minimizing the number of non-zero coefficients, leading to a minimal expression for the model. Another interesting tool for constitutive modeling is the symbolic regression (Wang et al., 2019), which optimize the parameters and the mathematical structure of the model during the fitting process. Based on those methods, Brunton et al. (2016) proposes a method to obtain the system of differential equations governing of a dynamical system from measured (noised) trajectories. It uses smoothed numerical differentiation and sparse regressions to recover

---

[3]Here, it means that no unnecessary assumptions are taken. It enables to reduce/remove the so-called model error.

the equations of a dynamical system from the trajectories. This technique has already been successfully applied in numerous physic problems (for instance, see the works of Beetham and Capecelatro (2020), Zanna and Bolton (2020), and Guan et al. (2021)). A similar approach has been taken by Flaschel et al. (2021, 2023). In this work, the authors fit the data using a library of pre-determined functions to "automatically discover" the underlying state and dissipation potential.

At the other end of the scope, others researchers focused on gradually replacing components of classic models with data-driven approach. In most case, the idea consists in replacing the parts that are too complicated to model satisfyingly (see for instance the work of Bonatti and Mohr (2022)). Another example is provided by Yvonnet et al. (2022, 2023) who focus on automatically formulating an anisotropic state model (based on finite element simulations of a volume element).

3.5   Damage models based on or enriched by discrete models

Let us finally highlight some works which formulated, at-least partially, damage models based on discrete simulations. Rinaldi and Lai (2007) and Rinaldi (2013) performed a statistical analysis of a regular spring network with random mechanical fracture properties. This analysis was performed in order to define a damage variable. Delaplace (2008) proposed to use a discrete model as virtual testing machine to perform tri-tension tests on a cube specimen. The virtual tests where used to study the sensitivity of the effective bulk modulus to hydrostatic stress. More recently, Misra and Poorsolhjouy (2015) proposed a damage and plasticity model at macro-scale for granular materials based on the inter-granular interaction at microscale. The same group of authors also proposed other models with a similar approach (Misra & Singh, 2013; Singh, 2014; Misra & Singh, 2015). Challamel et al. (2015) and Hérisson (2018) proposed to "continualize" (based on asymptotic expansion) discrete lattice system to formulate a non-local elastic and non-local damage model. Finally, the work of Oliver-Leblond et al. (2021), on which this thesis is based, also used the discrete model as a virtual testing machine. Square virtual specimens were submitted to several loads. During those loadings, they studied the evolution of the effective elastic properties of the virtual specimen. In particular, they showed that a second-order tensor, instead of a fourth-order tensor, is sufficient to represent the micro-cracking even when the micro-cracks are strongly interacting.

✒ Summary of the Chapter

This chapter gives the basis for the formulation of a continuous damage model based on discrete element simulations. It introduces the experimental observations on quasi-brittle materials as well as their modeling. Experimental results from mechanical tests on quasi-brittle material show different phenomena: loss of stiffness, damage-induced anisotropy, and crack closure effects. Those phenomena are all explained by the nucleation and growth of micro-cracks. To model quasi-brittle materials, we distinguish two types of models: the discrete models and the continuous ones. The discrete models are also subdivided into three subtypes: particular, lattice and hybrid models. They provide an accurate representation of

quasi-brittle material failure. However, their computational cost limits their use to model whole structures. Continuous damage models offer an averaged view of microscale effects and are easier to applied to structure. After choosing state variable to describe the state of the material, the construction of a continuous damage model is composed of three main ingredients: the state potential, the damage criterion function, and the evolution law.

2

Mathematical overview of elasticity tensors, invariance and symmetries

This chapter provides an overview of literature on the mathematical study of elasticity tensors. In a first part, it introduces the notions of elasticity tensors, symmetry classes, invariants and covariants. Then, different reconstructions of an elasticity tensor from its covariants are proposed. Those reconstruction formulas will be the basis to formulate the state model in the next chapters. Finally, the notion of distance from a symmetry class will be introduced. It will provide a rigorous mean to justify the modeling choice such as the type of damage variable.

In physics problems, the understanding of underlying symmetry, and consequently invariance, is crucial (Curie, 1894). Yet, in mechanics problems, the symmetries are often considered by making *a priori* assumptions. However, they may also change during the problem. For instance, quasi-brittle materials are often considered isotropic when undamaged, in other words, their initial behavior is invariant by rotation. It means that their material properties can be measured in any direction, the resulting property will always be the same. Yet, when micro-cracks nucleates, *i.e.*, when the state of the material changes, the initial symmetries might be lost due to the spatial distribution of micro-cracks and their orientation. This phenomenon is the damage-induced anisotropy. In the most used damage models (scalar damage models), this changes of symmetry is neglected; thus, neglecting the behavior variation with the orientation of the loading.

In this study, one of the main goal is to correctly account for damage-induced anisotropy in the proposed damage model. This objective raises different underlying mathematical questions. This chapter aims to introduce those different questions and summarize the answers proposed in the existing literature. As the damage model will be formulated in 2D, most mathematical notions are introduced in 2D. Yet, most of them can be extended to the 3D case (often at the cost of an increased complexity). The first question, tackled in Section 1, is to define the symmetry classes of 2D elasticity tensors, and the associated invariances. The notions of invariants and covariants are also defined in this section. The second question is whether it is possible to reconstruct an elasticity tensor from its invariants and covariants. Section 2 recalls the harmonic decomposition, to address this question. A reconstruction of

orthotropic elasticity tensors derived from the harmonic decomposition is also presented. The third question centers around determining whether a given elasticity tensor possesses a specific symmetry. Section 3 tackles this question by introducing the distances to isotropy and to orthotropy. An upper-bound of the distance to orthotropy is also recalled.

1 Notations and definitions: elasticity tensor, symmetry classes and invariance

This section is dedicated to the introduction of the fundamental mathematical notions used in this chapter. We refer to the work of Forte and Vianello (1996) and Auffray et al. (2014) for the main definitions concerning group theory, symmetry classes and symmetry strata.

Elasticity tensor. An elasticity tensor is a positive-definite fourth-order tensor $\mathbf{E}$ having the index symmetries $E_{ijkl} = E_{jikl} = E_{ijlk} = E_{klij}$. The vector space

$$\mathbb{Ela}(\mathbb{R}^2) = \left\{ \mathbf{E} \mid E_{ijkl} = E_{jikl} = E_{ijlk} = E_{klij} \right\}, \tag{2.1}$$

of bi-dimensional elasticity tensors, is of dimension 6. From a mechanical point of view, this tensor represents the linear relation $\boldsymbol{\sigma} = \mathbf{E} : \boldsymbol{\varepsilon}$ between two second-order symmetric tensors, the strain $\boldsymbol{\varepsilon}$ and stress $\boldsymbol{\sigma}$ tensors.

Orthogonal transformation. Let us now introduce the orthogonal group O(2), *i.e.*, the group of orthogonal transformations,

$$\mathrm{O}(2) = \left\{ Q \in \mathbb{S}^2(\mathbb{R}^2) \mid Q^T Q = Q Q^T = \mathbf{1} \right\}. \tag{2.2}$$

From a geometric point of the view, an orthogonal transformation is either a rotation, a reflection, or a combination of a rotation and a reflection. In its matrix representation, its elements can be generated by rotation and reflection (symmetry) matrices

$$\mathbf{r}(\theta) = \begin{bmatrix} \cos\theta & -\sin\theta \\ \sin\theta & \cos\theta \end{bmatrix}, \qquad \mathbf{s}(\boldsymbol{e}_2) = \begin{bmatrix} 1 & 0 \\ 0 & -1 \end{bmatrix}. \tag{2.3}$$

Note that a rotation Q has a determinant $\det Q = 1$, and a combination of a rotation with a reflection as a determinant $\det Q = -1$. The (left) action[1] of an orthogonal transformation $Q \in \mathrm{O}(2)$ on a second-order tensor $\mathbf{t}$ or a fourth-order tensor $\mathbf{T}$ is

$$(Q \star \mathbf{t})_{ij} = Q_{ik} Q_{jl} t_{kl}, \qquad (Q \star \mathbf{T})_{ijkl} = Q_{ip} Q_{jq} Q_{kr} Q_{ls} T_{pqrs}. \tag{2.4}$$

Symmetry classes for bi-dimensional elasticity tensors. Let us start by introducing the notion of symmetry group. The symmetry group of an elasticity tensor $\mathbf{E}$ is the subset $G_{\mathbf{E}} \subset \mathrm{O}(2)$ of the transformations that keeps $\mathbf{E}$ unchanged. Mathematically, a symmetry group $G_{\mathbf{E}}$ of an elasticity tensor $\mathbf{E}$ in the 6-dimensional real vector space $\mathbb{Ela}(\mathbb{R}^2)$, is defined as

$$G_{\mathbf{E}} = \{Q \in \mathrm{O}(2) \mid Q \star \mathbf{E} = \mathbf{E}\}. \tag{2.5}$$

---

[1]Such that $(Q_1 Q_2) \star \mathbf{t} = Q_1 \star (Q_2 \star \mathbf{t})$

The symmetry group enables to define an equivalence relation on $\mathbb{E}\text{la}(\mathbb{R}^2)$. Indeed, two elasticity tensors $\mathbf{E}_1$ and $\mathbf{E}_2$ are in the same symmetry class if their symmetry group are conjugate

$$\mathbf{E}_1 \sim \mathbf{E}_2 \iff \exists Q \in \text{O}(2) \text{ such that } G_{\mathbf{E}_1} = Q G_{\mathbf{E}_2} Q^{-1}. \tag{2.6}$$

In other words, two elasticity tensors $\mathbf{E}_1$ and $\mathbf{E}_2$ are equivalent, *i.e.* have the same symmetry class, if there exists at least one transformation $Q \in \text{O}(2)$ such that the representative symmetry groups of $\mathbf{E}_1$ and $\mathbf{E}_2$ are the same. It leads to the definition of a symmetry class as the conjugacy class

$$[G_{\mathbf{E}}] = \{Q G_{\mathbf{E}} Q^{-1}; \ Q \in \text{O}(2)\}. \tag{2.7}$$

Thus, the symmetry class $[G_{\mathbf{E}}]$ of an elasticity tensor $\mathbf{E}$ is a set of groups (not of elasticity tensors); more precisely, it is here a subset of $G = \text{O}(2)$. This subset contains all the conjugate $Q G_{\mathbf{E}} Q^{-1}$ of the symmetry group $G_{\mathbf{E}}$.

To have properly defined the symmetry classes enables us to introduce the notion of symmetry stratum. The symmetry stratum $\Sigma_{[G]}$ is a set of elasticity tensors that are invariant under the action of the symmetry class $[G]$. Formally, it is defined as

$$\Sigma_{[G]} = \{\mathbf{E} \in \mathbb{E}\text{la}(\mathbb{R}^2) \mid \forall Q \in [G], \ Q \star \mathbf{E} = \mathbf{E}\}. \tag{2.8}$$

In order to ease the notation, instead of denoting the symmetry stratum $\Sigma_{[G]}$ using the symmetry class symbol $[G]$, an abbreviation of the name of the associated symmetry class will be used. For instance, the isotropic stratum is the set of elasticity tensor that remains unchanged by any rotation and reflection, *i.e.*, any action of $\text{O}(2)$. Instead of noting $\Sigma_{[\text{O}(2)]}$, it will be denoted Σ_{Iso}.

Forte and Vianello (1996) showed that there are 8 symmetry classes 3D elasticity and Vianello (1997) showed that there are 4 symmetry classes in the 2D case. Each 2D symmetry classes for elasticity tensor, and their representative groups, are represented in Figure 2.1. In this figure, the group $\mathbb{D}_n$ is the dihedral of order $2n$, which is generated by the rotation $\mathbf{r}(2\pi/n)$ and the reflection $\mathbf{s}(\boldsymbol{e}_2)$. Moreover, the group $\mathbb{Z}_2$ is the cyclic group of order 2, which is generated by the rotation $\mathbf{r}(2\pi/n)$. This figure illustrates the four different classes, and their representative groups:

- **the isotropic class** Iso, whose stratum contains the elasticity tensors invariant under the action of the orthogonal group $\text{O}(2)$, *i.e.* invariant with respect to any rotations and reflections,

- **the tetragonal class** Tetra, whose stratum contains the elasticity tensors invariant under the action of the dihedral group of order 8, denoted $\mathbb{D}_4$, *i.e.* invariant with respect to the transformations keeping a square unchanged,

- **the orthogonal class** Ortho, whose stratum contains the elasticity tensors invariant under the action of the dihedral group of order 4, denoted $\mathbb{D}_2$, *i.e.* invariant with respect to the transformations keeping a rectangle unchanged,

- **the biclinic class** Bic, whose stratum contains the elasticity tensors invariant under the action of the cyclic group of order two, denoted $\mathbb{Z}_2$, *i.e.* invariant with respect to the identity and the reflection.

Classes	Biclinic	$\longrightarrow$	Orthotropic	$\longrightarrow$	Tetragonal	$\longrightarrow$	Isotropic
Groups	$\mathbb{Z}_2$	$\subset$	$\mathbb{D}_2$	$\subset$	$\mathbb{D}_4$	$\subset$	O(2)
Illustrations							

Figure 2.1 • Symmetry classes and their representative group for 2D elasticity tensors. The illustrations are geometric figures in $\mathbb{R}^2$ representative of each of the symmetry classes.

Figure 2.1 also contains the inclusion relationship between the groups. For instance, the dihedral group of order four $\mathbb{D}_2$ is included in the dihedral group of order eight $\mathbb{D}_4$. It means that an elasticity tensor invariant under the action of $\mathbb{D}_4$ is also invariants under the action of $\mathbb{D}_2$. Note that from a mathematical point of view, the symmetry classes are exclusive, *i.e* an orthotropic tensor is exactly orthotropic. Yet, from a mechanical point of view, an elasticity tensor in a specific symmetry strata is often supposed to also belong to the less restrictive stratum. For instance, a tetragonal tensor will also be considered as being at least orthotropic.

Invariants and covariants. A covariant of a bi-dimensional elasticity tensor $\mathbf{E}$ is a tensorial function $\mathbf{C}(\mathbf{E})$ such that

$$\mathbf{C}(Q \star \mathbf{E}) = Q \star \mathbf{C}(\mathbf{E}), \quad \forall Q \in \mathrm{O}(2). \tag{2.9}$$

An invariant of a bi-dimensional elasticity tensor $\mathbf{E}$ is a covariant of order zero of $\mathbf{E}$, *i.e.*, a scalar function $I(\mathbf{E})$ such that

$$I(Q \star \mathbf{E}) = I(\mathbf{E}), \quad \forall Q \in \mathrm{O}(2). \tag{2.10}$$

If a mechanical property is an invariant of the elasticity tensor, it means that this quantity is independent of the measurement direction. Similarly, a covariant is a (tensorial) mechanical quantity rotating with the measurement direction.

2 Reconstruction of an elasticity tensor from its covariants

To formulate a damage model, the first steps consist in defining the state variables (here, a damage variable must be introduced) and the state coupling. In our case, defining the state coupling corresponds to expressing the effective elasticity tensor as a function of damage. To measure the damage variable $\mathbf{D} = \mathbf{D}(\tilde{\mathbf{E}})$ equally in any base, it must be a covariant of the effective elasticity tensor $\tilde{\mathbf{E}}$

$$\forall Q \in \mathrm{O}(2), \quad \mathbf{D}(Q \star \tilde{\mathbf{E}}) = Q \star \mathbf{D}(\tilde{\mathbf{E}}). \tag{2.11}$$

Indeed, the micro-cracking rotates with the material. Thus, the state variable describing the micro-cracking must rotate with the effective elasticity tensor of the material. So, this section is dedicated to the presentation of reconstruction formulas of the elasticity tensor from its covariants (see also the work of Olive et al. (2017) in 3D and Oliver-Leblond et al. (2021) in 2D).

2.1 Harmonic decomposition

Harmonic tensor. Before introducing the harmonic decomposition, the notion of harmonic tensor must be introduced. A harmonic tensor is a traceless totally symmetric tensor. We denote by $\mathbb{H}^n(\mathbb{R}^2)$ the vector space of harmonic bi-dimensional tensors of order n. Remark that $\mathbb{H}^0(\mathbb{R}^2)$ is isomorphic to $\mathbb{R}$. A second-order harmonic tensor $\mathbf{h} \in \mathbb{H}^2(\mathbb{R}^2)$ is a symmetric deviatoric tensor,

$$\mathbf{h} \in \mathbb{H}^2(\mathbb{R}^2) = \left\{ \mathbf{h} \in \mathbb{S}^2(\mathbb{R}^2) \mid \operatorname{tr} \mathbf{h} = 0 \right\}, \qquad \mathbf{h} = \begin{bmatrix} h_{11} & h_{12} \\ h_{12} & -h_{11} \end{bmatrix} \tag{2.12}$$

in Cartesian components. A fourth-order harmonic tensor $\mathbf{H} \in \mathbb{H}^4(\mathbb{R}^2)$ is a totally symmetric and traceless tensor,

$$\mathbf{H} \in \mathbb{H}^4(\mathbb{R}^2) = \left\{ \mathbf{H} \in \mathbb{S}^4(\mathbb{R}^2) \mid \forall (i,j), \ \operatorname{tr}_{ij} \mathbf{H} = \mathbf{0} \right\}, \tag{2.13}$$

where $\operatorname{tr}_{ij} \mathbf{H}$ is the second-order tensor built from the contraction of the subscripts i and j of the harmonic tensor $\mathbf{H}$. The tensor $\mathbf{H}$ can be written in Kelvin notation,

$$[\mathbf{H}] = \begin{bmatrix} H_{1111} & -H_{1111} & \sqrt{2} H_{1112} \\ -H_{1111} & H_{1111} & -\sqrt{2} H_{1112} \\ \sqrt{2} H_{1112} & -\sqrt{2} H_{1112} & -2 H_{1111} \end{bmatrix} \tag{2.14}$$

Harmonic decomposition. The harmonic decomposition of a tensor is its equivariant decomposition into harmonic tensors (Spencer, 1970; Schouten, 1989). In particular, the harmonic decomposition of a 2D elasticity tensor $\mathbf{E}$ (Blinowski et al., 1996; Vianello, 1997) is

$$\mathbf{E} = (\mu, \kappa, \mathbf{d}', \mathbf{H}), \tag{2.15}$$

such that

$$\forall Q \in O(2), \quad Q \star \mathbf{E} = (\mu, \kappa, Q \star \mathbf{d}', Q \star \mathbf{H}). \tag{2.16}$$

The harmonic components of $\mathbf{E}$ are the invariants $\mu, \kappa \in \mathbb{H}^0(\mathbb{R}^2)$ (the generalized shear and bulk moduli, respectively), the second-order covariant $\mathbf{d}' = \mathbf{d}'(\mathbf{E}) \in \mathbb{H}^2(\mathbb{R}^2)$, and the fourth-order covariant $\mathbf{H} = \mathbf{H}(\mathbf{E}) \in \mathbb{H}^4(\mathbb{R}^2)$. Note that the harmonic decomposition introduces a bijection between the space of 2D elasticity tensor $\mathbb{E}\mathrm{la}(\mathbb{R}^2)$ and the direct sum of the spaces $\mathbb{H}^0(\mathbb{R}^2) \oplus \mathbb{H}^0(\mathbb{R}^2) \oplus \mathbb{H}^2(\mathbb{R}^2) \oplus \mathbb{H}^4(\mathbb{R}^2)$, *i.e.*, $\mathbf{E} = f(\mu, \kappa, \mathbf{d}', \mathbf{H})$ is a bijection. In the following paragraphs, both explicit formulas of this bijection are recalled.

Harmonic decomposition explicit reconstruction formula. The first direction of the bijection consists in going from the space of harmonic components to the space of elasticity tensors

$$\mathbb{H}^0(\mathbb{R}^2) \oplus \mathbb{H}^0(\mathbb{R}^2) \oplus \mathbb{H}^2(\mathbb{R}^2) \oplus \mathbb{H}^4(\mathbb{R}^2) \to \mathbb{E}\mathrm{la}(\mathbb{R}^2), \qquad (\mu, \kappa, \mathbf{d}', \mathbf{H}) \mapsto \mathbf{E}. \tag{2.17}$$

The harmonic decomposition provides a so-called reconstruction of the elasticity tensor $\mathbf{E}$ by means of its (covariant) harmonic components through

$$\mathbf{E} = 2\mu \mathbf{J} + \kappa \mathbf{1} \otimes \mathbf{1} + \frac{1}{2} \left(\mathbf{1} \otimes \mathbf{d}' + \mathbf{d}' \otimes \mathbf{1} \right) + \mathbf{H}, \tag{2.18}$$

where $\mathbf{1}$ is the second-order identity tensor, $\mathbf{I}$ is the fourth-order identity tensor (of components $I_{ijkl} = \frac{1}{2}(\delta_{ik}\delta_{jl} + \delta_{il}\delta_{jk})$), and $\mathbf{J} = \mathbf{I} - \frac{1}{2}\mathbf{1} \otimes \mathbf{1}$ is the so-called deviatoric projector. The reconstruction formula (2.18) applies to all 2D elasticity tensors, possibly fully anisotropic (*i.e.*, biclinic). An important property of the harmonic decomposition for this work is that each term of this expression is orthogonal to the others (Spencer, 1970). It means that each term is independent of the others. This property will be exploited for the constitution of the model in the next chapters. Let us also introduce the tensors $\mathbf{Iso}$ as the isotropic part of $\mathbf{E}$, $\mathbf{Dil}$ as its dilatation part, and $\mathbf{H}$ as its harmonic part

$$\mathbf{Iso} = 2\mu\mathbf{J} + \kappa\mathbf{1} \otimes \mathbf{1}, \qquad \mathbf{Dil} = \frac{1}{2}\left(\mathbf{1} \otimes \mathbf{d}' + \mathbf{d}' \otimes \mathbf{1}\right), \qquad \mathbf{H} = \mathbf{E} - \mathbf{Iso} - \mathbf{Dil}. \tag{2.19}$$

All three tensors $\mathbf{Iso}$, $\mathbf{Dil}$ and $\mathbf{H}$ are fourth-order covariants of $\mathbf{E}$. Note that the orthogonality of the harmonic decomposition terms means that

$$\mathbf{Iso} :: \mathbf{Dil} = 0, \qquad \mathbf{Iso} :: \mathbf{H} = 0, \qquad \mathbf{Dil} :: \mathbf{H} = 0 \tag{2.20}$$

Also note that in the present case, even the terms of the isotropic part are orthogonal ($\mathbf{I} :: (\mathbf{1} \otimes \mathbf{1}) = 0$).

Decomposition formula. The second direction of the bijection consists in going from the space of elasticity tensors to the space of harmonic components

$$\mathbb{Ela}(\mathbb{R}^2) \to \mathbb{H}^0(\mathbb{R}^2) \oplus \mathbb{H}^0(\mathbb{R}^2) \oplus \mathbb{H}^2(\mathbb{R}^2) \oplus \mathbb{H}^4(\mathbb{R}^2), \qquad \mathbf{E} \mapsto (\mu, \kappa, \mathbf{d}', \mathbf{H}). \tag{2.21}$$

First, the dilatation tensor $\mathbf{d}(\mathbf{E})$ and the Voigt tensor $\mathbf{v}(\mathbf{E})$ must be introduced

$$\mathbf{d} = \mathrm{tr}_{12}\mathbf{E} = \mathrm{tr}_{34}\mathbf{E} = \mathbf{E} : \mathbf{1}, \qquad \mathbf{v} = \mathrm{tr}_{13}\mathbf{E}. \tag{2.22}$$

Both the dilatation and the Voigt tensor are second-order covariants. Also note that in 2D, their deviatoric parts are equal $\mathbf{d}' = \mathbf{v}'$. The scalar components of the harmonic decomposition of $\mathbf{E}$ are

$$\mu = \frac{1}{8}\left(2\,\mathrm{tr}\mathbf{v} - \mathrm{tr}\mathbf{d}\right), \qquad \kappa = \frac{1}{4}\,\mathrm{tr}\mathbf{d}. \tag{2.23}$$

The covariant $\mathbf{d}'(\mathbf{E})$ is the deviatoric part

$$\mathbf{d}' = \mathbf{d} - \frac{1}{2}(\mathrm{tr}\mathbf{d}) \tag{2.24}$$

of the dilatation tensor $\mathbf{d}$. Finally, the covariant $\mathbf{H}(\mathbf{E})$ is the fourth-order harmonic part of $\mathbf{E}$, which is calculated thanks to the decomposition formula

$$\mathbf{H} = \mathbf{E} - 2\mu\mathbf{J} - \kappa\mathbf{1} \otimes \mathbf{1} - \frac{1}{2}\left(\mathbf{1} \otimes \mathbf{d}' + \mathbf{d}' \otimes \mathbf{1}\right). \tag{2.25}$$

Minimal integrity basis. In this work, others invariants of the elasticity will be used. Thus, let us also introduce the scalars

$$I_2(\mathbf{E}) = I_2(\mathbf{d}') = \|\mathbf{d}'\|^2 = \mathbf{d}' : \mathbf{d}', \qquad J_2(\mathbf{E}) = \|\mathbf{H}\|^2 = \mathbf{H} :: \mathbf{H}, \quad \text{and} \quad K_3(\mathbf{E}) = \mathbf{d} : \mathbf{H} : \mathbf{d}, \tag{2.26}$$

which are three other invariants of the elasticity tensor. Note that $(\mu, \kappa, I_2, J_2, K_3)$ forms a minimal integrity basis of the invariant algebra of the elasticity tensor in 2D under the action of the orthogonal group O(2) (Vianello, 1997).

2.2 Harmonic square – Reconstruction of orthotropic elasticity tensors

To obtain a reconstruction formula dedicated to orthotropic elasticity tensors, we have to introduce the harmonic product $\mathbf{h}_1 * \mathbf{h}_2 \in \mathbb{H}^4(\mathbb{R}^2)$ of two second-orders harmonic tensors $\mathbf{h}_1$, and $\mathbf{h}_2$. In 2D, it is defined as the fourth-order harmonic tensor (Olive et al., 2017)

$$\mathbf{h}_1 * \mathbf{h}_2 = \mathbf{h}_1 \otimes \mathbf{h}_2 - \frac{1}{2}(\mathbf{h}_1 : \mathbf{h}_2)\,\mathbf{J}, \qquad \mathbf{J} = \mathbf{I} - \frac{1}{2}\mathbf{1} \otimes \mathbf{1}, \tag{2.27}$$

where $\mathbf{J}$ is the so-called deviatoric projector[2]. Desmorat and Desmorat (2015) showed that any 2D fourth-order harmonic tensor $\mathbf{H} \in \mathbb{H}^4(\mathbb{R}^2)$ can be written as a harmonic square,

$$\mathbf{H} = 2\Lambda\,\mathbf{e} * \mathbf{e}, \qquad \operatorname{tr}\mathbf{e} = 0, \qquad \|\mathbf{e}\| = 1, \tag{2.28}$$

where $\mathbf{e} \in \mathbb{H}^2(\mathbb{R}^2)$ is a unit second-order deviatoric eigentensor associated with a non-zero eigenvalue Λ or $-\Lambda$ of the harmonic tensor $\mathbf{H}$. Note that Equation (2.28) is not a so-called reconstruction formula for $\mathbf{H}$ since $\mathbf{e}$ is defined up to a sign and is not a covariant of $\mathbf{H}$.

A more interesting formula is obtained when $\mathbf{H} = \mathbf{H}(\mathbf{E})$ is the fourth-order harmonic part of an (exactly) orthotropic elasticity tensor $\mathbf{E}$, still in 2D. In that case, we have (Oliver-Leblond et al., 2021),

$$\mathbf{H} = \frac{2K_3(\mathbf{E})}{I_2^2(\mathbf{E})}\,\mathbf{d}'(\mathbf{E}) * \mathbf{d}'(\mathbf{E}). \tag{2.29}$$

Remark that the covariants —including invariants— involved are covariants of the elasticity tensor, which is orthotropic, not of the harmonic tensor $\mathbf{H}$, which has the square ($[\mathbb{D}_4]$) symmetry (Verchery, 1982; Vianello, 1997; Vannucci, 2005). This means that we have the following (orthotropic) elasticity tensor reconstruction formula (by means of its covariants) in 2D

$$\mathbf{E} = 2\mu\mathbf{J} + \kappa\,\mathbf{1} \otimes \mathbf{1} + \frac{1}{2}\left(\mathbf{1} \otimes \mathbf{d}' + \mathbf{d}' \otimes \mathbf{1}\right) + \frac{2K_3}{I_2^2}\,\mathbf{d}' * \mathbf{d}', \tag{2.30}$$

where μ, κ, I_2 and K_3 are invariants of the elasticity tensor (defined by Equations (2.23) and (2.26)), and $\mathbf{d}$ is a second-order covariant of $\mathbf{E}$ (defined by Equation (2.22)). Remark that for this formula to hold, it is necessary that $\mathbf{d}' \neq 0$ since $I_2(\mathbf{d}' = 0) = 0$. In other words, it is necessary that the dilatation tensor $\mathbf{d} = \mathbf{d}(\mathbf{E})$ —which inherits the symmetry of $\mathbf{E}$ (Olive et al., 2022)— and therefore $\mathbf{E}$, are orthotropic.

2.3 Remark on harmonic decomposition and symmetry classes

Vianello (1997) proposes algebraic conditions to determine if an elasticity tensor $\mathbf{E} = (\kappa, \mu, \mathbf{d}', \mathbf{H})$ is in a specific symmetry stratum (see also the work of Vannucci (2005) in the polar decomposition framework). Those conditions are expressed as polynomial equations of its invariants. Let us consider an elasticity tensor $\mathbf{E}$ and its invariants

$$I_1 = \kappa, \qquad J_1 = 2\mu, \qquad I_2 = \mathbf{d}' : \mathbf{d}', \qquad J_2 = \mathbf{H} :: \mathbf{H}, \qquad K_3 = \mathbf{d}' : \mathbf{H} : \mathbf{d}'. \tag{2.31}$$

The 2D elasticity tensor $\mathbf{E}$ is

---

[2]Consider $\mathbf{t} \in \mathbb{S}^2(\mathbb{R}^2)$, then $\mathbf{J} : \mathbf{t} = \mathbf{t} - \frac{1}{2}\operatorname{tr}\mathbf{t}\mathbf{1} = \mathbf{t}'$.

- isotropic (circle symmetry) if

$$I_2 = 0 \text{ and } J_2 = 0, \tag{2.32}$$

- tetragonal (square symmetry) if

$$I_2 = 0 \text{ and } J_2 \neq 0, \tag{2.33}$$

- orthotropic (rectangle symmetry) if either

$$I_2 \neq 0 \text{ and } J_2 = 0, \quad \text{or} \quad I_2 \neq 0, J_2 \neq 0 \text{ and } I_2^2 J_2 - 2K_3^2 = 0, \tag{2.34}$$

- biclinic otherwise.

This classification is also represented in Figure 2.2 where the different symmetry breaking conditions are shown.

Symmetry classes	Symmetry bifurcations
Biclinic	$[\mathbb{Z}_2]$
	$\downarrow$ $\begin{array}{l} J_2 = 0, \text{ or} \\ I_2^2 J_2 - 2I_3^2 = 0 \text{ and } J_2 \neq 0 \end{array}$
Orthotropic	$[\mathbb{D}_2]$
	$\downarrow$ $I_2 = 0$
Tetragonal	$[\mathbb{D}_4]$
	$\downarrow$ $J_2 = 0$
Isotropic	$[O(2)]$
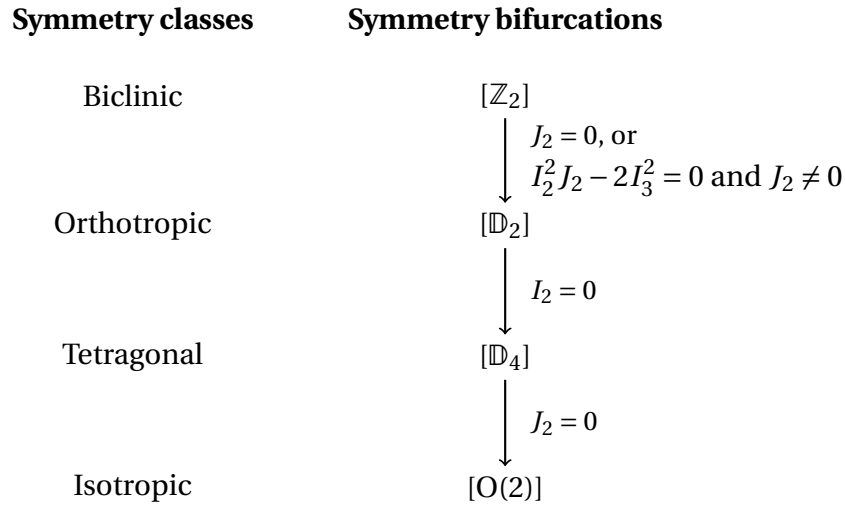
Figure 2.2 • Symmetry bifurcation diagram for bi-dimensional elasticity tensors (Vianello, 1997).

For illustration purposes, let us now apply the harmonic decomposition to an elasticity tensor of each symmetry stratum. It gives the following expressions of the elasticity tensor

- **E** is biclinic gives,

$$\mathbf{E} = 2\mu\mathbf{J} + \kappa\mathbf{1} \otimes \mathbf{1} + \frac{1}{2}\left(\mathbf{1} \otimes \mathbf{d}' + \mathbf{d}' \otimes \mathbf{1}\right) + \mathbf{H}, \tag{2.35}$$

- **E** is orthotropic (rectangle symmetric) gives,

$$\mathbf{E} = 2\mu\mathbf{J} + \kappa\mathbf{1} \otimes \mathbf{1} + \frac{1}{2}\left(\mathbf{1} \otimes \mathbf{d}' + \mathbf{d}' \otimes \mathbf{1}\right) + \frac{2K_3}{I_2^2}\mathbf{d}' * \mathbf{d}', \tag{2.36}$$

- **E** is tetragonal (square symmetric) gives,

$$\mathbf{E} = 2\mu\mathbf{J} + \kappa\mathbf{1} \otimes \mathbf{1} + \mathbf{H}, \tag{2.37}$$

- **E** is isotropic (circle symmetric) gives,

$$\mathbf{E} = 2\mu\mathbf{J} + \kappa\mathbf{1} \otimes \mathbf{1}. \tag{2.38}$$

Let us note the particular case in orthotropy where $J_2 = 0$, called the special orthotropy or the R_0-orthotropy by Vannucci ([2002](#)). In this case, the harmonic part vanishes, thus,

$$\mathbf{E} \text{ special orthotropic} \iff \mathbf{E} = 2\mu\mathbf{J} + \kappa\mathbf{1} \otimes \mathbf{1} + \frac{1}{2}\left(\mathbf{1} \otimes \mathbf{d}' + \mathbf{d}' \otimes \mathbf{1}\right). \tag{2.39}$$

3 Distance to isotropy – Distance to orthotropy

The determination of the symmetry class of a measured elasticity tensor is a difficult problem (Gazis et al., [1963](#); François, [1995](#); François et al., [1998](#); Moakher & Norris, [2006](#); Diner et al., [2011](#)). A cause is that the measurement orientation might not correspond to the principal direction of the expected symmetry class, which prevents direct identification by comparison to normal forms (in Kelvin notation). Furthermore, experimental measurements provide a noised approximation of the material's elastic properties (Roux et al., [1985](#); Migliori et al., [1993](#)); thus, preventing the direct application of the polynomial conditions presented in Equations (2.32) to (2.34). For those two reasons, the measured elasticity tensor will generically be biclinic in 2D (and triclinic in 3D).

3.1 Distance to a symmetry class

Those issues can be mitigated by calculating the distance to the expected elasticity symmetry class, more precisely, the distance to the considered symmetry stratum (which is the set of all tensors which have the same symmetry class). This usually consists, first, in finding the elasticity tensor $\mathbf{E}^*$ in the symmetry stratum $\overline{\Sigma}$ which is the closest to the measured elasticity tensor $\mathbf{E}$, and second, in calculating the distance between $\mathbf{E}$ and $\mathbf{E}^*$. The distance to the symmetry stratum $\overline{\Sigma}$ is

$$d_{\overline{\Sigma}}(\mathbf{E}) = \min_{\mathbf{E}^* \in \overline{\Sigma}} \|\mathbf{E} - \mathbf{E}^*\|. \tag{2.40}$$

If this distance is equal to 0, the elasticity tensor $\mathbf{E}$ is in the symmetry stratum. We also introduce the relative distance to the symmetry stratum $\overline{\Sigma}$ as

$$\Delta_{\overline{\Sigma}}(\mathbf{E}) = \min_{\mathbf{E}^* \in \overline{\Sigma}} \frac{\|\mathbf{E} - \mathbf{E}^*\|}{\|\mathbf{E}\|}. \tag{2.41}$$

Note that both Equations (2.40) and (2.41) have the same minimizer $\mathbf{E}^*$.

3.2 Distance to isotropy

In the case of isotropy, the harmonic decomposition provides, by orthogonal projection (Vianello, [1997](#)), the closest isotropic tensor $\mathbf{E}^*$ to $\mathbf{E}$ as its isotropic part $\mathbf{E}^* = \mathbf{Iso}(\mathbf{E})$ (as defined by Equation (2.19)),

$$d_{\mathrm{Iso}}(\mathbf{E}) = \min_{\mathbf{E}^* \in \Sigma_{Iso}} \|\mathbf{E} - \mathbf{E}^*\| = \|\mathbf{E} - \mathbf{Iso}(\mathbf{E})\| = \sqrt{\|\mathbf{Dil}(\mathbf{E})\|^2 + \|\mathbf{H}(\mathbf{E})\|^2}. \tag{2.42}$$

This result is obtained from the orthogonality of the harmonic terms (see Equation (2.20)). Indeed, as the tensor $\mathbf{E}^*$ is isotropic, its harmonic decomposition is $\mathbf{E}^* = \mathbf{Iso}(\mathbf{E}^*)$. These properties lead to the following triangular equality

$$\forall \mathbf{E}^* \in \Sigma_{Iso}, \quad \|\mathbf{E} - \mathbf{E}^*\|^2 = \|\mathbf{Iso}(\mathbf{E}) - \mathbf{Iso}(\mathbf{E}^*)\|^2 + \underbrace{\|\mathbf{Dil}(\mathbf{E})\|^2 + \|\mathbf{H}(\mathbf{E})\|^2}_{\text{constant } \forall \mathbf{E}^*}. \tag{2.43}$$

The last two terms are constant for any isotropic tensor $\mathbf{E}^*$ and only depends on the elasticity tensor $\mathbf{E}$. Thus, the minimum of the distance to isotropy is reached when

$$\mathbf{Iso}(\mathbf{E}^*) = \mathbf{Iso}(\mathbf{E}) \implies \mathbf{E}^* = \mathbf{Iso}(\mathbf{E}). \tag{2.44}$$

3.3 Distance to orthotropy

The calculation of the distance to 2D elastic orthotropy requires more mathematical development (Vianello, 1997; Antonelli et al., 2022). In this subsection, the results of Antonelli et al. (2022) are recovered via complementary developments.

The minimization problem to solve in order to obtain the distance to orthotropy is

$$d_{\text{Ort}}(\mathbf{E}) = \min_{\mathbf{E}^* \in \Sigma_{Ort}} \|\mathbf{E} - \mathbf{E}^*\|. \tag{2.45}$$

The first step to calculate this distance consists in parametrizing the orthotropic tensors $\mathbf{E}^*$, in Kelvin notation,

$$\mathbf{E}^* = Q \star \mathbf{A}, \qquad Q = \begin{pmatrix} \cos\theta & -\sin\theta \\ \sin\theta & \cos\theta \end{pmatrix}, \qquad [\mathbf{A}] = \begin{bmatrix} A_{1111} & A_{1122} & 0 \\ A_{1122} & A_{2222} & 0 \\ 0 & 0 & 2A_{1212} \end{bmatrix}, \tag{2.46}$$

where Q is a rotation matrix, $\mathbf{A}$ is the normal form of orthotropic 2D elasticity tensors, $[\mathbf{A}]$ stands for its Kelvin notation, and $(Q \star \mathbf{A})_{ijkl} = Q_{ip} Q_{jq} Q_{kr} Q_{ls} A_{pqrs}$ is the action of the rotation Q on the fourth-order tensor $\mathbf{A}$. With this parametrization, the minimization problem becomes

$$d_{\text{Ort}}(\mathbf{E}) = \min_{\substack{\theta \in [0, 2\pi], \\ \mathbf{A} \in \mathcal{N}_{\text{Ort}}}} \|\mathbf{E} - Q \star \mathbf{A}\|, \tag{2.47}$$

where $\mathcal{N}_{\text{Ort}}$ is the vector space of orthotropic elasticity tensor of normal form Equation (2.46). By applying the harmonic decomposition to $\mathbf{E}$ and $\mathbf{A}$, and using the orthogonality of its parts (by Equation (2.20)), we obtain

$$d_{\text{Ort}}(\mathbf{E})^2 = \min_{\theta, \mathbf{A}} \left(\|\mathbf{Iso}(\mathbf{E}) - \mathbf{Iso}(\mathbf{A})\|^2 + \|\mathbf{Dil}(\mathbf{E}) - Q \star \mathbf{Dil}(\mathbf{A})\|^2 + \|\mathbf{H}(\mathbf{E}) - Q \star \mathbf{H}(\mathbf{A})\|^2 \right). \tag{2.48}$$

Let us treat each part, *i.e.* each independent minimization problem, separately:

- For the isotropic part, by Equation (2.42),the closest isotropic tensor is the isotropic tensor itself,

$$\mathbf{Iso}(\mathbf{A}) = \mathbf{Iso}(\mathbf{E}). \tag{2.49}$$

- For the dilatation part term, we can introduce the deviatoric part of the dilatation tensor for the elasticity tensor **E**

$$\mathbf{d}'(\mathbf{E}) = \begin{bmatrix} d'_{11} & d'_{12} \\ d'_{11} & -d'_{11} \end{bmatrix}, \qquad \begin{aligned} d'_{11} &= \frac{1}{2}\left(E_{1111} - E_{2222}\right), \\ d'_{12} &= E_{1112} + E_{2212}, \end{aligned} \qquad (2.50)$$

and for the orthotropic elasticity tensor $Q \star \mathbf{A}$

$$\mathbf{d}'(\mathbf{A}) = d^* \begin{bmatrix} 1 & 0 \\ 0 & -1 \end{bmatrix}, \qquad Q \star \mathbf{d}'(\mathbf{A}) = d^* \begin{bmatrix} \cos 2\theta & \sin 2\theta \\ \sin 2\theta & -\cos 2\theta \end{bmatrix}, \qquad (2.51)$$

- For the harmonic part term, we can introduce the harmonic parts (in Kelvin notation) of the elasticity tensor **E**

$$[\mathbf{H}(\mathbf{E})] = \begin{bmatrix} H_{1111} & -H_{1111} & \sqrt{2} H_{1112} \\ -H_{1111} & H_{1111} & -\sqrt{2} H_{1112} \\ \sqrt{2} H_{1112} & -\sqrt{2} H_{1112} & -2 H_{1111} \end{bmatrix}, \qquad (2.52)$$

where,

$$H_{1111} = \frac{1}{8}\left(E_{1111} - 2E_{1122} - 4E_{1212} + E_{2222}\right), \qquad H_{1112} = \frac{1}{2}\left(E_{1112} - E_{2212}\right), \qquad (2.53)$$

and of the orthotropic elasticity tensor $Q \star \mathbf{A}$

$$[\mathbf{H}(\mathbf{A})] = H^* \begin{bmatrix} 1 & -1 & 0 \\ -1 & 1 & 0 \\ 0 & 0 & -2 \end{bmatrix}, \qquad (2.54)$$

$$[Q \star \mathbf{H}(\mathbf{A})] = H^* \begin{bmatrix} \cos 4\theta & -\cos 4\theta & \sqrt{2} \sin 4\theta \\ -\cos 4\theta & \cos 4\theta & -\sqrt{2} \sin 4\theta \\ \sqrt{2} \sin 4\theta & -\sqrt{2} \sin 4\theta & -2\cos 4\theta \end{bmatrix}. \qquad (2.55)$$

We have then, by Equation (2.18),

$$d_{\text{Ort}}(\mathbf{E})^2 = \min_{\theta, d^*, H^*} \left(\|\mathbf{d}'(\mathbf{E}) - Q \star \mathbf{d}'(\mathbf{A})\|^2 + \|\mathbf{H}(\mathbf{E}) - Q \star \mathbf{H}(\mathbf{A})\|^2 \right). \qquad (2.56)$$

The minimizations with respect to d^* and to H^* give

$$d^* = d'_{11} \cos 2\theta + d'_{12} \sin 2\theta, \qquad H^* = H_{1111} \cos 4\theta + H_{1112} \sin 4\theta. \qquad (2.57)$$

Moreover, the minimization with respect to θ ends up to the equation

$$A \cos 8\theta + B \sin 8\theta + C \cos 4\theta + D \sin 4\theta = 0, \qquad (2.58)$$

where (Antonelli et al., 2022):

$$\begin{aligned}
A &= 2(E_{1111} - 2E_{1122} - 4E_{1212} + E_{2222})(E_{1112} - E_{2212}) = 32 H_{1111} H_{1112}, \\
B &= 4(E_{1112} - E_{2212})^2 - \frac{1}{4}(E_{1111} - 2E_{1122} - 4E_{1212} + E_{2222})^2 = 16\left(H_{1112}^2 - H_{1111}^2\right), \\
C &= 2(E_{1111} - E_{2222})(E_{1112} + E_{2212}) = 4 d'_{11} d'_{12}, \\
D &= 2(E_{1112} + E_{2212})^2 - \frac{1}{2}(E_{1111} - E_{2222})^2 = 2\left(d_{12}'^2 - d_{11}'^2\right).
\end{aligned} \qquad (2.59)$$

Setting $\theta = \frac{1}{2} \arctan t$, we obtain the fourth-order polynomial in t,

$$(A - C)\, t^4 + (2D - 4B)\, t^3 - 6A\, t^2 + (2D + 4B)\, t + A + C = 0. \tag{2.60}$$

The roots t_k of the polynomial are obtained by symbolic resolution of the polynomial, using SymPy (Meurer et al., 2017), and then evaluated numerically. The root retained corresponds to either to the solution $\theta = \frac{1}{2} \arctan(t_k)$ or to the solution $\theta = \frac{1}{2} \arctan(t_k) - \frac{\pi}{2}$ that minimizes $d_{\mathrm{Ort}}(\mathbf{E})^2$. Finally, the distance to orthotropy is obtained by injecting the minimizers —d^* and H^* both from Equation (2.57), and θ— and taking the square root of Equation (2.56).

3.4 Upper-bounds of the distance to orthotropy

Using the orthotropic reconstruction formula (2.30), Oliver-Leblond et al. (2021) proposed an upper bound of this distance

$$d_{\mathrm{Ort}}(\mathbf{E}) = \min_{\mathbf{E}^* \in \Sigma_{Ort}} \|\mathbf{E} - \mathbf{E}^*\| \leqslant \|\mathbf{E} - \mathbf{E}^{\mathrm{up}}\| = d_{\mathrm{Ort}}^{\mathrm{up}}, \tag{2.61}$$

where

$$\mathbf{E}^{\mathrm{up}} = 2\mu \mathbf{J} + \kappa \mathbf{1} \otimes \mathbf{1} + \frac{1}{2}\left(\mathbf{1} \otimes \mathbf{d}' + \mathbf{d}' \otimes \mathbf{1}\right) + \frac{2K_3}{I_2^2}\, \mathbf{d}' * \mathbf{d}', \tag{2.62}$$

where the bulk κ and shear μ moduli are given by Equation (2.23), and the dilatation tensor is by Equation (2.22) as $\mathbf{d} = \mathbf{E} : \mathbf{1}$. This formula provides an estimation of the distance to orthotropy that is easier to calculate than the real distance. Note that if the upper-bound is close to 0, it means that the elasticity tensors is close to orthotropy. However, if the upper-bound is far from 0, no conclusion can be drawn.

✒ Summary of the Chapter

The objective of this chapter was to introduce the different mathematical tools used in the formulation of the model. After giving various fundamental definitions (elasticity tensor, symmetry stratum, invariant, covariant, ...) and their interpretation, the harmonic decomposition have been presented. Two different reconstruction formulas of the elasticity tensor have been recalled: one for any elasticity tensor and one for the orthotropic ones. Then, the distances to isotropy and to orthotropy have been presented, as well as an upper-bound of the distance to orthotropy.

 This chapter introduced the fundamental mathematical tools for this study. The distance to symmetry classes will enable to check in which symmetry stratum an elasticity tensor is. In Chapter 4, those distances will be applied to analyze the dataset of effective elasticity tensors generated in the Chapter 3. The results of the distances to symmetry stratum will enables to make and justify assumptions for the model. The reconstruction formulas proposed in this chapter will be used as the basis for the state model in Chapter 5. Now that all the fundamental tools are introduced, the next step consists in generating the reference dataset for the constitution the model.

3

From discrete to continuous: Measurement of effective elasticity tensor

This chapter aims to bridge the discrete beam-particle model to a continuous model. In particular, the objective is to measure the effective elasticity tensor associated with a discrete (beam-particle) area element. It begins with a presentation of the beam-particle model. Then, it raises different classical questions in homogenization: How to measure strains and stresses? Which type of boundary condition should be used on the area element? Those questions are treated individually to propose a complete measurement procedure, which is then summarized and discussed.

Before formulating a model, the first steps consist in gathering data on the phenomenon to represent. In this study, the continuous model will be based on virtual experiments. Virtual tests are an approach, complementary to experiments, which consists in performing numerical experiments using an accurate material model, at micro-scale or meso-scale, to get information on the macroscopic behavior. Performing virtual experimental campaign has the advantages of being simple to reproduce and to set up compared to a real experimental campaign (for instance, on concrete specimens in our case). However, the virtual experiments might be biased due to the potential modeling errors.

For instance, Wriggers and Moftah (2006) performed virtual experiments using a numerical model of concrete. In this work, the concrete meso-structure is represented by a matrix, which behavior is represented by an isotropic damage model, containing a randomly distributed aggregates, with an elastic behavior. The authors performed finite element simulations of 3D cubic specimens under uni-axial compression. The strain-stress responses of the model is found to accurately depicts the experimental results. Virtual testing has also been used by (Reese, 2003) for fiber-reinforced rubber membranes, Rinaldi and Lai (2007) and Rinaldi (2013) for quasi-brittle materials, amongst others.

In this work, we will use a discrete (beam-particle) model as the meso-scale model for quasi-brittle material. The main focus of this chapter is to propose and verify a procedure to measure the effective, *i.e.* damaged, elasticity tensor of 2D square area elements modelled with the discrete model.

1 Meso-scale model of quasi-brittle materials: Beam-particle model

1.1 Presentation of the beam-particle model

The discrete model used in this thesis comes from the work of Delaplace (2008), Vassaux (2015), and Vassaux et al. (2016). The latter reference provides an extensive description of the model, summarized here. The beam-particle model is confronted with experimental results by Oliver-Leblond (2019). It is suitable for predicting crack initiation, propagation, and closure effects. Here, the description of the beam-particle model is limited to the bi-dimensional case and the crack closure effects are not considered. Square 2D area elements — uncracked and cracked — will be modeled by the beam-particle model. In this subsection, the model is presented in distinct steps: generation of the geometry of rigid particles, modelling of elastic cohesion, modelling of failure and modelling of contact and friction.

Positioning particle centers. The procedure to generate the mesh is illustrated on Figure 3.1. The material is represented with an assembly of rigid particles. The spatial distribution of particles – based on the work of Moukarzel and Herrmann (1992) – is obtained by randomly placing the particle centers in the cells of a square grid (step 1). The cell size – length of a square cell side – is defined as $\bar{l}_b$. This length is proportional to the average distance between neighbor particle centers. Particle centers outside the boundary of the domain are removed. At this point, the mesh is a set of particle centers $\{\boldsymbol{x}_p | p \in [1, N_p]\}$ where p denotes the particle index and N_p is the total number of particles in the domain. As shown by D'Addetta et
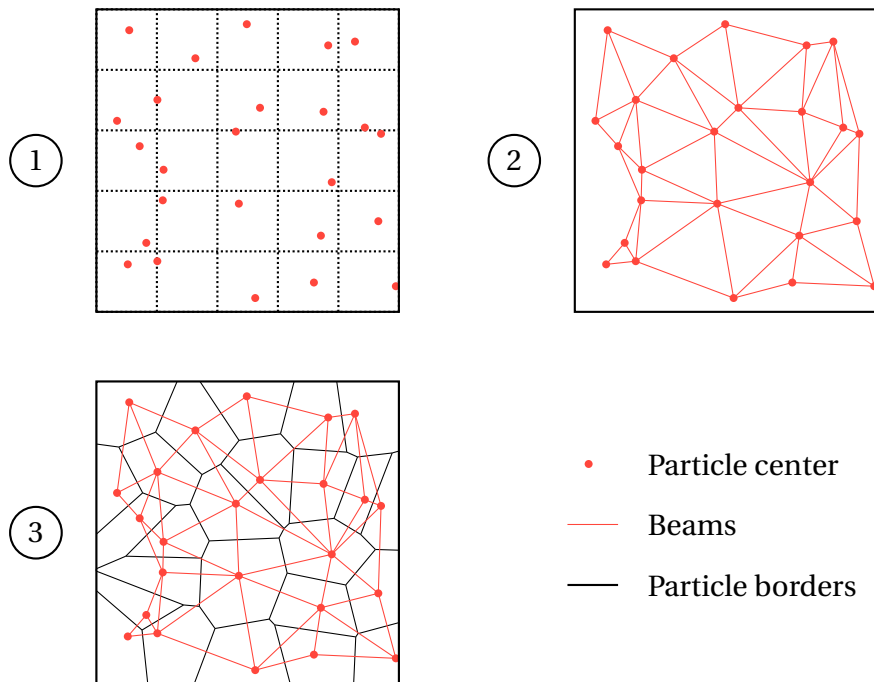

Figure 3.1 • Illustration of the mesh construction in the beam-particle model.

al. (2002), the spatial randomness in the particle positioning enables to obtain an (nearly)

isotropic beam orientation. This geometric isotropy directly relates to the isotropy of the mechanical behavior.

Cohesion. Beams are added between neighbor centers to model the cohesion between neighbor particles. The geometric supports of the beams is the Delaunay triangulation (Delaunay, 1934) of the set of particle centers (step 2). The borders of the particles are given by the dual of the Delaunay triangulation: the Voronoi tessellation of the particle centers (step 3). Each particle has three degrees of freedom in 2D, the displacements in $\boldsymbol{e}_1$ and $\boldsymbol{e}_2$ axis represented by the displacement vector $\boldsymbol{u}_p$ and the rotation along the out-of-plane axis θ_p. Figure 3.2 illustrates those degrees of freedom. The beams are modelled with Euler-Bernoulli
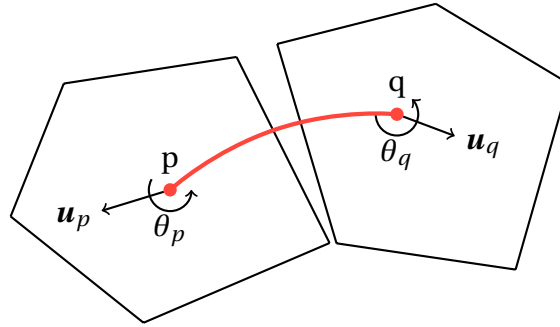
Figure 3.2 • Representation of a beam and illustration of the degrees of freedom.

behavior. The cohesion forces and moment relate to the displacement through the relations (in the beam local frame)

$$
\begin{aligned}
F_{n,pq} &= \frac{E_{pq}A_{pq}}{l_{pq}}(\boldsymbol{u}_p - \boldsymbol{u}_q)\cdot\boldsymbol{n}_{pq} \\
F_{t,pq} &= \frac{12E_{pq}I_{pq}}{l_{pq}^3}(\boldsymbol{u}_p - \boldsymbol{u}_q)\cdot\boldsymbol{t}_{pq} - \frac{6E_{pq}I_{pq}}{l_{pq}^2}(\theta_p - \theta_q) \\
M_{pq} &= \frac{6E_{pq}I_{pq}}{l_{pq}^2}(\boldsymbol{u}_q - \boldsymbol{u}_p)\cdot\boldsymbol{t}_{pq} + \frac{4E_{pq}I_{pq}}{l_{pq}}\left(\theta_p - \frac{\theta_q}{2}\right)
\end{aligned}
\tag{3.1}
$$

where $F_{n,pq}$ (respectively $F_{t,pq}$) is the cohesive force in the direction normal (respectively tangential) to the section of the beam pq, and M_{pq} is the cohesive moment in out-of-plane direction. At this step, the parameters of the beam b are its length l_b, its area A_b, its Young modulus E_b, and its coefficient of inertia $\alpha_b = \frac{64 I_b \pi}{A_b^2}$ (which is used to set the flexural moment of inertia $I_b = \alpha_b \frac{A_b^2}{64\pi}$). The geometric properties of the beams, length l_b and area A_b, are calculated from the mesh geometry. The length of the beam between particles p and q is the distance between the particles centers $l_{pq} = \|\boldsymbol{x}_p - \boldsymbol{x}_q\|_2$. The average beam length relates with the cell size $\bar{l}_b$ of the grid used to position particle centers. The area of the beam linked particles $p\,q$ is proportional to the size of the border between those particles. The mechanical properties, Young modulus E_b and coefficient of inertia, are constant for all beams. They are identified by fitting the macroscopic (initial) elastic properties of the material. At this point, the discrete model can represent an elastic material (with local rotation of the particles).

Failure. To incorporate cracking into the model, brittle failure properties are added to the beams. A Mohr-Coulomb failure criterion is chosen (Delaplace, 2008; Vassaux et al., 2016)

$$f_{pq} = \frac{\varepsilon_{pq}}{\varepsilon_{pq}^{\mathrm{cr}}} + \frac{|\Delta\theta_{pq}|}{\Delta\theta_{pq}^{\mathrm{cr}}} > 1, \qquad \varepsilon_{pq} = \|\boldsymbol{u}_p - \boldsymbol{u}_q\|_2, \qquad \Delta\theta_{pq} = \theta_p - \theta_q, \qquad (3.2)$$

where ε_{pq} is the beam extension, $\varepsilon_{pq}^{\mathrm{cr}}$ is the beam extension threshold, $\Delta\theta_{pq}$ is the difference of particle rotation, and $\Delta\theta_{pq}^{\mathrm{cr}}$ is the difference of particle rotation threshold. If this criterion is reached during a loading, the beam is removed from the beam network. In order to account for failure heterogeneity, the failure thresholds are randomly assigned to each beam following Weibull distributions. The probability density functions associated with each threshold are

$$W_\varepsilon(x) = \frac{k}{\lambda_{\varepsilon,\mathrm{cr}}}\left(\frac{x}{\lambda_{\varepsilon,\mathrm{cr}}}\right)^{k-1} e^{-\left(\frac{x}{\lambda_{\varepsilon,\mathrm{cr}}}\right)^k} \quad \text{and} \quad W_\theta(x) = \frac{k}{\lambda_{\theta,\mathrm{cr}}}\left(\frac{x}{\lambda_{\theta,\mathrm{cr}}}\right)^{k-1} e^{-\left(\frac{x}{\lambda_{\theta,\mathrm{cr}}}\right)^k} \qquad (3.3)$$

where $\lambda_{\varepsilon,\mathrm{cr}}$ is the scale factor in extension, $\lambda_{\theta,\mathrm{cr}}$ is the scale factor in rotation and k is the shape factor . As the failure thresholds in extension $\varepsilon_b^{\mathrm{cr}}$ and in rotation $\Delta\theta_b$ are supposed to be correlated, the shape factor is shared for both thresholds. In practice, a threshold are obtained in one draw of the Weibull distribution and scaled for extension and rotation. It induces a correlation between both failure thresholds $\varepsilon_b^{\mathrm{cr}}$ and $\Delta\theta_b$ of a beam.

Contact. Accounting for contact and friction between particles enables to model crack closure effects. It is essential when considering alternated loadings, where cracks might close (for instance, during a tensile cyclic loading). In this work, loadings are chosen such that cracks remain mainly open; thus, contact and friction between particles are not accounted for. For more details, Rima (2021) carried out a detailed study of contact and friction in the beam-particle model.

1.2 Parameters of the beam-particle model

For this work, the parameters of discrete model are given in Table 3.1. They correspond to a quasi-brittle material with a Young modulus $E = 36.35$ GPa, a Poisson ratio $\nu = 0.22$, and a tensile strength $f_t = 5$ MPa. Note that the elastic properties are equivalent to a bulk modulus $\kappa = 30.0$ GPa and a shear modulus $\mu = 19.4$ GPa. Note that this model has been

Name	Symbol	Value	Unit
Average beam length	$\bar{l}_b$	0.002	m
Young's modulus	E_b	60	GPa
Coefficient of inertia	α_b	0.85	-
Scale factor (extension)	$\lambda_{\varepsilon,\mathrm{cr}}$	5.0×10^{-4}	-
Scale factor (rotation)	$\lambda_{\theta,\mathrm{cr}}$	2.8×10^{-3}	-
Shape factor	k	1.0	-

Table 3.1 • Parameters of beam-particle model

validated (in 2D) through a range of experiments (tension, compression, 3-point bending

tests, mixed mode I-II failure, ...) with parameters of similar magnitudes (Vassaux et al., 2016; Oliver-Leblond, 2019).

1.3 Implementation and numerical resolution

Let us consider a domain defined by a set of particles $\mathscr{P}$ containing N_p particles and a set of beams $\mathscr{B}$ containing N_b beams. For each beam in the domain, there is a linear relationship between the cohesion forces $\boldsymbol{F}_{pq}$ and the movement of the particles ($\boldsymbol{u}_p, \theta_p, \boldsymbol{u}_q, \theta_q$, given by the Euler-Bernoulli behavior. Let us consider a beam b linking the particles p and q. The cohesion forces of the beam on each particles in the beam frame are

$$
\underbrace{\begin{bmatrix} F_{n,b\to p}^{\mathrm{coh}} \\ F_{t,b\to p}^{\mathrm{coh}} \\ M_{z,b\to p}^{\mathrm{coh}} \\ F_{n,b\to q}^{\mathrm{coh}} \\ F_{t,b\to q}^{\mathrm{coh}} \\ M_{z,b\to q}^{\mathrm{coh}} \end{bmatrix}}_{\mathbf{F}_{\mathrm{coh},pq}} = \underbrace{\begin{bmatrix} \frac{E_{pq}A_{pq}}{l_{pq}} & 0 & 0 & -\frac{E_{pq}A_{pq}}{l_{pq}} & 0 & 0 \\ 0 & \frac{12E_{pq}I_{pq}}{l_{pq}^3} & -\frac{6E_{pq}I_{pq}}{l_{pq}^2} & 0 & -\frac{12E_{pq}I_{pq}}{l_{pq}^3} & \frac{6E_{pq}I_{pq}}{l_{pq}^2} \\ 0 & -\frac{6E_{pq}I_{pq}}{l_{pq}^2} & \frac{4E_{pq}I_{pq}}{l_{pq}} & 0 & \frac{6E_{pq}I_{pq}}{l_{pq}^2} & -\frac{2E_{pq}I_{pq}}{l_{pq}} \\ -\frac{E_{pq}A_{pq}}{l_{pq}} & 0 & 0 & \frac{E_{pq}A_{pq}}{l_{pq}} & 0 & 0 \\ 0 & -\frac{12E_{pq}I_{pq}}{l_{pq}^3} & \frac{6E_{pq}I_{pq}}{l_{pq}^2} & 0 & \frac{12E_{pq}I_{pq}}{l_{pq}^3} & -\frac{6E_{pq}I_{pq}}{l_{pq}^2} \\ 0 & \frac{6E_{pq}I_{pq}}{l_{pq}^2} & -\frac{2E_{pq}I_{pq}}{l_{pq}} & 0 & -\frac{6E_{pq}I_{pq}}{l_{pq}^2} & \frac{4E_{pq}I_{pq}}{l_{pq}} \end{bmatrix}}_{\mathbf{K}_{\mathrm{loc},b}} \underbrace{\begin{bmatrix} u_{n,p} \\ u_{t,p} \\ \theta_p \\ u_{n,q} \\ u_{t,q} \\ \theta_q \end{bmatrix}}_{\mathbf{u}_b}
$$

$$(3.4)$$

Note that the cohesion forces can be written in the global coordinate system using the rotation matrix $\mathbf{R}_b$ associated to the beam pq. The global equilibrium of the medium is given by the equilibrium of each particles

$$\forall p \in \mathscr{P}, \quad \sum_{b\in\mathscr{B}_p} \left(\mathbf{F}_{b\to p}^{\mathrm{coh}} + \boldsymbol{F}_{\mathrm{ext}\to p} \right) = 0 \qquad (3.5)$$

where $\mathscr{B}_p$ is the set of beams linked to particle p and $\boldsymbol{F}_{\mathrm{ext}\to p}$ is the vector of external forces applied to the particle p. This set of equations can be written as a linear system

$$\left(\underset{b\in\mathscr{B}}{\mathrm{A}} \mathbf{K}_{\mathrm{loc},b} \right) \cdot \mathbf{u} + \mathbf{F}_{\mathrm{ext}} = 0 \qquad (3.6)$$

where $\underset{b\in\mathscr{B}}{\mathrm{A}}$ denotes the operator that assembles the global stiffness, $\mathbf{u}$ is the vector of displacements and rotations for all particles, and $\mathbf{F}_{\mathrm{ext}}$ is the vector of external forces.

1.4 Application of boundary conditions

Let us consider a domain Ω with boundary $\partial\Omega$. Each particle within the domain and in each direction can have either forces/moment or displacements/rotation imposed upon them. If nothing is imposed on a particle, it means that a null force is being applied to it. In homogenization, different types of classical boundary conditions are often used: Kinematically

Uniform Boundary Conditions (KUBC), Statically Uniform Boundary Conditions (SUBC), and Periodic Boundary Conditions (PBC).

❑ **Remark 3.1** *For Kinematically Uniform Boundary Conditions and Statically Uniform Boundary Conditions, particle rotations are free. It means that a null moment is applied to each particle on the boundary.*

Kinematically Uniform Boundary Conditions.   For Kinematically Uniform Boundary Conditions, the strain is imposed on the whole boundary of the domain

$$\forall p \in \partial \mathscr{P}, \quad \boldsymbol{u}_p = \varepsilon_{\text{imp}} \cdot \boldsymbol{x}_p \tag{3.7}$$

where $\partial \mathscr{P}$ is the set of particle on the boundary $\partial \Omega$ and ε_{imp} is the imposed strain. In the numerical implementation of the discrete model, the displacements are imposed by applying a substitution method.

Statically Uniform Boundary Conditions.   For Statically Uniform Boundary Conditions, the stress is imposed on the whole boundary of the domain

$$\forall p \in \partial \mathscr{P}, \quad \boldsymbol{F}_{\text{ext} \to p} = \sigma_{\text{imp}} \cdot \boldsymbol{n}_{\partial \Omega, p} S_p \tag{3.8}$$

where $\boldsymbol{n}_{\partial \Omega, p}$ is the normal to the boundary $\partial \Omega$ at the particle p, S_p is the generalized surface associated to the border of the particle [1], and σ_{imp} is the imposed stress. From the numerical point of view, Statically Uniform Boundary Conditions only requires to fill the vector of exterior forces $\mathbf{F}_{\text{ext}}$ with the force applied to each individual particle of the boundary. Note that rigid body motions must also be prevented. It is usually done by blocking the displacements (and rotation) of one particle.

Periodic Boundary Conditions.   For Periodic Boundary Conditions, a periodic strain is imposed on the whole boundary of the domain. In practice, this boundary condition is more complex than the previous ones. Firstly, it requires the domain to be geometrically periodic. As shown on Figure 3.3, this is achieved by adding a layer of guided particles on upper and right sides of the domain. Each guided particle is associated to a guiding particle on the opposite side of the area element. Note that a guiding particle might guide multiple particles. The Periodic Boundary Conditions induces a relation between displacements of the guiding and the guided particle

$$\boldsymbol{u}_{\text{guided}} = \boldsymbol{u}_{\text{guiding}} + \varepsilon_{\text{imp}} \cdot (\boldsymbol{x}_{\text{guided}} - \boldsymbol{x}_{\text{guiding}}), \tag{3.9}$$

$$\theta_{\text{guided}} = \theta_{\text{guiding}}. \tag{3.10}$$

In this work, different methods have been applied to impose Periodic Boundary Conditions: a penalization method, a substitution method and by introducing Lagrange multipliers. The penalization method is not retained as it requires the introduction of an arbitrary numerical

---

[1] In 2D, the length associated to the border of the particle p is the length of the cell border used in the grid to position particle centers (see Figure 3.1).
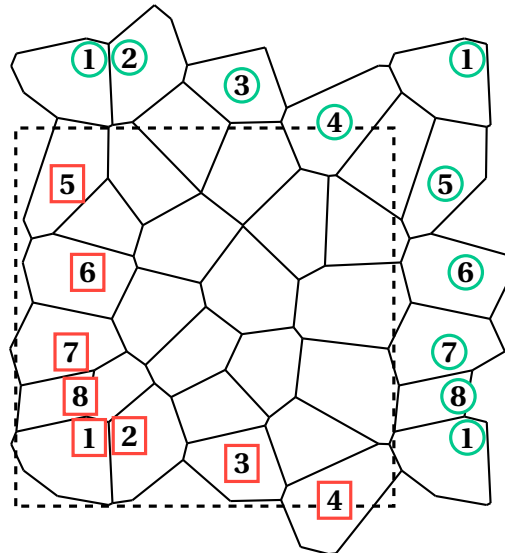
Figure 3.3 • Illustration of a periodic beam-particle mesh. The dashed square is the domain boundary $\partial\Omega$. Red boxed particles are guiding particles. Green circled particles are guided particles. Guided particles have the same number as their guiding particle.

parameter. The substitution method leads to changes in the stiffness matrix which are too complex to maintain. It adds complexity to the subtraction of broken beam stiffness. Finally, the only remaining option – and the chosen one – is the use of Lagrange multipliers. It has the advantages to not modify the initial stiffness matrix (only add rows and columns). However, the matrix with Lagrange multipliers is no longer positive definite.

🔍 **Remark 3.2** *The in-lab discrete model code, named* DEAP, *used in this work used a linear solver based on the Cholesky decomposition. Due to the loss of positive definiteness of the stiffness matrix, this solver could no longer be used. With the help of the Simulation Center at LMPS, we added support for SuiteSparse solvers* DEAP. *In particular, the* SPQR *solver (Davis, 2011) based on the* QR *decomposition is used.*

Finally, the rigid body motions must also be prevented, which is done by imposing the displacements and rotation of one particle to be zero.

2   Homogenization and its applications to discrete models

This section aims at presenting the existing approaches in homogenization – in general, and specifically for discrete medium . It also contains a discussion on the existence of a Representative Volume Element, which is a major assumption in homogenization.

2.1   General principle of homogenization

In general, homogenization studies consider (at least) three scales of observations

1. **Micro-scale.** It is the scale of the heterogeneities. Here, its characteristic length is the average size of the particle (or equivalently, the average length of the beams in the model).

2. **Meso-scale.** It is an intermediate scale which is large enough to consider the material as homogeneous but small relative to the macro-scale. Here, this scale will be chosen such that the average elastic properties does not change when its characteristic length increases. This will be the scale of the elementary domain.

3. **Macro-scale.** It is the scale of the structure. Its characteristic length depends on the size of the structure.

In homogenization, the material is considered as homogeneous at the macro-scale. The idea revolves around identifying a homogeneous material having mechanical properties equivalent to the average properties of the heterogeneous material at the meso-scale. Instead of representing the whole micro-structure, the homogeneous material can be used at the macro-scale. It leads to less complex models and simulations.

This scale transition is formalized by Hill's lemma (Hill, 1963), also called Hill-Mandel condition or macro-homogeneity condition:

$$\overline{\sigma : \varepsilon} - \overline{\sigma} : \overline{\varepsilon} = \frac{1}{V_\Omega} \int_{\partial\Omega} (\boldsymbol{u} - \overline{\varepsilon} \cdot \boldsymbol{x})(\sigma \cdot \boldsymbol{n} - \overline{\sigma} \cdot \boldsymbol{n}) \mathrm{d}\boldsymbol{x} \tag{3.11}$$

where $\overline{\bullet}$ denotes the averaging operator

$$\overline{\bullet} = \frac{1}{V_\Omega} \int_\Omega \bullet(\boldsymbol{x}) \mathrm{d}\boldsymbol{x}, \tag{3.12}$$

V_Ω is the volume of domain Ω, and $\boldsymbol{n}$ is the normal the boundary $\partial\Omega$. A recent proof of this lemma is provided by Qu and Cherkaoui (2006) among many others. A corollary of this condition states that for any statically admissible stress field and any kinematically admissible strain field, the average of the macro-scale energy $\frac{1}{2}\,\overline{\sigma} : \overline{\varepsilon}$ is equivalent to the average of the micro-scale energy $\frac{1}{2}\,\overline{\sigma : \varepsilon}$. From a mathematical point of view, it reads

$$\forall \boldsymbol{x} \in \partial\Omega, \quad \left(\sigma(\boldsymbol{x}) \cdot \boldsymbol{n} - \overline{\sigma}(\boldsymbol{x}) \cdot \boldsymbol{n}\right) \times \left(\boldsymbol{u}(\boldsymbol{x}) - \overline{\varepsilon}(\boldsymbol{x}) \cdot \boldsymbol{x}\right) = 0 \quad \implies \quad \overline{\sigma} : \overline{\varepsilon} = \overline{\sigma : \varepsilon}. \tag{3.13}$$

Any boundary conditions where either $\sigma(\boldsymbol{x}) \cdot \boldsymbol{n} = \overline{\sigma}(\boldsymbol{x}) \cdot \boldsymbol{n}$ or $\boldsymbol{u}(\boldsymbol{x}) = \overline{\varepsilon}(\boldsymbol{x}) \cdot \boldsymbol{x}$ is satisfied for each individual points of the boundary verifies the Hill's lemma. In particular, three types of boundary conditions verifying those conditions are frequently used:

- **Kinematically Uniform Boundary Conditions (KUBC).** The strain is imposed on the whole boundary

$$\forall x \in \partial\Omega, \quad \boldsymbol{u}(\boldsymbol{x}) = \varepsilon_{\mathrm{imp}} \cdot \boldsymbol{x}. \tag{3.14}$$

- **Statically Uniform Boundary Conditions (SUBC).** The stress is imposed on the whole boundary

$$\forall x \in \partial\Omega, \quad \sigma(\boldsymbol{x}) \cdot \boldsymbol{n} = \overline{\sigma}(\boldsymbol{x}) \cdot \boldsymbol{n}. \tag{3.15}$$

- **Periodic Boundary Conditions (PBC).** The boundary is split in two parts $\partial\Omega = \partial\Omega^+ \oplus \Omega^-$ where $\oplus$ denotes the direct sum[2]. $\partial\Omega^+$ and $\partial\Omega^-$ are the guiding and guided parts of the boundary. The Periodic Boundary Conditions impose the periodicity of displacement

$$\forall \boldsymbol{x}^+ \in \Omega^+ \text{ and associated } \boldsymbol{x}^- \in \Omega^-, \quad \boldsymbol{u}(\boldsymbol{x}^-) = \boldsymbol{u}(\boldsymbol{x}^+) + \varepsilon_{\text{imp}} \cdot (\boldsymbol{x}^- - \boldsymbol{x}^+), \quad (3.16)$$

and the anti-periodicity of stress

$$\forall \boldsymbol{x}^+ \in \Omega^+ \text{ and associated } \boldsymbol{x}^- \in \Omega^-, \quad \sigma(\boldsymbol{x}^+) \cdot \boldsymbol{n} = \sigma(\boldsymbol{x}^-) \cdot \boldsymbol{n}. \quad (3.17)$$

In practice, Kinematically Uniform Boundary Conditions give an upper bound of the effective elasticity tensor whereas Statically Uniform Boundary Conditions gives a lower bound. With Kinematically Uniform Boundary Conditions, the border of the domain are kept straight, as if they were infinitely rigid, leading to an artificial stiffening of the domain. Conversely, Statically Uniform Boundary Conditions tends to artificially soften the domain. The Periodic Boundary Conditions are usually considered as a good intermediate estimation of the effective elastic properties (Tian et al., 2019). Note that other mixed boundary conditions are also used in the literature and not considered here.

2.2 Existence of a Representative Volume Element for softening materials

The quasi-brittle material is modelled at a meso-scale using the beam-particle model. This model is discrete, meaning that the mechanical quantities (displacements and forces) are not defined continuously. Additionally, this model is also heterogeneous due to the randomness of the particle geometries and their spatial distribution. It means that if one could measure the local strain/stress in the material, the strain/stress field would be heterogeneous.

An important remark is that the effective heterogeneity of a material depends on the observation scale. Most materials are highly heterogeneous when observed at a micro-scale. In most practical cases, properties at a larger scale are sufficient to represent the material. Those properties are volume-average of the meso-scale quantities. In general, the overall properties can be seen as homogeneous at this new (macro-)scale. At this point, it is important to discuss the existence of such macro-scale.

Let us consider a material with heterogeneity at the meso-scale, which is order of magnitude smaller than the macro-scale. Finding an Representative Volume Element (RVE) consists in finding a volume of material such that the average of the meso-scale quantities is constant when increasing the size of the volume. Such volume always exists in elasticity. However, note that the studied structure might be smaller than this RVE. In this case, the scale cannot be separated. When a softening behavior is observed, the properties associated with the softening behavior will not converge when increasing the size of the averaging volume. This issue directly relates to the size effect. Present work does not aim at tackling those questions. In-depth discussions on the existence of an RVE can be found in the works of Stroeven et al. (2004), Gitman et al. (2007), Pelissou et al. (2009), Nguyen et al. (2010, 2011), and Shahin et al. (2022).

---

[2]The direct sum is defined such that $\Omega = \Omega_1 \oplus \Omega_2 \iff \Omega = \Omega_1 \cup \Omega_2$ and $\Omega_1 \cap \Omega_2 = \emptyset$.

An implicit aim of this work is to determine whether it is possible to formulate an anisotropic damage model able to correctly represent the effective elastic properties when the elastic properties soften. Note that it means that the material parameters linked to damage will depend on the size of the averaging volume used for identification, exactly as in experiments. In the present work, a bi-dimensional domain at the meso-scale of fixed size is considered. It is called an area element instead of a Representative area element, since its behavior is softening and thus not representative.

3   Measurement procedure for the elasticity tensor of discrete area elements

This section briefly presents the procedure applied to measure the effective elasticity tensor associated to a micro-cracked area element.

3.1   Foundations of the measurement procedure

Let us consider three linearly independent strain $\overline{\varepsilon}^{(i)}$ states and the associated stresses $\overline{\sigma}_i$ in Kelvin notation

$$\left[\overline{\varepsilon}^{(i)}\right] = \begin{bmatrix} \overline{\varepsilon}_{11}^{(i)} \\ \overline{\varepsilon}_{22}^{(i)} \\ \sqrt{2}\overline{\varepsilon}_{12}^{(i)} \end{bmatrix}, \quad \left[\overline{\sigma}^{(i)}\right] = \begin{bmatrix} \overline{\sigma}_{11}^{(i)} \\ \overline{\sigma}_{22}^{(i)} \\ \sqrt{2}\overline{\sigma}_{12}^{(i)} \end{bmatrix}. \tag{3.18}$$

The elasticity tensor in Kelvin notation is the 3×3 symmetric matrix

$$[\mathbf{E}] = \left(\left[\left[\overline{\sigma}^{(1)}\right], \left[\overline{\sigma}^{(2)}\right], \left[\overline{\sigma}^{(3)}\right] \right] \cdot \left[\left[\overline{\varepsilon}^{(1)}\right], \left[\overline{\varepsilon}^{(2)}\right], \left[\overline{\varepsilon}^{(3)}\right] \right]^{-1} \right)^S. \tag{3.19}$$

The strain states $\left[\overline{\varepsilon}^{(i)}\right]$ must be orthogonal to each others (*i.e.* linearly independent) so that the matrix associated to strains is invertible.

 Remark 3.3 *The strain states matrix is* 3×3. *For this matrix to be invertible, the vector family formed by its columns must be a basis of* $\mathbb{R}^3$. *Thus, the family of strain loads must have a cardinality of 3 and contains linearly independent vectors.*

This expression means that the effective elasticity tensor can be determined by applying three orthogonal (elastic) measurement loadings to the area element and measuring its strain and stress. Nevertheless, several questions need further details, namely, the determination of the appropriate loading/boundary conditions to be applied to the area element, the calculation of the strain, and the calculation of the stress. Those different questions are tackled in the next subsections.

3.2   Strain measurement

Different reviews of strain averaging in discrete (granular) material are available in the literature in 2D (Bagi, 2006) and in 3D (Drummen, 2006; Durán et al., 2010). In those works, the strain averaging methods are classified into two categories:

1. **Equivalent continuum.** The idea is to define an equivalent continuum from the geometry of the meso-structure. The average strain of this equivalent continuum is the average strain of the discrete domain.

2. **Best-fit.** This type of methods consists in finding the strain tensor that best fits the particle displacement field.

This subsection describes and compares the different strain measurement proposed in the literature. It mainly aims at comparing and verifying the validity of different methods to measure strain in presence of micro-cracks.

3.2.1 "Experimental" method

The principle of this method is to compute the strain tensor as it might be done experimentally. The measurement of strain is carried out by measuring the elongation of the area element in each directions. For this method, the strain definition is

$$\overline{\varepsilon} = \begin{bmatrix} \frac{1}{L_1}\left(u_1^{\text{top}} - u_1^{\text{bot}}\right) & \frac{1}{L_2}\left(u_1^{\text{right}} - u_1^{\text{left}}\right) \\ \frac{1}{L_1}\left(u_2^{\text{top}} - u_2^{\text{bot}}\right) & \frac{1}{L_2}\left(u_2^{\text{right}} - u_2^{\text{left}}\right) \end{bmatrix} \tag{3.20}$$

where $u_\bullet^{\text{face}}$ is the average displacement in the direction $\bullet$ of the specified face. In practice, the average displacement in all the directions of each faces of the square area element are computed in post-processing. The lengths L_1 and L_2 correspond to the side of the square domain.

3.2.2 Bagi's method

(Bagi, 1996) defined the strain tensor in a granular assembly by introducing an equivalent continuum. This equivalent continuum is the union of cells (surfaces in 2D) in the mesh. This method consists in calculating the strain of each cell and then average it over the equivalent continuum. The author proposed two equivalent continua:

- **Material Cell System (MCS).** In the MCS, the cells are the faces in the Voronoï tessellation of the particle centers, *i.e.* a cell is a particle.

- **Space/void Cell System (SCS).** In the SCS, the cells are the faces in the Delaunay triangulation of the particle centers, *i.e.* a cell is a space between three connected beams.

In the beam-particle model, the particle are considered as rigid. Moreover, the deformation is carried by the beams. It makes more sense to use the Space Cell System as the equivalent continuum. In this definition of a cell, the deformation of beams, as well as the discontinuous displacement resulting from their failure, are considered together as part of the overall deformation of the cell. The Space Cell System is represented on Figure 3.4. The average strain of equivalent continuum is defined as

$$\overline{\varepsilon} = \frac{1}{V_{\text{SCS}}} \int_{\text{SCS}} (\nabla \boldsymbol{u}(\boldsymbol{x}))^{\text{S}} \, \mathrm{d}\boldsymbol{x} \tag{3.21}$$
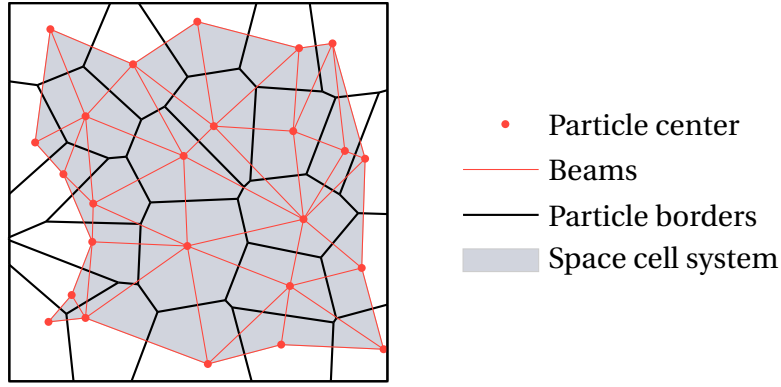
Figure 3.4 • Illustration of the space cell system as described by Bagi (1996).

where V_{SCS} is the (generalized) volume of the Space Cell System and $\bullet^{\text{S}} = \frac{1}{2}\left(\bullet + \bullet^{\text{T}}\right)$ is the symmetrization operator. In the discrete media, Bagi defined the average strain as the volume-weighted average of strain over the cells

$$\bar{\varepsilon} = \frac{1}{V_{\text{SCS}}} \sum_{c \in \mathscr{C}_{\text{SCS}}} V_c \varepsilon_c \, \mathrm{d}\boldsymbol{x} \tag{3.22}$$

where $\mathscr{C}_{\text{SCS}}$ is the set of cells in the Space Cell System, V_c is the volume of cell $c \in \mathscr{C}_{\text{SCS}}$ and ε_c is the strain of cell c.

◯ **Remark 3.4** *As shown by Figure 3.4, the volume V_{SCS} of the Space Cell System is not equal to the volume of the domain. The volume of the domain contains a part of the (rigid) particles which does not deform (the white part in the Figure 3.4). Thus, it does not contribute to the elastic behavior. The volume of the Space Cell System will be the volume of interest for averaging.*
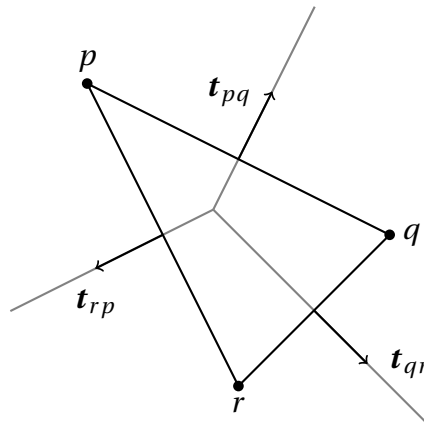
Figure 3.5 • Representation of a cell. The particle centers are represented by black circles, the grey line are the particle borders, and the black line are the beams.

The next, and final, step consists in defining the deformation of a (triangular) cell. A representation of the cell is proposed in Figure 3.5. Bagi (1996) proposed to define the strain of a cell c as

$$\varepsilon_c = \frac{1}{S_c} \sum_{(p,q) \in \mathscr{B}_c} l_{pq} \frac{\boldsymbol{u}_p + \boldsymbol{u}_q}{2} \odot \boldsymbol{t}_{pq} \tag{3.23}$$

where $\frac{1}{S_c}$ is the surface of the cell c, $\mathscr{B}_c$ is the set of beams in the cell c, $\odot$ is the symmetrized tensor product $(\mathbf{a} \odot \mathbf{b} = (\mathbf{a} \otimes \mathbf{b})^S)$ and $\boldsymbol{t}_{pq}$ is the tangent vector to the section of the beam pq. Note that $\boldsymbol{t}_{pq}$ and $\boldsymbol{t}_{qp}$ are opposed. The particles centers are ordered in the beams of the cell such that $\boldsymbol{t}_{pq}$ is the outward-pointing normal to the border of the cell.

3.2.3 Bagi's method on boundary

The direct application of Bagi's method is computationally costly. Instead of averaging the displacement gradient over the Space Cell System, we can apply the divergence theorem to rewrite the average as a surface integral. The average (symmetric) strain is defined as

$$\overline{\varepsilon} = \frac{1}{V_{\text{SCS}}} \int_{\partial \text{SCS}} \boldsymbol{u}(\boldsymbol{x}) \odot \boldsymbol{n}(\boldsymbol{x}) \, \mathrm{d}\boldsymbol{x} \tag{3.24}$$

where $\odot$ denotes the symmetrized tensor product $(\mathbf{a} \odot \mathbf{b} = \frac{1}{2}(\mathbf{a} \otimes \mathbf{b} + \mathbf{b} \otimes \mathbf{a}))$, and $\boldsymbol{n}(\boldsymbol{x})$ is the outward-pointing normal to the boundary of the Space Cell System ∂SCS. Expressing the average strain as a function of the discrete quantities leads to

$$\overline{\varepsilon} = \frac{1}{V_{\text{SCS}}} \sum_{(p,q) \in \partial \mathscr{B}} l_{pq} \frac{\boldsymbol{u}_p + \boldsymbol{u}_q}{2} \odot \boldsymbol{t}_{pq} \tag{3.25}$$

where $\partial \mathscr{B}$ is the set of beams on the boundary of the Space Cell System.

3.2.4 Cundall's method

This approach was proposed by Cundall and is described by Bagi (2006). This definition originates from the study of granular materials. Its principle is to fit the average strain to the displacement gradient of the particle centers.

Let us approximate the displacement $\boldsymbol{u}_p$ of a particle p as

$$\forall p \in \mathscr{P}, \quad \boldsymbol{u}_p \approx \overline{\boldsymbol{u}} + \overline{\varepsilon} \cdot \boldsymbol{x}_p \tag{3.26}$$

where $\overline{\boldsymbol{u}} = \frac{1}{N_p} \sum_{p \in \mathscr{P}} \boldsymbol{u}_p$ is the average displacement of the particle which corresponds to a rigid body motion, and N_p is the number of particles. In order to simplify this expression, the average – over all the particles – of both side is subtracted to obtain

$$\forall p \in \mathscr{P}, \quad \boldsymbol{u}_p - \frac{1}{N_p} \sum_{p \in \mathscr{P}} \boldsymbol{u}_p \approx \overline{\varepsilon} \cdot \boldsymbol{x}_p - \frac{1}{N_p} \sum_{q \in \mathscr{P}} \overline{\varepsilon} \cdot \boldsymbol{x}_q. \tag{3.27}$$

Let us introduce the particle position $\Delta \boldsymbol{x}_p = \boldsymbol{x}_p - \overline{\boldsymbol{x}}$ relative to the average particle position $\overline{\boldsymbol{x}}$ (geometrical center), and the displacement $\Delta \boldsymbol{u}_p = \boldsymbol{u}_p - \overline{\boldsymbol{u}}$ relative to the average particle displacement $\overline{\boldsymbol{u}}$. The expression simplifies into

$$\forall p \in \mathscr{P}, \quad \Delta \boldsymbol{u}_p \approx \overline{\varepsilon} \Delta \boldsymbol{x}_p \tag{3.28}$$

Replacing the approximation by an equality leads to an overdetermined linear system of equations. The principle of this approach consists in minimizing the least-square error LSE associated to this relation

$$\overline{\varepsilon} = \arg\min_{\overline{\varepsilon}^*} \underbrace{\sum_{p \in \mathscr{P}} \left(\Delta \boldsymbol{u}_p - \overline{\varepsilon}^* \Delta \boldsymbol{x}_p \right)^{\mathrm{T}} \left(\Delta \boldsymbol{u}_p - \overline{\varepsilon}^* \Delta \boldsymbol{x}_p \right)}_{\text{LSE}(\overline{\varepsilon}^*)} \tag{3.29}$$

The expression of the average strain is obtained by minimizing LSE($\overline{\varepsilon}$), which gives

$$\frac{\partial \text{LSE}(\overline{\varepsilon})}{\partial \overline{\varepsilon}} = \mathbf{0} 2 \implies \overline{\varepsilon} = \left(\sum_{p \in \mathscr{P}} \Delta \boldsymbol{u}_p \Delta \boldsymbol{x}_p^{\text{T}} \right) \left(\sum_{p \in \mathscr{P}} \Delta \boldsymbol{x}_p \Delta \boldsymbol{x}_p^{\text{T}} \right)^{-1} \tag{3.30}$$

The developments to obtain this expression are given in Appendix A.

3.2.5   Cundall's method on boundary

Then, Cundall's strain definition as also been applied by considering only the particles on the boundary. The whole development is the same as for the previous method. Thus, the average strain rewrites

$$\overline{\varepsilon} = \left(\sum_{p \in \partial \mathscr{P}} \Delta \boldsymbol{u}_p \Delta \boldsymbol{x}_p^{\text{T}} \right) \left(\sum_{p \in \partial \mathscr{P}} \Delta \boldsymbol{x}_p \Delta \boldsymbol{x}_p^{\text{T}} \right)^{-1} \tag{3.31}$$

where $\partial \mathscr{P}$ denotes the set of particles on the boundary of the domain.

3.2.6   Comparison

The five different definitions of the average strain are compared in this paragraph. To verify and assess the averaging methods, three strain loadings (Kinematically Uniform Boundary Conditions) are applied to a square area element until its failure. Those loadings are

$$\varepsilon_{\text{imp}}^{\text{bitension}} = 10^{-4} \, t \begin{bmatrix} 1 & 0 \\ 0 & 1 \end{bmatrix}, \quad \varepsilon_{\text{imp}}^{\text{tension}} = 2 \times 10^{-4} \, t \begin{bmatrix} 1 & 0 \\ 0 & 0 \end{bmatrix}, \quad \varepsilon_{\text{imp}}^{\text{shear}} = 2 \times 10^{-4} \, t \begin{bmatrix} 0 & 1 \\ 1 & 0 \end{bmatrix}, \tag{3.32}$$

where $t \in [0,1]$ is the loading parameters which is discretized into 100 load steps. For illustration purpose, Figure 3.6 shows measured strains $\overline{\varepsilon}_{11,\text{meas}}$ as functions of the imposed strain $\overline{\varepsilon}_{11,\text{imp}}$. Ideally, the measured strain is equal to the imposed strain. One can readily discern the difference between the strain predicted by Cundall's method on the whole domain and the other methods. This difference is explained further in this section.

Error analysis.   For a better comparison of the different methods, let us introduce the relative error between the measured strain with method "meas" and the imposed strain

$$e_{\varepsilon,\text{meas}} = \frac{\| \overline{\varepsilon}_{\text{meas}} - \varepsilon_{\text{imp}} \|}{\| \varepsilon_{\text{imp}} \|} \tag{3.33}$$

where $\varepsilon_{\text{meas}}$ is the average strain measured with one of the methods, and $\| \bullet \|$ denotes the Frobenius norm. Figures 3.7 to 3.9 contain the evolution of the error during the three proposed loadings. Those figures show that most methods gives an average strain close to the imposed strain. However, Cundall's ($\mathscr{P}$) method and the "Experimental" method give results that are far from the imposed strains. Those errors are explained in the following paragraphs.

Figure 3.6 • Comparison of the measured strain with the imposed strain for a tension imposed strain (with Kinematically Uniform Boundary Conditions) in the direction e_1.

Figure 3.7 • Comparison of the measured strain with the imposed strain for a bitension imposed strain (with Kinematically Uniform Boundary Conditions) via error calculation. The methods with $\mathscr{P}$ are applied on the whole domain whereas the methods whit $\partial\mathscr{P}$ are applied on the boundary.

Figure 3.8 • Comparison of the measured strain with the imposed strain for a tension imposed strain (with Kinematically Uniform Boundary Conditions) via error calculation. The methods with $\mathscr{P}$ are applied on the whole domain whereas the methods whit $\partial\mathscr{P}$ are applied on the boundary.
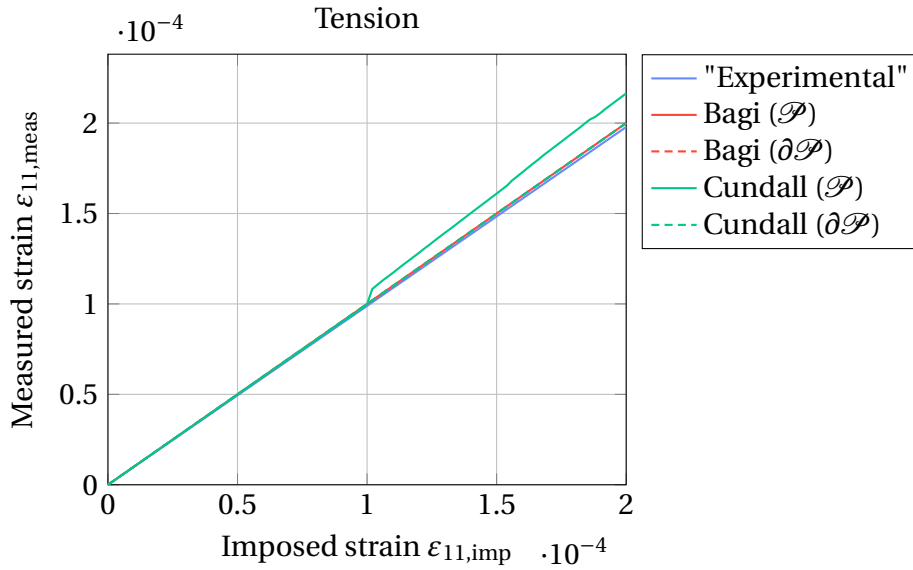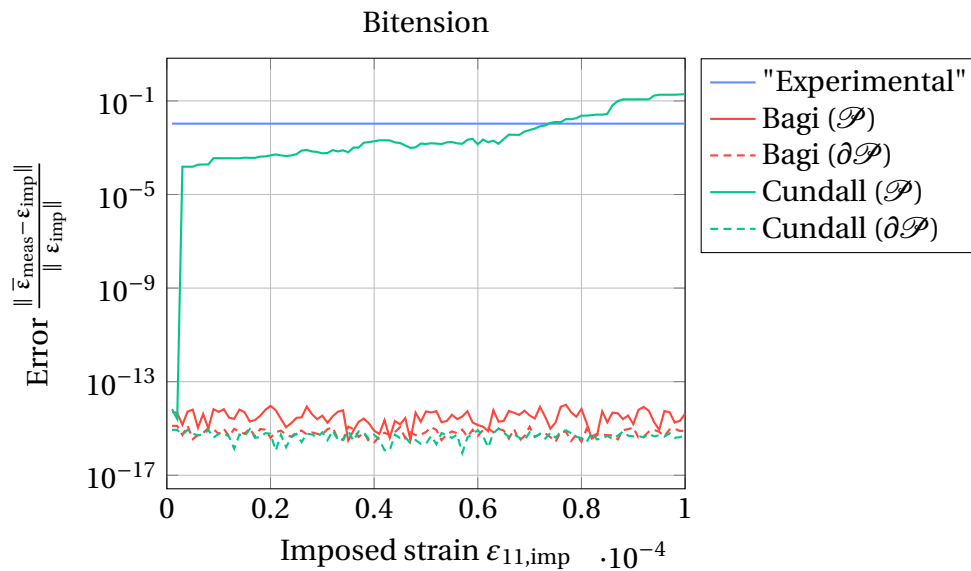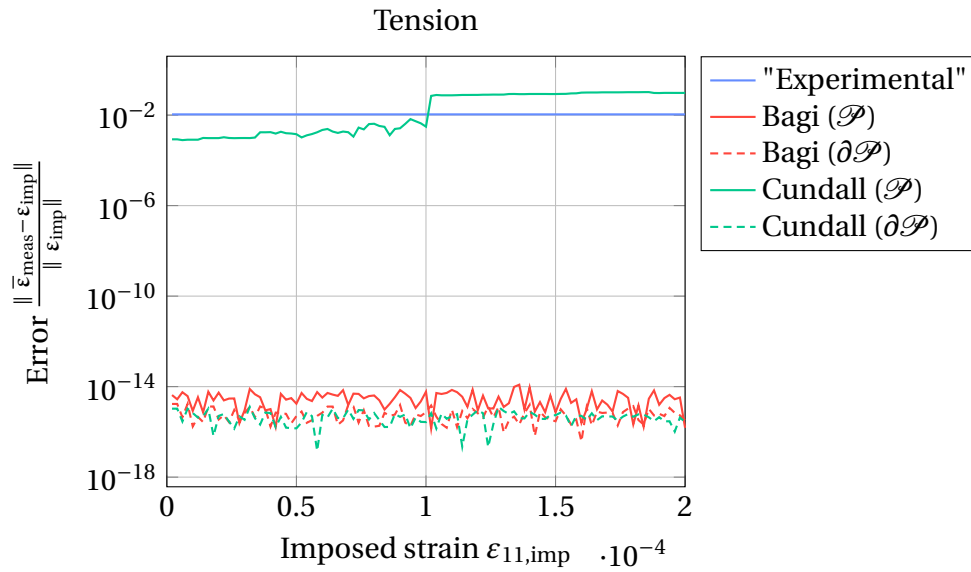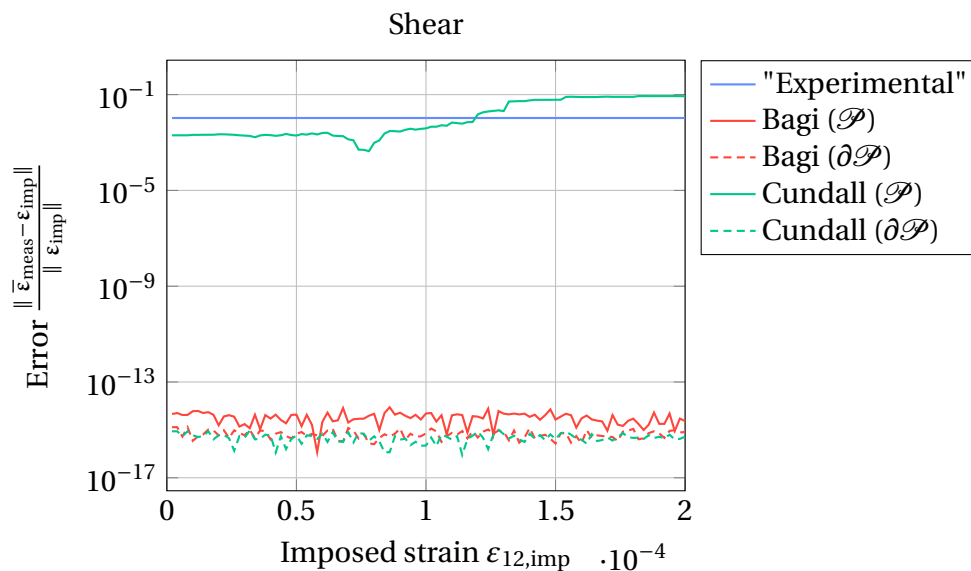

Figure 3.9 • Comparison of the measured strain with the imposed strain for a shear imposed strain (with Kinematically Uniform Boundary Conditions) via error calculation. The methods with $\mathscr{P}$ are applied on the whole domain whereas the methods whit $\partial\mathscr{P}$ are applied on the boundary.

"Experimental" method error.   The main source of error in the "Experimental" method is mainly due to the choice of length. Currently, the geometric length, corresponding to the side of the area element, is utilized as the reference length for measuring average strain. However, this length does not correctly represent the region of the area element capable of undergoing deformation, *i.e.* the length of the lattice domain. It is important to highlight that this effective length is smaller than the geometric length of the area element, as depicted in Figure 3.4. To rectify this measurement error, it is necessary to substitute the geometric length of the area element with the effective length. The latter can be obtained as the average distance between opposed particle along boundaries in the direction e_1 and e_2. For instance, the effective distance L_1 in the direction e_1 would be

$$L_1 = \frac{1}{N_{p,\text{top}}} \sum_{p \in \mathscr{P}_{\text{top}}} \left| x_{p,\text{top}} \cdot e_1 - x_{p,\text{bot}} \cdot e_1 \right| \tag{3.34}$$

where $N_{p,\text{top}}$ is the number of particles on the top face, $\mathscr{P}_{\text{top}}$ is the set of particle on the top face, $x_{p,\text{top}}$ is the position of the particle p on the top face, and $x_{p,\text{bot}}$ is the position of the particle on the bottom face associated to particle p. As this error on the effective distance outweighs others sources of errors and acts as a factor of the measured average strain (see Equation (3.20)), the error seems to stay constant during the loadings.

Cundall's method error.   For Cundall's best-fit strain, the measured average strain deviates from the imposed strain when micro-cracking occurs. It is even more pronounced when there is a macro-crack. The main issue is that the measured average strain depends on the location of cracks. In Figure 3.10, a regular square area element consisting of 10×10 particles is depicted. Each particle has a side length of 0.1 m. The area element is subjected to a tensile strain in the horizontal direction

$$\varepsilon_{\text{imp}} = \begin{bmatrix} 0.1 & 0 \\ 0 & 0 \end{bmatrix}. \tag{3.35}$$

We examine four distinct cases: one where the area element remains uncracked under the applied loading (a), and three cases where the cracks localized at different locations in the material. According to Cundall's best-fit strain, the deformation for those cases are

$$\varepsilon^{\text{a}}_{\text{Cundall}} = \begin{bmatrix} 0.10 & 0 \\ 0 & 0 \end{bmatrix}, \qquad \varepsilon^{\text{b}}_{\text{Cundall}} = \begin{bmatrix} 0.094 & 0 \\ 0 & 0 \end{bmatrix}, \tag{3.36}$$

$$\varepsilon^{\text{c}}_{\text{Cundall}} = \begin{bmatrix} 0.12 & 0 \\ 0 & 0 \end{bmatrix}, \qquad \varepsilon^{\text{d}}_{\text{Cundall}} = \begin{bmatrix} 0.094 & 0 \\ 0 & 0 \end{bmatrix}. \tag{3.37}$$

For a same applied strain, crack localization influences the average strain value in the area element. For this work, it means that Cundall's best-fit strain is not adequate. Note that, in this exemple, Cundall's strain restricted to the boundary should not be affected by this issue as it is neglect the particle inside the domain. As shown by Figure 3.10, the particles on the boundary of each specimen have the same displacements. Yet, for another loading, such as an "experimental" loading, the same issue could arise.

📝 Conclusion – Strain measurement

In this subsection, several strain averaging approaches are compared, namely the "Experimental", Bagi, and Cundall methods. The last two were applied both on the boundary and

a. Uncracked

b. Cracked at 0.2 m
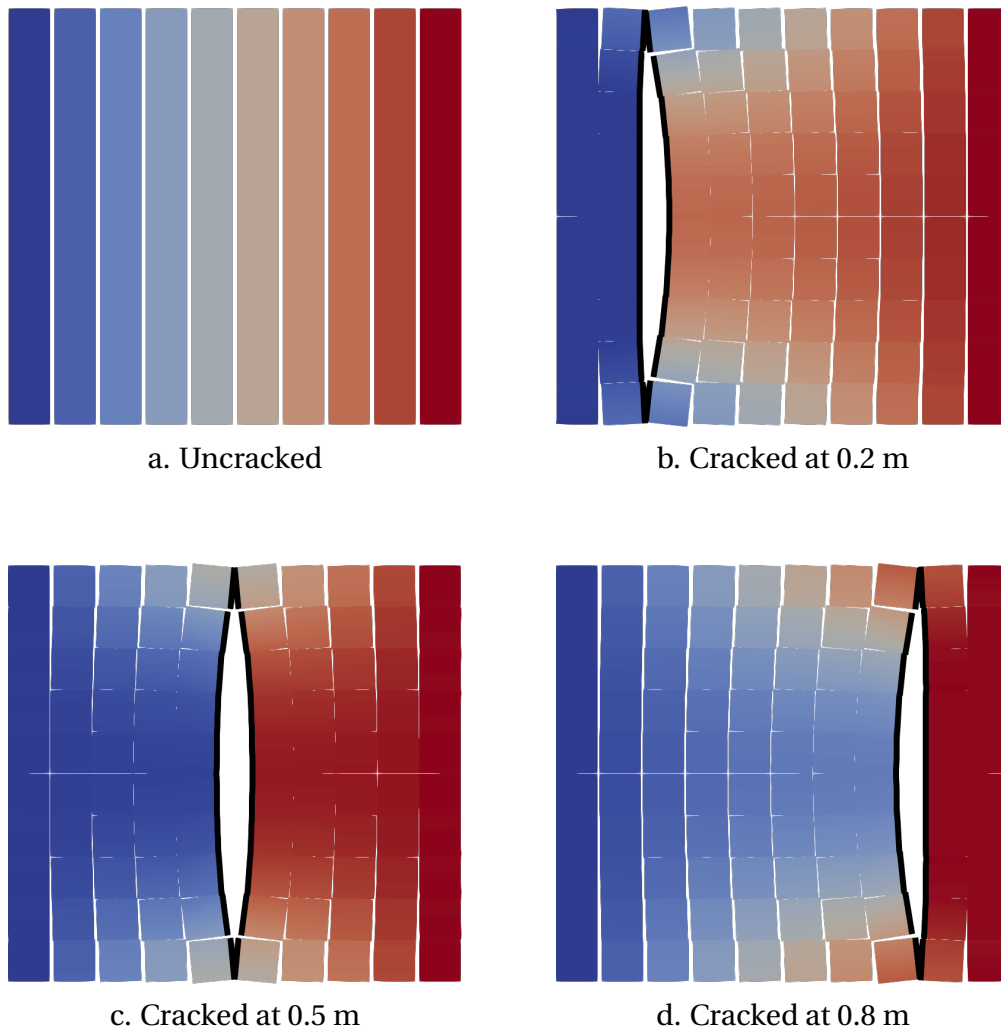
c. Cracked at 0.5 m

d. Cracked at 0.8 m

Figure 3.10 • Illustration depicting the dependency of Cundall's average strain on the position of the crack. The colors corresponds to displacement magnitude. The deformation is depicted without any scale factor. The black lines corresponds to the cracks.

the entire domain of the area element. To evaluate their performance, specific strains are imposed, and the average strain is computed using each method. Both imposed and measured strains are then compared. The "Experimental" and Cundall approaches have been shown to be flawed. In particular, the Cundall approach is not well-defined when a strain localization occurs. In contrast, Bagi's method demonstrated sufficient accuracy in calculating average strain. Additionally, when applied to the boundary of the domain, Bagi's method showed lower computational costs compared to applying it to the entire domain. Furthermore, the implementation of Bagi's method on the boundary is more straightforward. Therefore, for the rest of this document, Bagi's method will be employed to compute the average strain in the area element.

3.3   Stress measurement

The definition of average stress are less discussed than the definitions of average strain in the literature. To our knowledge, the first definition of the average stress in a granular material – with spherical particles – have been proposed by Drescher and de Josselin de Jong (1972). After the work of Drescher and de Josselin de Jong (1972), many authors – Christoffersen et al. (1981), Rothenburg and Selvadurai (1981) among others – proposed similar definitions of the average stress tensor based on the contact forces between particles with arbitrary shape. Like for the strain, local definitions of the stress have also been proposed in the literature. Those methods are also based on the definition of an equivalent continuum. As the forces are transmitted by particles borders (through the beam), the equivalent continuum proposed by Bagi (1996) is the Material Cell System (see Section 3.2.2). More recent propositions in the literature mainly tackle the definition of generalized stress in higher-order continua, which is out of the scope of this study. Here, only the definition proposed by Drescher and de Josselin de Jong (1972) is presented and studied.

3.3.1   Drescher's method

According to Drescher and de Josselin de Jong (1972), the average stress tensor in the area element Ω can be defined as

$$\overline{\sigma} = \frac{1}{V_\Omega} \int_\Omega \sigma(\boldsymbol{x}) \, \mathrm{d}\boldsymbol{x} \quad \overset{\text{divergence theorem}}{\Longrightarrow} \quad \overline{\sigma} = \frac{1}{V_\Omega} \int_{\partial\Omega} \boldsymbol{x} \odot \boldsymbol{t}(\boldsymbol{x}) \, \mathrm{d}\boldsymbol{x} \tag{3.38}$$

where $\boldsymbol{t}$ is the traction vector. In order to define the stress from the discrete quantities, an equivalent continuum must be considered, here the Space Cell System. As the forces on the boundary of the Space Cell System are concentrated at particle centers, the surface integral reads

$$\overline{\sigma} = \frac{1}{V_{SCS}} \sum_{p \in \partial\mathscr{P}} \boldsymbol{x}_p \odot \mathbf{f}_p \, \mathrm{d}\boldsymbol{x} \tag{3.39}$$

where $\mathbf{f}_p$ is the sum of cohesion forces – from the beams – applied to the particle.

3.3.2   Verification of Drescher's method

Verification procedure.   Due to cracking, applying a stress on the boundary of the domain may result in a complete failure right after peak stress. Furthermore, after cracking, the area

element may split into different independent parts. It leads to an ill-posed problem due to the apparition of rigid body motions in those parts. This is an issue as we want to verify the stress averaging in the presence of cracks. Based on those remarks, the verification of stress averaging cannot be carried out with the same method as for the strain. Instead, a strain loading is first applied on the area element to gradually crack it. This loading is discretized into 100 load steps. Then, the cracks at each load steps are extracted to generate a pre-cracked area element. Finally, a stress is applied on the pre-cracked area element using Statically Uniform Boundary Conditions.

Application. Let us consider a square area element of 0.2×0.2 m^2 with a beam length of $\bar{l}_b = 0.02$ m leading to 10 square particles in each direction. The geometric length of the domain is $L = 0.02$ m whereas the effective length (length of the lattice) is $L - \bar{l}_b = 9 \times 0.02$ m. To apply a bitension stress loading, we apply a force $f_p = 1$ N on each particle of the boundary in the direction normal to the boundary (see Figure 3.11). It corresponds to applying a stress
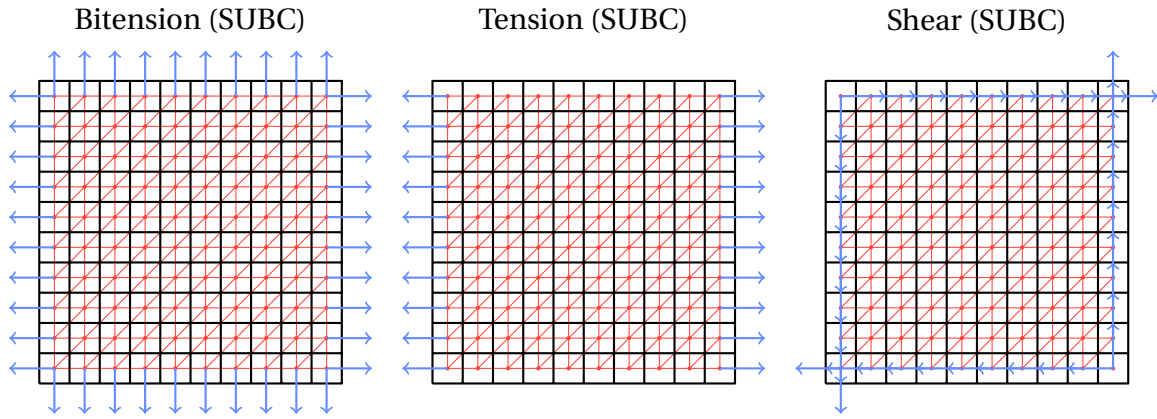
Figure 3.11 • Illustration of the loadings for the verification of the stress averaging.

tensor

$$\sigma_{\text{imp}}^{\text{bitension}} = \frac{10 \times f_p}{L - \bar{l}_b} \begin{bmatrix} 1 & 0 \\ 0 & 1 \end{bmatrix} = \frac{10}{0.18} \begin{bmatrix} 1 & 0 \\ 0 & 1 \end{bmatrix} \approx 55.55... \begin{bmatrix} 1 & 0 \\ 0 & 1 \end{bmatrix}. \tag{3.40}$$

The same procedure is applied for tension and shear loadings (also illustrated on Figure 3.11). For those methods, the imposed tensors are

$$\sigma_{\text{imp}}^{\text{tension}} = \frac{10 \times f_p}{L - \bar{l}_b} \begin{bmatrix} 1 & 0 \\ 0 & 0 \end{bmatrix} \quad \text{and} \quad \sigma_{\text{imp}}^{\text{shear}} = \frac{10 \times f_p}{L - \bar{l}_b} \begin{bmatrix} 0 & 1 \\ 1 & 0 \end{bmatrix}. \tag{3.41}$$

After applying this procedure, we obtain 101 stress measurements for different cracking of the area element. The average and standard deviation of each components of the stress tensor are computed for each damaging loadings. As the imposed stress is constant during those loadings, the average should be the imposed stress and the standard deviation should be null. The results are summarized in the Table 3.2. The average measured stress tensors are close the imposed value. The standard deviations are several orders of magnitude below the imposed value. It validates the stress averaging method of Drescher in this case.

		Imposed	Measured (average)	Measured (standard deviation)
Bitension	σ_{11} [MPa]	$\frac{10}{0.18} = 55.5...$	55.56	1.82×10^{-7}
	σ_{22} [MPa]	$\frac{10}{0.18} = 55.5...$	55.56	1.57×10^{-7}
	σ_{12} [MPa]	0	5.21×10^{-7}	1.28×10^{-7}
Tension	σ_{11} [MPa]	$\frac{10}{0.18} = 55.5...$	55.56	1.74×10^{-7}
	σ_{22} [MPa]	0	-1.32×10^{-7}	1.29×10^{-7}
	σ_{12} [MPa]	0	-1.46×10^{-8}	2.72×10^{-7}
Shear	σ_{11} [MPa]	0	-2.40×10^{-13}	2.30×10^{-13}
	σ_{22} [MPa]	0	-1.96×10^{-13}	-1.12×10^{-13}
	σ_{12} [MPa]	$\frac{10}{0.18} = 55.5...$	55.56	0

Table 3.2 • Comparison of imposed stress and measured stress for pre-cracked area elements.

📝 Conclusion – Stress averaging

In this subsection, Drescher's stress averaging method has been presented and validated in the context of our study.

3.4   Measurement loadings

The last question to tackle in the measurement procedure is the choice of the measurement loading. As presented in the Section 2, this choice is highly important in the homogenization process.

Presentation.   In this study, only Kinematically Uniform, Periodic and Statically Uniform Boundary Conditions are considered. Note that Oliver-Leblond et al. (2021) proposed other type of boundary conditions and measurement loadings – which do not necessarily verify Hill's lemma – that are not studied here. For Kinematically Uniform and Periodic Boundary Conditions, three orthogonal strain loadings are applied

$$\varepsilon_{\text{imp}}^{(1)} = \begin{bmatrix} \varepsilon & 0 \\ 0 & 0 \end{bmatrix}, \quad \varepsilon_{\text{imp}}^{(2)} = \begin{bmatrix} 0 & 0 \\ 0 & \varepsilon \end{bmatrix}, \text{ and } \quad \varepsilon_{\text{imp}}^{(3)} = \begin{bmatrix} 0 & \varepsilon \\ \varepsilon & 0 \end{bmatrix} \tag{3.42}$$

where ε is a small strain value such that the behavior remains elastic during measurement loadings. In practice, we choose $\varepsilon = 10^{-8}$. For Statically Uniform Boundary Conditions, three orthogonal stress loadings are applied

$$\sigma_{\text{imp}}^{(1)} = \begin{bmatrix} \sigma & 0 \\ 0 & 0 \end{bmatrix}, \quad \sigma_{\text{imp}}^{(2)} = \begin{bmatrix} 0 & 0 \\ 0 & \sigma \end{bmatrix}, \text{ and } \quad \sigma_{\text{imp}}^{(3)} = \begin{bmatrix} 0 & \sigma \\ \sigma & 0 \end{bmatrix} \tag{3.43}$$

where σ is a small stress value such that the behavior remains elastic during measurement loadings. In practice, we choose σ such a force on 1 N is applied on each particles of the boundary that contribute to the stress.

Comparison. In order to choose one of the measurement loading, the results given by each method are compared. For this comparison, let us consider an area element of 0.2×0.2 m^2 with the parameters proposed in Table 3.1. Figure 3.12 shows different cracking patterns obtained during loadings of the area element. The columns correspond – from left to right – to an uncracked area element, one with diffuse micro-cracking due to tension, another with localized cracking due to tension, and a last area element with a localized cracking due to bitension. In the rows, the associated elasticity tensors are given for, from top to bottom, Kinematically Uniform, Periodic and Statically Uniform measurement loadings. By comparing the first three area elements, we can observe that – for each types of elementary loading – the stiffness will decrease with the "amount" of micro-cracking. Moreover, the damage-induced anisotropy can already be observed: the uncracked area element displays nearly isotropic[3] whereas the second and third area elements show a loss of isotropy. For instance, this loss of anisotropy is manifested by the difference between the two first diagonal components ($E_{1111} \neq E_{2222}$). From now, let us restrain ourself from any more mechanical interpretations and keep them for the remaining chapters. From the perspectives of the measurement of elasticity tensors, the classical results from homogenization are recovered: Kinematically Uniform Boundary Conditions predict stiffer elastic properties, whereas Statically Uniform Boundary Conditions predict more compliant elastic properties. Periodic Boundary Conditions provide intermediate results. Note that for the area element 4 – with localized cracking from bitension – Statically Uniform elementary loadings lead to undefined components. As explained before for the application of the stress on the area element, rigid body motions arises due to the cracking of the area element into multiple parts.

$\bigcirc$ **Remark 3.5** *The rigid body motions of each part could be blocked individually. However, this method will tends to rigidify the area element by blocking a previously free movement; thus, leading to an over-estimation of the stiffness. Another option is to introduce a negligible residual stiffness between each independent parts. Yet, this option is also biased. By adding a beam with a negligible stiffness between independent parts, the relative rotation of the independent components will depend on the positions of beam extermities in each parts.*

✎ **Conclusion – Measurement loadings**

In this subsection, different measurement loadings based on homogenization theory are compared. The classical results from homogenization are recovered: Kinematically Uniform Boundary Conditions (respectively Statically Uniform Boundary Conditions) gives an upper-bound (respectively a lower-bound) of stiffness. The Periodic Boundary Conditions give an intermediate estimation of the effective elasticity tensor. Based on this motivation, the Periodic Boundary Conditions measurement loadings are retained for the measurement procedure.

3.5 Summary and illustration of the measurement procedure

To summarize and illustrate the procedure, Figure 3.13 is a schematic of the whole measurement process. The input of this process is an area element (cracked or uncracked). The first

---

[3]The distance to a symmetry class will be quantifier further in the thesis.
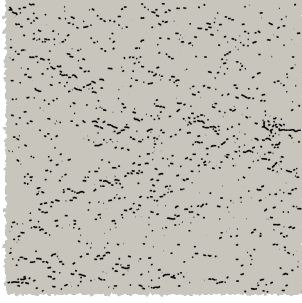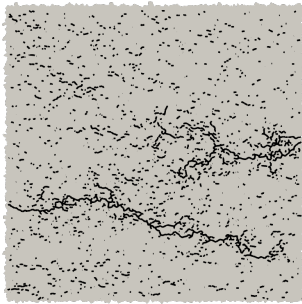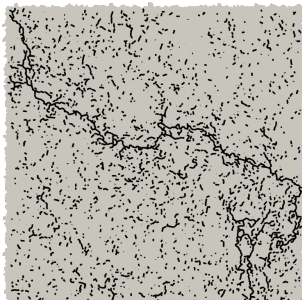
Specimens	Undamaged	Diffuse micro-cracking (tension)	Localized micro-cracking (tension)	Localized micro-cracking (bitension)
Cracking				
E (KUBC)	$\begin{bmatrix} 50.4 & 10.3 & 0.10 \\ 10.3 & 50.4 & -0.10 \\ 0.10 & -0.10 & 38.6 \end{bmatrix}$	$\begin{bmatrix} 35.1 & 8.23 & 0.11 \\ 8.23 & 48.2 & 0.03 \\ 0.11 & 0.03 & 33.3 \end{bmatrix}$	$\begin{bmatrix} 12.2 & 2.91 & -0.19 \\ 2.91 & 39.1 & 2.22 \\ -0.19 & 2.22 & 20.4 \end{bmatrix}$	$\begin{bmatrix} 10.7 & 2.14 & 5.77 \\ 2.14 & 15.6 & 8.00 \\ 5.77 & 8.00 & 13.5 \end{bmatrix}$
E (PBC)	$\begin{bmatrix} 49.8 & 10.2 & 0.09 \\ 10.2 & 49.8 & -0.09 \\ 0.08 & -0.09 & 38.2 \end{bmatrix}$	$\begin{bmatrix} 34.1 & 8.08 & 0.00 \\ 8.08 & 47.6 & 0.04 \\ 0.00 & 0.04 & 32.7 \end{bmatrix}$	$\begin{bmatrix} 7.18 & 1.62 & 1.18 \\ 1.62 & 37.4 & 3.79 \\ 1.18 & 3.79 & 15.6 \end{bmatrix}$	$\begin{bmatrix} 7.15 & 3.81 & 5.89 \\ 3.81 & 9.56 & 7.08 \\ 5.89 & 7.08 & 11.5 \end{bmatrix}$
E (SUBC)	$\begin{bmatrix} 48.2 & 10.1 & -0.01 \\ 10.1 & 49.8 & -0.39 \\ -0.01 & -0.39 & 37.4 \end{bmatrix}$	$\begin{bmatrix} 29.0 & 6.63 & 0.02 \\ 6.63 & 46.9 & -0.18 \\ 0.02 & -0.18 & 31.2 \end{bmatrix}$	$\begin{bmatrix} 0.85 & -0.38 & 1.47 \\ -0.38 & 28.9 & 2.00 \\ 1.47 & 2.00 & 8.48 \end{bmatrix}$	$\begin{bmatrix} \text{nan} & \text{nan} & \text{nan} \\ \text{nan} & \text{nan} & \text{nan} \\ \text{nan} & \text{nan} & \text{nan} \end{bmatrix}$

Figure 3.12 • Comparison of measured elasticity tensors for the different types of elementary loadings. The elasticity tensors are given in Kelvin notation and their components are in GPa. nan denotes an undefined component.

steps consist in applying the three measurement loadings using Periodic Boundary Conditions. Then, the strain is measured using Bagi's method on the boundary of the domain as proposed in Equation (3.25). The stress is also measured using Drescher's method as defined in Equation (3.39). Once the strain and stress is computed for each measurement loadings, the elasticity tensor is computed using Equation (3.19). To conclude this summary, the procedure to measure the effective elasticity tensor is formally recapitulated in Algorithm 1.

Algorithm 1: Measurement of the evolution of effective elasticity tensor

Data: Area element (uncracked or cracked)

foreach *measurement loading i* **do**

  Apply Periodic (elastic) measurement loading $\varepsilon_{\text{imp}}^{(i)}$;

  Compute average strain $\overline{\varepsilon}^{(i)}$ from Equation (3.25);

  Compute average stress $\overline{\sigma}^{(i)}$ from Equation (3.39);

end

Compute effective elasticity tensor from Equation (3.19);

Result: Effective elasticity tensor **E**

3.6 Limitations of the measurement procedure

This section aims at recalling the different assumptions in the measurement procedure and discussing the different sources of error.

Symmetrization of strain/stress. The first important assumption in this procedure is that the discrete medium is supposed to be a linear elastic medium in small strains. It means that the behavior of the material is assumed to be represented by a fourth-order tensor with minor and major symmetries. In the discrete model, the particles also have rotation degrees of freedom. It means that the discrete medium would be better modelled using a generalized medium (Forest & Sab, 1998).

✒ Summary of the Chapter

This chapter aims to establish a connection between the discrete beam-particle model and a continuous model. Firstly, a presentation of the beam-particle model is provided, followed by a brief introduction to homogenization to structure the measurement procedure. Based on homogenization theory, a procedure to measure the effective elasticity tensors of cracked square area elements, with possible micro-cracking, is proposed. The procedure involves applying three independent (measurement) loadings to the area element. Different choices for the measurement loadings (Kinematically Uniform, Periodic, Statically Uniform Boundary Conditions) are compared and the Periodic boundary Conditions are retained. After comparing different averaging methods for strain and stress, the average strain is computed using Bagi's method and the average stress with Drescher's method. Using the average strains and stresses from the three measurement loadings, the effective elasticity tensor is calculated.

Cracked specimen

Apply measurement loading (PBC)

$$\varepsilon_{\text{imp}}^{(1)} = \begin{bmatrix} \varepsilon & 0 \\ 0 & 0 \end{bmatrix}$$

$$\varepsilon_{\text{imp}}^{(2)} = \begin{bmatrix} 0 & 0 \\ 0 & \varepsilon \end{bmatrix}$$

$$\varepsilon_{\text{imp}}^{(3)} = \begin{bmatrix} 0 & \varepsilon \\ \varepsilon & 0 \end{bmatrix}$$

Measure strain

$$\overline{\varepsilon}^{(1)} = 10^{-8} \begin{bmatrix} 1 & 0 \\ 0 & 0 \end{bmatrix}$$

Measure strain

$$\overline{\varepsilon}^{(2)} = 10^{-8} \begin{bmatrix} 0 & 0 \\ 0 & 1 \end{bmatrix}$$

Measure strain

$$\overline{\varepsilon}^{(3)} = 10^{-8} \begin{bmatrix} 0 & 1 \\ 1 & 0 \end{bmatrix}$$

and stress (Pa)

$$\overline{\sigma}^{(1)} = \begin{bmatrix} 71.8 & 7.90 \\ 7.90 & 16.3 \end{bmatrix}$$

and stress (Pa)

$$\overline{\sigma}^{(2)} = \begin{bmatrix} 16.3 & 25.3 \\ 25.3 & 374 \end{bmatrix}$$

and stress (Pa)

$$\overline{\sigma}^{(3)} = \begin{bmatrix} 15.8 & 156 \\ 156 & 50.6 \end{bmatrix}$$

Compute elasticity tensor (GPa)

$$\mathbf{E} = \begin{bmatrix} 7.18 & 1.62 & 1.18 \\ 1.62 & 37.4 & 3.79 \\ 1.18 & 3.79 & 15.6 \end{bmatrix}$$

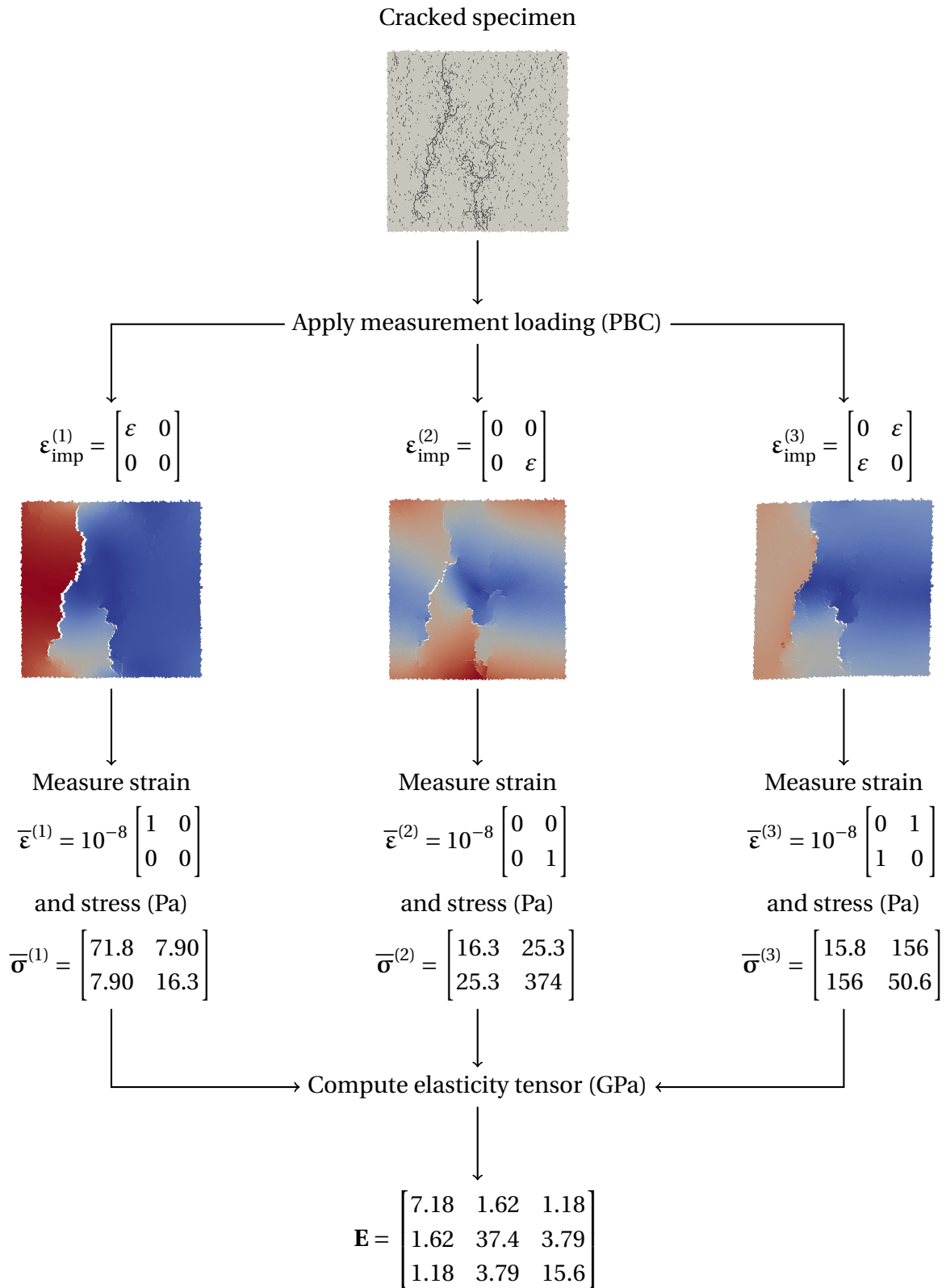**Figure 3.13** • Illustration of the measurement of an elasticity tensor

An algorithm and a schematic illustration of an elasticity tensor measurement from the discrete model are proposed to summarize the procedure. It is important to remark that this procedure is restricted to the transition from a discrete model to a linear elastic medium.

Part II

Contributions to the modeling of quasi-brittle materials

4

Generation and analysis of the dataset of effective elasticity tensors

This chapter introduces the generation and analysis of the dataset of effective elasticity tensors that will be the foundation for formulating the damage model. Proportional and non-proportional loadings are applied to area elements, and the evolution of the effective elasticity tensor is measured at each time step of the different loading cases. These measurements form the reference dataset. For illustration purposes, we analyze a measurement during a non-proportional loading. A validity check is then performed over the dataset by evaluating the symmetrization errors in the measurement procedure. The positive definiteness and the decrease of the measured elasticity tensors during the cracking process are also checked. Finally, a quantified anisotropy analysis is performed.

In the previous chapter, a procedure to measure the effective elasticity tensor of — uncracked or cracked— discrete area elements has been presented. In this chapter, proportional and non-proportional damaging loadings are applied to the area elements. The measurement procedure is used at each load step of the loadings to obtain the evolution of the elasticity tensor during the loadings. All the measured evolutions are then stored in one dataset, which will be used to formulate an anisotropic damage model in the following chapters. Verification of the dataset is also presented in this chapter to display its limits and prevent potential mechanical inconsistencies. For instance, both the positive definiteness and the irreversible decrease of the elastic properties are checked. Finally, the dataset is analyzed from a mechanical point of view.

1 Generation of a dataset of effective elasticity tensors

This section is dedicated to generating a large dataset of effective elasticity tensors. To constitute the dataset, 36 area elements with different microstructures (but with the same discrete model properties) are submitted to 21 mechanical loadings. "Different microstructures" means different random positioning of the particle centers and different random draw for the beam failure properties. Thus, the particle distribution at the meso-scale are different for

each distinct area elements (see Section 1.1 of Chapter 3). Each area element is a square of $0.2\text{m} \times 0.2\text{m}$, with an average beam length $\bar{l}_b = 0.002\text{m}$. Thus, the area elements comprise 100×100 particles.

1.1 Measuring the evolution of an effective elasticity tensor

The procedure from Chapter 3 is now applied to measure the evolution of the effective elasticity tensor during damaging loading. The whole evolution measurement is illustrated
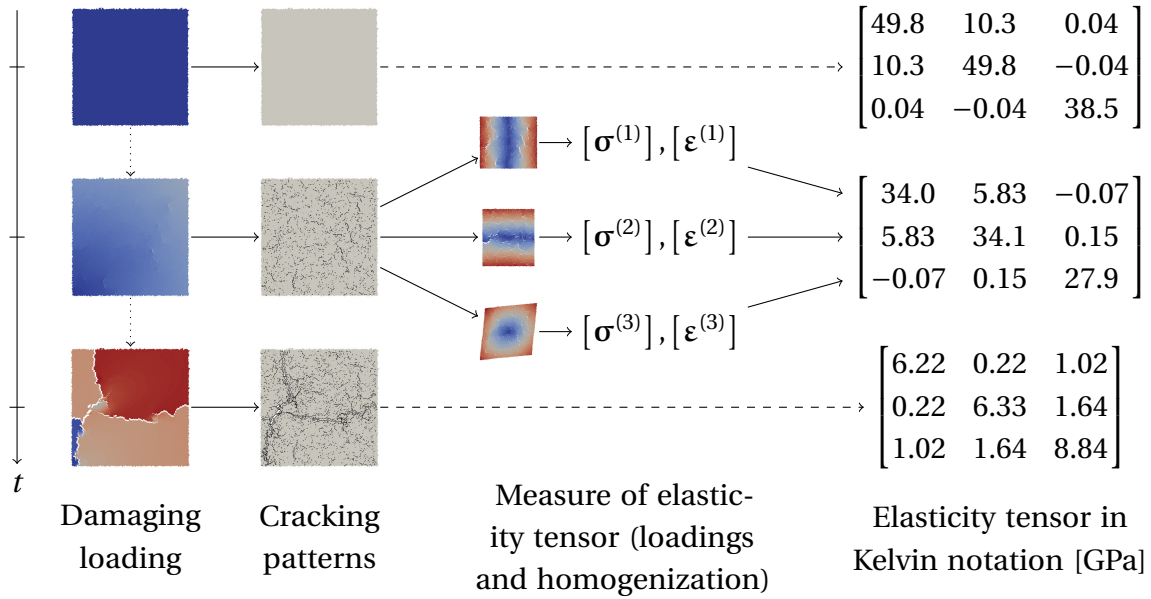

$$\begin{bmatrix} 49.8 & 10.3 & 0.04 \\ 10.3 & 49.8 & -0.04 \\ 0.04 & -0.04 & 38.5 \end{bmatrix}$$

$$[\sigma^{(1)}], [\varepsilon^{(1)}]$$

$$[\sigma^{(2)}], [\varepsilon^{(2)}] \begin{bmatrix} 34.0 & 5.83 & -0.07 \\ 5.83 & 34.1 & 0.15 \\ -0.07 & 0.15 & 27.9 \end{bmatrix}$$

$$[\sigma^{(3)}], [\varepsilon^{(3)}]$$

$$\begin{bmatrix} 6.22 & 0.22 & 1.02 \\ 0.22 & 6.33 & 1.64 \\ 1.02 & 1.64 & 8.84 \end{bmatrix}$$

t

Damaging loading | Cracking patterns | Measure of elasticity tensor (loadings and homogenization) | Elasticity tensor in Kelvin notation [GPa]

Figure 4.1 • Illustration of the procedure for measuring the effective elasticity tensor evolution during a damaging loading.

in Figure 4.1. The first step consists of applying a damaging loading to the area element. The damaging loadings are applied until the failure of the area element, *i.e.* the localization of micro-cracking. The cracking patterns are then extracted at each load step of the damaging loading, and pre-cracked meshes are generated from the patterns. Finally, the procedure to measure the effective elasticity tensor is applied to each pre-cracked mesh, *i.e.* each load step. The measured tensors are then grouped to obtain the whole evolution of the effective elasticity tensor.

1.2 Damaging loadings

Various damaging loadings are applied to the area elements. Different types of boundary conditions (kinematically uniform, periodic, and "experimental" boundary conditions) are imposed among the loadings. During kinematically uniform and periodic loadings, the strain is set on the area element's whole boundary $\partial\Omega$. Each load step adds an increment of strain $\Delta\varepsilon(\boldsymbol{x})$ to the currently imposed strain. The strain at load step i is

$$\varepsilon^0 = \boldsymbol{0}, \qquad \varepsilon^i = \varepsilon^{i-1} + \Delta\varepsilon^i. \tag{4.1}$$

During "experimental" loading, a displacement is imposed on the sub-parts of the boundary $\partial\Omega$. Each load step adds an increment of displacement $\Delta u(x)$ to the currently imposed displacement. The displacement at load step i, on a sub-part of the boundary $\partial\Omega_u$, is

$$\forall x \in \partial\Omega_u, \quad \begin{cases} u^0(x) = 0, \\ u^i(x) = u^{i-1}(x) + \Delta u^i(x). \end{cases} \tag{4.2}$$

In practice, the boundary $\partial\Omega_u = \{x = (x, y) \mid x = 0\}$ corresponds to the layer of particle having their center in the rectangle defined by $[0, \bar{l}_b] \times [0, L]$. Tables 4.1 and 4.2 provide a description of all the damaging loadings included in the dataset. The first important remark is that the

| Type | Name | Load steps (i) | | Strain incs $\Delta\varepsilon^i \times 10^6$ | | |
		Start	End	ε_{11}	ε_{22}	ε_{12}
KUBC	bitension	1	100	6	6	0
	shear	1	100	0	0	15
	tension	1	100	10	0	0
	shear → tension	1	50	0	0	10
		50	100	20	0	0
	tension → shear	1	50	10	0	0
		50	100	0	0	20
	tension → tension	1	50	10	0	0
		50	100	0	10	0
	(Willam et al., 1989)	1	100	4	0	0
		100	200	2	1	3
PBC	bitension	1	100	5	5	0
	shear	1	100	0	0	10
	tension	1	100	3	0	0
	shear → tension	1	50	0	0	10
		50	100	40	0	0
	tension → shear	1	50	10	0	0
		50	100	0	0	20
	tension → tension	1	50	6	0	0
		50	100	0	6	0
	(Willam et al., 1989)	1	100	8	0	0
		100	200	4	6	2

Table 4.1 • Kinematically Uniform (KUBC) and Periodic PBC damaging loadings. For periodic (PBC) loadings, a particle is locked in displacement to prevent rigid body motions.

| Name | Load steps | | Displacement incs $\Delta \boldsymbol{u}^i(\boldsymbol{x})$ (μm) | | | | | | | |
| | | | $x = 0$ | | $x = L$ | | $y = 0$ | | $y = L$ | |
	Start	End	u_1	u_2	u_1	u_2	u_1	u_2	u_1	u_2
bitension	1	100	0	-	1.2	-	-	0	-	1.2
tension	1	100	0	-	1	-	-	-	-	-
shear	1	100	-	0	-	0.8	0	-	0.8	0
simple shear	1	100	-	-	-	-	0	0	0	4
shear $\rightarrow$ tension	1	50	-	0	-	1.6	0	-	1.6	0
	50	100	0	-	2	-	-	-	-	-
tension $\rightarrow$ shear	1	50	0	-	1	-	-	-	-	-
	50	100	-	0	-	1.6	0	-	1.6	-
tension $\rightarrow$ tension	1	50	0	-	1.2	-	-	-	-	-
	50	100	-	-	-	-	-	0	-	1.2

Table 4.2 • "Experimental" (EXPE) loadings. The cells $x = \dots$ and $y = \dots$ denotes the face of the area element on which the displacement is applied. For most of those loadings, an additional constraint is applied to a particle to prevent rigid body motion.

loadings are all such that the area element is mostly loaded in extension. It is necessary as the contact and friction between micro-crack faces is neglected; thus, the loadings are such that most cracks remain open. Also, note that loadings are separated into proportional and non-proportional loadings. For this dataset, the non-proportional loadings are highly important as they enable the rotation of the principal strain/stress directions during the loading. It leads to a misalignment of the loading direction with the initial cracks, thus changing the damaging direction during the loading.

 Remark 4.1 *Instead of using physical loadings to generate micro-cracks, one could try to create random micro-cracking patterns by randomly breaking beams. This method does not account for the interactions of micro-cracks during the loading. We preferred to apply true mechanical loadings, as they constrain the micro-cracking patterns to "physically reachable" ones.*

1.3   A dataset of 76 356 effective elasticity tensors

The dataset of effective elasticity tensors is constituted by applying the measurement method (described in Section 1.1) to 36 different area elements submitted to the damaging loading (presented in Section 1.2). Each of the 21 mechanical loading is discretized into 100 loading steps. The database contains $36 \times 21 = 756$ evolutions of elasticity tensors, each containing 101 elasticity tensors, leading to 76 356 elasticity tensors. Note that some elasticity tensors appear multiple times in the dataset (in particular when the area element is not yet damaged). Thus, the dataset contains the evolution of the effective elasticity tensor for various proportional and non-proportional loadings until failure. This dataset (Loiseau et al., 2023b) is available at
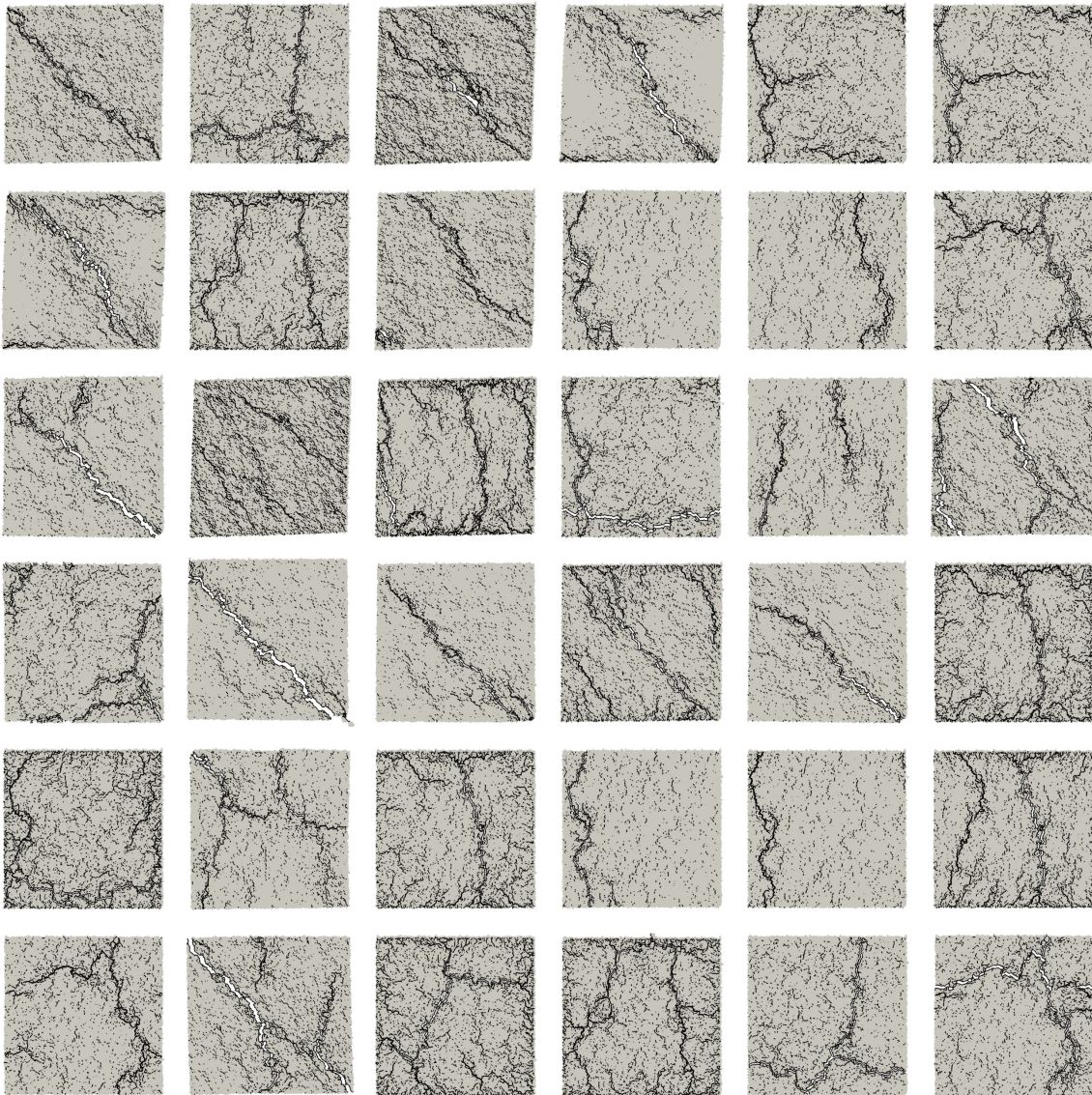
Figure 4.2 • Illustration of localized cracking patterns in the dataset.

. To illustrate the content of the dataset, Figure 4.2 shows a grid of final cracking patterns for various loadings.

2 Illustration of the evolution of the effective elasticity tensor

This section aims to illustrate, on a specific loading, the quantities and tools used to analyze the dataset.

2.1 Presentation of the non-proportional loading

For this study, we choose a non-proportional periodic "tension → tension" loading (as defined in Table 4.1). This loading is composed of two parts: the first one during which a tension along the x-axis is gradually applied, then, in the second part, the tension along x-axis is maintained, and a tension along y-axis is gradually applied. The evolution of the measured strain and stress during the loading is represented on Figure 4.3. At each 20 load step, the cracking patterns are also displayed in Figure 4.4.
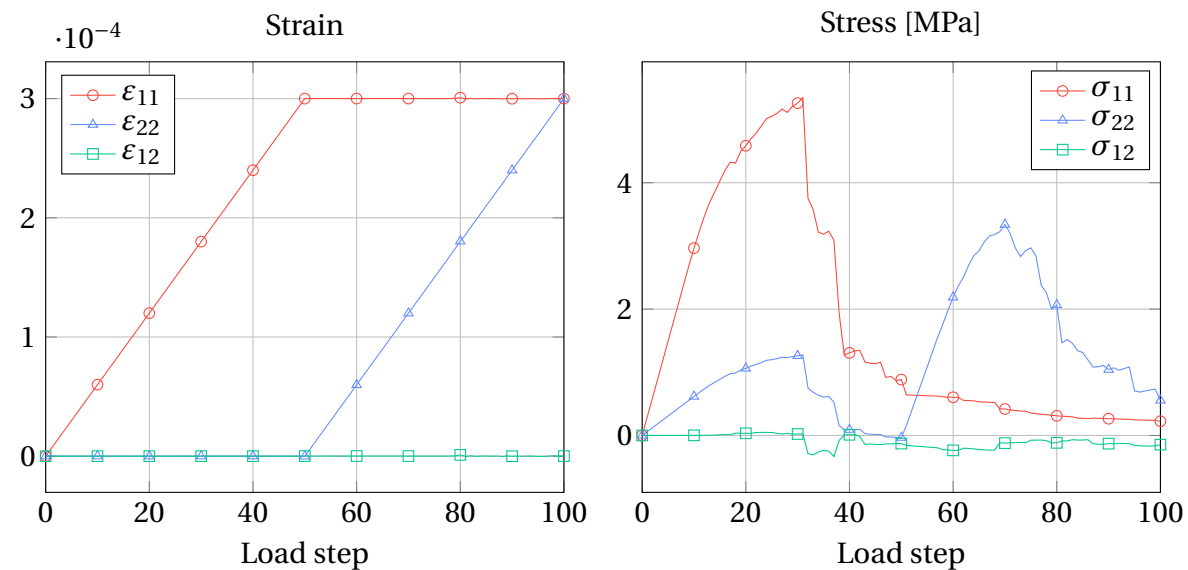

Figure 4.3 • Evolution of strain and stress during the periodic "tension→tension" loading.

During the first half of the loading, the classic behavior of quasi-brittle material is recovered. First, we observe an elastic phase where the stress component σ_{11} grows linearly with the imposed strain. The Poisson effect also induces the growth the stress component σ_{22}. This initial elastic phase is followed by a loss of stiffness. The cracking pattern at $t = 20$ shows that diffuse micro-cracking occurred. Also, note that most cracks are orthogonal to the loading direction. It is then followed by stress drop, which is explained by the localization of the micro-cracking process where the micro-cracks bridge into a macro-crack[1]. At the middle of the loading, the stress component σ_{11} is highly reduced, reflecting a loss of rigidity along the x-axis. When the second half of the loading starts, the stress σ_{22} grows linearly

---

[1]Remark that the area element is periodic, and the crack crosses the boundary.
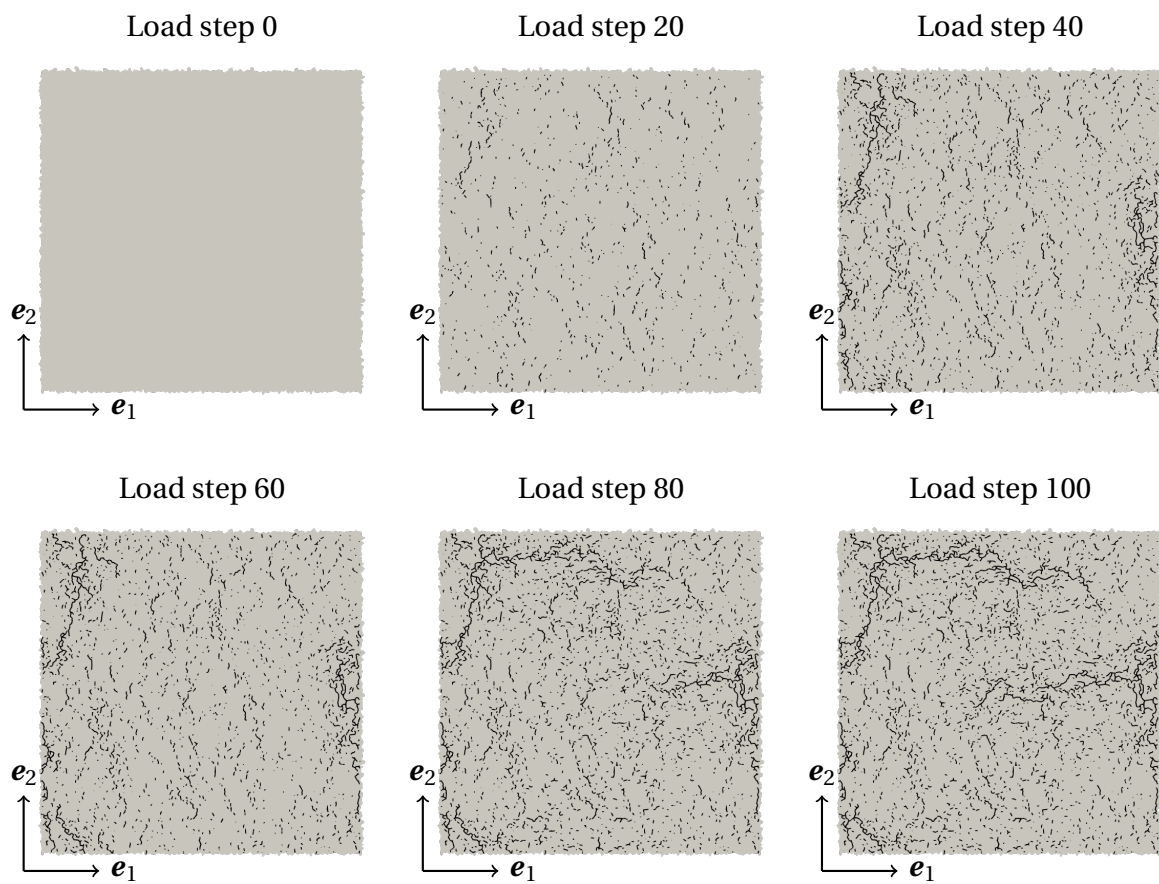
Figure 4.4 • Evolution of micro-cracking during the periodic "tension→tension" loading.

with (nearly) the initial stiffness previously observed along the x-axis. Also note that the Poisson effect is also reduced due to the micro-cracking. It means that the y-axis direction has been less affected by the micro-cracking. This goes until load step 60 when micro-cracks nucleate in the direction normal to the y-axis. Once again, we observe a first diffuse micro-cracking followed by a localization of the cracking process. A stress drop once again marks this transition.

2.2 Evolution of the effective elasticity tensor

This subsection aims to briefly investigate the evolution of the effective elastic properties during the loading.

2.2.1 Cartesian components

Let us start by analyzing the evolution of the effective elasticity tensor in a "classic" way using its Cartesian components. Their evolution is represented in Figure 4.5. The elasticity tensors associated to the load steps represented in this figure are, in GPa and using Kelvin notation,

$$
\begin{array}{ccc}
\text{Load step 0} & \text{Load step 20} & \text{Load step 40} \\[4pt]
\begin{bmatrix} 49.73 & 10.27 & 0.05 \\ 10.27 & 49.73 & -0.05 \\ 0.05 & -0.05 & 99.45 \end{bmatrix} &
\begin{bmatrix} 37.27 & 8.71 & 0.39 \\ 8.71 & 48.28 & 0.04 \\ 0.39 & 0.04 & 96.57 \end{bmatrix} &
\begin{bmatrix} 5.44 & 0.38 & 0.09 \\ 0.38 & 39.78 & -0.57 \\ 0.09 & -0.57 & 79.55 \end{bmatrix}
\end{array}
\tag{4.3}
$$

$$
\begin{array}{ccc}
\text{Load step 60} & \text{Load step 80} & \text{Load step 100} \\[4pt]
\begin{bmatrix} 2.08 & -0.32 & -0.81 \\ -0.32 & 37.34 & -1.78 \\ -0.81 & -1.78 & 74.69 \end{bmatrix} &
\begin{bmatrix} 1.45 & -0.69 & -0.17 \\ -0.69 & 9.00 & -0.42 \\ -0.17 & -0.42 & 18.00 \end{bmatrix} &
\begin{bmatrix} 1.14 & -0.39 & -0.15 \\ -0.39 & 2.24 & -0.58 \\ -0.15 & -0.58 & 4.48 \end{bmatrix}
\end{array}
$$

This first part shows a significant decrease in the elastic component E_{1111}. It starts to decrease almost linearly with the loading till around the load step 30. Note that this load step corresponds to the stress peak in Figure 4.3. After this point, the localization of micro-cracking occurs (see Figure 4.4) and there is a sharp decrease in E_{1111}. In this first part, the component E_{2222} is less affected by cracking than E_{1111}. Thus, we expect a loss of isotropy during this first part of the loading. We also observe a significant drop of E_{1212} and E_{1122}. In the second half of the loading, the component E_{2222} gradually decreases as the loading along the y axis increases.

2.2.2 Harmonic components

To illustrate the harmonic decomposition, Figure 4.6 displays the evolution of the effective elasticity tensor in terms of the harmonic components. It shows that the micro-cracking during the first half of the loading causes a decrease in the shear modulus μ and the bulk modulus κ. This decrease is accompanied by an increase (in norm) of the dilatation tensor deviatoric part through its component d'_{11}. As shown in the Chapter 2, it means that the isotropy is lost (otherwise, only the invariants μ and κ would be non-null). More specifically, it means that the elasticity tensor is at least orthotropic. A slight increase in the harmonic
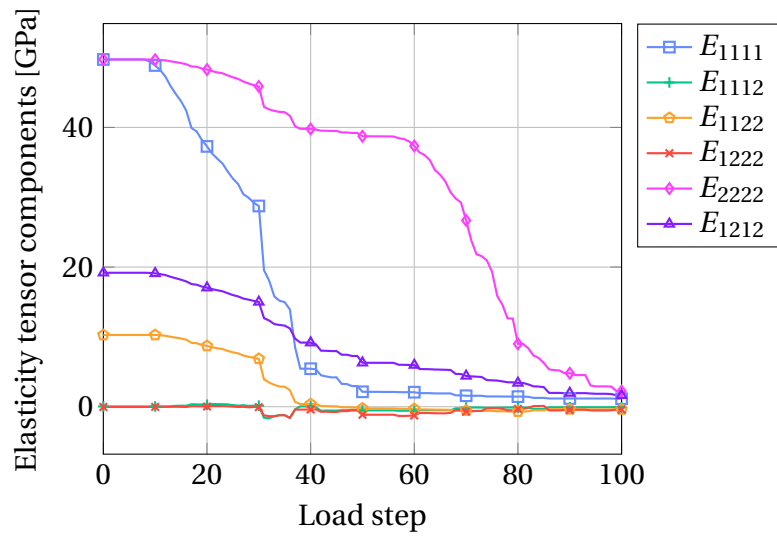
Figure 4.5 • Evolution of the Cartesian components of the effective elasticity tensor during a PBC "tension→tension" loading.
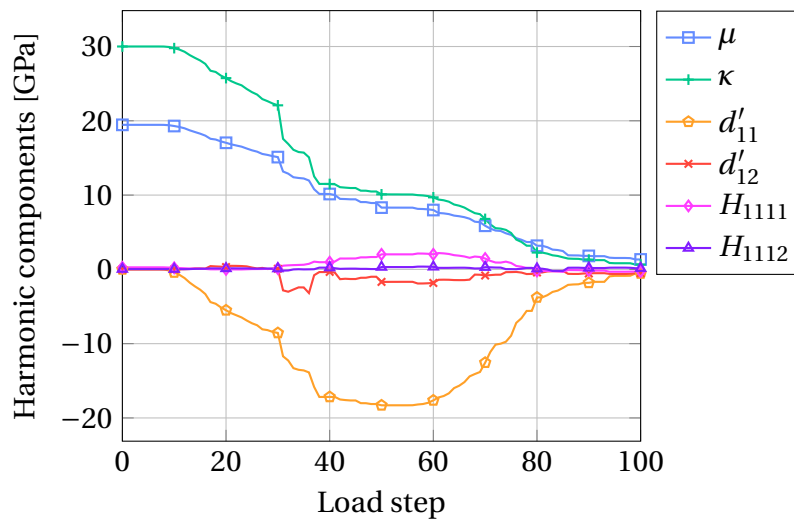

Figure 4.6 • Evolution of the harmonic components of the effective elasticity tensor during a PBC "tension→tension" loading.

part is also observed. The elasticity tensor may also be anisotropic depending on the relative orientation between the dilatation and the harmonic components. Note that the deviatoric part of the dilatation tensor decrease at the end of the loading as the micro-cracking increases and, thus, the overall stiffness tends to zero.

2.3   Evolution of the distances to symmetry class

To obtain a quantitative view of the anisotropy, the relative distances of the effective elasticity tensor to isotropy and orthotropy (introduced in Section 3) are the focus of this subsection. Figure 4.7 presents their evolution during the loading. The first observation is that the initial
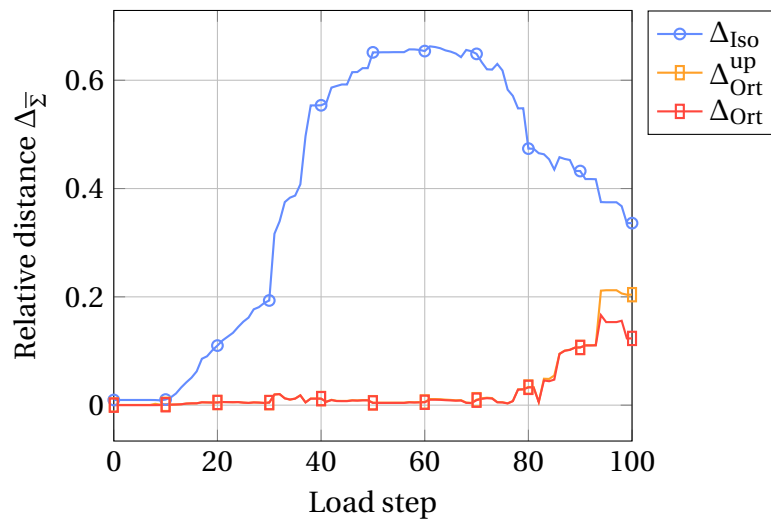

Figure 4.7 • Evolution of the relative distances $\Delta_{\bar{\Sigma}} = d_{\bar{\Sigma}} / \|\mathbf{E}\|$ of the effective elasticity tensor to isotropy and orthotropy during a PBC "tension→tension" loading.

distance to isotropy is small. The distance to isotropy grows when the cracking starts (around load step number 10). The damaged material will react differently to the same strain loading applied in two different directions. Note that the distance to orthotropy (and its upper bound) stays null during the first part of the loading. It means that the effective elasticity tensor stays orthotropic during the first half of the loading, which is consistent with the growth of the dilatation part. However, the effective elasticity grows farther from orthotropy at the end of the loading. Note that it also get closer to isotropy at the end of the loading.

$\mathbb{Q}$ **Remark 4.2**   *The two last statements may seem incompatible. Yet, it means that the isotropic part become a higher proportion of the tensor. As the distance to orthotropy remains unaffected by the isotropic part, it may grow even if distance to isotropy decreases. Note that the distance to isotropy is also an upper-bound of the distance to orthotropy.*

3   Assessment of the dataset

Before starting any mechanical analysis of the dataset, let us check the validity of the measured elasticity tensors. When the area element in uncracked, it behaves like an isotropic linear elastic material. However, when micro-cracking occurs and induces heterogeneity, it

may become more complex. In this thesis, we assume that the macroscopic behavior of the area elements stay linear elastic. This section focuses on the verification of this assumption. Actually, higher-order continuum might be required to correctly represent the deformation and cohesive force in the area element. In this case, an effective elasticity tensor is not sufficient to represent the current state in the material.

3.1 Evaluation of symmetrization errors

In the measurement procedure, different index symmetrizations have been applied to represent the behavior of the area element with linear elasticity. The symmetrization errors represent the difference between the behavior of the area element and its equivalent linear elastic material.

Symmetrization of the strain tensor. Let us start by studying the symmetrization errors on the strain measurement. Before defining the symmetrization error, let us introduce the un-symmetrized deformation, which is Equation (3.25) with a tensorial product $\otimes$ instead of the symmetrized one $\odot$,

$$\overline{\mathbf{e}} = \frac{1}{V_{\mathrm{SCS}}} \sum_{(p,q)\in\partial\mathscr{B}} l_{pq} \frac{\boldsymbol{u}_p + \boldsymbol{u}_q}{2} \otimes \boldsymbol{t}_{pq}, \qquad \overline{\varepsilon} = \frac{1}{2}\left(\overline{\mathbf{e}} + \overline{\mathbf{e}}^{\mathrm{T}}\right). \tag{4.4}$$

Thus, the relative symmetrization error on the strain tensor is

$$e_{\varepsilon}^{\mathrm{sym}} = \frac{\|\overline{\mathbf{e}} - \overline{\varepsilon}\|}{\|\overline{\mathbf{e}}\|} = \frac{\|\overline{\mathbf{e}}^{\mathrm{A}}\|}{\|\overline{\mathbf{e}}\|} \tag{4.5}$$

where $\overline{\mathbf{e}}^{\mathrm{A}} = \frac{1}{2}\left(\overline{\mathbf{e}} - \overline{\mathbf{e}}^{\mathrm{T}}\right)$ is the antisymmetric part of $\overline{\mathbf{e}}$.

For each measurement loading (three per elasticity tensor), the un-symmetrized deformation $\mathbf{e}$ is calculated. Table 4.3 contains different percentiles of the error distribution over the whole dataset. It shows that the strain symmetrization error can reach up to 11.1% of the total

Percentage	Percentile of strain symmetrization error		
	Loading (1)	Loading (2)	Loading (3)
50%	0.0052%	0.0051%	0.0065%
90%	0.045%	0.033%	0.044%
95%	0.091%	0.056%	0.086%
99%	0.32%	0.14%	0.21%
100%	11.1%	4.5%	10.2%

Table 4.3 • Percentiles of the strain symmetrization errors for each measurement loading.

measured strain. However, 99% of the strain measurements for each of the measurement loadings have a symmetrization error below 0.32%. It means that a symmetric second-order strain tensor can represent most of the deformation states.

Symmetrization of the stress tensor. Now, we can study the symmetrization errors in the stress measurement. Once again, let us introduce the un-symmetrized stress tensor, which is Equation (3.39) with a tensorial product instead of the symmetrized one,

$$\bar{\mathbf{s}} = \frac{1}{V_{SCS}} \sum_{p \in \partial \mathscr{P}} \boldsymbol{x}_p \otimes \mathbf{f}_p \, \mathrm{d}\boldsymbol{x}, \qquad \overline{\boldsymbol{\sigma}} = \frac{1}{2} \left(\bar{\mathbf{s}} + \bar{\mathbf{s}}^{\mathrm{T}} \right) \tag{4.6}$$

As for the strain, we define the relative symmetrization error on the stress tensor as

$$e_{\boldsymbol{\sigma}}^{\mathrm{sym}} = \frac{\| \bar{\mathbf{s}} - \overline{\boldsymbol{\sigma}} \|}{\| \bar{\mathbf{s}} \|} = \frac{\| \bar{\mathbf{s}}^{\mathrm{A}} \|}{\| \bar{\mathbf{s}} \|} \tag{4.7}$$

where $\bar{\mathbf{s}}^{\mathrm{A}} = \frac{1}{2} \left(\bar{\mathbf{s}} - \bar{\mathbf{s}}^{\mathrm{T}} \right)$ is the antisymmetric part of $\bar{\mathbf{s}}$.

We compute the un-symmetrized stress for each measurement loading associated with each measured elasticity tensor. Then, the associated error is also calculated. Table 4.4 contains different percentiles of the stress symmetrization error distribution over the whole dataset. A small part of the measured stress tensors (less than 1%) have a large stress sym-

Percentage	Percentile of stress symmetrization error		
	Loading (1)	Loading (2)	Loading (3)
50%	0.0022%	0.0017%	0.0035%
90%	0.014%	0.0088%	0.027%
95%	0.024%	0.018%	0.062%
99%	0.21%	0.062%	1.7%
100%	67.3%	28.1%	70.7%

Table 4.4 • Percentiles of the stress symmetrization errors for each measurement loading.

metrization error. Note that all the stress tensors with an error above 1% are associated to highly damaged area element (with a localized cracking pattern).

Major symmetrization. Finally, the last symmetrization performed is the major symmetrization of the effective elasticity tensor from Equation (3.19). To simplify the calculation, let us consider the un-symmetrized elasticity tensor in Kelvin notation

$$\left[\mathbf{E}_{\mathrm{nsym}} \right] = \left[\left[\overline{\boldsymbol{\sigma}}^{(1)} \right], \left[\overline{\boldsymbol{\sigma}}^{(2)} \right], \left[\overline{\boldsymbol{\sigma}}^{(3)} \right] \right] \cdot \left[\left[\overline{\boldsymbol{\varepsilon}}^{(1)} \right], \left[\overline{\boldsymbol{\varepsilon}}^{(2)} \right], \left[\overline{\boldsymbol{\varepsilon}}^{(3)} \right] \right]^{-1}, \quad [\mathbf{E}] = \frac{1}{2} \left(\left[\mathbf{E}_{\mathrm{nsym}} \right] + \left[\mathbf{E}_{\mathrm{nsym}} \right]^{\mathrm{T}} \right). \tag{4.8}$$

The major symmetrization error is defined as

$$e_{\mathrm{maj}}^{\mathrm{sym}} = \frac{\| \, [\mathbf{E}^{\mathrm{nsym}}] - [\mathbf{E}] \, \|}{\| \, [\mathbf{E}^{\mathrm{nsym}}] \, \|}. \tag{4.9}$$

This error has been computed for each measurement in the dataset. Table 4.5 contains different percentiles of the major symmetrization error distribution over the whole dataset. This table shows that more than 20% of the measurements have a major symmetrization error above 10%. Those results again highlight that an effective elasticity tensor might only partially describe the behavior of the (damaged) area element. Yet, most of the measured effective elasticity tensors have a small major symmetrization error.

Percentage	Percentile of major symmetrization error
50%	2.93%
60%	5.18%
70%	8.85%
80%	16.3%
90%	20.3%
95%	21.5%
99%	23.1%
99.5%	23.5%
100%	59.7%

Table 4.5 • Percentiles of the major symmetrization errors for each measurement loading.

Q **Remark 4.3** *As this is a fundamental assumption in the modeling process, those errors cannot be compensated. The discrete model's tensile curves will not match the curve reconstructed from the effective elasticity tensor.*

Strain–Stress curve reconstruction. Now, let us show how the symmetrizations change the predicted stress. To do this, let us consider the non-proportional loading (periodic "tension→tension") used in Section 2. During this loading, the (symmetric) stress σ has been measured. This measured stress is compared to the stress $\mathbf{E} : \varepsilon$ predicted using the measured effective elasticity tensor $\mathbf{E}$ and the measured (symmetric) strain ε. Figure 4.8
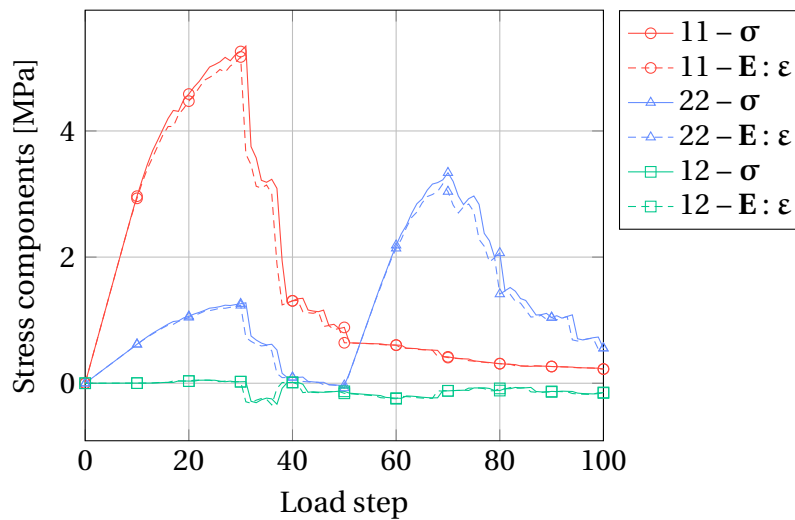

Figure 4.8 • Comparison the symmetrized stress from the discrete model σ (reference) to the stress from the measured effective elasticity tensor $\mathbf{E} : \varepsilon$.

contains the evolution of stress during this non-proportional periodic loading. When the micro-cracks start to nucleate (when the response is no longer linear), the stress obtained from the effective elasticity tensor slightly deviates from the measured stress. It is due to the major symmetrization. It means that an effective elasticity tensor cannot exactly describe the behavior of the area element.

3.2 Positive definiteness of elasticity tensors

The next assumption needing a check is the positive definiteness of the effective elasticity tensors. For that, we have to compute the eigenvalues E_1, E_2, and E_3 for each tensor in the dataset and check that they are all positive or null. Figure 4.9 shows the histogram of the eigenvalues for the whole dataset. The whole range of eigenvalues goes from $\min(E_1, E_2, E_3) = -1.29$ GPa
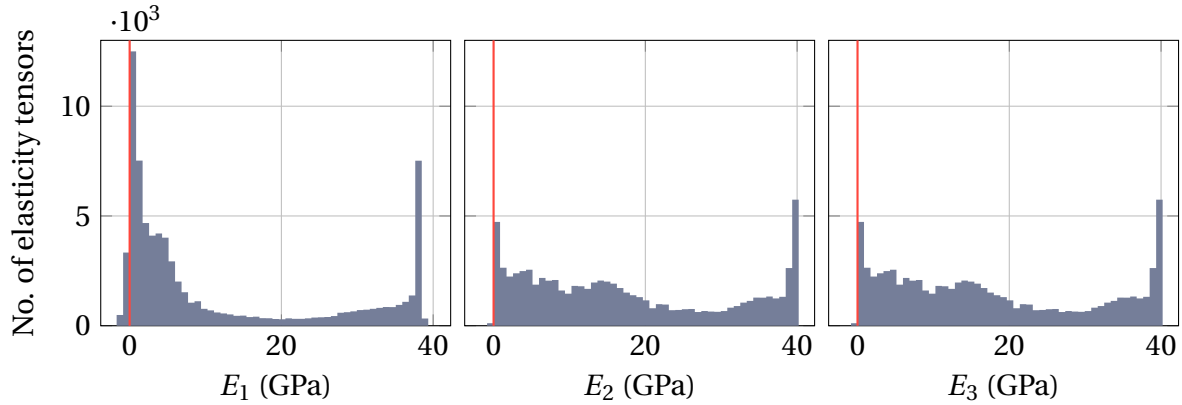

Figure 4.9 • Histograms of elasticity tensor eigenvalues.

to $\max(E_1, E_2, E_3) = 39.8$ GPa. This range is discretized into 50 intervals to constitute this histogram. Those intervals are chosen such that no interval contains both positive and negative values, *i.e.* there is an interval with 0 as upper-bound and another with 0 as lower-bound. The main observation is that some tensors have negative eigenvalues. Note that negative eigenvalues happen for highly cracked tensors. The tensors with at least one negative eigenvalue are filtered out for the remainder of this work to avoid any physical inconsistency in the data set.

Q **Remark 4.4** *The symmetrization errors (from Tables 4.3 to 4.5) have been computed once again after filtering the dataset and are reported in Appendix B. Globally, the symmetrization errors decreased by filtering the dataset. It means that elasticity tensors with a high symmetrization error are more likely to not be positive definite.*

3.3 Irreversible decrease of the elasticity tensors

The second assumption we must check is the irreversible decrease of the effective elasticity tensor during a damaging loading. Indeed, in the discrete simulation, the micro-cracking is either constant or increasing. Furthermore, micro-cracks cannot be closed. Thus, no increase in stiffness should be observed.

From an energetic perspective, if a constant strain ε is applied to the material, the elastic energy must decrease as the micro-cracking grows. At a given instant t and for any applied strain ε, the elastic energy stored in the material is

$$\forall \varepsilon \in \mathbb{S}^2(\mathbb{R}^2), \quad \mathscr{E} = \frac{1}{2}\varepsilon : \mathbf{E}(t) : \varepsilon, \tag{4.10}$$

where $\mathbb{S}^2(\mathbb{R}^2)$ is the space of symmetric second-order tensors in $\mathbb{R}^2$. The irreversible decrease of the effective elasticity tensor corresponds to

$$\forall \varepsilon \in \mathbb{S}^2(\mathbb{R}^2), \quad \frac{\partial \mathscr{E}}{\partial t} = \frac{1}{2} \varepsilon : \frac{\partial \mathbf{E}(t)}{\partial t} : \varepsilon \leqslant 0, \tag{4.11}$$

which can be written in Kelvin notation

$$\forall \begin{bmatrix} \varepsilon_{11} \\ \varepsilon_{22} \\ \sqrt{2}\varepsilon_{12} \end{bmatrix} \in \mathbb{R}^3, \quad \frac{\partial \mathscr{E}}{\partial t} = \frac{1}{2} \begin{bmatrix} \varepsilon_{11} \\ \varepsilon_{22} \\ \sqrt{2}\varepsilon_{12} \end{bmatrix} : \frac{\partial}{\partial t} \begin{bmatrix} E_{1111} & E_{1122} & \sqrt{2}E_{1112} \\ E_{1122} & E_{2222} & \sqrt{2}E_{1222} \\ \sqrt{2}E_{1112} & \sqrt{2}E_{1222} & 2E_{1212} \end{bmatrix} : \begin{bmatrix} \varepsilon_{11} \\ \varepsilon_{22} \\ \sqrt{2}\varepsilon_{12} \end{bmatrix} \leqslant 0, \tag{4.12}$$

This inequality is verified if and only if the (pseudo-)temporal derivative of the effective elasticity tensor is negative semi-definite (by definition of the negative definiteness). Note that a second-order (real) symmetric tensor is negative definite if and only if its eigenvalues are negative.

🔍 **Remark 4.5** *At this point, it seems necessary to recall that the derivative of the eigenvalue $\frac{\partial E_{\text{eig}}}{\partial t}$ are not equal to the eigenvalues of the derivative $\left(\frac{\partial \mathbf{E}}{\partial t}\right)_{\text{eig}}$ (see the proof based on the polar decomposition in Appendix C). Indeed, the derivative of eigenvalues does not account for a rotation of the eigenbasis. During a rotation of the eigenbasis (which happens during non-proportional loadings), one of the elasticity tensor eigenvalues might increase, whereas the other decreases while the elasticity tensor still decreases.*

The measured evolution is discrete; thus, we must check that the eigenvalues of the elasticity tensor increments $(\Delta \mathbf{E})_i$ are all negative. Figure 4.10 contains the histogram of eigenvalues
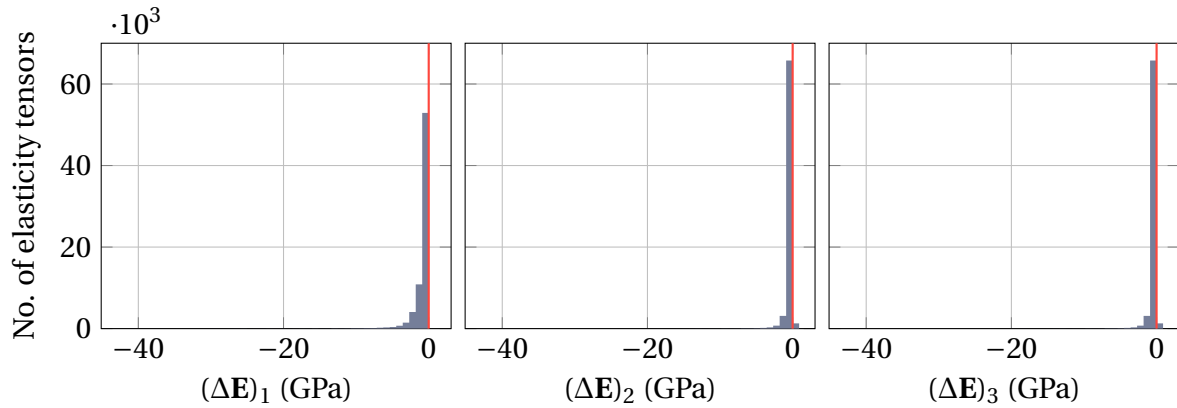

Figure 4.10 • Histograms of eigenvalues of the increments of effective elasticity tensor.

of the increments. The range of increments eigenvalues goes from -43 GPa to 0.89 GPa and is discretized into 50 intervals to constitute this histogram. Note that, unlike conventional histograms, the intervals are half-open on the left to include the zeros on the negative side (the intervals around zero are $]-0.89, 0]$ and $]0, 0.89]$ in GPa). The histogram shows that some increments are not negative definite. It is most likely due to the index symmetrizations. Note that this is an issue for the construction of the evolution model. As the negative increments are small, we choose to enforce the growth of damage (*i.e.* decrease of the stiffness tensor) in the evolution model instead of further modifying the dataset.

✏ Conclusion – Assessment of the dataset

The produced dataset contains inconsistencies from the mechanical point of view. In a minority of cases, the stress and strain symmetrization errors are non-negligible. It means that an elastic material cannot necessarily model the effective behavior of the area element. After studying the tensors positive definiteness, we decided to filter out the effective elasticity tensors with at least one negative eigenvalue. We have also seen that some evolution contains positive increments of rigidity, which is inconsistent. This issue will be circumvented by assuming that the damage is increasing in the evolution model.

4 Anisotropy analysis

This section analyzes the anisotropy of the effective elasticity tensors in the dataset. This analysis will allow us to make and justify different assumptions in the formulation of the model. The distances to symmetry classes (introduced in Section 3) are applied to the dataset to analyze (i) the initial distance to isotropy for each microstructure, and (ii) the distribution of relative distance to isotropy and orthotropy in the dataset.

4.1 Initial distance to isotropy

As specified before, most existing anisotropic damage models consider that the material is initially isotropic. Thus, we must check to what extent the initial (elastic) area element is isotropic. This subsection aims to check whether this assumption is valid in the dataset. To check it, we compute the distance to isotropy by Equation (2.42) for the 36 microstructures in the dataset. The initial distance to isotropy, for each micro-structures, are reported in
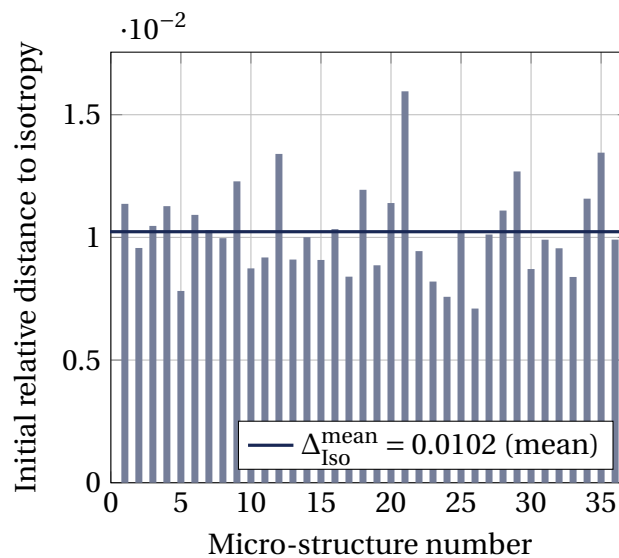

Figure 4.11 • Initial distance to isotropy for each microstructure in the dataset.

Figure 4.11. The initial relative distances to isotropy are between $\Delta_{\text{Iso}}^{\min} = 0.007$ and $\Delta_{\text{Iso}}^{\max} = 0.016$. Moreover, the mean value is $\Delta_{\text{Iso}}^{\text{mean}} = 0.0102$, and the standard deviation is $\Delta_{\text{Iso}}^{\text{mean}} = 0.0018$. It means that the initial elastic properties of the effective elasticity tensors can be

represented by an isotropic elasticity tensor with an error smaller than 1.6%. This error is considered sufficiently small to assume, in the formulation of the damage model, that the behavior is initial isotropic. If there is any anisotropic effective elasticity tensor in the data, which we will change in the next subsection, it means that the anisotropy is damage-induced.

🔾 **Remark 4.6** *In practice, the initial distance to isotropy directly correlates with the number of particles in the area element. Area elements containing fewer particles, for instance 20×20, will exhibit a higher distance to isotropy than area elements with more particles, for instance 100×100. We fixed the beam length in the beam-particle model to obtain a good compromise between the distance to isotropy and the computational cost. Thus, we set the beam length such that the distance to isotropy is around 1%.*

4.2 Analysis of distance to isotropy and orthotropy

Another key question in damage mechanics is which type of damage variable to use (one scalar damage variable, one second-order tensor, two second-order tensors, one fourth-order tensor). An underlying question is whether the effective elasticity tensor of a damaged quasi-brittle area element is close to a specific symmetry class. For instance, if it is close to isotropy, a single scalar variable is sufficient to fully represent the effect of micro-cracking[2]. On the other hand, if it is close to orthotropy, then at least a second-order damage variable is necessary.

To answer this question, let us now analyze the distributions of distances to isotropy and orthotropy in the dataset. Those analyses will be used in the next chapter to justify modeling choices. For instance, the distances of the elasticity tensors to isotropy or to orthotropy can also be used to justify the tensorial nature of the damage variable (Oliver-Leblond et al., 2021). These distances have been computed for each elasticity tensor in the dataset. The corresponding histograms are plotted in Figures 4.12a and 4.12b. In Figure 4.12a, the distribution of the relative distance to isotropy, defined in Equation (2.42), shows that a large part of effective elasticity tensors in the dataset is far from being isotropic. It means that a scalar (isotropic) damage variable is insufficient to represent the loss of stiffness (due to micro-cracking). In the Figure 4.12b, the distribution of the relative distance to orthotropy, defined in Equation (2.61), shows that most of the tensors in the dataset are close to being orthotropic. It means that the effective elasticity tensor can be modeled as remaining orthotropic during the mechanical loadings of the whole dataset. It also means that a second-order damage variable might be sufficient to represent the impact of micro-cracking on the elasticity tensor. From the reconstruction formula (2.30) and in accordance with Desmorat and Desmorat (2016), this implies that at most two second-order tensors are required to represent the impact of micro-cracking on the bi-dimensional elasticity tensor.

---

[2]However, it does not mean that the effective elasticity tensor is proportional to the initial elasticity tensor (with a relation of the type $\tilde{\mathbf{E}}(D) = (1 - D)\mathbf{E}_0$). It might be a more complex function of scalar damage $\tilde{\mathbf{E}}(D)$.
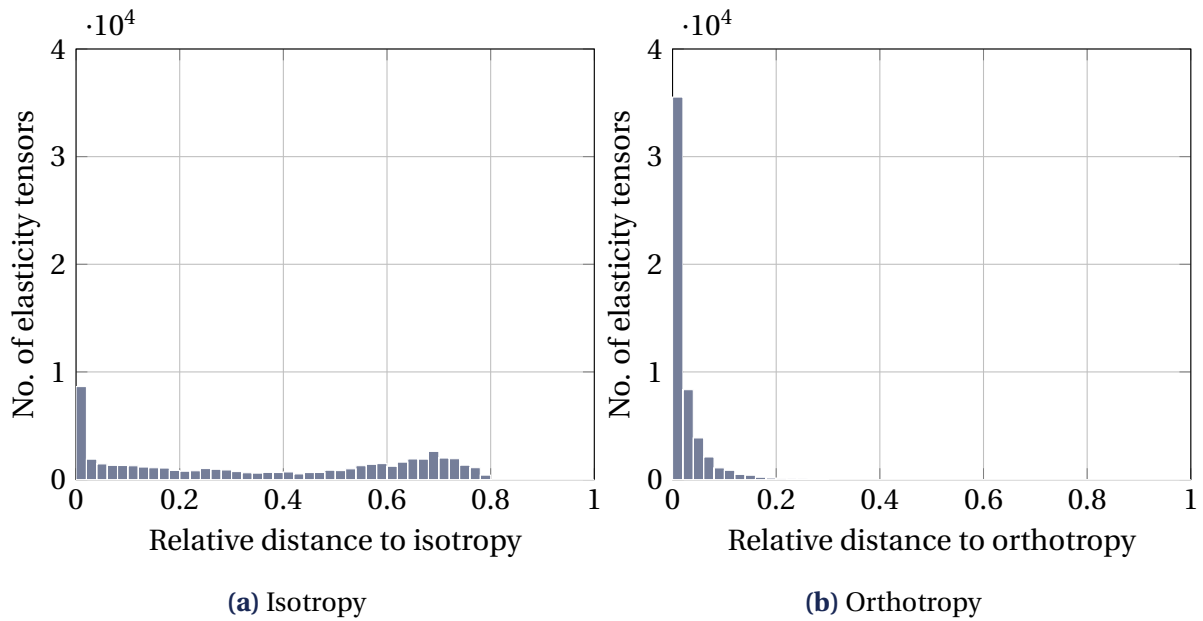
(a) Isotropy **(b)** Orthotropy

Figure 4.12 • Histograms of relative distances to symmetry classes over the dataset

✒ Summary of the Chapter

The objective of this chapter was to generate a dataset of effective elasticity tensors and analyze it. By submitting an area element to 21 proportional and non-proportional multiaxial loadings and applying the measurement procedure, a dataset of 76 756 effective elasticity tensors has been constituted. This data will serve as our reference in the following chapters.

After illustrating its content, we showed that some symmetrization errors are not negligible, indicating that an elasticity tensor cannot exactly represent the micro-cracked specimen. Then, we showed that some measured tensors have negative eigenvalues values. Those tensors have been filtered out. A few inconsistencies are also present in the effective elasticity tensors evolution, as a minority of increments are positive. We will impose damage growth in the damage evolution model to verify the second principle.

Calculating the distance of the tensors to isotropy and orthotropy provides other essential results. First, the effective elasticity tensor of the area elements are initially isotropic. Then, the distance to isotropy is significant for a large part of tensors; thus, most effective elasticity tensors deviates from isotropy due to micro-cracking. Thus, we will be able to assume that the anisotropy of the effective elasticity tensor is damage-induced. It also justifies the need for an anisotropic (tensorial) damage variable, and more precisely for an orthotropic (second-order tensorial) one. Indeed, most effective elasticity tensors stay close to orthotropy during the degradation process, meaning that the orthotropic reconstruction by covariant, presented in Section 2.2, can be used to model the effective elasticity tensor.

5

Formulation of an anisotropic state model

This chapter focuses on developing an anisotropic damage state model using harmonic decomposition, where each harmonic component of the effective elasticity tensor is modeled as a function of damage. First, we introduce an anisotropic damage variable from the literature, based on a second-order covariant of the effective elasticity tensor, enabling an exact modeling of both the bulk modulus and the deviatoric part of the dilatation tensor. Then, we model the shear modulus and the harmonic part using the dataset of computed effective elasticity tensors to complete the state model. It gives a model of the effective elasticity tensor as a function of the initial elastic properties and the damage variable. Finally, its accuracy is evaluated by comparing it with results from the beam-particle model.

In the previous chapter, a reference dataset based on a discrete beam-particle model has been constructed and analyzed. Our objective in this chapter is to formulate an anisotropic damage state model to model the effective elasticity tensor in this dataset. In other words, we aim to determine the general coupling of elasticity with damage $\tilde{\mathbf{E}} = \tilde{\mathbf{E}}(\mathbf{D})$. As specified in Chapter 2 (Section 2), the harmonic decomposition provides a bijection between an elasticity tensor $\mathbf{E}$ and its harmonic components $(\mu, \kappa, \mathbf{d}', \mathbf{H})$. It means that an anisotropic damage model can be formulated by expressing each harmonic component as a function of a damage variable (to be defined) and apply the harmonic reconstruction formula

$$\tilde{\mathbf{E}}(\mathbf{D}) = 2\tilde{\mu}(\mathbf{D})\mathbf{J} + \tilde{\kappa}(\mathbf{D})\mathbf{1} \otimes \mathbf{1} + \frac{1}{2}\left(\mathbf{1} \otimes \tilde{\mathbf{d}}'(\mathbf{D}) + \tilde{\mathbf{d}}'(\mathbf{D}) \otimes \mathbf{1}\right) + \tilde{\mathbf{H}}(\mathbf{D}). \tag{5.1}$$

As seen in the Chapter 1 (Section 3.2), to reach this objective we need to (1) introduce a damage variable to represent the micro-cracking (in Section 1), and (2) model its impact on the elastic behavior (in Section 2). After reaching this first objective, the proposed model is then assessed by comparing its prediction to the reference in Section 3. It is then applied to illustrate its results in Section 4.

1   Definition of a covariant (tensorial) damage variable

This section introduces the damage variable $\mathbf{D}$, *i.e.* the internal state variable representing the micro-cracking of the quasi-brittle material. As shown in Chapter 4 (Section 2), the elasticity

tensor $\mathbf{E}$ of a quasi-brittle material evolves during loading, for instance, due to damage. In accordance with the analysis of the dataset performed in the Chapter 4 (Section 4.1), we will assume that it has the initial isotropic value

$$\mathbf{E}_0 = 2\mu_0 \mathbf{J} + \kappa_0 \mathbf{1} \otimes \mathbf{1}. \tag{5.2}$$

The initial dilatation tensor is then isotropic (*i.e.*, spherical),

$$\mathbf{d}_0 = \mathbf{E}_0 : \mathbf{1} = 2\kappa_0 \mathbf{1}. \tag{5.3}$$

The damage variable is set to zero when the effective elasticity tensor $\mathbf{E}$ is the initial elasticity tensor $\mathbf{E}_0$. The eigenvalues of the damage tensor are usually bounded by one.

Definition of a damage variable.   The analysis of distance to orthotropy in the dataset (see the Section 4.2 of Chapter 4) showed that most the effective elasticity tensors are close to orthotropy. Thus, a second-order damage tensor may be sufficient to represent damage. By Equation (2.23), the bulk modulus κ is exactly reconstructed from the dilatation tensor $\mathbf{d}$. This has led (Oliver-Leblond et al., 2021) to define the dimensionless damage variable $\mathbf{D}$ as the second-order tensor

$$\mathbf{D} = \mathbf{1} - \frac{\mathbf{d}}{2\kappa_0}. \tag{5.4}$$

This damage variable is indeed zero when the effective elasticity tensor $\mathbf{E}$ is the initial elasticity tensor $\mathbf{E}_0$ and its eigenvalues are bounded by one.

◌ **Remark 5.1** *Since the initial dilatation tensor is given by* $\mathbf{d}_0 = \mathrm{tr}_{12}\,\mathbf{E}_0 = 2\kappa_0\mathbf{1}$*, we have the equalities*

$$\mathbf{D} = \frac{1}{2\kappa_0}\,\mathrm{tr}_{12}(\mathbf{E}_0 - \mathbf{E}) = (\mathbf{d}_0 - \mathbf{d}) \cdot \mathbf{d}_0^{-1} = \mathbf{d}_0^{-1} \cdot (\mathbf{d}_0 - \mathbf{d}). \tag{5.5}$$

Advantage of the damage definition.   The mapping in Equation (5.4) provides a bijection between the damage variable $\mathbf{D}$ and the effective dilatation tensor $\widetilde{\mathbf{d}}$. Indeed, the latter is related to $\mathbf{D}$ as

$$\widetilde{\mathbf{d}}(\mathbf{D}) = 2\kappa_0\,(\mathbf{1} - \mathbf{D}). \tag{5.6}$$

Thus, the deviatoric part of the dilatation tensor can be expressed as the function of damage

$$\widetilde{\mathbf{d}}'(\mathbf{D}) = -2\kappa_0 \mathbf{D}'. \tag{5.7}$$

Moreover, the bulk modulus κ also directly relates to damage $\mathbf{D}$

$$\widetilde{\kappa}(\mathbf{D}) = \frac{1}{4}\,\mathrm{tr}\,\widetilde{\mathbf{d}}(\mathbf{D}) = \kappa_0\left(1 - \frac{1}{2}\,\mathrm{tr}\,\mathbf{D}\right). \tag{5.8}$$

It means that only the models of the effective shear modulus $\widetilde{\mu}$ and the effective harmonic part $\widetilde{\mathbf{H}}$ as damage functions are required to complete the state model. Also note that if the damage $\mathbf{D}$ and the initial elastic properties μ_0 and κ_0 are known, the bulk modulus and the dilatation tensor are also exactly modeled.

2 Completing the state model

Currently, the damage state model is already half formulated. Indeed, the Equations (5.6) and (5.8) enable to model two terms (the bulk modulus and the deviatoric part of the dilatation tensor) out of four in the harmonic reconstruction formula

$$\mathbf{E} = 2\widetilde{\mu}(\mathbf{D})\mathbf{J} + \widetilde{\kappa}(\mathbf{D})\mathbf{1} \otimes \mathbf{1} + \frac{1}{2}\left(\mathbf{1} \otimes \widetilde{\mathbf{d}}'(\mathbf{D}) + \widetilde{\mathbf{d}}'(\mathbf{D}) \otimes \mathbf{1}\right) + \widetilde{\mathbf{H}}(\mathbf{D}). \tag{5.9}$$

In this section, we will use the dataset to model the shear modulus μ and the harmonic part $\mathbf{H}$ as damage functions.

2.1 Modeling the shear modulus

2.1.1 Basis of the model

We recall first the expression of the generalized shear modulus μ of the elasticity tensor $\mathbf{E}$,

$$\mu = \frac{1}{8}(2\,\mathrm{tr}\,\mathbf{v} - \mathrm{tr}\,\mathbf{d}), \qquad \mathbf{d} = \mathbf{E} : \mathbf{1}, \qquad \mathbf{v} = \mathrm{tr}_{13}\,\mathbf{E}. \tag{5.10}$$

The Equation (5.6) already expresses the dilatation tensor from damage. Thus, to express μ as a function of damage tensor $\mathbf{D}$, we need to exhibit a relation between the trace $\mathrm{tr}\,\mathbf{v}$ of the Voigt tensor and the damage tensor $\mathbf{D}$. To ease the modeling process, an intermediate scalar variable $D_{\mathbf{v}}$, such that $\mathrm{tr}\,\mathbf{v} = \mathrm{tr}\,\mathbf{v}_0(1 - D_{\mathbf{v}})$, is introduced,

$$D_{\mathbf{v}} = \frac{\mathrm{tr}\,\mathbf{v}_0 - \mathrm{tr}\,\mathbf{v}}{\mathrm{tr}\,\mathbf{v}_0}. \tag{5.11}$$

It can be interpreted as a damage variable based on $\mathrm{tr}(\mathbf{v})$. Since it represents the same micro-cracking pattern as $\mathbf{D}$, and it is independent of $\mathbf{D}$ (from a mathematical point of view), it could be considered as an additional thermodynamic (internal) variable. However, Figure 5.1 shows that, from a mechanical point of view, the variable $D_{\mathbf{v}}$ can be modeled as a function of the damage variable $\mathbf{D}$. Thus, it only serves as a intermediate variable to ease the modeling formulation of the model. Indeed, Figure 5.1 contains a scatter plot of $D_{\mathbf{v}}$ as a function of the two eigenvalues D_1 and D_2 of the damage tensor $\mathbf{D}$ for each elasticity tensor of the dataset. It shows that the dataset's points $(D_1, D_2, D_{\mathbf{v}})$ are grouped around a surface. Thus, $D_{\mathbf{v}}$ can be modeled as a function of damage by a constitutive equation $D_{\mathbf{v}} = D_{\mathbf{v}}^{\mathrm{m}}(\mathbf{D})$, where the upper script m stands for model. In practice, we approximate $D_{\mathbf{v}}$ by the linear combination of invariants of $\mathbf{D}$,

$$D_{\mathbf{v}}^{\mathrm{m}}(\mathbf{D}) = c_1\,I_1(\mathbf{D}) + c_2\,I_2(\mathbf{D}), \qquad I_k(\mathbf{D}) = \mathrm{tr}(\mathbf{D}^k) = D_1^k + D_2^k, \tag{5.12}$$

where $I_k(\mathbf{D})$ are invariants of $\mathbf{D}$, and c_k are the parameters of the model. A second expression

$$D_{\mathbf{v}}^{\mathrm{m}}(\mathbf{D}) = c_1\,I_1(\mathbf{D}) + c_2\,I_2(\mathbf{D}) + c_3\,I_3(\mathbf{D}), \qquad I_3(\mathbf{D}) = \frac{1}{2}\left(3I_1(\mathbf{D})I_2(\mathbf{D}) - I_1^3(\mathbf{D})\right), \tag{5.13}$$

will also be studied (but the two-term expansion in Equation (5.12) will prove sufficient).

The modeling process will be carried out in two steps. The first step involves deriving and justifying some physical constraints on the material constants c_k. Those constraints will limit the number of independent parameters of the model. The second step consists in identifying the parameters c_k.
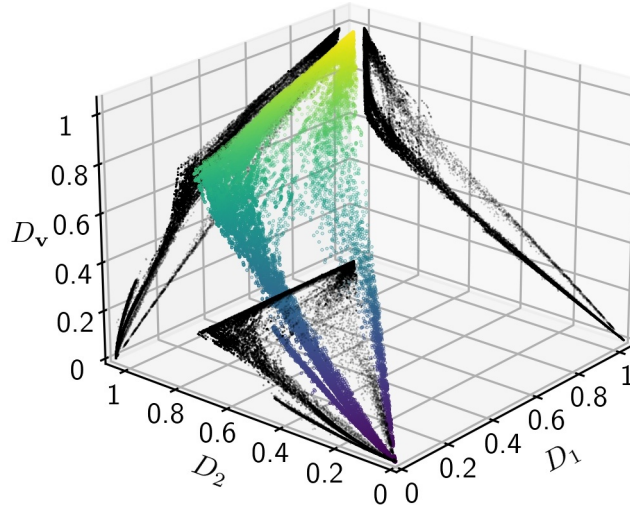
Figure 5.1 • Damage $D_{\mathbf{v}}$ as a function of the eigenvalues D_1 and D_2 ($D_2 > D_1$) of the damage variable $\mathbf{D}$ over the dataset. Each colored point is the value of $D_{\mathbf{v}}$ for an elasticity tensor of the dataset. The black dots are the projections of the data points onto the planes $(D_1, D_{\mathbf{v}})$, $(D_2, D_{\mathbf{v}})$ and (D_1, D_2).

2.1.2 Physical constraints

Constraint 1 – Undamaged state.   For an undamaged state, the trace of the Voigt tensor keeps its initial value, $\mathrm{tr}\,\mathbf{v} = \mathrm{tr}\,\mathbf{v}_0$,

$$D_{\mathbf{v}}^{\mathrm{m}}(\mathbf{D} = \mathbf{0}) = 0 \tag{5.14}$$

This constraint is satisfied by both Equation (5.12) and Equation (5.13) since the invariants of $\mathbf{D}$ vanish ($I_k(\mathbf{D} = \mathbf{0}) = 0$).

Constraint 2 – Fully damaged state.   The effective elasticity tensor is a null fourth-order tensor for a fully damaged state. We have then $\mathrm{tr}\,\mathbf{v} = 0$, which implies $D_{\mathbf{v}}^{\mathrm{m}}(\mathbf{D} = \mathbf{1}) = 1$ and,

$$2 \sum_{k=1}^{n} c_k = 1, \qquad n = 2,3. \tag{5.15}$$

Constraints 3 – Diffuse micro-cracking.   In the early degradation stage, the micro-cracking is diffuse (in the sense that it is not localized within the area element). In Figure 5.1, this stage corresponds to the region where the damage eigenvalues D_1 and D_2 are small. We observe that the points $(D_1, D_2, D_{\mathbf{v}})$ are close to a plane in this region. It corresponds to the assumption of non-interacting cracks (as defined by Kachanov (1992)). Kachanov (1992) shows that — in 2D — as long as the micro-cracks are not interacting, the gain in compliance is a totally symmetric fourth-order tensor. This property is not satisfied anymore when the micro-cracking is localized. This observation guided us to check if this property is satisfied by the weakly damaged elasticity tensors of the dataset. Assuming in the early damage stage that the stiffness loss $\Delta\mathbf{E} = \mathbf{E} - \mathbf{E}_0$ is totally symmetric implies

$$\mathrm{tr}_{12}\,(\mathbf{E} - \mathbf{E}_0) = \mathrm{tr}_{13}\,(\mathbf{E} - \mathbf{E}_0) \tag{5.16}$$

which leads to

$$\operatorname{tr}\mathbf{d} - \operatorname{tr}\mathbf{d}_0 = \operatorname{tr}\mathbf{v} - \operatorname{tr}\mathbf{v}_0. \tag{5.17}$$

It means that we have, at low damage,

$$D_{\mathbf{v}} = \frac{\operatorname{tr}\mathbf{d}_0 - \operatorname{tr}\mathbf{d}}{\operatorname{tr}\mathbf{v}_0}. \tag{5.18}$$

Taking the trace of the definition in Equation (5.6), giving $\operatorname{tr}\mathbf{d} = 2\kappa_0(2 - \operatorname{tr}\mathbf{D})$, and using the relation between initial properties, $\operatorname{tr}\mathbf{d}_0 = 4\kappa_0$ and $\operatorname{tr}\mathbf{v}_0 = 4\mu_0 + 2\kappa_0$, we get, at low damage still,

$$D_{\mathbf{v}} = \frac{\kappa_0}{2\mu_0 + \kappa_0} I_1(\mathbf{D}), \tag{5.19}$$

and

$$\left.\frac{\partial D_{\mathbf{v}}}{\partial \mathbf{D}}\right|_{\mathbf{D}=\mathbf{0}} = \frac{\kappa_0}{2\mu_0 + \kappa_0}\mathbf{1} \qquad \text{(diffuse micro-cracking assumption).} \tag{5.20}$$

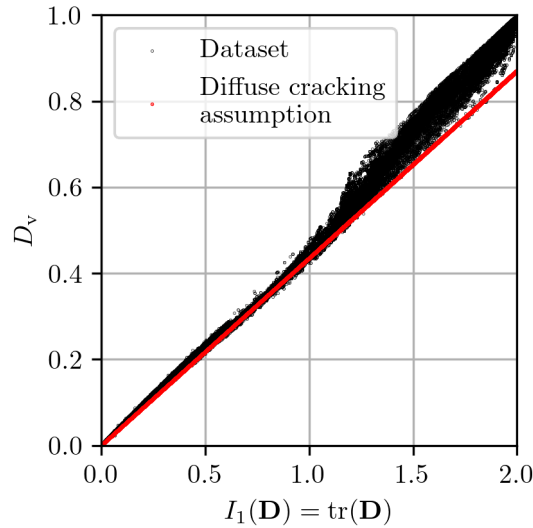Figure 5.2 provides a check of this assumption in the dataset of elasticity tensor. For small

Figure 5.2 • Check of the assumption of total symmetry of the stiffness loss tensor: the dots in black correspond to the value in the dataset, and the red dots correspond to the $D_{\mathbf{v}}$ computed via Equation (5.20).

values of the damage ($\operatorname{tr}\mathbf{D} < 1$), the values of $D_{\mathbf{v}}$ obtained by the diffuse micro-cracking assumption provide an accurate model for the values from the dataset.

For both constitutive Equations (5.12) and (5.13), the diffuse micro-cracking constraint leads to

$$\left.\frac{\partial}{\partial \mathbf{D}}\right|_{\mathbf{D}=\mathbf{0}}\left(\sum_{k=1}^{n} c_k I_k(\mathbf{D})\right) = \frac{\kappa_0}{2\mu_0 + \kappa_0}\mathbf{1}, \quad i.e., \quad c_1 = \frac{\kappa_0}{2\mu_0 + \kappa_0}. \tag{5.21}$$

2.1.3 Determination of the parameters c_k

Model with two terms. For the first two-term expression in Equation (5.12), the physical constraints lead to

$$c_1 = \frac{\kappa_0}{2\mu_0 + \kappa_0}, \quad \text{and} \quad c_2 = \frac{1}{2} - c_1, \tag{5.22}$$

so that,

$$D_{\mathbf{v}}^{\mathrm{m}}(\mathbf{D}) = \frac{\kappa_0}{2\mu_0 + \kappa_0}\,(I_1(\mathbf{D}) - I_2(\mathbf{D})) + \frac{1}{2}I_2(\mathbf{D}). \tag{5.23}$$

Thanks to the physical constraints, no material parameter needs to be introduced for this first model.

Model with three terms. Applying the physical constraints to the three-term expression in Equation (5.13) leads to

$$c_1 = \frac{\kappa_0}{2\mu_0 + \kappa_0}, \qquad c_2 = \frac{1}{2} - c_1 - c_3, \tag{5.24}$$

and

$$D_{\mathbf{v}}^{\mathrm{m}}(\mathbf{D}) = \frac{\kappa_0}{2\mu_0 + \kappa_0}\,(I_1(\mathbf{D}) - I_2(\mathbf{D})) + \frac{1}{2}I_2(\mathbf{D}) + c_3\,(I_3(\mathbf{D}) - I_2(\mathbf{D})). \tag{5.25}$$

The parameter c_3 is determined via a regression over the whole dataset. We get the small value

$$c_3 = 0.103, \tag{5.26}$$

to be compared to the particular case $c_3 = 0$ giving the two-term expression in Equation (5.23).

Unification of both models. The effective shear modulus has been derived as

$$\widetilde{\mu}(\mathbf{D}) = \frac{1}{8}\left(2\operatorname{tr}\widetilde{\mathbf{v}} - \operatorname{tr}\widetilde{\mathbf{d}}\right), \qquad \operatorname{tr}\widetilde{\mathbf{v}} = \operatorname{tr}_{13}\operatorname{tr}\widetilde{\mathbf{E}} = \operatorname{tr}\mathbf{v}_0(1 - D_{\mathbf{v}}^{\mathrm{m}}(\mathbf{D})) \tag{5.27}$$

with for $D_{\mathbf{v}}^{\mathrm{m}}(\mathbf{D})$, function of the invariants $\operatorname{tr}\mathbf{D}$, $\mathbf{D}:\mathbf{D}$ and $I_3(\mathbf{D}) = \operatorname{tr}(\mathbf{D}^3)$, either the no-additional parameter function in Equation (5.23) or the one-additional parameter function in Equation (5.25). Replacing the intermediate variable $D_{\mathbf{v}}$ by its expression as a function of damage $\mathbf{D}$ in the expression of the shear modulus gives

$$\widetilde{\mu}(\mathbf{D}) = \mu_0 - \frac{1}{4}\kappa_0\operatorname{tr}\mathbf{D} + \frac{1}{4}\left(\kappa_0 - 2\mu_0\right)\mathbf{D}:\mathbf{D} + m\left(\mathbf{D}:\mathbf{D} - \operatorname{tr}(\mathbf{D}^3)\right), \tag{5.28}$$

where the non-linear shear-damage coupling parameter is

$$m = \frac{1}{2}\left(\kappa_0 + 2\mu_0\right)c_3, \qquad c_3 = 0.103. \tag{5.29}$$

This expression unifies both models into a single one as $m = 0$ corresponds to Equation (5.23) and $m \neq 0$ to Equation (5.25).

2.2   Modeling the harmonic part

2.2.1   Basis of the model

The next step consists of modeling the harmonic part as a damage function. The relative distance to orthotropy remains small for most elasticity tensors of the dataset as shown in the Section 4.2 of Chapter 4. We thus make the simplifying assumption that the effective elasticity tensors $\mathbf{E}$ are orthotropic. It means that we can apply the harmonic square formula

in Equation (2.29) to model the harmonic part. By Equation (2.29), the harmonic part of a 2D orthotropic elasticity tensor can be written as the harmonic square

$$\mathbf{H} = \frac{2K_3}{I_2^2}\mathbf{d}' * \mathbf{d}' = \pm \|\mathbf{H}\| \; \frac{\mathbf{d}' * \mathbf{d}'}{\|\mathbf{d}' * \mathbf{d}'\|}, \qquad \|\mathbf{d}' * \mathbf{d}'\| = \frac{1}{\sqrt{2}}\mathbf{d}' : \mathbf{d}' = \frac{1}{\sqrt{2}}I_2, \tag{5.30}$$

depending on the sign of the invariant of the elasticity tensor $K_3(\mathbf{E}) = \mathbf{d} : \mathbf{H} : \mathbf{d}$. Let us recall that the Equation (5.6) already gives the relation between the dilatation tensor $\mathbf{d}$ and damage $\mathbf{D}$. Based on this parametrization, the modeling of the harmonic part of the elasticity tensors in the dataset can be carried out in two steps:

1. choosing an orientation (the sign) and

2. modeling the harmonic part norm $\|\mathbf{H}\|$ as a function of the damage variable $\mathbf{D}$.

$\bigcirc$ **Remark 5.2** *Note that the orientation must be well-predicted when the relative norm of the harmonic part $\|\mathbf{H}\|/\|\mathbf{E}\|$ is large. When the harmonic part is small (when $\|\mathbf{H}\|/\|\mathbf{E}\| \ll 1$), a misprediction of the orientation has a negligible effect on the predicted elasticity tensor.*

2.2.2 Orientation of the harmonic part

A first indicator of the harmonic part $\mathbf{H}$ orientation is the sign of the invariant $K_3(\mathbf{E})$ or, in an equivalent manner, the sign of $K_3^{1/3}(\mathbf{E})$ (which is in GPa). Figure 5.3a shows the histogram of
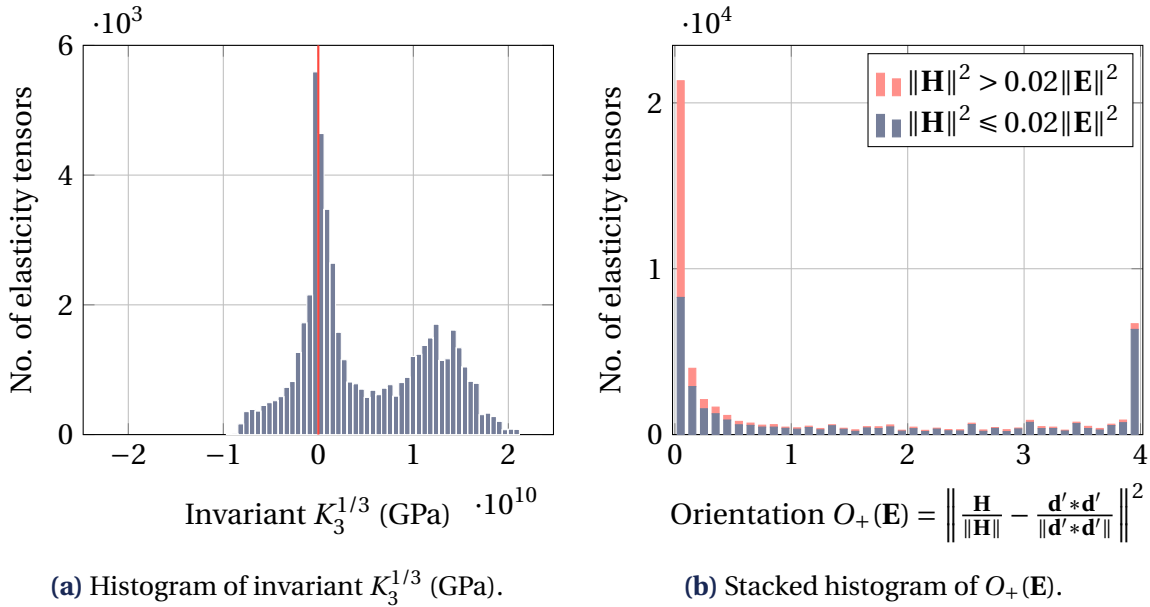

(a) Histogram of invariant $K_3^{1/3}$ (GPa).

(b) Stacked histogram of $O_+(\mathbf{E})$.

Figure 5.3 • Histogram of two indicators for the sign of the harmonic part over the dataset.

the invariant $K_3(\mathbf{E})^{1/3}$ over the dataset. It shows that the negative values of $K_3(\mathbf{E})^{1/3}$ are smaller (in absolute value) than the positive values of $K_3(\mathbf{E})^{1/3}$. When taking the cube of $K_3(\mathbf{E})^{1/3}$, the positive values are an order of magnitude larger than the negative values. However, a large value of K_3 does not mean that the harmonic part is large, whereas a small value of K_3 does mean that the harmonic part is small (see Equation (2.29) and remark 5.2).

Another orientation indicator is the norm of the difference between the normalized harmonic part and the normalized harmonic square

$$O_+(\mathbf{E}) = \left\| \frac{\mathbf{H}}{\|\mathbf{H}\|} - \frac{\mathbf{d}' * \mathbf{d}'}{\|\mathbf{d}' * \mathbf{d}'\|} \right\|^2. \tag{5.31}$$

The histogram of the orientation indicator $O_+(\mathbf{E})$ over the dataset is plotted in Figure 5.3b. It mainly exhibits two peaks, one at 0, corresponding to the plus sign in Equation (5.30), and one at 4, corresponding to the minus sign. To decide which sign is the best for the model, the dataset is split into two colored parts:

- a blue part when the harmonic part is negligible ($\|\mathbf{H}\|^2/\|\mathbf{E}\|^2$ lower than 2%), and

- a red part when the harmonic part is significant ($\|\mathbf{H}\|^2/\|\mathbf{E}\|^2$ larger than 2%).

Figure 5.3b shows that a higher number of elasticity tensors have a significant harmonic part in the positive orientation ($O_+(\mathbf{E}) = 0$) than in the negative orientation ($O_+(\mathbf{E}) = 4$). This observation is consistent with the analysis based on the invariant K_3. It also indicates that the preferred orientation is $+\frac{\mathbf{d}' * \mathbf{d}'}{\|\mathbf{d}' * \mathbf{d}'\|}$ (plus sign in Equation (5.30)).

For the remaining of this subsection, we use the proportionality of the deviatoric part of the dilatation tensor with damage $\mathbf{d}' = -2\kappa_0 \mathbf{D}'$ (by Equation (5.6)), and model the harmonic part of the effective elasticity tensors with a plus sign, by setting (with a slight abuse of notation)

$$\mathbf{H} = \mathbf{H}(\mathbf{D}) = H^{\mathrm{m}}(\mathbf{D}) \frac{\mathbf{D}' * \mathbf{D}'}{\mathbf{D}' : \mathbf{D}'}, \qquad \mathbf{D}' * \mathbf{D}' = \mathbf{D}' \otimes \mathbf{D}' - \frac{1}{2}(\mathbf{D}' : \mathbf{D}') \mathbf{J}, \tag{5.32}$$

where $H^{\mathrm{m}} = \sqrt{2}\,\|\mathbf{H}\|$ is a positive function (to be determined) of the tensorial damage variable $\mathbf{D}$.

2.2.3 Is the harmonic part norm a function of damage ?

To identify the constitutive equation $H^{\mathrm{m}}(\mathbf{D})$, the first step is to check if the norm $\|\mathbf{H}\|$ of the harmonic part can be represented by a function of the tensorial damage variable $\mathbf{D}$ (through its invariants). Figure 5.4 shows the harmonic part norm $\|\mathbf{H}\|$ versus the damage invariants $I_1(\mathbf{D}) = \mathrm{tr}\,\mathbf{D}$ and $I_2(\mathbf{D}') = \mathbf{D}' : \mathbf{D}'$. Even if the discrepancy is large, especially in the region where $I_1(\mathbf{D}) > 1$, this figure indicates that it should be possible to approximate the norm $\|\mathbf{H}\|$ by a function of the two damage invariants $I_1(\mathbf{D})$ and $I_2(\mathbf{D}')$.

🔍 **Remark 5.3** *Figure 5.4 shows that the norm of the harmonic part does not vanish when the damage variable $\mathbf{D}$ is equal to the second-order identity $\mathbf{1}$. Moreover, for the effective elasticity tensors in the dataset such that $I_1(\mathbf{D}) \approx 2$ and $I_2(\mathbf{D}') \approx 0$, different values of the norm $\|\mathbf{H}\|$ are associated with the same value of damage. This means that the definition in Equation (5.4) of the damage variable is insufficient in these few cases to fully represent the variations of the effective elasticity tensor due to highly interacting micro-cracks. To account for those variations, a second (internal) damage variable, possibly of higher order, could be used (see the works of Cormery and Welemane (2010) and Desmorat and Desmorat (2016) for instance). Yet, the accuracy gain might not be worth the increased modeling complexity.*
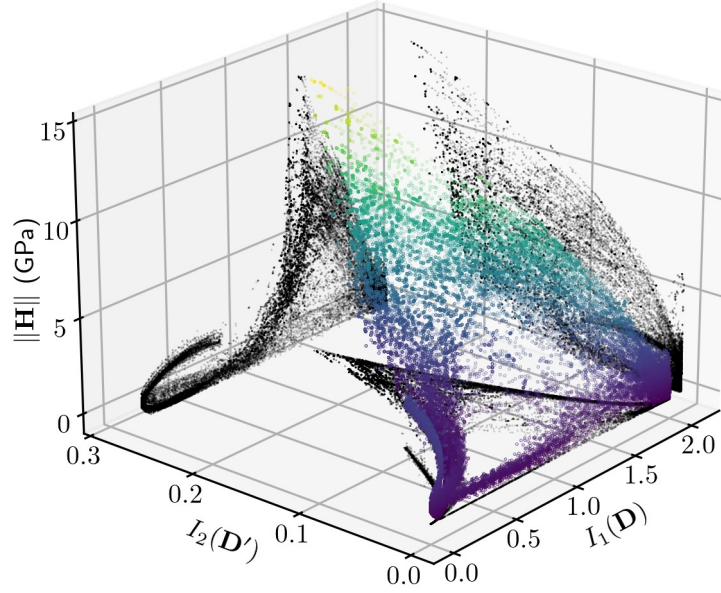
Figure 5.4 • Norm of the harmonic part (in GPa) as a function of the damage invariants $I_1(\mathbf{D})$ and $I_2(\mathbf{D}') = \mathbf{D}' : \mathbf{D}'$. The black dots are the projection of the data onto the planes $(I_1(\mathbf{D}), I_2(\mathbf{D}'))$, $(I_1(\mathbf{D}), \|\mathbf{H}\|)$ and $(I_2(\mathbf{D}'), \|\mathbf{H}\|)$.

2.2.4 Physical constraints

As for the modeling of shear modulus, let us frame the (state) modeling of the function $H^{\mathrm{m}}(\mathbf{D})$ by physical assumptions/constraints.

Constraint 1 – Initial isotropy. The assumption of initial isotropy imposes that

$$H^{\mathrm{m}}(\mathbf{D} = \mathbf{0}) = 0. \tag{5.33}$$

Constraint 2 – Full damaged state. We also assume that the effective elasticity tensor $\mathbf{E}$ vanishes when the material is fully damaged. It implies that the harmonic part $\mathbf{H}$ must vanish when the damage grows to $\mathbf{D} = \mathbf{1}$,

$$H^{\mathrm{m}}(\mathbf{D} = \mathbf{1}) = 0. \tag{5.34}$$

Constraint 3 – Hydrostatic damage. Figure 5.4 shows that the harmonic part norm $\|\mathbf{H}\|$ remains small when the damage invariant $I_2(\mathbf{D}')$ is small. We can assume that

$$H^{\mathrm{m}}(I_1(\mathbf{D}), I_2(\mathbf{D}') = 0) = 0. \tag{5.35}$$

This new condition includes both previous assumptions.

🔍 **Remark 5.4** *The condition in Equation (5.35) is satisfied when the damage is purely hydrostatic (i.e., when $\mathbf{D} = \frac{1}{2}(\mathrm{tr}\,\mathbf{D})\,\mathbf{1}$). If the damage is hydrostatic, both the dilatation part $\mathbf{Dil}$ and the harmonic part $\mathbf{H}$ are obtained null (by the formula in Equation (2.18)). Thus, the modeled 2D effective elasticity tensor $\mathbf{E}(\mathbf{D})$ is isotropic during a hydrostatic damaging process.*

2.2.5 Modeling the harmonic part norm

The modelling of the harmonic part is intricate due to the complex shape of the surface and the discrepancy. To overcome this difficulty, we choose to use a sparse regression method to guide the modeling process. This method enables us to postulate a generic parametrized function for the model, such as a polynomial, and let the regression filter out the unnecessary parameters.

Q **Remark 5.5** *As a first approach, multiple attempts to intuit a model of the harmonic part have been made in this work but proved to be inconclusive. In particular, we tried to intuit models of the amplitude of the harmonic part both via the invariant K_3 and via the harmonic part norm $\|\mathbf{H}\|$. Yet, most attempts to formulate the model by fitting various functions failed. We choose to use the sparse regression has a means to solve this initial setback.*

Sparse regression. A sparse regression method, the LASSO regression proposed by Tibshirani (1996), has been applied to a (multivariate) polynomial in the damage invariants $I_1(\mathbf{D})$ and $I_2(\mathbf{D}')$. This optimization method aims at fitting a parametrized function to data while penalizing the number of non-zero parameters. Adding minimization constraints provides the means to enforce physical assumptions (Gaines et al., 2018). The constrained LASSO regression for the polynomial modeling of the function $H^{\mathrm{m}}(\mathbf{D}) = \sqrt{2}\|\mathbf{H}(\mathbf{D})\|$ (introduced in Equation (5.32)) recasts as the minimization problem

$$\min_{h_{n_1 n_2}} \quad \sum_{i=1}^{N_{\mathrm{ela}}} \left(\sqrt{2}\|\mathbf{H}_i\| - \sum_{n_1,n_2} h_{n_1 n_2} I_1(\mathbf{D}_i)^{n_1} I_2(\mathbf{D}'_i)^{n_2} \right)^2 + \alpha \sum_{n_1,n_2} |h_{n_1 n_2}|, \tag{5.36}$$

where N_{ela} is the number of elasticity tensors in the dataset, $h_{n_1 n_2}$ are the coefficients of the sought polynomial, *i.e.*, the model parameters, and α is an arbitrary hyperparameter of the method. The first term corresponds to a classical regression with a least-square error. The second term (with the factor α) penalizes the sum of the absolute values of the parameters $h_{n_1 n_2}$. In practice, the higher the hyperparameter α, the fewer the non-zero parameters. The coefficient of determination of the regression

$$r^2 = 1 - \frac{\sum_{i=1}^{N_{ela}} \left(\sqrt{2}\|\mathbf{H}_i\| - \sum_{n_1,n_2} h_{n_1 n_2} I_1(\mathbf{D}_i)^{n_1} I_2(\mathbf{D}'_i)^{n_2} \right)^2}{\sum_{i=1}^{N_{ela}} \left(\sqrt{2}\|\mathbf{H}_i\| - \mathrm{mean}\left(\sum_{n_1,n_2} h_{n_1 n_2} I_1(\mathbf{D}_i)^{n_1} I_2(\mathbf{D}'_i)^{n_2} \right) \right)^2} \tag{5.37}$$

is introduced as an indicator of the accuracy of the regression. In practice, we carry out the minimization for different values of α to find a good compromise between the model accuracy and the number of non-zero parameters.

Application of the sparse regression. As shown in Figure 5.5, the best compromise between the model's accuracy (evaluated via the coefficient of determination r^2 and the number of non-zero parameters) has been obtained for $\alpha = 0.0023$ GPa. After this value, the number of non-zero parameters rises while the coefficient of determination r^2 reaches a plateau. The retained model is the one-parameter polynomial expression

$$H^{\mathrm{m}}(\mathbf{D}) = h\, I_1^4(\mathbf{D})\, I_2(\mathbf{D}'), \qquad h = h_{41} = 18.8 \text{ GPa}, \tag{5.38}$$
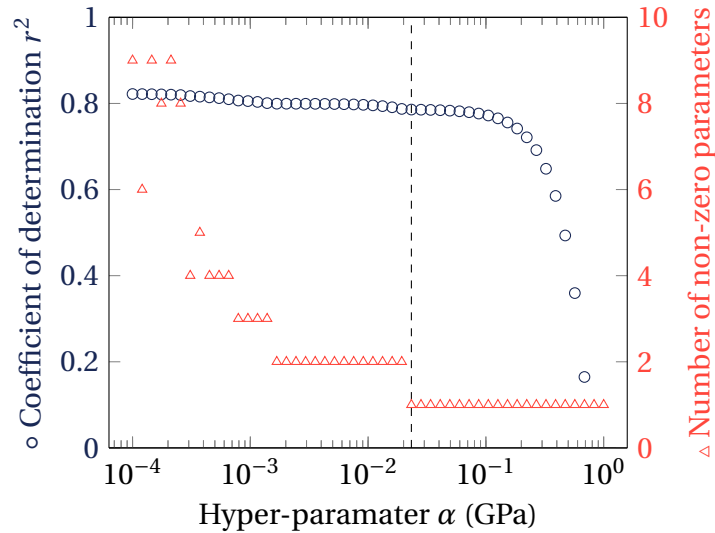
Figure 5.5 • Illustration of the compromise between the precision and the number of non-zero parameters in the constrained LASSO regression. The dashed line shows the best compromise for us ($\alpha = 0.0023$ GPa).

where h is the so-called harmonic pre-factor. Combined with Equations (2.27) and (5.32), the previous expression means that the simple constitutive equation should satisfyingly model the effective harmonic part of the elasticity tensors of our large dataset

$$\widetilde{\mathbf{H}}(\mathbf{D}) = h\,(\mathrm{tr}\,\mathbf{D})^4\,\mathbf{D}' * \mathbf{D}', \qquad \mathbf{D}' * \mathbf{D}' = \mathbf{D}' \otimes \mathbf{D}' - \frac{1}{2}(\mathbf{D}' : \mathbf{D}')\,\mathbf{J}, \tag{5.39}$$

which expresses the harmonic part of the 2D effective elasticity tensors as a function of the damage variable $\mathbf{D}$ only. Recall that $\mathbf{J} = \mathbf{I} - \frac{1}{2}\mathbf{1} \otimes \mathbf{1}$ is the deviatoric projector.

Q **Remark 5.6** *The sparse regression has also been applied to the invariant K_3 to obtain its model $K_3^{\mathrm{m}}(\mathbf{D})$. Yet, the "accurate" models of the harmonic based on K_3 required too many parameters to be attractive.*

2.2.6   Neglecting the harmonic part

As an alternative to the polynomial expression in Equation (5.39), it is also worth neglecting the harmonic part $\mathbf{H}$ and simply setting $h = 0$, *i.e.,*

$$\mathbf{H}(\mathbf{D}) = 0. \tag{5.40}$$

Indeed, as shown in Figure 5.6, the harmonic part is a small proportion of the effective elasticity tensor in most cases. Due to these observations, it is sometimes possible to neglect the harmonic part.

Q **Remark 5.7** *The modelling assumption $h = 0$, being equivalent to $\mathbf{H}(\mathbf{D}) = 0$ or $J_2(\mathbf{E}) = \mathbf{H} :: \mathbf{H}$, makes the effective elasticity tensor r_0-orthotropic in the sense of Vannucci (2002, 2005).*
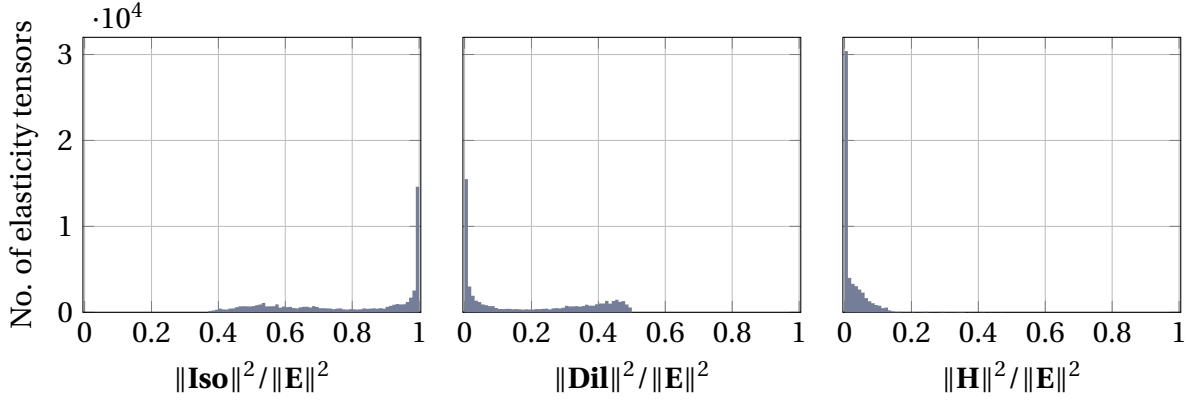
Figure 5.6 • Proportion of each part of the elasticity tensor for each tensor in the dataset.

2.3   Summary of the proposed anisotropic damage state model

Let us summarize the constitutive equations obtained previously. These equations are obtained from the elasticity tensors reconstruction formulas in Equations (2.18) and (2.30), the performed virtual beam-particle computations, and cross-identification over the large effective elasticity tensors dataset. Let us also switch to standard Continuum Mechanics notations and mark with a tilde the effective (damaged) quantities, such as the effective elasticity tensor $\widetilde{\mathbf{E}} = \widetilde{\mathbf{E}}(\mathbf{D})$, the effective generalized shear and bulk moduli $\widetilde{\mu} = \widetilde{\mu}(\mathbf{D})$, $\widetilde{\kappa} = \widetilde{\kappa}(\mathbf{D})$, the effective harmonic tensor $\widetilde{\mathbf{H}} = \widetilde{\mathbf{H}}(\mathbf{D})$. We recall and rewrite the state equations obtained by using the relation

$$\widetilde{\mathbf{d}} = 2\kappa_0 \left(\mathbf{1} - \mathbf{D}\right), \tag{5.41}$$

between the effective dilatation tensor $\widetilde{\mathbf{d}} = \widetilde{\mathbf{E}} : \mathbf{1}$ and the second-order damage variable $\mathbf{D}$.

Effective elasticity tensor.   The proposed anisotropic damage coupling is based on the damage dependency of each component of the harmonic decomposition

$$\widetilde{\mathbf{E}}(\mathbf{D}) = 2\widetilde{\mu}(\mathbf{D})\,\mathbf{J} + \widetilde{\kappa}(\mathbf{D})\,\mathbf{1} \otimes \mathbf{1} - \kappa_0 \left(\mathbf{1} \otimes \mathbf{D}' + \mathbf{D}' \otimes \mathbf{1}\right) + \widetilde{\mathbf{H}}(\mathbf{D}), \tag{5.42}$$

of the effective bi-dimensional elasticity tensor. Table 5.1 summarizes the simplified expres-

Quantity	Model
Shear modulus	$\widetilde{\mu}(\mathbf{D}) = \mu_0 - \frac{1}{4}\kappa_0 \operatorname{tr}\mathbf{D} + \frac{1}{4}\left(\kappa_0 - 2\mu_0\right)\mathbf{D} : \mathbf{D} + m\left(\mathbf{D} : \mathbf{D} - \operatorname{tr}(\mathbf{D}^3)\right)$
Bulk modulus	$\widetilde{\kappa}(\mathbf{D}) = \kappa_0\left(1 - \frac{1}{2}\operatorname{tr}\mathbf{D}\right)$
Dilatation tensor	$\widetilde{\mathbf{d}} = 2\kappa_0\left(\mathbf{1} - \mathbf{D}\right)$
Harmonic part	$\widetilde{\mathbf{H}}(\mathbf{D}) = h\left(\operatorname{tr}\mathbf{D}\right)^4 \mathbf{D}' * \mathbf{D}'$

Table 5.1 • Summary of the constitutive equations for the proposed anisotropic damage state model.

sions of each harmonic component as functions of the initial elastic properties (μ_0 and κ_0) and the damage state variable.

State potential. The corresponding elasticity law coupled with anisotropic damage derives from a thermodynamic potential, the Helmholtz free energy density $\rho\psi$ function of the strain and the damage, as

$$\sigma = \rho\frac{\partial\psi}{\partial\varepsilon} = \widetilde{\mathbf{E}}(\mathbf{D}) : \varepsilon, \tag{5.43}$$

where

$$\rho\psi = \frac{1}{2}\varepsilon : \widetilde{\mathbf{E}}(\mathbf{D}) : \varepsilon = \widetilde{\mu}(\mathbf{D})\,\varepsilon' : \varepsilon' + \frac{1}{2}\widetilde{\kappa}(\mathbf{D})\,(\mathrm{tr}\,\varepsilon)^2 - \kappa_0\,\mathbf{D}' : \varepsilon'\,\mathrm{tr}\,\varepsilon + \frac{1}{2}h\,(\mathrm{tr}\,\mathbf{D})^4\,\varepsilon' : \left(\mathbf{D}' * \mathbf{D}'\right) : \varepsilon', \tag{5.44}$$

is a polynomial of simple and joint invariants of the state variables, *i.e.*, of the strain and damage tensors. It details as

$$\rho\psi(\varepsilon,\mathbf{D}) = \left(\mu_0 - \frac{1}{4}\kappa_0\,\mathrm{tr}\,\mathbf{D} + \frac{1}{4}\left(\kappa_0 - 2\mu_0\right)\mathbf{D} : \mathbf{D} + m\left(\mathbf{D} : \mathbf{D} - \mathrm{tr}\left(\mathbf{D}^3\right)\right)\right)\varepsilon' : \varepsilon'$$
$$+ \frac{1}{2}\kappa_0\left(1 - \frac{1}{2}\mathrm{tr}\,\mathbf{D}\right)(\mathrm{tr}\,\varepsilon)^2 - \kappa_0\,\mathbf{D}' : \varepsilon'\,\mathrm{tr}\,\varepsilon + \frac{1}{2}h\,(\mathrm{tr}\,\mathbf{D})^4\,\varepsilon' : \left(\mathbf{D}' * \mathbf{D}'\right) : \varepsilon'. \tag{5.45}$$

Using the definition of the harmonic product in Equation (2.27), this state potential can be rewritten as

$$\rho\psi(\varepsilon,\mathbf{D}) = \left(\mu_0 - \frac{1}{4}\kappa_0\,\mathrm{tr}\,\mathbf{D} + \frac{1}{4}\left(\kappa_0 - 2\mu_0\right)\mathbf{D} : \mathbf{D} + m\left(\mathbf{D} : \mathbf{D} - \mathrm{tr}\left(\mathbf{D}^3\right)\right) - \frac{1}{4}h\,(\mathrm{tr}\,\mathbf{D})^4\,\mathbf{D}' : \mathbf{D}'\right)\varepsilon' : \varepsilon'$$
$$+ \frac{1}{2}\kappa_0\left(1 - \frac{1}{2}\mathrm{tr}\,\mathbf{D}\right)(\mathrm{tr}\,\varepsilon)^2 - \kappa_0\,\mathbf{D}' : \varepsilon'\,\mathrm{tr}\,\varepsilon + \frac{1}{2}h\,(\mathrm{tr}\,\mathbf{D})^4\left(\mathbf{D}' : \varepsilon'\right)^2. \tag{5.46}$$

Thermodynamic force associated with damage. The thermodynamic force associated with the damage is then the symmetric second-order tensor

$$\mathbf{Y} = -\rho\frac{\partial\psi}{\partial\mathbf{D}}$$
$$= \left(\frac{1}{4}\kappa_0\mathbf{1} + \frac{1}{2}\left(2\mu_0 - \kappa_0\right)\mathbf{D} + m\left(3\mathbf{D}^2 - 2\mathbf{D}\right) + h\,(\mathrm{tr}\,\mathbf{D})^3\left(\frac{1}{2}(\mathrm{tr}\,\mathbf{D})\,\mathbf{D}' + \left(\mathbf{D}' : \mathbf{D}'\right)\mathbf{1}\right)\right)\varepsilon' : \varepsilon' \tag{5.47}$$
$$+ \frac{1}{4}\kappa_0\,(\mathrm{tr}\,\varepsilon)^2\,\mathbf{1} + \kappa_0\,(\mathrm{tr}\,\varepsilon)\,\mathbf{D}' - h\,(\mathrm{tr}\,\mathbf{D})^4\left(\mathbf{D}' : \varepsilon'\right)\varepsilon'.$$

Parameters of the model. The parameters of the final model are the initial shear modulus μ_0, the initial bulk modulus κ_0, the (optional) shear-damage coupling parameter $m = \frac{1}{2}\left(\kappa_0 + 2\mu_0\right)c_3$ and the harmonic pre-factor h. They are summarized, with their value identified from the dataset, in Table 5.2.

◯ **Remark 5.8** *At this point, it seems necessary to point out that, for certain values of the parameters, this state model might not be positive definite for all possible damage values. The damage tensors for which the effective elasticity tensor is not positive definite are not reached in our dataset. It means no damage evolution enables reaching regions (in the damage space) where the effective elasticity tensor is negative definite. This problem is discussed in more detail in the next chapter.*

Name	Symbol	Value in GPa
Initial shear modulus	μ_0	19.4
Initial bulk modulus	κ_0	30
Non-linear shear-damage coupling parameter	m	3.54
Harmonic pre-factor	h	18.8

Table 5.2 • Summary of the constitutive parameters (and their value for the 76 356 elasticity tensors dataset).

3 Assessment of the models

This section provides assessments over the dataset of several modeling choices —summarized in the previous section— for the coupling bi-dimensional elasticity-anisotropic damage:

- simplified modeling with vanishing parameters $m = 0$ and/or $h = 0$, and

- full modeling with non-zero parameters $m = 3.54$ GPa and/or $h = 18.8$ GPa.

Each computed (micro-cracked) elasticity tensor $\mathbf{E}_i$ from the dataset has an isotropic part $\mathbf{Iso}_i$, a dilatation part $\mathbf{Dil}_i$ and a harmonic part $\mathbf{H}_i$ (determined by harmonic decomposition in Equation (2.18)). For the assessments, the damage $\mathbf{D} = \mathbf{D}_i$ is taken as equal to the damage variable $\mathbf{D}_i = \mathbf{1} - \mathbf{d}_i / 2\kappa_0 = \mathbf{1} - \mathbf{E}_i : \mathbf{1}/2\kappa_0$ measured for $\mathbf{E}_i$ in the dataset.

To be quantitative, the error between a tensor $\mathbf{E}_i$ of the dataset and the anisotropic damage modeling $\widetilde{\mathbf{E}} = \widetilde{\mathbf{E}}(\mathbf{D})$ is defined as

$$\left\| \mathbf{E}_i - \widetilde{\mathbf{E}}(\mathbf{D}_i) \right\| = \sqrt{\|\mathbf{Iso}_i - \widetilde{\mathbf{Iso}}(\mathbf{D}_i)\|^2 + \|\mathbf{Dil}_i - \widetilde{\mathbf{Dil}}(\mathbf{D}_i)\|^2 + \|\mathbf{H}_i - \widetilde{\mathbf{H}}(\mathbf{D}_i)\|^2}, \qquad (5.48)$$

where, by the formulas of the previous section,

$$\begin{aligned}
\widetilde{\mathbf{Iso}}(\mathbf{D}) &= 2\widetilde{\mu}(\mathbf{D})\,\mathbf{J} + \widetilde{\kappa}(\mathbf{D})\,\mathbf{1} \otimes \mathbf{1}, \\
\widetilde{\mathbf{Dil}}(\mathbf{D}) &= -\kappa_0\left(\mathbf{1} \otimes \mathbf{D}' + \mathbf{D}' \otimes \mathbf{1}\right), \\
\widetilde{\mathbf{H}}(\mathbf{D}) &= h\,(\mathrm{tr}\,\mathbf{D})^4\,\mathbf{D}' \ast \mathbf{D}'.
\end{aligned} \qquad (5.49)$$

Since the fourth-order isotropic (**Iso**), dilatation (**Dil**) and harmonic (**H**) parts are orthogonal (see Equation (2.20)), the errors associated with each part are uncorrelated. It implies that the parameter m influences the isotropic part only and that the parameter h influences the harmonic part only.

Q **Remark 5.9** *Note that the dilatation part has no modeling error since*

$$\widetilde{\mathbf{Dil}}(\mathbf{D}_i) = -\kappa_0\left(\mathbf{1} \otimes \mathbf{D}'_i + \mathbf{D}'_i \otimes \mathbf{1}\right) = \mathbf{Dil}(\mathbf{E}_i). \qquad (5.50)$$

Q **Remark 5.10** *In this section, duplicated tensors during a loading (two successive tensors with no crack growth) are filtered out to construct the histogram plots.*

3.1   Assessment of the isotropic part model

Let us first analyze the contribution of the isotropic part to the modeling error. A histogram of the relative error on the isotropic part $\|\mathbf{Iso}_i - \widetilde{\mathbf{Iso}}(\mathbf{D}_i)\| / \|\mathbf{E}_0\|$ is plotted in Figure 5.7a. The relative error range $[0, 1]$ is discretized in 500 intervals for this histogram and all the following ones. It shows that both modeling, with vanishing value $m = 0$ and with non-zero value $m = 3.54$ GPa, can represent well the isotropic part of all micro-cracked tensors in the dataset (with a relative error below 10%). Figure 5.7b provides the Cumulative Distribution Function
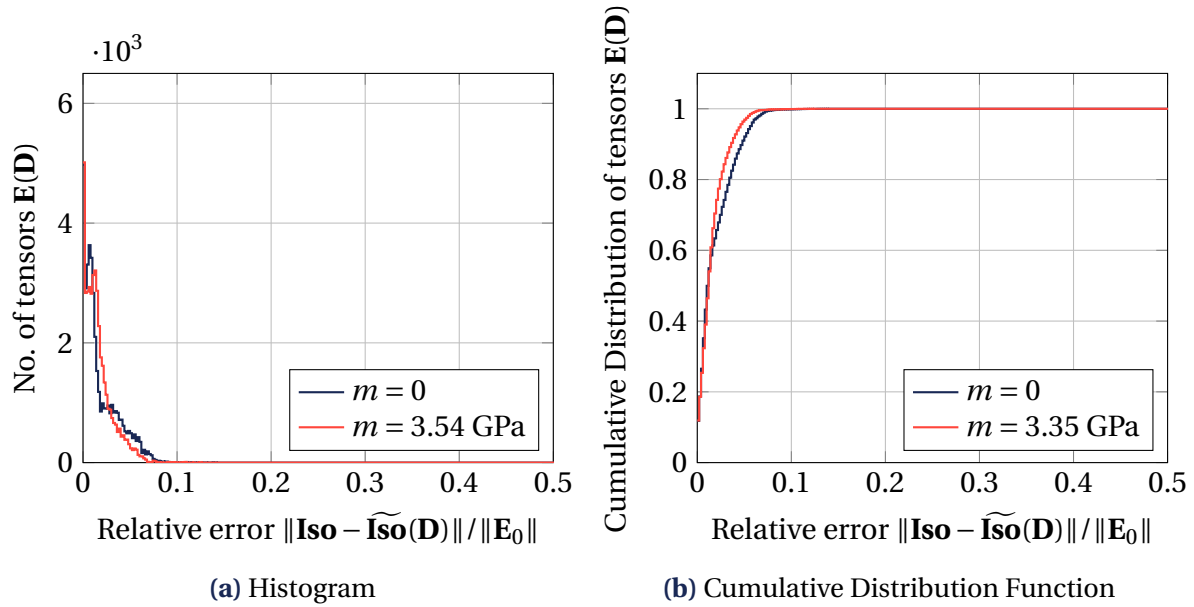

(a) Histogram

(b) Cumulative Distribution Function

Figure 5.7 • Histograms and Cumulative Distribution Functions of the relative error on the isotropic part over the dataset for both values of the parameter m (results independent of the harmonic pre-factor h).

associated with this histogram. The numbers of tensors in each interval are cumulated with the relative error going from 0 to 1. Afterward, the cumulated number is divided by the total number of tensors to define the Cumulative Distribution Function (such that it reaches 1 when the error is 1). This plot shows that most isotropic parts are modeled with an error below 10%.

Percentile (error)	1 %	2 %	5 %	10 %
$m = 0$	50.0 %	65.7 %	92.2 %	99.9 %
$m = 3.54$ GPa	46.4 %	74.3 %	97.0 %	99.9 %

Table 5.3 • Proportion of tensors with a relative error on the isotropic part below 1%, 2%, 5% and 10% for both value of m (results independent of the harmonic pre-factor h).

More quantitative results are provided in Table 5.3, which focuses on different percentiles of the histogram. Each percentile corresponds to a percentage of elasticity tensors $\mathbf{E}_i$ with a modeling error — on the isotropic part — below the given threshold. For instance, the

5-percentile gives the proportion of tensors modeled with an error below 5%. This table is obtained from the Cumulative Distribution of the error by fixing the error (in the x-axis) and reading the associated cumulative proportion of tensors (in the y-axis). The Table 5.3 shows that the case $m = 3.54$ GPa models 74.3% of the effective elasticity tensor with less than 2% of error, whereas the case $m = 0$ models only 65.7% of them. Thus, the case $m = 3.54$ GPa provides a slightly more accurate model of the isotropic part than the simplified case $m = 0$. However, it requires the introduction of the additional material parameter $m = \frac{1}{2}(\kappa_0 + 2\mu_0) c_3$. As the gain in accuracy is small compared to the increase of modeling/identification complexity by adding a parameter, we propose to retain $m = 0$ (*i.e.*, Equation (5.23)) for the modeling of the coupling of the shear modulus with anisotropic damage.

3.2 Assessment of the harmonic part model

Let us now analyze the contribution of the harmonic part to the modeling error. Figure 5.8a

(a) Histogram

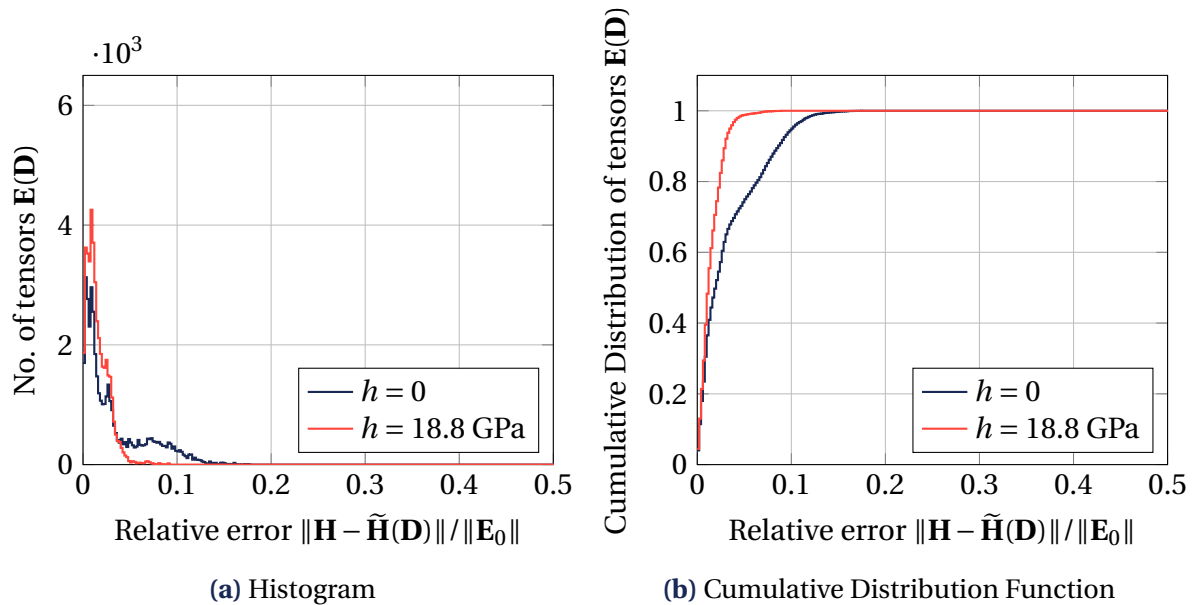**(b)** Cumulative Distribution Function

Figure 5.8 • Histograms and Cumulative Distributions Functions of the relative error on the harmonic part over the dataset for both values of the harmonic pre-factor h (results independent of the parameter m).

shows the histogram of the relative error on the harmonic part $\|\mathbf{H}_i - \widetilde{\mathbf{H}}(\mathbf{D}_i)\| / \|\mathbf{E}_0\|$. It indicates that the case $h = 18.8$ GPa substantially improves the modeling compared to neglecting the harmonic part (case $h = 0$). Note that for $h = 18.8$ GPa, the contribution of the error on the harmonic part is at the same level as the contribution due to the isotropic part. Figure 5.8b provides the Cumulative Distribution Function of this histogram. It shows that setting $h = 18.8$ GPa enables predicting most harmonic parts of the dataset with an error below 5%. In contrast, the errors associated with the case $h = 0$ reach around 12% before modeling most harmonic parts.

More quantitative results are provided in Table 5.4, where different percentiles of the histogram are given (as in Table 5.3). Once again, a percentile corresponds to the percentage

Percentile (error)	1%	2%	5%	10%
$h = 0$	36.5%	52.1%	75.0%	95.0%
$h = 18.8$ GPa	48.3%	74.5%	98.8%	100%

Table 5.4 • Proportion of tensors with an error on harmonic part below 1%, 2%, 5% and 10% for both values of the harmonic pre-factor h (results independent of the parameter m).

of elasticity tensors with a modeling error – on the harmonic part – below a given threshold. It shows that setting $h = 18.8$ GPa enables the modeling of most harmonic parts of the dataset (98.8%) with an error below 5%, which is far higher than in the case for $h = 0$ (75.0 %). Thus, the case $h = 18.8$ GPa, thus using Equation (5.38) instead of neglecting the harmonic part ($h = 0$), significantly improves the accuracy of the modeling.

3.3   Assessment of the complete elasticity tensor model

Let us complete the previous independent results by analyzing the modeling error on the whole elasticity tensor. Below, we gradually add each ingredient of the modeling (the isotropic part, then the dilatation part, then the harmonic part) up to the complete modeling $\widetilde{\mathbf{E}}(\mathbf{D})$. It allows us to quantify the exact contribution of the different parts of the anisotropic damage model.

(a) Histogram
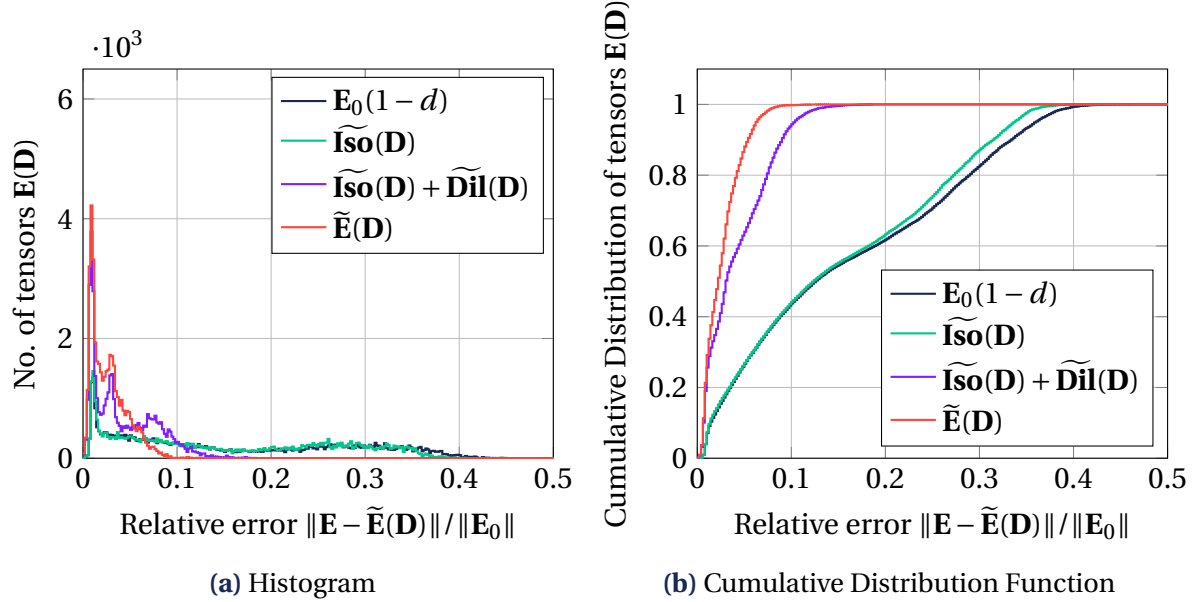
(b) Cumulative Distribution Function

Figure 5.9 • Histogram and Cumulative Distribution Functions of the total relative error on the effective elasticity tensors over the dataset for $m = 0$ and $h = 18.8$ GPa.

Figure 5.9 shows the relative error's histogram and Cumulative Distribution Function on the effective elasticity tensor for the different modelings. Different percentiles of the histogram are provided in Table 5.5. The first line of the table,

$$\mathbf{E}_0(1 - d), \qquad d = 1 - \|\mathbf{E}\| / \|\mathbf{E}_0\|, \tag{5.51}$$

Percentile (error)	1%	2%	5%	10%	20%	30%	40%
$(1-d)\mathbf{E}_0$	7.14%	13.3%	26.7%	43.8%	61.8%	82.7%	99.4%
$\widetilde{\mathbf{Iso}}(\mathbf{D})$	7.45%	14.2%	27.0%	44.2%	63.3%	87.2%	99.9%
$\widetilde{\mathbf{Iso}}(\mathbf{D}) + \widetilde{\mathbf{Dil}}(\mathbf{D})$	25.6%	36.6%	64.0%	94.4%	100%	100%	100%
$\widetilde{\mathbf{E}}(\mathbf{D})$	27.2%	47.8%	88.1%	99.8%	100%	100%	100%

Table 5.5 • Proportion of tensors with a total error below 1%, 2%, 5%, 10%, 20%, 30% and 40%.

corresponds to an isotropic model (with scalar damage variable D) as it can be found in the classic literature (Mazars, 1984; Lemaitre & Chaboche, 1985; Lemaitre, 1992). The second line of the table $\widetilde{\mathbf{Iso}}(\mathbf{D})$ corresponds to the isotropic part only of the proposed modeling ($\widetilde{\mathbf{E}} = \widetilde{\mathbf{Iso}}(\mathbf{D})$ with $m = 0$). The third line $\widetilde{\mathbf{E}} = \widetilde{\mathbf{Iso}}(\mathbf{D}) + \widetilde{\mathbf{Dil}}(\mathbf{D})$ (with $m = 0$ still, and $h = 0$) adds the modeling of the dilatation part, and the fourth line considers the whole damage model $\widetilde{\mathbf{E}} = \widetilde{\mathbf{Iso}}(\mathbf{D}) + \widetilde{\mathbf{Dil}}(\mathbf{D}) + \widetilde{\mathbf{H}}(\mathbf{D})$ with $m = 0$ and $h = 18.8$ GPa.

   Both isotropic models provide a poor estimation of the elasticity tensors of the dataset. This outcome was expected due to the predicted effective elasticity tensors being isotropic. However, they should be anisotropic, as shown in Chapter 4. Adding the dilatation part to the model, *i.e.,* modeling anisotropic damage, clearly improves its accuracy as it enables to account for anisotropy induced by micro-cracking. Accounting for the harmonic part (by the second-order damage tensor $\mathbf{D}$ still) also improves the modeling, bringing the proportion of the effective elasticity tensors with less than 5% of error from 64.0% of the dataset (for the model with $h = 0$, *i.e.* $\widetilde{\mathbf{H}}(\mathbf{D}) = 0$) to 88.1% of the dataset(for $h = 18.8$ GPa).

   Let us finally check whether it is possible or not to model the influence of micro-cracking on the elasticity tensor up to high levels of damage. This modeling feature is particularly challenging to obtain from a micro-mechanics homogenization approach (Kachanov, 1993; Ponte Castañeda & Willis, 1995; Cormery & Welemane, 2010; Dormieux & Kondo, 2016).

Percentile (error)	1%	2%	5%	10%	20%	30%	40%
$(1-d)\mathbf{E}_0$	1.26%	4.28%	15.7%	29.4%	39.8%	69.1%	98.9%
$\widetilde{\mathbf{E}}(\mathbf{D})$	10.1%	30.0%	78.9%	99.6%	100%	100%	100%

Table 5.6 • Proportion of highly damaged tensors ($D_{\max} > 0.7$) with a total error below 1%, 2%, 5%, 10%, 20%, 30% and 40%.

In Figure 5.10, we reproduce the histogram and Cumulative Distribution of relative errors with a filter to keep only the elasticity tensors associated with high damage value ($D_{\max} = \max(D_1, D_2) > 0.7$). The differences between the filtered and the unfiltered distributions correspond to the relative errors for tensors with low damage (diffuse micro-cracking). The histogram in Figure 5.10 shows that isotropic models do not correctly describe the effective elasticity tensors with high damage values. Table 5.5 shows that only 15.7% of highly damaged tensors (with $D_{\max} > 0.7$) are reconstructed with an error below 5% (versus 26.7% for the whole dataset). It indicates that the isotropic model does not predict the highly damaged
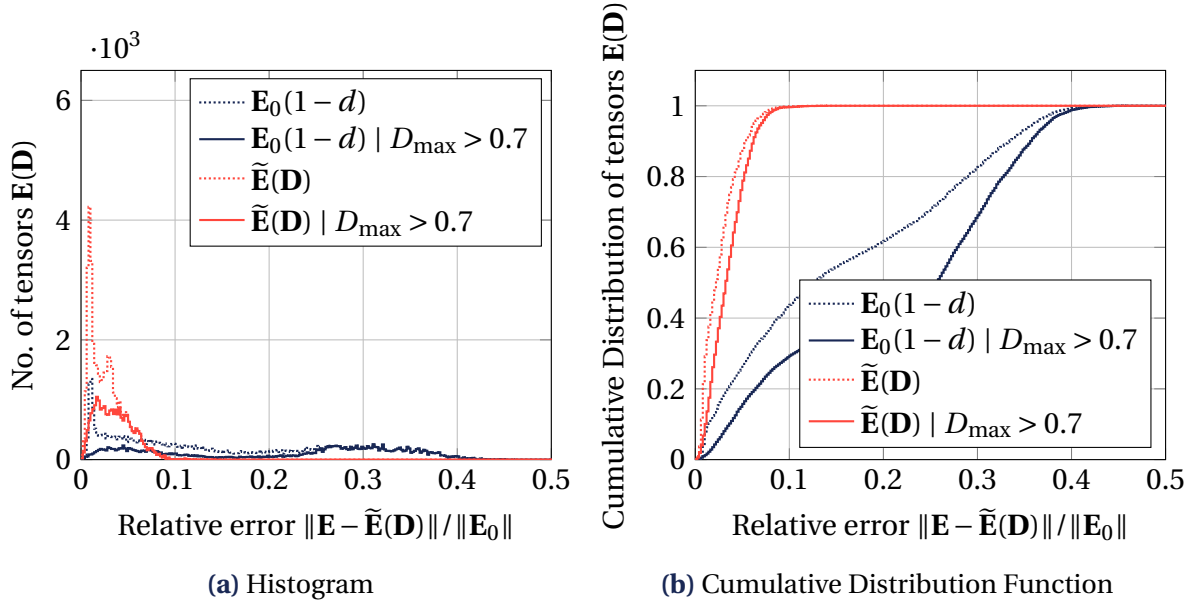
(a) Histogram

(b) Cumulative Distribution Function

Figure 5.10 • Histograms and Cumulative Distribution Functions of total error for large values of damage. The histogram and cumulative distribution of total error over the elasticity tensors in the dataset is also reproduced.

tensors well; thus, it does not accurately model the strong micro-cracks interactions stage. The complete anisotropic damage modeling $\widetilde{\mathbf{E}} = \widetilde{\mathbf{Iso}}(\mathbf{D}) + \widetilde{\mathbf{Dil}}(\mathbf{D}) + \widetilde{\mathbf{H}}(\mathbf{D})$ (with $m = 0$ and $h = 18.8$ GPa) is able to model 78.9% of the tensors with an error below 5% (and 99.6% of the tensors with an error below 10%). It thus provides an accurate damage state coupling for the effective elasticity tensor, even for highly damaged specimens. This result emphasizes the strength of the proposed approach based on a beam-particle discrete element description to model the anisotropic damage in quasi-brittle materials.

4   Illustration of the state model accuracy: Non-proportional loading analysis

To illustrate the ability of the model to represent the coupling between anisotropic damage and effective elastic properties, let us detail both the beam-particle model response and the anisotropic damage $\widetilde{\mathbf{E}} = \widetilde{\mathbf{E}}(\mathbf{D})$ response for the Periodic Boundary Condition (PBC) "tension→tension" loading of Table 4.1 of Chapter 4.

Q **Remark 5.11** *A similar analysis has been carried out for a periodic (PBC) "shear→tension" loading Loiseau et al. (2023a).*

Damaging loading.   The evolution of strain $\boldsymbol{\varepsilon}$ and damage $\mathbf{D}$ —computed by the beam-particle model— for this loading are represented in Figure 5.11. It is composed of two stages. A periodic (PBC) tension loading along the direction $\boldsymbol{e}_1$ is applied during the first stage until load step 50. Then, in the second stage, the tension loading is maintained while another tension is applied along the direction $\boldsymbol{e}_2$. Figure 5.12 shows the micro-cracking progression
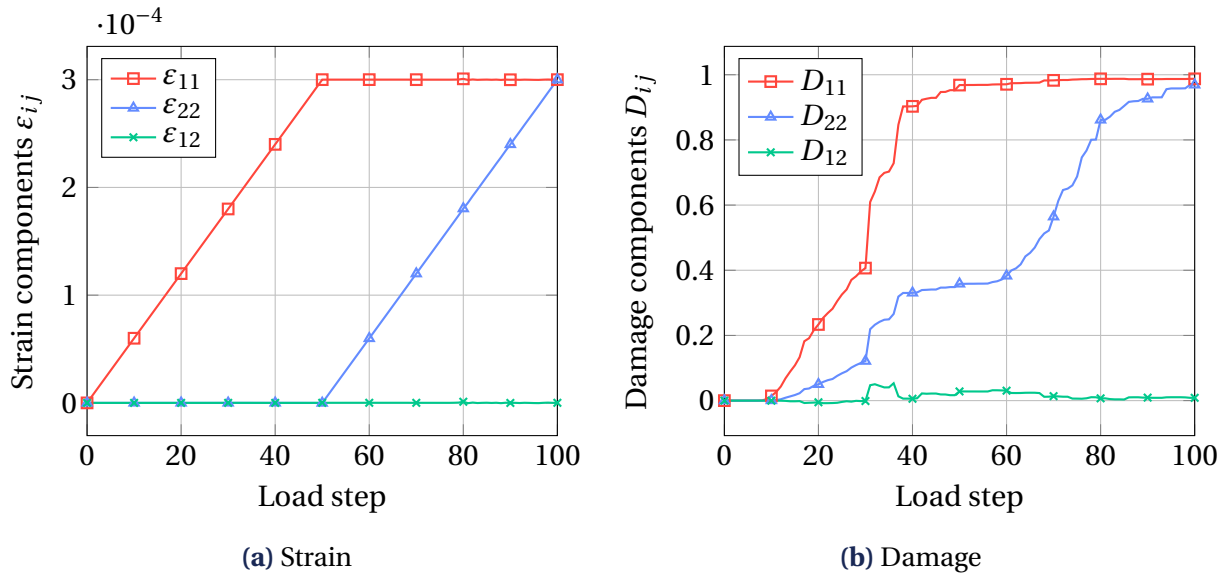
(a) Strain

(b) Damage

Figure 5.11 • Evolution of strain and damage during the periodic (PBC) "tension→tension" loading.
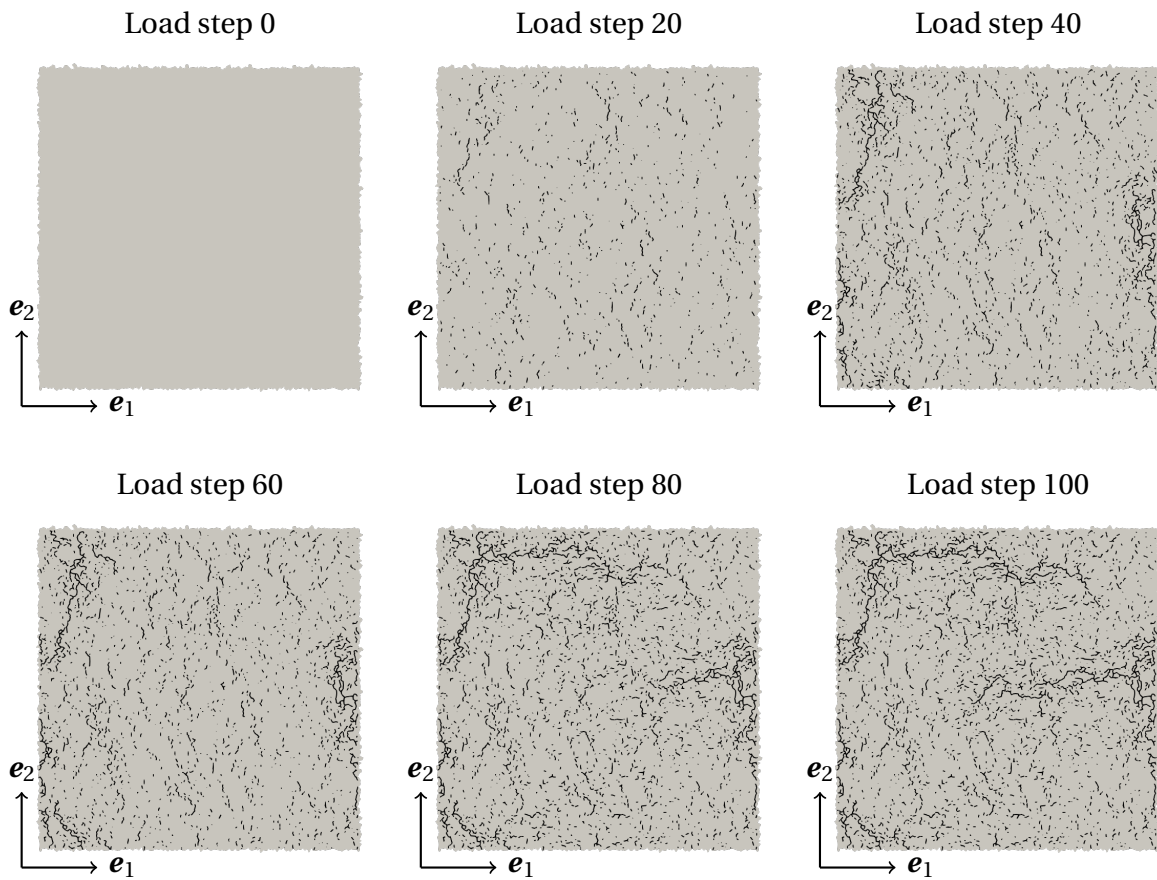

Figure 5.12 • Evolution of micro-cracking during the periodic "tension→tension" loading (reproduced from Chapter 4).

at load steps 0, 20, 40, 60, 80, and up to the final step 100. At the start of the loading, the area element is uncracked. The first micro-cracking localization (orthogonal to e_1) between step 20 and 40 corresponds to the significant increase of damage D_{11} around the load step 30. The second micro-cracking localization (orthogonal to e_2) leads to the significant increase of damage D_{22} (between steps 60 and 80).

The periodic (PBC) tension→tension non-proportional loading case is used to investigate the different damage state couplings, by comparing them to the reference discrete element data: an elasticity–damage coupling with isotropic damage variable d (by $\boldsymbol{\sigma} = \mathbf{E}_0(1-d) : \boldsymbol{\varepsilon}$) and elasticity–anisotropic damage couplings with damage variable $\mathbf{D}$ (by $\boldsymbol{\sigma} = \widetilde{\mathbf{E}} : \boldsymbol{\varepsilon}$),

- the first one $\widetilde{\mathbf{E}} = \widetilde{\mathbf{Iso}}(\mathbf{D}) + \widetilde{\mathbf{Dil}}(\mathbf{D})$, with material parameters $m = 0$ and $h = 0$,

- the second one $\widetilde{\mathbf{E}} = \widetilde{\mathbf{Iso}}(\mathbf{D}) + \widetilde{\mathbf{Dil}}(\mathbf{D}) + \widetilde{\mathbf{H}}(\mathbf{D})$, with material parameters $m = 3.35$ GPa and $h = 17$ GPa.

Thanks to the orthogonality of the harmonic decomposition terms, it covers all the possible combinations of parameters m and h.

Stress history.   Let us first illustrate the proposed model by calculating the stress evolution during a non-proportional loading. We consider that the state of the material, *i.e.* strain $\boldsymbol{\varepsilon}$ and damage $\mathbf{D}$, is known exactly at each load step. The proposed anisotropic damage state model is applied to recover the stress evolution during the periodic (PBC) "tension→tension" loading. Figure 5.13 shows that a simple isotropic damage model (black line) is not sufficient to correctly predict the macroscopic stress state of the material. Even in the (early) diffuse micro-cracking stage, the stress component σ_{11} are overestimated compared to the reference values (red line). After the first localization, the reference stress σ_{11} drops, whereas the stress σ_{11} predicted with the isotropic model stagnates for a few load steps and then grows. During the second stage of the loading, the stress σ_{11} from the isotropic model is completely mispredicted. Also note that the slope of the component σ_{11} between steps 50 and 60 is underestimated by the isotropic model. On the other hand, the proposed anisotropic damage modeling provides an accurate stress state prediction up to the very end of the loading, close to the discrete element reference for both values $h = 0$ and $h = 18.8$ MPa.

Effective elasticity tensor evolution.   To complete the analysis, we provide in Figure 5.14, for the different models, the history of the six harmonic components of the effective elasticity tensor, namely $\widetilde{\kappa}$, $\widetilde{\mu}$, $\widetilde{\mathbf{d}}' = (\widetilde{d}'_{ij})$ and $\widetilde{\mathbf{H}} = (\widetilde{H}_{ijkl})$. The components of the reference discrete element elasticity tensors are reported as red lines. As the damage $\mathbf{D} = \mathbf{1} - \mathbf{E} : \mathbf{1}/2\kappa_0$ is known, both the bulk modulus $\widetilde{\kappa}$ and the deviatoric part of the dilatation tensor $\widetilde{\mathbf{d}}'$ are exactly modeled (as explained in Section 1). The shear modulus is correctly predicted by both $m = 0$ and $m = 3.54$ GPa cases, close to each other. This tension→tension non-proportional loading leads to the significant growth of the dilatation part, which is neglected by the isotropic model. It also induces the growth of the harmonic part, which is neglected by both the isotropic model and the proposed model when $h = 0$. Yet, setting $h = 18.8$ GPa provides a good modeling of the harmonic part.
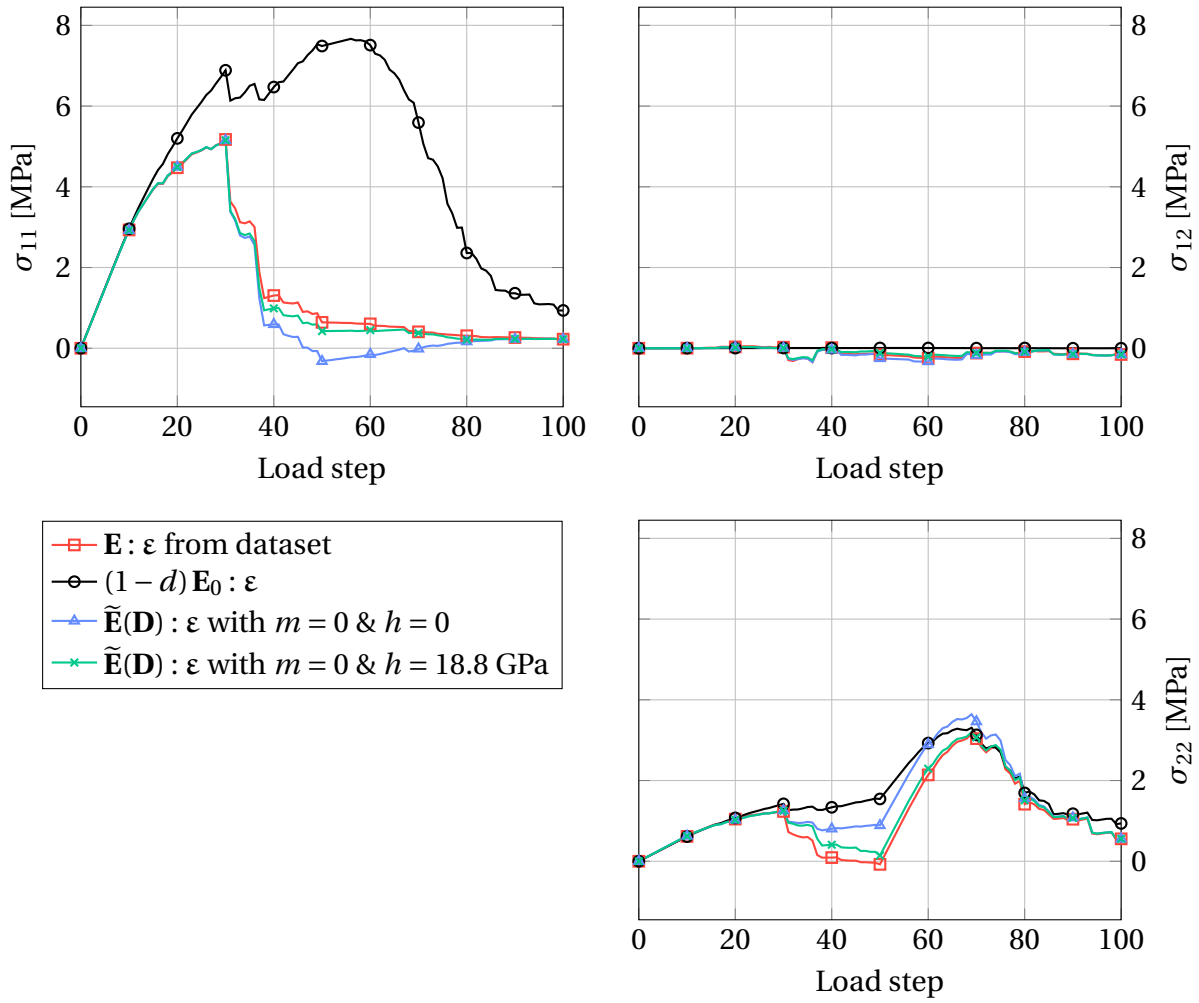
Figure 5.13 • Estimation of the stress tensor from the (exact) state during the periodic (PBC) "tension→tension" loading. In this plot, the green line is with $m = 0$.
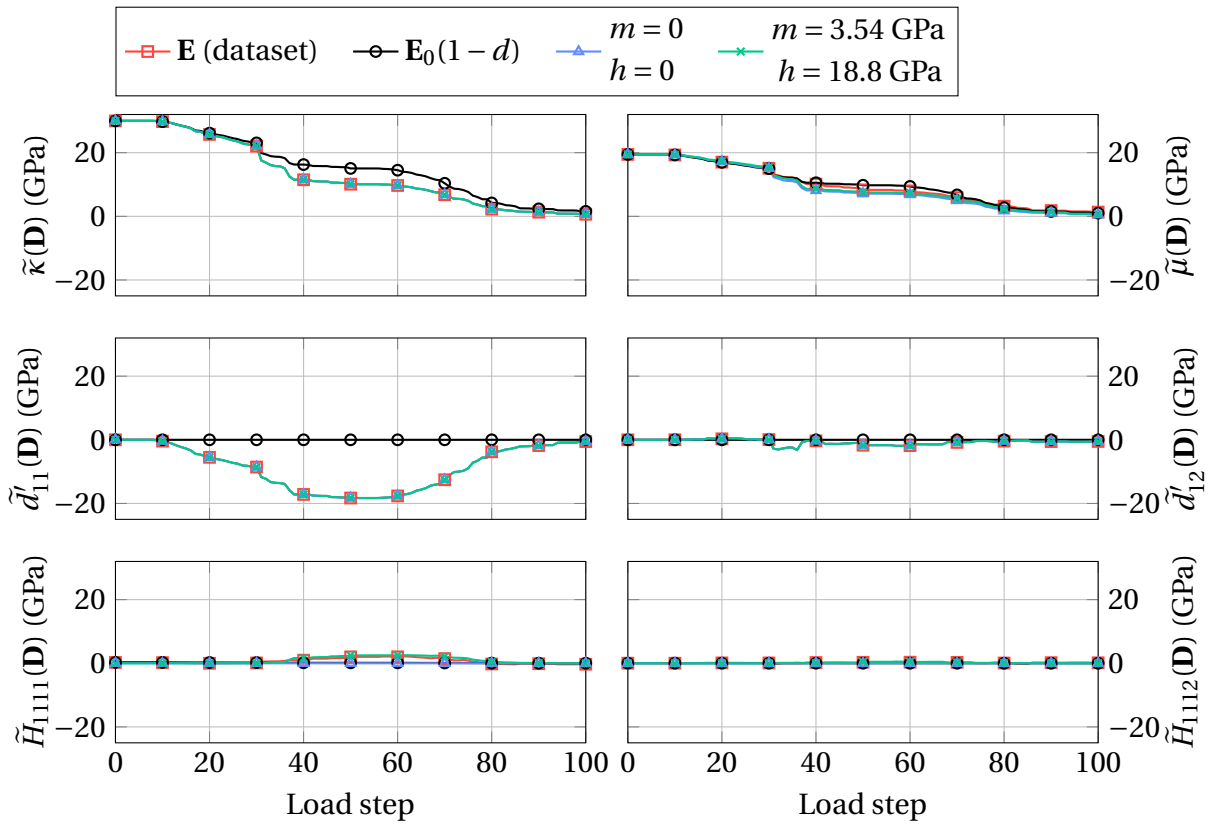
Figure 5.14 • Comparison of the evolutions of elasticity tensors obtained via the two modelings ($m = h = 0$ in blue, and $m = 3.54$ GPa, $h = 18.8$ GPa in green) with the reference data (**E**, in red) during the periodic (PBC) "tension→tension" loading.
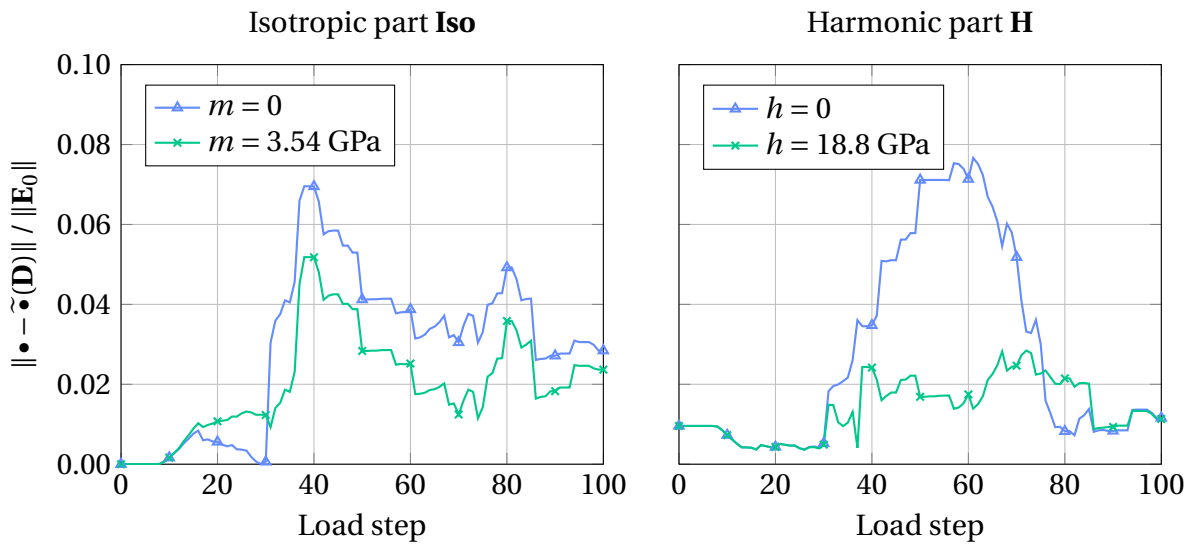

Figure 5.15 • Evolution of relative errors during the non-proportional periodic (PBC) "tension→tension" loading.

To conclude, Figure 5.15 displays the relative errors associated with the isotropic and harmonic parts during this loading. For $h = 0$, the most significant part of the error is due to the modeling of the harmonic part. Accounting for the harmonic part in the model halves the error on the harmonic part.

🖋 Summary of the Chapter

This chapter aims to develop an anisotropic damage state model. We employed an orthotropic reconstruction of the effective elasticity tensor (from covariants) based on the harmonic decomposition to ease the formulation. It shifts the formulation process from modeling the entire elasticity tensor to its harmonic components. First, the damage variable is introduced to represent the micro-cracking. It is based on the dilatation tensor, a covariant of the effective elasticity tensor. The damage variable is itself a covariant of the effective elasticity tensor. This choice of damage variable enables us to model exactly two (out of four) harmonic components: the bulk modulus and the deviatoric part of the dilation tensor. By analyzing the dataset, we proposed a model for the effective shear modulus as a function of damage. This model introduces an optional parameter, the non-linear shear-damage coupling parameter. We then applied a sparse regression to fit a polynomial of damage invariants to the dataset to obtain a model for the harmonic part. This model also introduces a parameter, the harmonic pre-factor. The effective elasticity tensor model is assessed by comparison to the dataset. It shows that the proposed model of the effective elasticity tensor is well-predicted, thus showing that a second-order tensor for this dataset accurately represents the micro-cracking. The necessity of considering damage-induced anisotropy in the model is also emphasized.

6

Formulation of an evolution model

This chapter presents the formulation of a non-standard damage evolution law aiming at representing the continuous (macroscopic) damage evolution computed from the discrete area elements. The cross-modeling process to formulate the model is composed of three steps. The first step aims to determine the initial yield surface (or criterion function) of discrete area elements. The initial yield surface of multiple area elements is measured using an efficient method proposed in this work. The equivalent strain is then defined by fitting a polynomial of strain invariants to the measured yield surface. The second step is to analyze the damage evolution during some loading cases applied with periodic strain boundary conditions. This analysis identifies and highlights the phenomena occurring during the degradation process, which need to be considered in the model. Subsequently, a macroscopic damage evolution model is proposed.

The state model proposed in the Chapter 5 must be completed with a damage evolution law to formulate an anisotropic damage model. The damage evolution model describes, given the state of the area element (here, described by strain and damage), (1) whether the damage grows in the material, and (2) how the damage evolves (when it evolves). We will first focus on determining the damage criterion in order to address the first question. This step will be carried out in two stages. First, a method to efficiently measure the yield surface of a discrete area element is proposed and applied to multiple area elements. Then, we will exploit the results to define a damage criterion function, particularly the equivalent strain. Then, the second stage consists in defining how the damage evolves. A damage evolution law is proposed after investigating the damage evolution in the reference dataset. Different changes of damage variables are compared to naturally bound the principal damages to 1 and to ease the modeling. A damage evolution law, based on the introduced variable, is then proposed and compared to the reference damage evolution from the dataset. Finally, non-local damage is briefly discussed to show how the proposed model can be adapted to structures.

1 Determination of the damage criterion function from virtual testing

Let us first focus on the determination of the initial damage criterion function at zero damage $f = f(\varepsilon, \mathbf{D} = 0)$. More precisely, we focus on the definition of the equivalent strain $\varepsilon_{\text{eq}} = \varepsilon_{\text{eq}}(\varepsilon)$ (in the spirit of Mazars (1984), de Vree et al. (1995), and Ragueneau et al. (2008)) associated with a bi-dimensional discrete (beam-particle) area element. The equivalent strain ε_{eq} is assumed to be a function of the strain tensor (to be determined). The criterion function f defines the elasticity domain as

$$f = \varepsilon_{\text{eq}} - \varepsilon_D < 0 \;\rightarrow\; \text{elasticity.} \tag{6.1}$$

As in the previous Chapter, our cross-modeling approach consists in applying Periodic Boundary Condition (PBC) to the area element, with (multi-axial) applied strains. One then measures (or calculates) when damage initiates. The first step is to define the criterion corresponding to the onset of damage (*i.e.,* to "when the damage starts") for a given loading on an area element. Once the criterion is defined, we have to measure the elasticity limit locus by applying loadings in different directions. To make this procedure efficient, we want to carry out the measurement with as few simulations as possible.

1.1 Measurement of the yield surface of a beam-particle area element

Micro-cracking criterion. First, we need to define "when the damage starts" in a (discrete) area element. To achieve that, we must first define what means the onset of macroscopic damage from the beam-particle model. Several definitions could be considered, such as a significant loss of linearity in the macroscopic stress-strain relationship (as done in experiments) or a significant growth of the damage variable (since we can compute it). Here, as a first approach, we choose to define the damage criterion based on the first appearing micro-crack. Recall that the failure criterion f_b of a beam b (between particles p and q) is

$$f_b = \frac{\varepsilon_{pq}}{\varepsilon_{pq}^{\text{cr}}} + \frac{|\Delta\theta_{pq}|}{\Delta\theta_{pq}^{\text{cr}}} > 1, \qquad \varepsilon_{pq} = \|\boldsymbol{u}_p - \boldsymbol{u}_q\|, \qquad \Delta\theta_{pq} = \theta_p - \theta_q, \tag{6.2}$$

where ε_{pq} is the beam extension and $\varepsilon_{pq}^{\text{cr}}$ its associated failure threshold, $\Delta\theta_{pq}$ is the difference of particle rotation and $\Delta\theta_{pq}^{\text{cr}}$ its associated failure threshold. As we want to determine when the first beam breaks, we must determine which beam will reach the failure criterion first.

A fast method to measure the yield surface. Let us consider that a periodic boundary conditions strain proportional loading ε_{imp} with a norm $\|\varepsilon_{\text{imp}}\|$ is applied to the area element. The norm must be sufficiently small so that the behavior remains linear (in our case so that no beam breaks). To find the first broken beam b^*, one must determine the first beam to reach this criterion. Thus, the beam b^* with the largest failure criterion function f_{b^*} is then

$$b^* = \underset{b}{\arg\max}\, f_b. \tag{6.3}$$

As the behavior remains linear, the displacements and rotations of each particle p are proportional to the norm of the imposed strain

$$\boldsymbol{u}_p = \|\varepsilon_{\text{imp}}\|\boldsymbol{u}_p^{(1)}, \qquad \theta_p = \|\varepsilon_{\text{imp}}\|\theta_p^{(1)}, \tag{6.4}$$

where $\bullet^{(1)}$ denotes the displacement/rotation for unitary loading (with a norm $\|\varepsilon_{\text{imp}}\| = 1$ and no beam breaking, *i.e.* an elastic behavior), which only depend on the loading orientation. Only monotonic proportional loadings are considered here, so the factor $\|\varepsilon_{\text{imp}}\|$ is assumed to be positive. Thanks to this proportionality property, the beam failure criterion function is a homogeneous function of the loading amplitude, *i.e.* of the norm of the imposed strain $\|\varepsilon_{\text{imp}}\|$, and can be rewritten

$$f_{b^*} = \|\varepsilon_{\text{imp}}\| f_{b^*}^{(1)}, \qquad f_{b^*}^{(1)} = \left(\frac{\varepsilon_{b^*}^{(1)}}{\varepsilon_{b^*}^{\text{cr}}} + \frac{|\Delta\theta_{b^*}^{(1)}|}{\Delta\theta_{b^*}^{\text{cr}}}\right) = \frac{f_{b^*}}{\|\varepsilon_{\text{imp}}\|}. \tag{6.5}$$

Finally, the first failing beam b^* breaks (and thus the macroscopic damage starts) when the criterion function attains $f_{b^*} = 1$. The associated strain ε_D is the yield strain (tensor)

$$\|\varepsilon_D\| f_{b^*}^{(1)} = 1 \implies \|\varepsilon_D\| = \frac{\|\varepsilon_{\text{imp}}\|}{f_{b^*}}, \text{ thus } \varepsilon_D = \|\varepsilon_D\|\frac{\varepsilon_{\text{imp}}}{\|\varepsilon_{\text{imp}}\|} = \frac{1}{f_{b^*}}\varepsilon_{\text{imp}} \tag{6.6}$$

where ε_{imp} is the imposed strain (such that no beam break) and f_* is the value of the highest failure criterion, *i.e.* the failure criterion associated to the first breaking beam. This method requires only one elastic resolution per loading direction to obtain the yield strain. It is thus an efficient technique to determine the yield surface of an area element.

Q **Remark 6.1** *This method also works for other types of simulation, as far as the mesoscale damage indicator (here, the beam failure criterion) is homogeneous in the loading amplitude.*

Application to an area element. Let us now apply this method to area elements. The first step is to discretize the imposed loading. As all possible strain loads can be diagonalized in their principal basis (as the strain is symmetric real), it can be parametrized as

$$\varepsilon_{\text{imp}}^{(k)} = \|\varepsilon_{\text{imp}}\| \begin{bmatrix} \cos\frac{2k\pi}{N_{\text{dir}}} & 0 \\ 0 & \sin\frac{2k\pi}{N_{\text{dir}}} \end{bmatrix}, \qquad k \in \{0, ..., N_{\text{dir}} - 1\}, \tag{6.7}$$
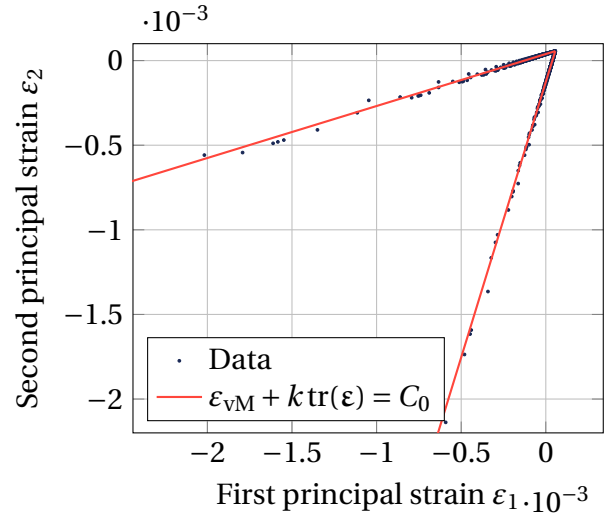
where N_{dir} is the number of loading directions. Here, we chose to use $N_{\text{dir}} = 256$ directions and a loading amplitude $\|\varepsilon_{\text{imp}}\| = 10^{-8}$.

Q **Remark 6.2** *Note that this parametrization works here because we consider the material to be initial isotropic. Otherwise, another strain parametrization where the principal basis of the loading rotates is required to cover the loading space fully.*

The measurements have been replicated onto eight different area elements, *i.e.* with different micro-structures and spatial distributions of failure threshold. The procedure to measure the yield surface is summarized in Algorithm 2. The results from applying this measurement procedure are reported in the Figure 6.1. In particular, the Figure 6.1a displays the yield strains
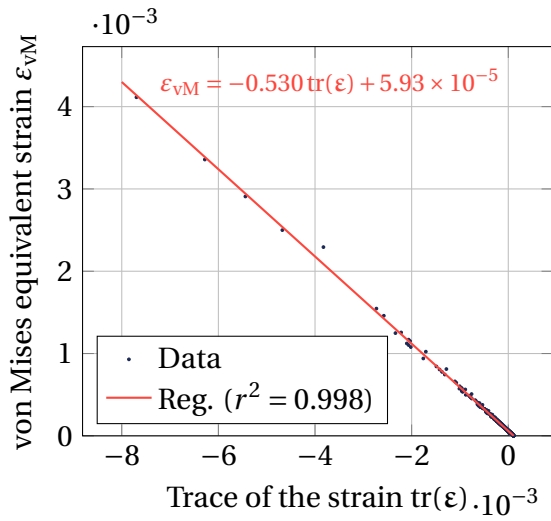
(a) Strain invariants

(b) Principal strains
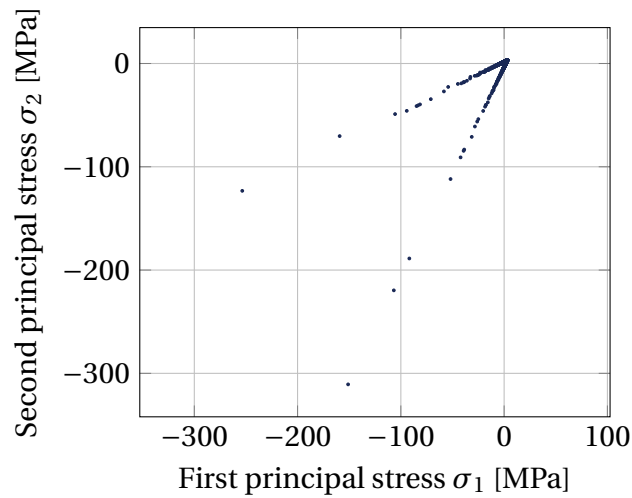
(c) Principal stresses
($\mu_0 = 19.4$ GPa and $\kappa_0 = 30.0$ GPa)

Figure 6.1 • Measurement of the yield surface.

Algorithm 2: Procedure to measure the yield surface

Set the imposed strain norm $\|\varepsilon_{\text{imp}}\|$;
Set the number of loading directions N_{dir};
Initialize the list of yield strain tensors;
for $k \leftarrow 0$ **to** $N_{\text{dir}} - 1$ **do**

> Set the imposed strain $\varepsilon_{\text{imp}} = \|\varepsilon_{\text{imp}}\| \begin{bmatrix} \cos\frac{2k\pi}{N_{\text{dir}}} & 0 \\ 0 & \sin\frac{2k\pi}{N_{\text{dir}}} \end{bmatrix}$;
> Apply the strain loading ε_{imp} to the area element;
> Calculate the failure threshold f_b for each beam;
> Find the first failing beam $b^* = \arg\max_{b'} f_{b'}$;
> Calculate the yield strain tensor $\varepsilon_D = \frac{1}{f_{b^*}} \varepsilon_{\text{imp}}$;
> Store the yield strain tensor ε_D into the list;

Result: List of yield strain tensors for varying loading directions.

---

in the space of strain trace $\text{tr}(\varepsilon)$ and von Mises equivalent strain $\varepsilon_{\text{vM}} = \sqrt{2\varepsilon' : \varepsilon'}$. Applying a linear regression on the strain invariants shows that the yield strain fits the linear equation

$$\varepsilon_{\mathbf{D},\text{vM}} = -0.530\,\text{tr}(\varepsilon_D) + 5.93 \times 10^{-5}, \tag{6.8}$$

which a coefficient of determination $r^2 = 0.998$. Thus, damage starts to grow when

$$\varepsilon_{\text{eq}} = \varepsilon_{\text{vM}} + k\,\text{tr}(\varepsilon) > C_0, \qquad k = 0.530, \qquad C_0 = 5.93 \times 10^{-5}. \tag{6.9}$$

This criterion is a Drucker-Prager criterion and introduces two material parameters: κ_0 the initial yield strain and k the dilatation parameter. For illustration purposes, the criterion is also reported in the space of principal strains in the Figure 6.1b and in the space of principal stresses in the Figure 6.1c.

🔍 **Remark 6.3** *The Appendix D shows the yield surface data in the space* $(\text{tr}(\varepsilon), \sqrt{\langle\varepsilon\rangle_+ : \langle\varepsilon\rangle_+})$. *A line in this space corresponds to the 2D Mazars-Drucker-Prager equivalent strain*

$$\varepsilon_{\text{eq}} = \sqrt{\langle\varepsilon\rangle_+ : \langle\varepsilon\rangle_+} + k\,\text{tr}(\varepsilon). \tag{6.10}$$

Nevertheless, this appendix shows that the data points do not form a line in this space.

2   Analysis of damage evolution

Before formulating a complete damage model, we have first to investigate the evolution of the damage variable **D** during various loadings on the discrete area elements. For each effective elasticity tensor $\tilde{\mathbf{E}}$ of the dataset, damage is calculated from the dilatation tensor using the damage definition proposed in Equation (5.4).
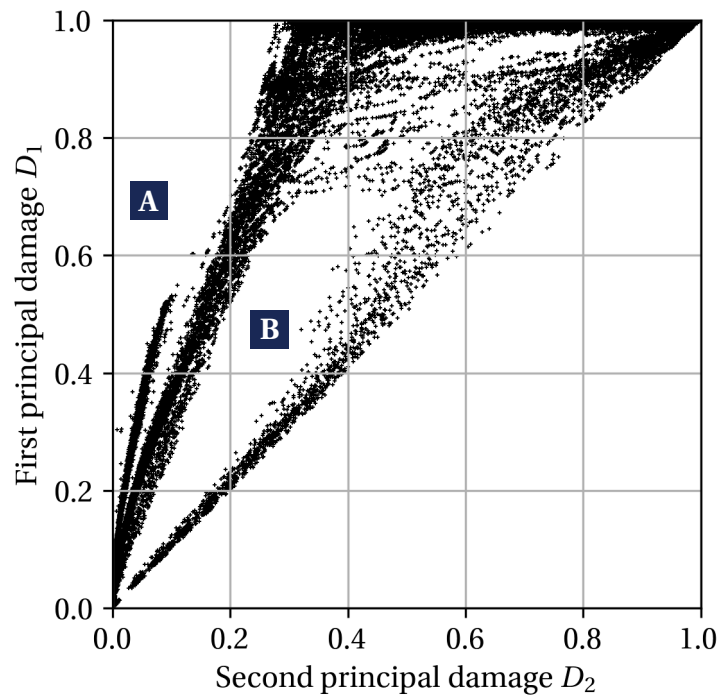
Figure 6.2 • Principal damages for the whole dataset. The principal damages are sorted such that $D_1 \geqslant D_2$ during most of the loading. A and B denotes two regions that are not represented in the dataset.
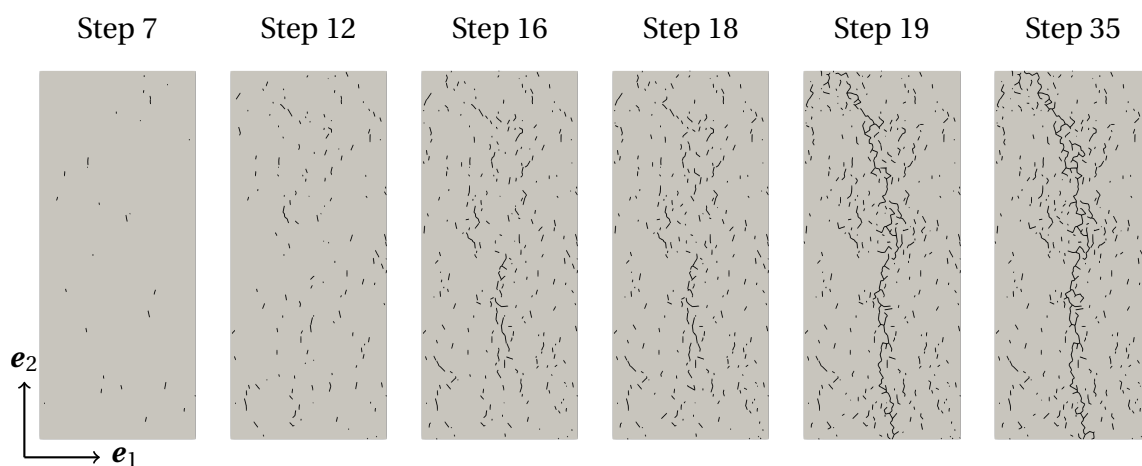

Figure 6.3 • Formation of a macro-crack during a Kinematically Uniform Boundary Condition tension loading along the direction e_1. Only the part of the area element where the macro-crack occurs is shown.

2.1   Damage multi-axiality

Figure 6.2 contains the principal damages associated with each second-order damage tensor measured for our dataset.   Observe that the dataset does not cover the whole principal damage space. Two regions are not covered: the region A ($D_1 > 0$ and $D_2 \approx 0$) and the region B. Adding more load cases to the dataset would enable it to reach region B. However, the void in region A is due to physical reasons. To illustrate these reasons, Figure 6.3 shows the formation of a macro-crack during a tension loading with Kinematically Uniform Boundary Conditions along the direction $\boldsymbol{e}_1$. The damage must evolve such that only one principal damage grows ($D_1 > 0$ and $D_2 = 0$) to reach the region A. Thus, the damage must be purely uni-axial to reach this region. However, during micro-cracking initiation, a statistical effect predominates: the weakest beams tend to fail first (see steps 7 and 12). In this phase, the micro-cracks predominantly form perpendicular to the loading direction. Still, some weaker beams might not be exactly aligned with the loading direction, thus being a first source of damage multi-axiality. Following this initial diffuse (statistical) micro-cracking phase, the micro-cracking localizes (see steps 16, 18, and 19). Several phenomena prevent the damage from being purely uni-axial in this phase. First, the micro-cracking becomes deterministic, primarily due to stress localization around existing micro-cracks during the localization. Beams fail where the stress localizes, even if they are not in the direction of the loading, thus generating cracks that are not orthogonal to the loading. Moreover, macro-cracks will form by bridging (possibly misaligned) micro-cracks during this phase. The micro-cracks contributing to bridging the initial micro-cracks (being bridged) are not necessarily aligned, thus generating new misaligned micro-cracks and further contributing to the damage multi-axiality. Furthermore, geometric heterogeneity prevents micro-cracking from localizing into a straight line/plane. Note that all those phenomena are directly linked to the quasi-brittleness property. Indeed, the existence of a process zone prevents the damage variable from having exactly null principal damage components.

2.2   Focusing on three proportional loadings

As a first approach, we start by investigating three specific proportional loading cases with periodic strain boundary conditions: bitension (purely hydrostatic), tension (both hydrostatic and deviatoric), and shear (purely deviatoric).

Bitension loading.   Let us start by examining damage evolution during bitension loading cases with periodic boundary conditions. Figure 6.4a displays the evolution of the damage components when this loading is applied to 36 micro-structures. An initial phase of elasticity is observed, where the damage remains zero. Then, damage starts to grow almost linearly with the loading. This phase corresponds to diffuse micro-cracking. The variability starts to grow at some point, and the damage accelerates. It is when the micro-cracking localizes, ending up in the failure of the area element. In the final stage, the damage rate reduces, the components D_{11} and D_{22} asymptotically tend to 1, and the component D_{12} tends to zero. The Figure 6.4b shows the principal damages D_1 and D_2 evolution. They are sorted such that $D_1 > D_2$ during most of the loading. This plot shows that there is almost always a

direction in which the micro-cracking localizes before the other one. Thus, even if the loading is hydrostatic, the damage tensor is not purely hydrostatic, leading to a loss of isotropy. This phenomenon is not restricted to our discrete model and also occurs in experiments.

🔍 **Remark 6.4** *This phenomenon is purely due to statistical effects, and accounting for it in a deterministic model might not be possible. In macroscopic modeling, we will assume that the damage state remains equi-biaxial ($D_1 = D_2$).*
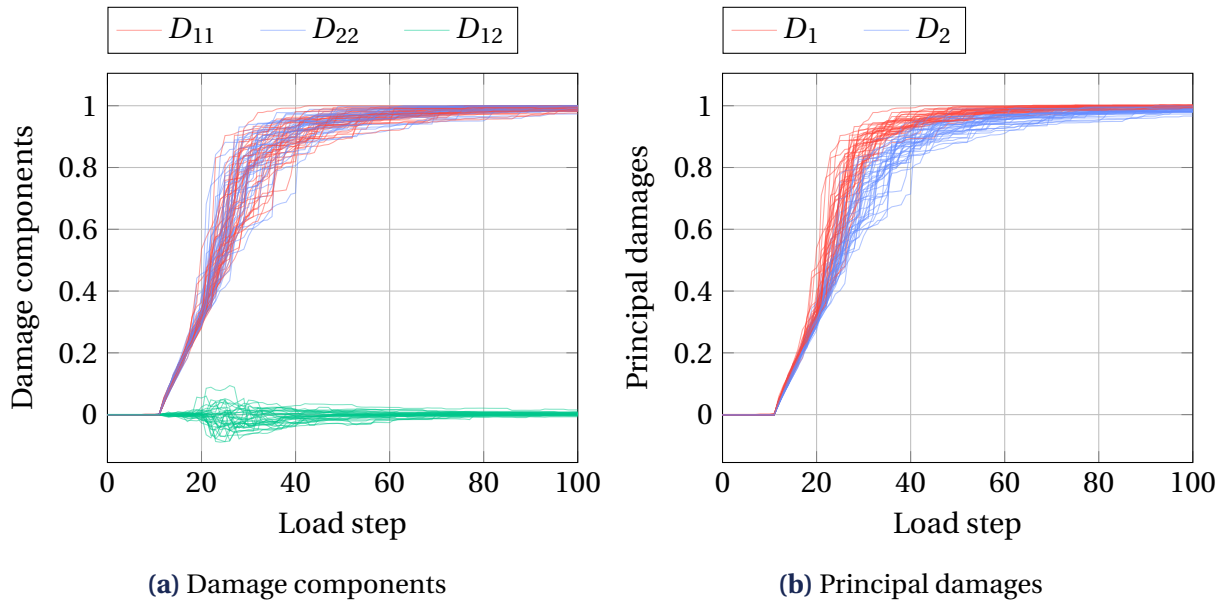

(a) Damage components   (b) Principal damages

Figure 6.4 • Damage evolution during bitension loads with periodic boundary conditions.

Tension loading. Let us now study damage evolution during tension loading along the axis e_1-axis with periodic boundary conditions. Figure 6.5a displays the evolution of the damage components when this loading is applied to the 36 area elements. Once again, we first observe an elastic phase where the damage remains zero. Then, damage starts to grow almost linearly with the loading during the diffuse micro-cracking phase. The damage not only grows along the e_1-axis but also along the e_2-axis. When the micro-cracking localization occurs, the damage rate increases. Note that the damage localization does not always happen at the same load step. It is mainly due to the mesoscale heterogeneity, particularly the randomness of failure thresholds. After the localization, the damage rate reduces, and the component D_{11} asymptotically tends to 1. Figure 6.5b shows that the principal damages are indeed bounded in the interval $[0,1]$. Moreover, even on the principal basis, the damage is not uni-axial.

Shear loading. Figure 6.6 displays the damage components evolution during a shear loading with periodic strain boundary conditions for the 36 area elements. The observations are similar to the case in tension. The main difference is that the localization process is slower than in bitension and tension, and the variability is smaller.

(a) Damage components

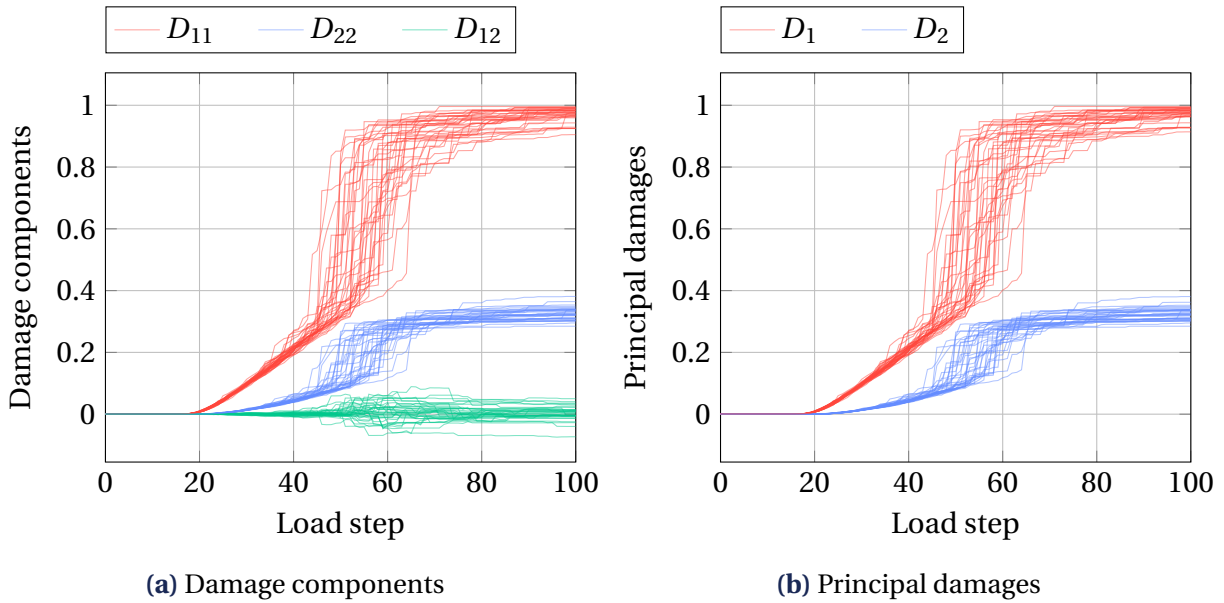(b) Principal damages

Figure 6.5 • Damage evolution during tension loads with periodic boundary conditions.

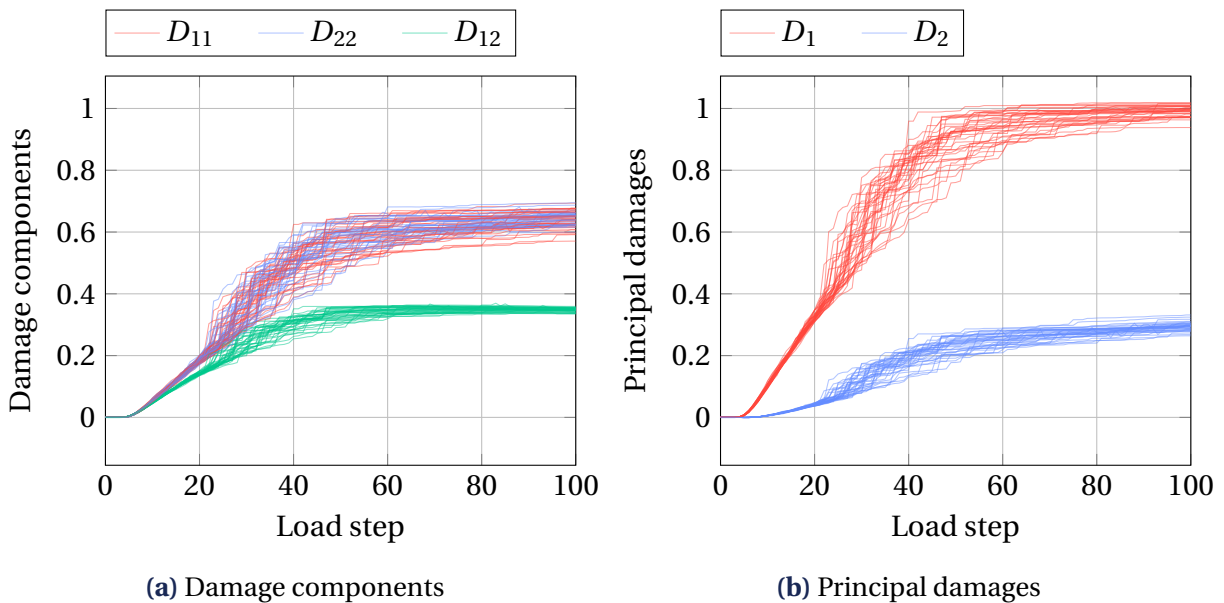(a) Damage components

(b) Principal damages

Figure 6.6 • Damage evolution during shear loads with periodic boundary conditions.

Analysis using invariants. To analyze the results, let us use the parametrization, presented in Appendix E, of the second-order damage tensor **D**,

$$\mathbf{D} = \frac{\|\mathbf{D}\|}{\sqrt{2}}\left(D_m\mathbf{1} + \sqrt{1-D_m^2}\mathbf{R}(\theta)\right), \qquad \mathbf{R}(\theta) = \begin{bmatrix} \cos 2\theta & \sin 2\theta \\ \sin 2\theta & -\cos 2\theta \end{bmatrix} \tag{6.11}$$

Indeed any symmetric second-order tensor **D** can be parameterized by its (invariant) norm $\|\mathbf{D}\|$, its (invariant) hydrostatic (mean) damage biaxiality D_m and the orientation of its deviatoric part θ, defined as

$$\|\mathbf{D}\| = \sqrt{\mathbf{D}:\mathbf{D}}, \qquad D_m = \frac{\text{tr}(\mathbf{D})}{\sqrt{2}\|\mathbf{D}\|}, \qquad \theta = \frac{1}{2}\arctan\left(\frac{D'_{12}}{D'_{11}}\right). \tag{6.12}$$

Note that the deviatoric angle θ is undefined when the deviatoric part is null, *i.e.* when $D_m = -1$ or $D_m = 1$. Let us now analyze the damage evolution based on invariant the
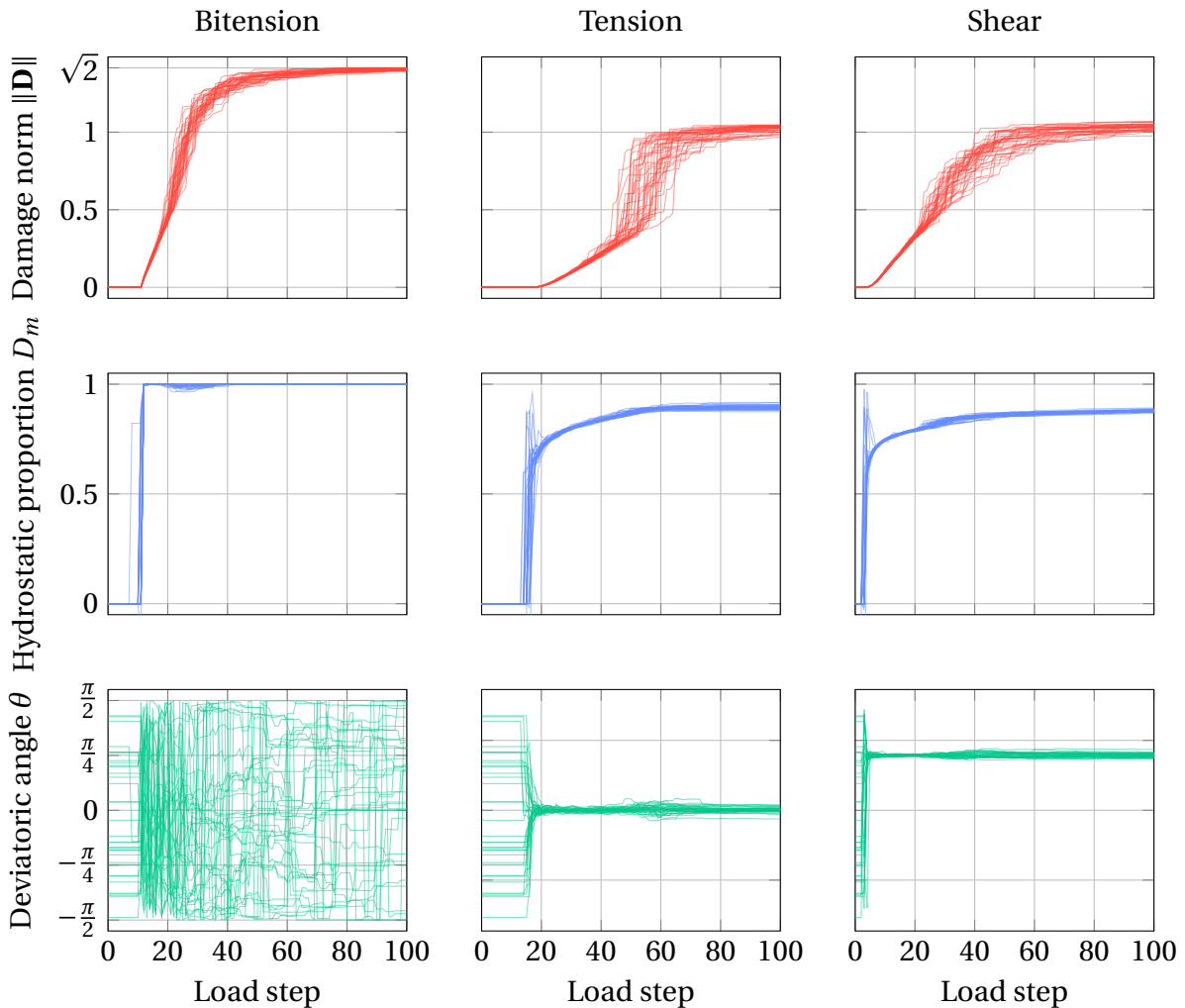

Figure 6.7 • Damage evolution using the proposed parametrization during three load cases with periodic boundary conditions: bitension, tension, and shear.

invariant damage norm $\|\mathbf{D}\|$, invariant hydrostatic damage bixiality D_m, and the deviatoric angle θ, represented in Figure 6.7. Let us first focus on the bitension load cases. The negative

point around load step 10 for the hydrostatic damage biaxiality D_m is due to a numerical approximation errors biasing the ratio $\mathrm{tr}(\mathbf{D})/(\sqrt{2}\|\mathbf{D}\|)$ when both the trace $\mathrm{tr}(\mathbf{D})$ and $\|\mathbf{D}\|$ are close to zero. The figure also shows that the damage biaxiality D_m slightly decreases in almost all the cases during the localization stage (between load steps 20 and 40). It means the deviatoric part grows for almost all the micro-structures during the localization phase. However, the orientation of the deviatoric part, given by the deviatoric angle θ, is mostly random. As explained before, it is due to the random variations in the micro-crack orientations.

For the tension load cases, we can observe that the hydrostatic damage biaxiality D_m gradually increases during the diffuse micro-cracking phase and then stabilizes after the damage localization. The orientation of the deviatoric part slightly varies during the loading. Note that the deviatoric angle corresponds to the deviatoric angle of the applied tensile strain.

3 Anisotropic non-standard damage evolution law for proportional loadings

The evolution law is assumed of the form

$$\dot{\mathbf{D}} = \begin{cases} 0 & \text{if } f < 0 \text{ or } \dot{f} < 0, \\ \dot{\lambda}_{\mathbf{D}} \mathbf{P}_{\mathbf{D}} & \text{if } f = 0 \text{ and } \dot{f} = 0, \end{cases} \tag{6.13}$$

where $\dot{\lambda}_{\mathbf{D}}$ the damage multiplier, which usually derives from the damage criterion function $f = f(\varepsilon, \mathbf{D})$ (using the Kuhn-Tucker conditions $\dot{\lambda}_{\mathbf{D}} \geq 0, f \leq 0, \dot{\lambda}_{\mathbf{D}} f = 0$), and where $\mathbf{P}_{\mathbf{D}}$ is the damaging direction. In the case of proportional loadings, the choice of damage criterion function can be restricted to (Mazars, 1986)

$$f(\varepsilon, \mathbf{D}) = \varepsilon_{\mathrm{eq}} - C(\mathbf{D}), \qquad \varepsilon_{\mathrm{eq}} = \varepsilon_{\mathrm{vM}} + k\,\mathrm{tr}(\varepsilon), \qquad C(\mathbf{D} = \mathbf{0}) = C_0, \tag{6.14}$$

where $\varepsilon_{\mathrm{eq}}$ is the equivalent strain (the Drucker-Prager equivalent strain in our case, by Equation (6.9)), and $C(\mathbf{D})$ is the consolidation function.

3.1 Bounding damage

One can apply a change of variable to guarantee that damage eigenvalues are bounded in the interval $[0, 1]$ and simplify the modeling. For instance, Ladevèze (1983a, 1995) proposed to use the variable $\mathbf{h} = (\mathbf{1} - \mathbf{D})^{-\frac{1}{2}}$. Moreover, Mattiello and Desmorat (2021) proposed to ease the formulation of the evolution model by generalizing the change of variable as

$$\dot{\boldsymbol{\Delta}} = \mathscr{G}(\mathbf{D}, \dot{\mathbf{D}}), \tag{6.15}$$

where $\dot{\boldsymbol{\Delta}}$ is a positive semi-definite symmetric second-order tensor. The idea consists in defining an auxiliary variable $\boldsymbol{\Delta}$, being a function of the damage $\mathbf{D}$, whose evolution is simpler to describe from the mechanical quantities. Ideally, we want to define an auxiliary variable whose evolution is linear in strain.

Let us consider the two following auxiliary variables

$$\mathbf{D} = \mathbf{1} - (\mathbf{1} + \mathbf{\Delta}_a)^{-\alpha} \iff \mathbf{\Delta}_a = (\mathbf{1} - \mathbf{D})^{-\frac{1}{\alpha}} - \mathbf{1}, \qquad (6.16)$$

$$\mathbf{D} = \frac{2}{\pi} \arctan(\mathbf{\Delta}_b^\alpha) \iff \mathbf{\Delta}_b = \left(\tan\left(\frac{\pi}{2} \mathbf{D} \right) \right)^{\frac{1}{\alpha}}, \qquad (6.17)$$

where α is a parameter, called damage exponent, controlling the early damage rate. The function (here, power and arctan), noted g in the following example, are applied in terms of principal values

$$g(\mathbf{D}) = \sum_{I=1}^{2} g(D_I) \boldsymbol{n}_I \otimes \boldsymbol{n}_I, \qquad \mathbf{D} = \sum_{I=1}^{2} D_I \boldsymbol{n}_I \otimes \boldsymbol{n}_I, \qquad \|\boldsymbol{n}_I\| = 1, \qquad (6.18)$$

where D_I is the I-th principal value of $\mathbf{D}$ and $\boldsymbol{n}_I$ is its I-th unit eigenvector. Other methods to apply such functions are proposed by Higham (2008). The proposition in Equation (6.16) is a generalization of the variable proposed by Ladevèze (1983a, 1995) (when $\alpha = 2$). It is also modified to be null when the damage is null.

For illustration purposes, the Figure 6.8 shows the principal damage as a function of the auxiliary variable for both changes of variable and different values of the damage exponent α. With both functions, the principal damage tends asymptotically to 1, as expected. Nevertheless, one main difference between both variable changes is the slope monotonicity. Indeed, the slope of $\mathbf{\Delta}_a$, from Equation (6.16), is strictly decreasing with damage. However, the slope of $\mathbf{\Delta}_b$, from Equation (6.17), is first small, then grows till the principal damage reaches 0.5, and decreases such that the principal damage asymptotically tends to 1. In the following, we will see that this non-monotonicity of the slope is crucial to account for the (early) diffuse micro-cracking stage correctly.
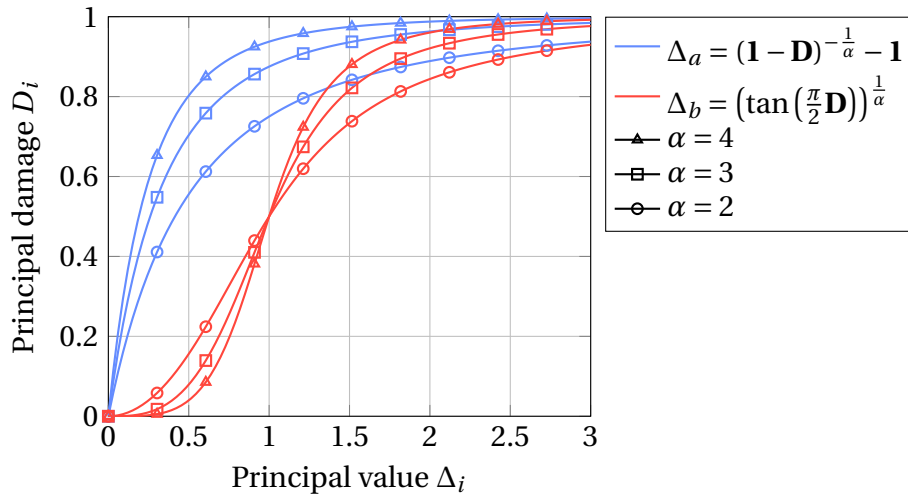

Figure 6.8 • Relation between the principal damages D_i and the principal values of the auxiliary variables Δ_i.

Q **Remark 6.5** *For more flexibility, one could introduce the change of variable*

$$\mathbf{D} = \frac{2}{\pi} \arctan\left((\mathbf{\Delta}_c / \beta)^\alpha \right) \iff \mathbf{\Delta}_c = \beta \left(\tan\left(\frac{\pi}{2} \mathbf{D} \right) \right)^{\frac{1}{\alpha}}, \qquad (6.19)$$

where the parameter β is the principal value of $\mathbf{\Delta}_c$ at which the slope starts to decrease.

We can now study the evolution of both auxiliary variables during the bitension and tension loading cases. We calculate the mean damage evolution during both loading cases and then applied both changes of variables (in Equation (6.16) and Equation (6.17)). The evolution of both auxiliary variables, for different values of the damage exponent α, are reported in Figure 6.9 for the bitension load case. The first observation is that, during the early damage stage (damage starts when $\varepsilon_{11} = C_0/(2k) \approx 5.6 \times 10^{-5}$), the variable $\mathbf{\Delta}_a$, from Equation (6.16), does grow at a small rate. However, the second variable $\mathbf{\Delta}_b$, from Equation (6.17), grows almost linearly during the whole damage process for $\alpha = 3$ (red line with square marks). For the tension load case, both auxiliary variables are reported in Figure 6.10. Once again, the auxiliary variable $\mathbf{\Delta}_a$ evolves in two stages (after the elastic phase). Indeed, it grows at a small rate in the diffuse micro-cracking stage and then grows (almost linearly for $\alpha = 4$) after the localization. For this case, the auxiliary variable $\mathbf{\Delta}_b$ is again almost linear with the strain. It also better catches the diffuse micro-cracking phase.
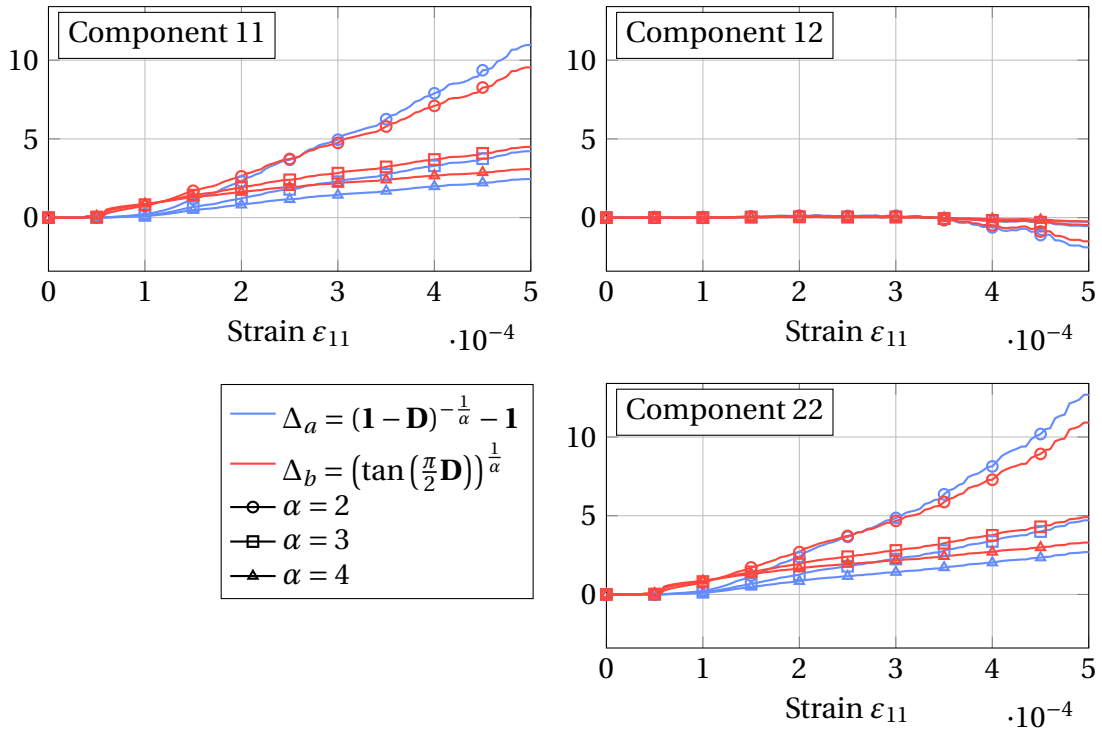

Figure 6.9 • Evolution of the proposed auxiliary variables (to describe damage evolution) during a bitension loading for different values of the damage exponent α.

3.2   A first evolution law for bitension load cases

To model the damage evolution, our process is to start with a simple law that can be progressively enhanced to cover more loading cases. So, let us start with the non-standard damage evolution law defined by

$$\dot{\mathbf{\Delta}} = \dot{\lambda}\frac{\langle\varepsilon\rangle_+}{\|\langle\varepsilon\rangle_+\|}, \qquad f(\varepsilon,\mathbf{\Delta}) = \varepsilon_{\text{eq}} - C(\mathbf{\Delta}), \qquad C(\mathbf{\Delta}) = C_0 + S_1\,\text{tr}(\mathbf{\Delta}) + \frac{S_2}{2}\mathbf{\Delta}' : \mathbf{\Delta}', \qquad (6.20)$$

where $\langle\varepsilon\rangle_+$ denotes the positive part of the strain, S_1 and S_2 are the hydrostatic and deviatoric damage strength parameters: the higher S_i, the higher the damage resistance and the lower
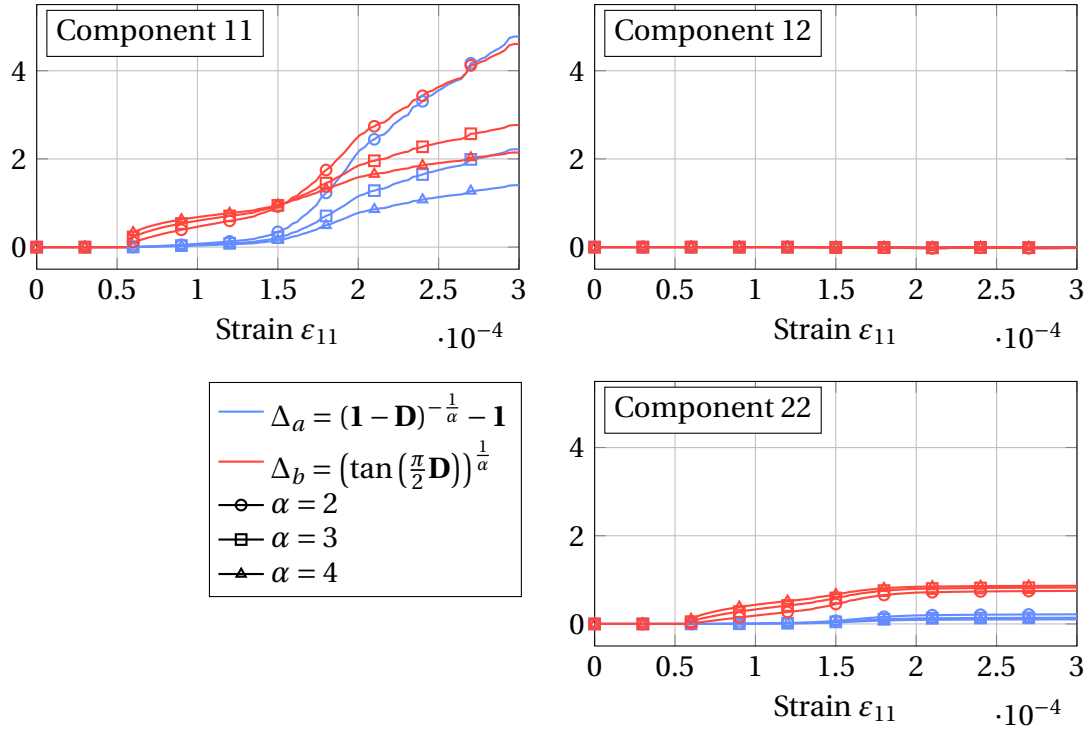
Figure 6.10 • Evolution of the proposed alternative variables (to describe damage evolution) during a tension loading for different values of the damage exponent α.

the damage rate (as shown below in Equation (6.21)). For this choice of consolidation function, the damage multiplier $\dot{\lambda}$ is calculated in Appendix F, and its expression is

$$\dot{\lambda} = \frac{\dot{\varepsilon}_{\text{eq}}}{S_1 \operatorname{tr}(\mathbf{P}) + S_2 \mathbf{P}' : \mathbf{\Delta}''}, \tag{6.21}$$

where the damaging direction is $\mathbf{P} = \langle \varepsilon \rangle_+ / \|\langle \varepsilon \rangle_+\|$. This damage evolution law, with both changes of variable, has been implemented using MFront (Helfer et al., 2015). The MFront code of the model is available in Appendix G.

Fitting bitension load case. As a first test, we fit the model, with each change of variable, to the bitension load case from the discrete model using the procedure explained in Appendix H. We chose to fit all the parameters linked to evolution (α, S_1, and S_2) and the parameters of the yield surface (C_0 and k). The elastic parameters are left unchanged. As the strain is hydrostatic, the damage will be hydrostatic during the loading. Thus, the term associated with the deviatoric strength S_2 in the consolidation will have no influence. For now, we chose to set it to zero.

Q **Remark 6.6** *In the bitension case, the loading criterion is*

$$k \operatorname{tr}(\varepsilon) > C_0 \implies \operatorname{tr}(\varepsilon) > \frac{C_0}{k}. \tag{6.22}$$

It means that when we fit the models to a bitension load case, only the ratio C_0/k is fitted for the damage criterion, i.e. different couples (C_0, k) gives the same results.

Name	Symbol	Unit	$\mathbf{D} = \mathbf{1} - (\mathbf{1} + \mathbf{\Delta}_a)^{-\alpha}$	$\mathbf{D} = \frac{2}{\pi}\arctan(\mathbf{\Delta}_b^\alpha)$
Initial shear modulus	μ_0	GPa	19.5	19.5
Initial bulk modulus	κ_0	GPa	30.0	30.0
Harmonic pre-factor	h	GPa	17.0	17.0
Initial damage threshold	C_0	1	$1.82 \cdot 10^{-4}$	$3.40 \cdot 10^{-5}$
Dilatation parameter	k	1	1.149	1.076
Damage exponent	α	1	7.47	3.187
Hydrostatic damage strength	S_1	1	$3.95 \cdot 10^{-4}$	$1.08 \cdot 10^{-4}$
Deviatoric damage strength	S_2	1	0	0

Table 6.1 • Parameters of the model fitted to the bitension load case.

The fitted parameters are reported in Table 6.1. The damage and stress evolution during the bitension load cases are shown in Figure 6.11 and Figure 6.12. The reference results from the discrete simulations are also shown for comparison purposes. Both auxiliary variables
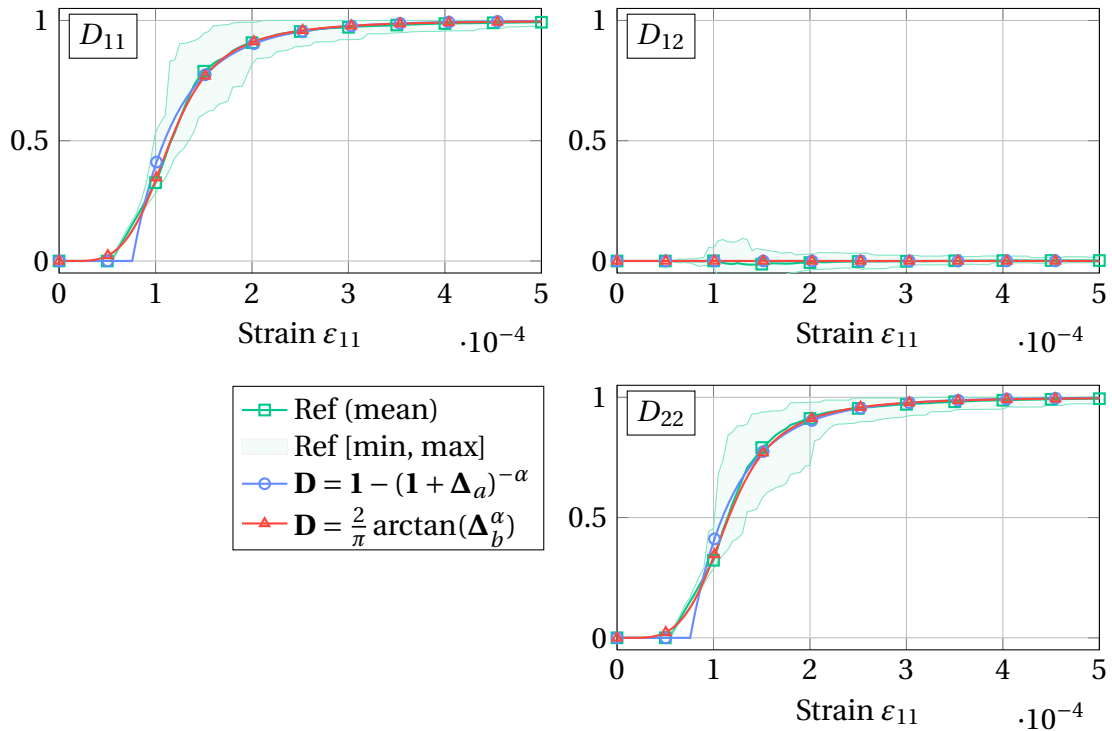

Figure 6.11 • Comparison of the damage evolution during a bitension load case predicted with both changes of variable.

give a good fit in terms of late damage evolution. However, in both cases, the damage initiation is modified to enable fitting the later stage. Indeed, using the auxiliary variable $\mathbf{\Delta}_a = \mathbf{1} - (\mathbf{1} + \mathbf{\Delta}_a)^{-\alpha}$ leads to a highly delayed damage initiation. The damage starts when $\varepsilon_{11} = C_0/(2k) \approx 8 \times 10^{-5}$, when using $\mathbf{\Delta}_a$ from Equation (6.16), instead of $\varepsilon_{11} \approx 5.6 \times 10^{-5}$ for the reference. It is caused by the early damage rate being too high (and only decreasing afterward), which causes the damage initiation to be delayed to compensate. It is due to the derivative of
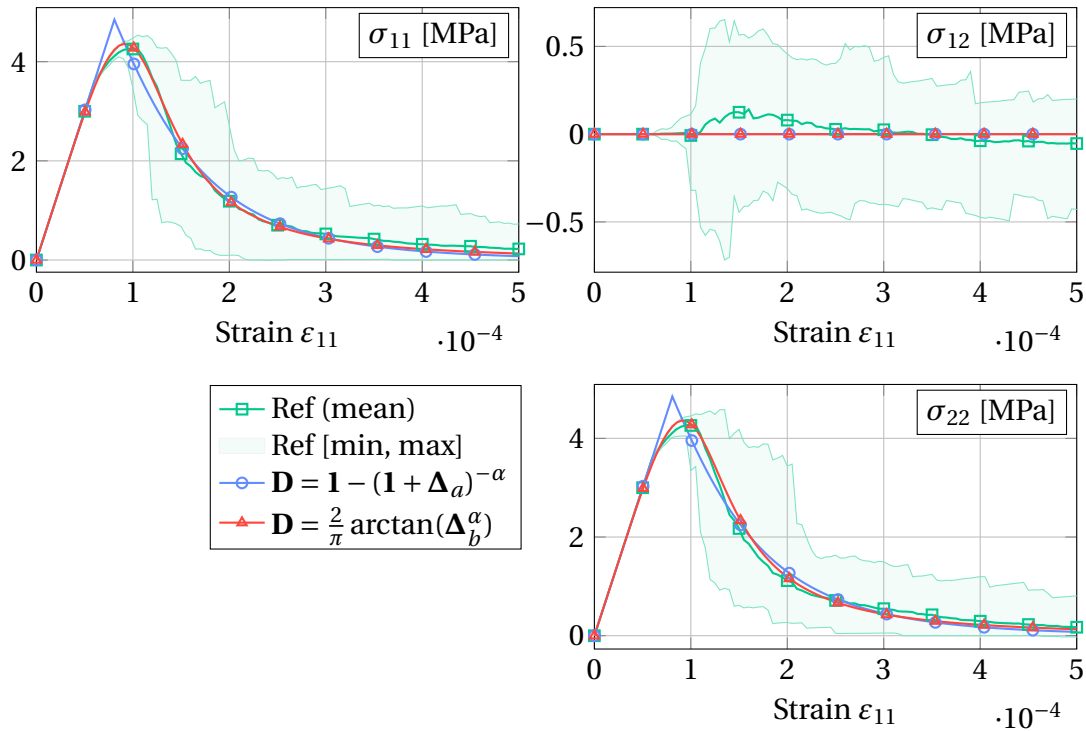
Figure 6.12 • Comparison of the stress evolution during a bitension load case predicted with both changes of variable.

the change of variable being monotonic, which makes the damage rate decreasing as shown in Figure 6.8). On the contrary, the damage starts when $\varepsilon_{11} = C_0/(2k) \approx 1.68 \times 10^{-5}$ when using $\mathbf{\Delta}_b$, from Equation (6.17), instead of $\varepsilon_{11} \approx 5.6 \times 10^{-5}$ for the reference. Nevertheless, the damage growth starts with a very small damage rate. As this second auxiliary variable $\mathbf{\Delta}_b$ has a non-monotonic derivative, the damage rate can first be small, then grow during the localization of micro-cracking, and finally decrease after the micro-cracking localization. It is important to note that this auxiliary variable provides a better fit of early damage and thus of the stress peak as shown on Figure 6.12. For now, we choose to use the auxiliary variable $\mathbf{\Delta} = \mathbf{\Delta}_b$ from Equation (6.17) for the proposed model.

4 Summary of damage model

In this section, the damage model is summarized. Possible extensions to non-local damage are also presented to enable its application to structures.

4.1 Damage model

The proposed local anisotropic damage model for quasi-brittle materials comprises the following components.

- **Elasticity coupled with damage.**

$$\boldsymbol{\sigma} = \tilde{\mathbf{E}}(\mathbf{D}) : \boldsymbol{\varepsilon} \tag{6.23}$$

- **Effective elasticity tensor.**

$$\tilde{\mathbf{E}}(\mathbf{D}) = 2\tilde{\mu}(\mathbf{D})\mathbf{J} + \tilde{\kappa}(\mathbf{D})\mathbf{1} \otimes \mathbf{1} - \kappa_0(\mathbf{1} \otimes \mathbf{D}' + \mathbf{D}' \otimes \mathbf{1}) + \tilde{\mathbf{H}}(\mathbf{D}), \qquad (6.24)$$

where

$$\tilde{\mu}(\mathbf{D}) = \mu_0 - \frac{1}{4}\kappa_0 \operatorname{tr}\mathbf{D} + \frac{1}{4}\left(\kappa_0 - 2\mu_0\right)\mathbf{D}:\mathbf{D} + m\left(\mathbf{D}:\mathbf{D} - \operatorname{tr}(\mathbf{D}^3)\right), \qquad (6.25)$$

$$\tilde{\kappa}(\mathbf{D}) = \kappa_0\left(1 - \frac{1}{2}\operatorname{tr}\mathbf{D}\right), \qquad (6.26)$$

$$\tilde{\mathbf{H}}(\mathbf{D}) = h\,(\operatorname{tr}\mathbf{D})^4\,\mathbf{D}' * \mathbf{D}', \qquad \mathbf{D}' * \mathbf{D}' = \mathbf{D}' \otimes \mathbf{D}' - \frac{1}{2}(\mathbf{D}':\mathbf{D}')\,\mathbf{J}. \qquad (6.27)$$

- **Auxiliary damage variable.**

$$\mathbf{\Delta} = \left(\tan\left(\frac{\pi}{2}\mathbf{D}\right)\right)^{\frac{1}{\alpha}} \iff \mathbf{D} = \frac{2}{\pi}\arctan(\mathbf{\Delta}^{\alpha}), \qquad (6.28)$$

where the functions are applied to the principal damages as specified in Equation (6.18).

- **Damage criterion.**

$$f = \bar{\varepsilon}_{\text{eq}} - C(\mathbf{\Delta}) \leqslant 0, \qquad \varepsilon_{\text{eq}} = \varepsilon_{\text{vM}} + k\operatorname{tr}(\varepsilon), \qquad C(\mathbf{\Delta}) = C_0 + S_1\operatorname{tr}\mathbf{\Delta} + \frac{S_2}{2}\mathbf{\Delta}':\mathbf{\Delta}', \quad (6.29)$$

where $\varepsilon_{\text{vM}} = \sqrt{2\varepsilon':\varepsilon'}$ is the von Mises equivalent strain, and $\bar{\varepsilon}_{\text{eq}}$ is the non-local equivalent strain. The non-local equivalent strain for the local damage model is $\bar{\varepsilon}_{\text{eq}} = \varepsilon_{\text{eq}}$. Different choices of non-local equivalent strain are proposed in Section 4.3 for the non-local damage model.

- **Evolution law.**

$$\dot{\mathbf{\Delta}} = \dot{\lambda}\mathbf{P}, \qquad \mathbf{P} = \frac{\langle\varepsilon\rangle_+}{\|\langle\varepsilon\rangle_+\|}, \qquad \dot{\lambda} = \frac{\dot{\bar{\varepsilon}}_{\text{eq}}}{S_1\operatorname{tr}(\mathbf{P}) + S_2\mathbf{P}':\mathbf{\Delta}'}, \qquad (6.30)$$

where the damage multiplier $\dot{\lambda}$ is obtained from the Kuhn-Tucker loading-unloading conditions $f \leqslant 0, \dot{\lambda} \geqslant 0, \dot{\lambda}f = 0$.

🔾 **Remark 6.7** *This model still has to be extended for loading cases other than bitension. As a short-term perspective, the damaging direction* **P** *must be studied to fully model damage in tension.*

4.2 Parameters of the local damage model

There are eight parameters (excluding the optional non-linear shear-damage parameter m):

- the initial bulk modulus κ_0, the initial shear modulus μ_0, and the (new) harmonic prefactor h for the constitutive equation,

- the damage exponent α for the change of variable,

- the initial damage threshold C_0 and the dilatation parameter k for the damage criterion function (with no damage),

- the hydrostatic damage strength S_1 and the deviatoric damage strength S_2 for the consolidation.

4.3   Non-local damage

In order to make the present damage model non-local, let us recall different definitions of the non-local equivalent strain from the literature.

Integral Non-Local (Pijaudier-Cabot & Bažant, 1987).   The non-local equivalent strain is

$$\bar{\varepsilon}_{\text{eq}}(\boldsymbol{x}) = \frac{1}{V_\Omega(\boldsymbol{x})} \int_\Omega w(\|\boldsymbol{x} - \boldsymbol{y}\|/\ell_c)\,\varepsilon_{\text{eq}}(\boldsymbol{y})\mathrm{d}\boldsymbol{y}, \qquad w(\|\boldsymbol{x} - \boldsymbol{y}\|/\ell_c) = \exp\left(-\frac{4\|\boldsymbol{x} - \boldsymbol{y}\|^2}{\ell_c^2}\right), \quad (6.31)$$

where Ω is the domain of the structure, $V_\Omega(\boldsymbol{x}) = \int_\Omega w(\|\boldsymbol{x} - \boldsymbol{y}\|/\ell_c)\mathrm{d}\boldsymbol{y}$ normalizes the integral, w is a weight function, and ℓ_c is a characteristic length.

Implicit Gradient Non-Local (Peerlings et al., 1996).   The non-local equivalent strain is the solution of the boundary value problem

$$\bar{\varepsilon}_{\text{eq}} - c\nabla^2 \bar{\varepsilon}_{\text{eq}} = \varepsilon_{\text{eq}}, \qquad \text{in } \Omega, \tag{6.32}$$

$$\nabla\bar{\varepsilon}_{\text{eq}} \cdot \boldsymbol{n} = 0, \qquad \text{on } \partial\Omega, \tag{6.33}$$

where c is homogeneous to a square length and can be related to the characteristic length ℓ_c, $\partial\Omega$ is the boundary of the domain Ω, and $\boldsymbol{n}$ is the outward-pointing normal to the boundary.

Eikonal Integral Non-Local (Desmorat et al., 2015).   The non-local equivalent strain is expressed as

$$\bar{\varepsilon}_{\text{eq}}(\boldsymbol{x}) = \frac{1}{V_\Omega} \int_\Omega w(\ell(\boldsymbol{x}, \boldsymbol{y})/\ell_c)\varepsilon_{\text{eq}}(\boldsymbol{y})\mathrm{d}\boldsymbol{y}, \tag{6.34}$$

where ℓ is an effective (Riemannian) distance influenced by the damage field, which verifies an eikonal equation

$$\nabla\ell(\boldsymbol{x}, \boldsymbol{y}) \cdot \mathbf{g}^{-1} \cdot \nabla\ell(\boldsymbol{x}, \boldsymbol{y}) = 1, \qquad \ell(\boldsymbol{x}, \boldsymbol{x}) = 0, \qquad \mathbf{g}^{-1} = \mathbf{1} - \mathbf{D}, \tag{6.35}$$

where $\mathbf{g}$ is an arbitrarily chosen symmetric second-order (metric) tensor, function of damage. Rastiello et al. (2018) and Thierry (2021) discussed the numerical aspects associated with this model.

Eikonal Gradient Non-Local (Desmorat et al., 2015).   In this model, the non-local equivalent strain is the solution of

$$\bar{\varepsilon}_{\text{eq}} - c\frac{1}{\sqrt{\det\mathbf{g}}}\nabla \cdot \left(\sqrt{\det\mathbf{g}}\,\mathbf{g}^{-1} \cdot \nabla\bar{\varepsilon}_{\text{eq}}\right) = \varepsilon_{\text{eq}}, \qquad \text{in } \Omega, \tag{6.36}$$

$$\nabla\bar{\varepsilon}_{\text{eq}} \cdot \boldsymbol{n} = 0, \qquad \text{on } \partial\Omega, \tag{6.37}$$

where $\mathbf{g}$ is the metric and can be defined as proposed in Equation (6.35). A non-intrusive implementation of this approach, based on a thermo-mechanical finite element solver, has been proposed by Marconi (2022). This approach has also been further studied and formalized by Ribeiro Nogueira et al. (2023).

Localizing Gradient Non-Local (Poh & Sun, 2017). With this non-local model, the equivalent strain is the solution of

$$\bar{\varepsilon}_{eq} - c\nabla \cdot \left(g(D) \cdot \nabla\bar{\varepsilon}_{eq}\right) = \varepsilon_{eq}, \qquad \text{in } \Omega, \tag{6.38}$$

$$\nabla\bar{\varepsilon}_{eq} \cdot \boldsymbol{n} = 0, \qquad \text{on } \partial\Omega, \tag{6.39}$$

where g is an interaction function of damage. The authors proposed to use

$$g(D) = \frac{(1-R)\exp(-\eta D) + R - \exp(\eta)}{1 - \exp(-\eta)}, \tag{6.40}$$

where D is the damage in the isotropic case, and that could be set as a damage invariant, such as $\text{tr}(\mathbf{D})$, in the anisotropic case, η is a material parameter, and R is the parameter controlling residual interactions when the material is fully damaged.

Stress-based Integral Non-Local (Giry et al., 2011). In this model, the non-local equivalent strain is expressed as

$$\bar{\varepsilon}_{eq}(\boldsymbol{x}) = \frac{1}{V_\Omega(\boldsymbol{x})} \int_\Omega w(\|\boldsymbol{x}-\boldsymbol{y}\|/\ell_c)\, \varepsilon_{eq}(\boldsymbol{y})\mathrm{d}\boldsymbol{y}, \quad w(\|\boldsymbol{x}-\boldsymbol{y}\|/\ell_c) = \exp\left(-\left(\frac{2\|\boldsymbol{x}-\boldsymbol{y}\|}{\ell_c\rho(\boldsymbol{x},\boldsymbol{\sigma}(\boldsymbol{y}))}\right)^2\right), \tag{6.41}$$

where ρ is a scalar function of the stress quantifying the interactions.

Stress-based Gradient Non-Local (Vandoren & Simone, 2018). The non-local equivalent strain verifies the boundary value problem

$$\bar{\varepsilon}_{eq} - \nabla \cdot \left(\mathbf{c} \cdot \nabla\bar{\varepsilon}_{eq}\right) = \varepsilon_{eq}, \qquad \text{in } \Omega, \tag{6.42}$$

$$\left(\mathbf{c} \cdot \nabla\bar{\varepsilon}_{eq}\right) \cdot \boldsymbol{n} = 0, \qquad \text{on } \partial\Omega, \tag{6.43}$$

where $\mathbf{c}$ is called the symmetric anisotropic gradient matrix, which weights the contributions to the Helmholtz equation of the different gradient terms. Vandoren and Simone (2018) proposed a first expression for $\mathbf{c}$ based on the principal stress,

$$\mathbf{c} = \mathbf{c}_\sigma = c\left(\frac{\sigma}{f_t}\right)^2, \tag{6.44}$$

where $f_t = EC_0$ is the tensile strength, E is the Young modulus, and the square is applied to the principal stresses (as in Equation (6.18)). In order to differentiate the behavior in tension and compression, the authors also proposed to define the matrix $\mathbf{c}$ as

$$\mathbf{c} = \frac{\bar{\sigma}_{eq}f_t}{\max(\sigma_1,\sigma_2)}\mathbf{c}_\sigma, \tag{6.45}$$

where $\bar{\sigma}_{eq}$ is a non-local equivalent stress defined as $\bar{\sigma}_{eq} = (1-D)E\bar{\varepsilon}_{eq}$ in the isotropic case, σ_i is the i-th principle stress, and $\mathbf{c}_\sigma$ is given by Equation (6.44). For this second choice of $\mathbf{c}$, the extension to anisotropic damage does not seem straightforward.

✏ Summary of the Chapter

In this chapter, the model is completed by proposing a preliminary (non-standard) damage evolution model and discussing its extension for structure computations as a non-local damage model.

The first step in the construction of the model is the analysis of the micro-cracking initiation in the area elements. In particular, an efficient method is proposed to obtain the yield surface of the discrete area element. Based on those results, the equivalent strain in the damage criterion is shown to be a Drucker-Prager equivalent strain. This result may seem surprising, but recall that the present work is dedicated to 2D.

Then, the damage evolution in the area elements is analyzed. In particular, the importance of damage bi-axiality is emphasized: even in uni-axial loading cases the damage will be bi-axial. Then, a non-standard damage evolution law is proposed. To ease the damage bounding, two (parametrized) change of variables are studied. A consolidation function, being a linear combination of damage invariants, is proposed. By fitting the damage evolution to a bitension load case, both changes of variables are compared. Choosing a change of variable with a non-monotonic derivative enables to better model the damage evolution during the diffuse micro-cracking stage. The non-standard damage evolution law proposed in this work still has to be extended, especially the damaging direction **P**.

Finally, with the aim of applying the model in structural simulations, non-local damage is discussed. The classic models, with constant interactions, and more recent models, with varying interactions, are presented and discussed. The application to structure is left for future work.

Conclusion

This work aimed at formulating an anisotropic damage model based on virtual tests performed using a discrete model. A literature review in Chapter 1 presented the complex macroscopic behavior observed in quasi-brittle materials, such as concrete, and the physical mechanisms causing its degradation. In this work, we focused on the coupling between elasticity and damage, by studying the impact of microcrack formation and coalescence on the material behavior (and neglected certain phenomena such as crack closure effects). In particular, the damage-induced anisotropy is one of the main focus.

Due to the complexity of conducting a representative experimental campaign, we decided to perform a virtual testing campaign. To this end, we presented the beam-particle model in Chapter 3, which explicitly represents micro-cracking and accurately describes its impact on the macroscopic behavior of the material. We performed virtual experiments on area elements by applying various complex loadings. In Chapter 4, the effective elasticity tensors of the area elements were measured during those virtual experiments. The results have been compiled into a dataset of 76 356 effective elasticity tensors (Loiseau et al., 2023b).

One of this thesis main focuses is the anisotropy induced by mechanical degradation. In the Chapter 4, an analysis of the dataset, using distances to a symmetry class, shows that most effective elasticity tensors are not isotropic. It means that micro-cracking indeed induces an anisotropic behavior. Moreover, it is shown in Chapter 5 that an isotropic model completely mispredicts the evolution of the stress tensor during a non-proportional loading. The analysis of the dataset also suggested that a second-order tensor can be sufficient to represent the state of micro-cracked area elements.

The next step was to formulate a model for the coupling between effective elasticity and (anisotropic) damage. For this purpose, a reconstruction formula of an elasticity tensor from its (tensorial) covariants is presented in Chapter 2. This formula is based on the harmonic decomposition, which enables to represent an elasticity tensor $\mathbf{E}$ from its four harmonic components: the shear modulus μ, the bulk modulus κ, the deviatoric part of the dilatation tensor $\mathbf{d}'$ and the harmonic part $\mathbf{H}$. The idea to formulate the model consists in expressing each effective harmonic component as a function of damage $\mathbf{D}$. The corresponding definition of damage coupled with the reconstruction formula explicitly gives back the exact expression of both the effective bulk modulus $\tilde{\kappa}$ and the deviatoric part of the dilatation tensor $\tilde{\mathbf{d}}'$ in terms of damage $\mathbf{D}$. To model the effective shear modulus $\tilde{\mu}$, we chose to express it as a linear combination of damage invariants. Different assumptions are taken to determine the coefficients introduced in this expression, being potential model parameters, as function of the known initial elastic parameters. In particular, we assume that the rigidity loss stays totally symmetric when the cracks do not interact (mostly during early damage). Thanks to

those assumptions, an accurate model of the effective shear modulus $\tilde{\mu}$ is obtained without introducing any new model parameter. The modeling of the harmonic part has been a more difficult task. Its dependency on damage is less obvious, and discrepancies are observed. Still, a simple model could be obtained by applying a sparse and interpretable data-driven technique (the sparse regression, called LASSO, with optimization constraints). This model introduces one new parameter: the harmonic pre-factor h. Finally, the effective elasticity tensor is then obtained by applying the reconstruction formula $\tilde{\mathbf{E}}(\mathbf{D}) = \tilde{\mathbf{E}}(\tilde{\mu}(\mathbf{D}), \tilde{\kappa}(\mathbf{D}), \tilde{\mathbf{d}}'(\mathbf{D}), \tilde{\mathbf{H}}(\mathbf{D}))$. This coupling between elasticity and damage is then formalized into a thermodynamic state potential.

To complete the model, we formulate, in Chapter 6, a model for the damage evolution during the micro-cracking process. We first determined the yield surface of the discrete area elements through an efficient method. Based on the homogeneity of the meso-scale degradation criterion with respect to the loading amplitude, this method enables us to determine one point of the yield surface with only one elastic resolution. By performing a linear regression on the invariants of the measured yield strains, we showed that the damage criterion of the area elements is —in the present case— a Drucker-Prager criterion. An analysis of the damage evolution highlighted that the damage growth is multi-axial, even if the load is purely uni-axial. To propose a non-standard damage evolution model, a change of variable is first applied so as to bound damage and ease the evolution formulation. A change of variable with a non-monotonic derivative, *i.e.* rate, is essential to capture the early damage evolution correctly. A preliminary damage evolution model is then proposed and applied to a bitension loading case. In the previsions of future applications of the proposed model to structures, non-local damage models are briefly discussed. Moreover, non-local formulations of the anisotropic damage model have been proposed.

Various extensions to this work are possible. The dataset could easily be extended in the short term to cover the principal damage space better. In particular, using the parametrization in Appendix E has enabled us to set a loading amplitude and to systematically discretize the loading direction (as both orientation parameters belong in a closed space). Moreover, generating another dataset, using another mesoscale model for virtual testing, and fitting the proposed damage model to this new dataset would enable us to check whether the proposed model is generic or specific to our dataset. The damage evolution model should also be completed to predict damage evolution during proportional multi-axial loadings better. It means determining the damage direction $\mathbf{P_D}$ predicting (1) the ratio between the hydrostatic and deviatoric parts and (2) the orientation of the damage tensor.

The modeling of damage evolution in non-proportional loading cases is also not much discussed in this work. Indeed, it highly complexifies the evolution modeling problem, requiring accounting for the crack closure effect. From the virtual testing point of view, contact and friction between particles can be enabled. Desmorat and Desmorat (2016) showed that in a 2D isotropic medium, the effect of open and frictionless closed crack on the effective elasticity tensor can be modeled by two second-order tensors. Their framework, general in 2D, could be used to extend the model proposed in the present thesis, where only open cracks were considered.

Finally, another extension of this work is reproducing this study in a tri-dimensional setting. In this case, the number of symmetry classes to study goes from 4 to 8. However, the 3D harmonic decomposition (Olive et al., 2017) could be used as a basis of the model. One of the main difficulties is the growing number of independent harmonic components to model. Indeed, in 2D, there are two invariants, one second-order and one fourth-order covariant. In contrast, there are two invariants, two second-order covariants, and one fourth-order covariant in the 3D case. Moreover, even if a generic method to compute the distance of an elasticity tensor to symmetry classes has been proposed by Azzi et al. (2022), these methods have yet to be applied to each of the eight symmetry classes in 3D. Finally, due to the increased complexity of the 3D case, it might need to rely even more on interpretable data-driven tools. Note that another approach, in the 3D case, could be to rely on an integrity basis of the couple $(\varepsilon, \mathbf{D})$ as done in the work of Taurines et al. (2022, 2023) to model a magneto-mechanical coupling.

To conclude, this study illustrates the potential benefits of adopting sparse and interpretable data-driven approaches for modeling. Their use, often overshadowed by more popular "black box" deep learning approaches, enables us to systematically and efficiently cover diverse possible models while accounting for physical constraints. Coupling sparse data-driven approaches with adapted mathematical tools (decomposition, invariants, etc.) simplifies the modeling process while efficiently using available data.

Appendices

A Calculation of Cundall's best-fit strain

This appendix describe the calculation to obtain the average strain by Cundall's best-fit method. Let us recall that the average strain is defined as

$$\overline{\varepsilon} = \arg\min_{\overline{\varepsilon}^*} \underbrace{\sum_{p\in\mathscr{P}} \left(\Delta\boldsymbol{u}_p - \overline{\varepsilon}^*\Delta\boldsymbol{x}_p\right)^{\mathrm{T}}\left(\Delta\boldsymbol{u}_p - \overline{\varepsilon}^*\Delta\boldsymbol{x}_p\right)}_{\mathrm{LSE}(\overline{\varepsilon}^*)} \tag{46}$$

The minimization of $\mathrm{LSE}(\overline{\varepsilon}^*)$ is obtained by finding a stationary point

$$\frac{\partial\mathrm{LSE}(\overline{\varepsilon})}{\partial\overline{\varepsilon}} = \boldsymbol{0}2 \tag{47}$$

Let us start by developing the expression of the least-square error LSE

$$\mathrm{LSE}(\overline{\varepsilon}) = \sum_{p\in\mathscr{P}} (\Delta\boldsymbol{u}_p - \overline{\varepsilon}\Delta\boldsymbol{x}_p)^{\mathrm{T}}(\Delta\boldsymbol{u}_p - \overline{\varepsilon}\Delta\boldsymbol{x}_p) \tag{48}$$

$$\Longleftrightarrow \mathrm{LSE}(\overline{\varepsilon}) = \sum_{p\in\mathscr{P}} (\Delta\boldsymbol{u}_p^{\mathrm{T}} - \Delta\boldsymbol{x}_p^{\mathrm{T}}\overline{\varepsilon}^{\mathrm{T}})(\Delta\boldsymbol{u}_p - \overline{\varepsilon}\Delta\boldsymbol{x}_p) \tag{49}$$

$$\Longleftrightarrow \mathrm{LSE}(\overline{\varepsilon}) = \sum_{p\in\mathscr{P}} \Delta\boldsymbol{u}_p^{\mathrm{T}}\Delta\boldsymbol{u}_p - \Delta\boldsymbol{x}_p^{\mathrm{T}}\overline{\varepsilon}^{\mathrm{T}}\Delta\boldsymbol{u}_p - \boldsymbol{u}_p^{\mathrm{T}}\overline{\varepsilon}\Delta\boldsymbol{x}_p + \Delta\boldsymbol{x}_p^{\mathrm{T}}\overline{\varepsilon}^{\mathrm{T}}\overline{\varepsilon}\Delta\boldsymbol{x}_p \tag{50}$$

Before deriving LSE with respect to the average strain $\overline{\varepsilon}$, let us introduce derivation formulas

$$\frac{\partial\mathbf{a}^{\mathrm{T}}\mathbf{Xb}}{\partial\mathbf{X}} = \mathbf{ab}^{\mathrm{T}}, \quad \frac{\partial\mathbf{a}^{\mathrm{T}}\mathbf{X}^{\mathrm{T}}\mathbf{b}}{\partial\mathbf{X}} = \mathbf{ba}^{\mathrm{T}}, \text{ and } \quad \frac{\partial\mathbf{a}^{\mathrm{T}}\mathbf{X}^{\mathrm{T}}\mathbf{Xb}}{\partial\mathbf{X}} = \mathbf{Xba}^{\mathrm{T}} + \mathbf{Xab}^{\mathrm{T}}. \tag{51}$$

The derivation leads to

$$\frac{\partial\mathrm{LSE}(\overline{\varepsilon})}{\partial\overline{\varepsilon}} = \sum_{p\in\mathscr{P}} \left(\boldsymbol{0}2 - \Delta\boldsymbol{u}_p\Delta\boldsymbol{x}_p^{\mathrm{T}} - \Delta\boldsymbol{u}_p\Delta\boldsymbol{x}_p^{\mathrm{T}} + 2\overline{\varepsilon}\Delta\boldsymbol{x}_p\Delta\boldsymbol{x}_p^{\mathrm{T}}\right) \tag{52}$$

$$\Longleftrightarrow \frac{\partial Z}{\partial\overline{\varepsilon}} = 2\overline{\varepsilon}\sum_{p\in\mathscr{P}} \left(\Delta\boldsymbol{x}_p\Delta\boldsymbol{x}_p^{\mathrm{T}}\right) - 2\sum_{p\in\mathscr{P}} \left(\Delta\boldsymbol{u}_p\Delta\boldsymbol{x}_p^{\mathrm{T}}\right) \tag{53}$$

The stationnary point is attained if this derivative is equal to zero $\boldsymbol{0}2$. The average strain $\overline{\varepsilon}$ is solution of the equation

$$2\overline{\varepsilon}\sum_{p\in\mathscr{P}} \left(\Delta\boldsymbol{x}_p\Delta\boldsymbol{x}_p^{\mathrm{T}}\right) - 2\sum_{p\in\mathscr{P}} \left(\Delta\boldsymbol{u}_p\Delta\boldsymbol{x}_p^{\mathrm{T}}\right) = 0 \Longleftrightarrow \overline{\varepsilon} = \left(\sum_{p\in\mathscr{P}} \Delta\boldsymbol{u}_p\Delta\boldsymbol{x}_p^{\mathrm{T}}\right)\left(\sum_{p\in\mathscr{P}} \Delta\boldsymbol{x}_p\Delta\boldsymbol{x}_p^{\mathrm{T}}\right)^{-1} \tag{54}$$

Finally, Cundall's average strain is obtained as

$$\overline{\varepsilon} = \left(\sum_{p\in\mathscr{P}} \Delta\boldsymbol{u}_p\Delta\boldsymbol{x}_p^{\mathrm{T}}\right)\left(\sum_{p\in\mathscr{P}} \Delta\boldsymbol{x}_p\Delta\boldsymbol{x}_p^{\mathrm{T}}\right)^{-1} \tag{55}$$

B Symmetrization errors in the filtered dataset

In this section, the symmetrization errors (from Tables 4.3 to 4.5) have been computed after filtering the dataset to remove the elasticity tensors that are negative definite. The new results are reported in Tables 2 to 4

Percentage	Percentile of strain symmetrization error		
	Loading (1)	Loading (2)	Loading (3)
50%	0.0044%	0.0043%	0.0064%
90%	0.0401%	0.0271%	0.0404%
95%	0.0743%	0.0429%	0.0837%
99%	0.277%	0.0972%	0.197%
100%	2.15%	0.369%	3.41%

Table 2 • Percentiles of the strain symmetrization errors for each measurement loading in the filtered dataset.

Percentage	Percentile of stress symmetrization error		
	Loading (1)	Loading (2)	Loading (3)
50%	0.0020%	0.0016%	0.0041%
90%	0.0137%	0.0080%	0.0310%
95%	0.0229%	0.0163%	0.0692%
99%	0.0784%	0.0511%	0.552%
100%	6.40%	0.893%	9.68%

Table 3 • Percentiles of the stress symmetrization errors for each measurement loading in the filtered dataset.

Percentage	Percentile of major symmetrization error
50%	1.33%
60%	2.03%
70%	3.04%
80%	4.59%
90%	6.75%
95%	8.12%
99%	9.59%
99.5%	9.78%
100%	9.99%

Table 4 • Percentiles of the major symmetrization errors for each measurement loading in the filtered dataset.

C Eigenvalues of the derivative vs. Derivative of the eigenvalue

In this Appendix, let us quickly show the difference between (i) the eigenvalues of the derivative of the effective elasticity tensor, and (ii) the derivative of the eigenvalues of the effective elasticity tensor. This illustration is made with second-order tensor $\mathbf{t}$ of $\mathbb{R}^2$. Yet, it generalizes to higher order tensors and higher dimensions.

Let us recall the polar decomposition of the second-order tensor $\mathbf{t}$

$$\mathbf{t} = \frac{1}{2}\operatorname{tr}(\mathbf{t})\mathbf{1} + \mathbf{t}_{\text{vM}}\mathbf{r}(\theta_{\mathbf{t}}), \qquad \mathbf{r}(\theta_{\mathbf{t}}) = \begin{bmatrix} \cos(2\theta_{\mathbf{t}}) & \sin(2\theta_{\mathbf{t}}) \\ \sin(2\theta_{\mathbf{t}}) & -\cos(2\theta_{\mathbf{t}}) \end{bmatrix}. \tag{56}$$

Derivative of eigenvalues. Let us find the eigenvalues of $\mathbf{t}$ using the polar decomposition to parametrize $\mathbf{t}$. The eigenvalues of $\mathbf{t}$ are the roots of characteristic polynomial

$$\det(\mathbf{t} - \lambda\mathbf{1}) \implies \lambda^2 - \operatorname{tr}(\mathbf{t})\lambda + \frac{1}{4}\operatorname{tr}(\mathbf{t})^2 - \mathbf{t}_{\text{vM}}^2 = 0. \tag{57}$$

The eigenvalues are

$$T_1 = \frac{1}{2}\operatorname{tr}(\mathbf{t}) + \mathbf{t}_{\text{vM}}, \qquad T_2 = \frac{1}{2}\operatorname{tr}(\mathbf{t}) - \mathbf{t}_{\text{vM}}. \tag{58}$$

Their derivatives are

$$\frac{\partial T_1}{\partial t} = \frac{1}{2}\frac{\partial\operatorname{tr}(\mathbf{t})}{\partial t} + \frac{\partial\mathbf{t}_{\text{vM}}}{\partial t}, \qquad \frac{\partial T_2}{\partial t} = \frac{1}{2}\frac{\partial\operatorname{tr}(\mathbf{t})}{\partial t} - \frac{\partial\mathbf{t}_{\text{vM}}}{\partial t}. \tag{59}$$

Eigenvalues of derivative. Let us now compute the eigenvalues of the derivative of $\mathbf{t}$. Using the polar decomposition, the derivative is

$$\frac{\partial\mathbf{t}}{\partial t} = \frac{1}{2}\frac{\partial\operatorname{tr}(\mathbf{t})}{\partial t}\mathbf{1} + \frac{\partial}{\partial t}(\mathbf{t}_{\text{vM}}\mathbf{r}(\theta_{\mathbf{t}})) = \frac{1}{2}\frac{\partial\operatorname{tr}(\mathbf{t})}{\partial t}\mathbf{1} + \frac{\partial\mathbf{t}_{\text{vM}}}{\partial t}\mathbf{r}(\theta_{\mathbf{t}}) + \mathbf{t}_{\text{vM}}\frac{\partial\mathbf{r}(\theta_{\mathbf{t}})}{\partial t}. \tag{60}$$

Note that the expression is similar to the polar decomposition with an additional term corresponding to the rotation of the deviatoric part. This rotation also induces a rotation of the eigenbasis. At this point, we can already conclude that, in the general case,

$$\left(\frac{\partial\mathbf{t}}{\partial t}\right)_1 = \frac{1}{2}\frac{\partial\operatorname{tr}(\mathbf{t})}{\partial t} + \frac{\partial\mathbf{t}_{\text{vM}}}{\partial t} + f\left(\mathbf{t}_{\text{vM}}\frac{\partial\mathbf{r}(\theta_{\mathbf{t}})}{\partial t}\right), \qquad \left(\frac{\partial\mathbf{t}}{\partial t}\right)_2 = \frac{1}{2}\frac{\partial\operatorname{tr}(\mathbf{t})}{\partial t} - \frac{\partial\mathbf{t}_{\text{vM}}}{\partial t} + g\left(\mathbf{t}_{\text{vM}}\frac{\partial\mathbf{r}(\theta_{\mathbf{t}})}{\partial t}\right) \tag{61}$$

Conclusion. The derivative of the eigenvalues do not account for the variation due to the rotation of the eigenbasis. It only accounts for the variations of amplitude.

D Mazars-Drucker-Prager equivalent strain

(a) All data points

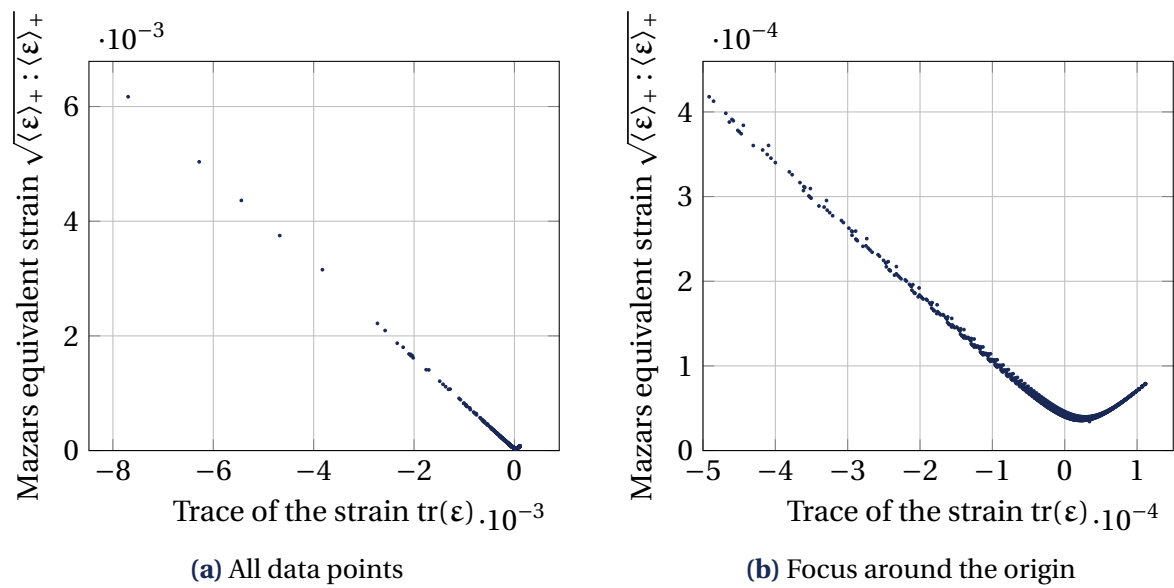**(b)** Focus around the origin

Figure 13 • Representation of the yield surface in the space of invariants corresponding to the modified Mazars-Drucker-Prager equivalent strain ($\varepsilon_{eq} = \sqrt{\langle \varepsilon \rangle_+ : \langle \varepsilon \rangle_+} + k \operatorname{tr}(\varepsilon)$).

E Another parametrization of second-order tensors

In this appendix, we introduce a parametrization of symmetric second-order tensor in $\mathbb{R}^2$ and describe how it is derived from the polar decomposition.

Polar decomposition. First, the polar decomposition of a symmetric second-order tensor **t** in $\mathbb{R}^2$ is (Verchery, 1982; Vannucci, 2005; Desmorat & Desmorat, 2015)

$$\mathbf{t} = \frac{1}{2}\operatorname{tr}(\mathbf{t})\mathbf{1} + t_{\text{vM}}\mathbf{R}(\theta), \quad \mathbf{R}(\theta) = \begin{bmatrix} \cos 2\theta & \sin 2\theta \\ \sin 2\theta & -\cos 2\theta \end{bmatrix} \tag{62}$$

where

$$\operatorname{tr}(\mathbf{t}) = \mathbf{t} : \mathbf{1}, \qquad t_{\text{vM}} = \sqrt{\frac{1}{2}\mathbf{t}' : \mathbf{t}'}, \qquad \theta = \frac{1}{2}\arctan\left(\frac{t'_{12}}{t'_{11}}\right), \tag{63}$$

are the polar components of the tensor **t**.

Hydrostatic proportion. This parametrization aims to separate the amplitude and the direction of the tensor. First, we factor the norm of the tensor (which will become the amplitude parameter)

$$\mathbf{t} = \|\mathbf{t}\| \left(\frac{1}{2}\frac{\operatorname{tr}(\mathbf{t})}{\|\mathbf{t}\|}\mathbf{1} + \frac{t_{\text{vM}}}{\|\mathbf{t}\|}\mathbf{R}(\theta) \right). \tag{64}$$

The next step consists in highlighting that there is a triangular equality due to the orthogonality between the hydrostatic and deviatoric parts

$$\|\mathbf{t}\|^2 = \left\| \frac{1}{2}\operatorname{tr}(\mathbf{t})\mathbf{1} \right\|^2 + \|\mathbf{t}'\|^2 \implies \|\mathbf{t}\|^2 = \frac{1}{2}\operatorname{tr}(\mathbf{t})^2 + 2t_{\text{vM}}^2. \tag{65}$$

Let us introduce the (signed) hydrostatic proportion D_m of **t**,

$$D_m = \frac{\operatorname{tr}(\mathbf{t})}{\sqrt{2}\|\mathbf{t}\|} \in [-1, 1] \tag{66}$$

which is an invariant of the tensor **t**. The hydrostatic proportion D_m directly relates to the deviatoric proportion through Equation (65)

$$t_{\text{vM}} = \|\mathbf{t}\|\frac{1}{\sqrt{2}}\sqrt{1 - D_m^2} \tag{67}$$

By replacing in the polar decomposition Equation (62), we obtain

$$\mathbf{t} = \frac{\|\mathbf{t}\|}{\sqrt{2}}\left(D_m\mathbf{1} + \sqrt{1 - D_m^2}\mathbf{R}(\theta) \right), \tag{68}$$

where $\|\mathbf{t}\|$ is the norm of the strain tensor, D_m is the hydrostatic proportion, and θ is the deviatoric angle.

Interpretation of the hydrostatic proportion. Some specific values of the hydrostatic proportion D_m are

- $D_m = -1$, when the tensor $\mathbf{t}$ is purely hydrostatic with a negative trace;

- $D_m = 0$, when the tensor $\mathbf{t}$ is purely deviatoric;

- $D_m = +1$, when the tensor $\mathbf{t}$ is purely hydrostatic with a positive trace.

Q **Remark .8** *By setting $D_m = \cos(\phi_h)$, we obtain*

$$\mathbf{t} = \frac{\|\mathbf{t}\|}{\sqrt{2}} \left(\cos(\phi_h)\mathbf{1} + \sin(\phi_h)\mathbf{R}(\theta) \right). \tag{69}$$

This decomposition can be qualified as "spherical" as the tensor is parametrized by an amplitude $\|\mathbf{t}\|$ and two angles: the hydrostatic angle ϕ_h and the deviatoric angle θ. However, the physical interpretation of ϕ_h is less direct.

F Calculation of the damage multiplier

The damage multiplier $\dot{\lambda}$ is obtained from the Kuhn-Tucker conditions ($\dot{\lambda} \geqslant 0, f \leqslant 0, \dot{\lambda} f = 0$). When the damage grows

$$\dot{f} = 0 \implies \dot{\varepsilon}_{\text{eq}} - \dot{C}(\mathbf{\Delta}) = 0 \implies \dot{\varepsilon}_{\text{eq}} - \dot{\mathbf{\Delta}} : \frac{\partial C}{\partial \mathbf{\Delta}} = 0. \tag{70}$$

By replacing the (auxiliary) damage evolution $\dot{\mathbf{\Delta}} = \dot{\lambda} \mathbf{P}$, we obtain

$$\dot{\varepsilon}_{\text{eq}} - \dot{\lambda} \mathbf{P} : \frac{\partial C}{\partial \mathbf{\Delta}} = 0 \implies \dot{\lambda} = \frac{\dot{\varepsilon}_{\text{eq}}}{\mathbf{P} : \frac{\partial C}{\partial \mathbf{\Delta}}}. \tag{71}$$

In the proposed model, the consolidation is

$$C(\mathbf{\Delta}) = C_0 + S_1 \operatorname{tr}(\mathbf{\Delta}) + \frac{S_2}{2} \mathbf{\Delta}' : \mathbf{\Delta}' \implies \frac{\partial C}{\partial \mathbf{\Delta}} = S_1 \mathbf{1} + S_2 \mathbf{\Delta}'. \tag{72}$$

Thus, the multiplier is

$$\dot{\lambda} = \frac{\dot{\varepsilon}_{\text{eq}}}{\mathbf{P} : (S_1 \mathbf{1} + S_2 \mathbf{\Delta}')} \implies \dot{\lambda} = \frac{\dot{\varepsilon}_{\text{eq}}}{S_1 \operatorname{tr}(\mathbf{P}) + S_2 \mathbf{P}' : \mathbf{\Delta}'} \tag{73}$$

G MFront code for the proposed model

The MFront code for the model is composed of two files (provided below),

1. the `model.mfront` file containing the main parts of the model and the integrator function,

2. the `TFEL_loiseau.hxx` file containing auxiliary functions.

With MFront installed and both files in the current directory, the model can be compiled for the `Cast3m` using the command

```
mfront -I $PWD --obuild --interface=castem loiseau.mfront
```

The codes for both files are provided in the following listings. This version of the code proposed here is working on the version `4.0` and `4.10` of MFront. It is now guaranteed to work with other versions.

Listing 1 • `model.mfront` file

```
@DSL ImplicitII;

@Behaviour loiseau;

@ModellingHypothesis PlaneStrain ;

@Includes {
#include "TFEL_loiseau.hxx"
}

// Define pi
@Parameter pi = 3.141592653589793;

// Define the parameters
@MaterialProperty stress young;
young.setGlossaryName("YoungModulus");
@MaterialProperty real nu;
nu.setGlossaryName("PoissonRatio");
@MaterialProperty real h;
@MaterialProperty real k;
@MaterialProperty real C0;
@MaterialProperty real alpha;
@MaterialProperty real S1;
@MaterialProperty real S2;
@MaterialProperty real gamma;

// Define the state variables
@StateVariable stensor<2u,real> HD;

// Define damage
@AuxiliaryStateVariable stensor<2u,real> Da;

// Define initial elastic properties as local variables
```

```
@LocalVariable stress mu0;
@LocalVariable stress ka0;

// Define invariants and covariants
@LocalVariable stress           mu;
@LocalVariable stress           ka;
@LocalVariable stensor<2u,real> dp;
@LocalVariable st2tost2<2u,real> H;
@LocalVariable st2tost2<2u,real> E;
@LocalVariable st2tost2<2u,real> E0;
@LocalVariable st2tost2<2u,real> E0_inv;

// Define constant local variables
@LocalVariable stensor<2u,real>  I2;
@LocalVariable st2tost2<2u,real> I4;
@LocalVariable st2tost2<2u,real> I2xI2;
@LocalVariable st2tost2<2u,real> J4;

@InitializeLocalVariables{
    // Define tensorial constants
    I2(0) = 1.;
    I2(1) = 1.;
    I2(2) = 0.;
    I2(3) = 0.;
    I2xI2 = I2^I2;
    I4(0,0) = 1.;
    I4(1,1) = 1.;
    I4(3,3) = 1.;
    J4 = I4 - 1./2. * I2xI2;
    // Store initial elasticity properties
    mu0 = young/(2.*(1.+nu));
    ka0 = young/(2.*(1.-nu));
    // Store initial invariants and covariants
    E0  = 2.*mu0*J4 + ka0*I2xI2;
    E0_inv  = 1./(2.*mu0)*J4 + 1./(4*ka0)*I2xI2;
    // Compute deviatoric part of damage
    const auto Da_dev = tfel::math::extensions::dev(Da, I2);
    // Compute damage invariants
    const auto I1_Da = Da|I2;
    const auto I2_Da = Da|Da;
    // Update the bulk modulus
    ka = tfel::math::extensions::ka(ka0, I1_Da);
    // Update the shear modulus
    mu = tfel::math::extensions::mu(mu0, ka0, I1_Da, I2_Da);
    // Update the dilatation tensor
    dp = tfel::math::extensions::dp(ka0, Da_dev);
    // Update the harmonic tensor
    H = tfel::math::extensions::H(h, I1_Da, Da_dev, J4);
    // Update the elasticity tensor
    E = 2.*mu*J4 + ka*I2xI2 + (1./2.)*((I2^dp) + (dp^I2)) + H;
}


@PredictionOperator{
```

```
    // Set the effective elasticity tensor as the prediction operator
    Dt = E;
}

@Predictor{
    sig = E*eval(eto+deto);
}

@Integrator{
    // Compute equivalents strain at previous load step (n-1)
    const real eto_eq_nm1 = tfel::math::extensions::epseq(eto, k, I2);
    // Compute equivalent strain at current load step (n)
    const stensor<2u,real> eto_n = eval(eto+deto);
    const real eto_eq_n = tfel::math::extensions::epseq(eto_n, k, I2);
    // Compute H(D) and its invariants at previous load step (n-1)
    const stensor<2u,real> HD_nm1 = HD;
    const stensor<2u,real> HD_dev_nm1 =
        tfel::math::extensions::dev(HD_nm1, I2);
    // Compute H(D) and its invariants at previous load step (1)
    const stensor<2u,real> HD_n = eval(HD + dHD);
    const stensor<2u,real> HD_dev_n =
        tfel::math::extensions::dev(HD_n, I2);
    // Compute consolidation function
    const real C1_nm1 = S1*(HD_nm1|I2) + 1./2.*S2*(HD_dev_nm1|
  HD_dev_nm1);
    // Compute the damage residual
    if (eto_eq_n - (C0 + C1_nm1) > 0) {
        // Increment of equivalent strain
        const real d_eto_eq = eto_eq_n - eto_eq_nm1;
        // Compute the denimator for the model
        const stensor<2u,real> dCdHD = S1*I2 + S2*HD_dev_n;
        // Compute the damage direction
        stensor<2u,real> p_HD_n = positive_part(eto_n);
        // Normalize the damaging direction
        p_HD_n /= sqrt(p_HD_n|p_HD_n);
        // Compute the Lagrange multiplier increment
        const auto dl = d_eto_eq / (p_HD_n|dCdHD);
        // Compute damage increment (from the model)
        const auto dHD_mod = dl * p_HD_n;
        // Residual associated to HD
        fHD -= dHD_mod;
    }
}

@UpdateAuxiliaryStateVariables{
    // Update damage damage
    Da = tfel::math::extensions::compute_damage(HD, alpha);
}

@ComputeFinalStress{
    // Compute deviatoric part of damage
    const auto Da_dev = tfel::math::extensions::dev(Da, I2);
    // Compute damage invariants
```

```
    const auto I1_Da = Da|I2;
    const auto I2_Da = Da|Da;
    // Update the bulk modulus
    ka = tfel::math::extensions::ka(ka0, I1_Da);
    // Update the shear modulus
    mu = tfel::math::extensions::mu(mu0, ka0, I1_Da, I2_Da);
    // Update the dilatation tensor
    dp = tfel::math::extensions::dp(ka0, Da_dev);
    // Update the harmonic tensor
    H = tfel::math::extensions::H(h, I1_Da, Da_dev, J4);
    // Update the elasticity tensor
    E = 2.*mu*J4 + ka*I2xI2 + (1./2.)*((I2^dp) + (dp^I2)) + H;
    // Compute the stress
    sig = E*eto;
}


@TangentOperator{
    // This should be L in dsig/dt=L:deps/dt
    Dt = E;
}
```

Listing 2 • `TFEL_loiseau.hxx` file

```
#ifndef LOISEAU_TFEL
#define LOISEAU_TFEL 1

namespace tfel::math::extensions {
    /**
     * Compute the deviatoric part of a second order tensor.
     */
    template <typename real>
    stensor<2u, real> dev(const stensor<2u, real> &T,
                          const stensor<2u, real> &I2) {
        return T - 1. / 2. * (T | I2) * I2;
    }


    /**
     * Compute damage.
     */
    template <typename real>
    stensor<2u, real> compute_damage(const stensor<2u, real> &HD,
                                     const real &alpha) {
        // Make a local copy of HD
        stensor<2u, real> ls(HD);
        // Declare and compute eigenvalues and eigenvectors
        tvector<3u, real> vp;
        tmatrix<3u, 3u, real> m;
        ls.computeEigenVectors(vp, m);
        // Compute eigentensors
        stensor<2u, real> n0, n1, n2;
        stensor<2u, real>::computeEigenTensors(n0, n1, n2, m);
        // Add terms associated to each eigenvalues
        real pi = 3.141592653589793;
```

```cpp
      stensor<2u, real> func_HD = 2./pi*atan(pow(vp(0), alpha))*n0 +
                                  2./pi*atan(pow(vp(1), alpha))*n1 +
                                  2./pi*atan(pow(vp(2), alpha))*n2;
    // // Uncomment to use the change of variable based on Ladeveze
    // stensor<2u,real> func_HD = (1.-pow(1.+vp(0), -alpha)) * n0 +
    //                            (1.-pow(1.+vp(1), -alpha)) * n1 +
    //                            (1.-pow(1.+vp(2), -alpha)) * n2;
    // Return the tensor
    return func_HD;
}


/**
 * Compute the bulk modulus.
 */
template <typename real> real ka(const real &ka0,
                                 const real &I1_Da) {
    return ka0 * (1. - 1. / 2. * I1_Da);
}


/**
 * Compute the shear modulus.
 */
template <typename real>
real mu(const real &mu0,
        const real &ka0,
        const real &I1_Da,
        const real &I2_Da) {
    return mu0 - 1./4.*ka0*I1_Da + 1./4.*(ka0-2.*mu0)*I2_Da;
}


/**
 * Compute the deviatoric part of the dilatation tensor.
 */
template <typename real>
stensor<2u, real> dp(const real &ka0,
                     const stensor<2u, real> &Da_dev) {
    return -2.*ka0*Da_dev;
}


/**
 * Compute the harmonic part.
 */
template <typename real>
st2tost2<2u, real> H(const real &h, const real &I1_Da,
                     const stensor<2u, real> &Da_dev,
                     const st2tost2<2u, real> &J4) {
    return h*pow(I1_Da, 4.) *
           ((Da_dev ^ Da_dev) - 1./2.*(Da_dev | Da_dev)*J4);
}


/**
 * Compute Drucker-Prager equivalent strain.
 */
```

```cpp
    template <typename real>
    real epseq(const stensor<2u, real> &eps,
               const real &k,
               const stensor<2u, real> &I2) {
        // Compute the deviatoric part of the tensor
        const auto eps_dev = dev(eps, I2);
        // Compute von Mises equivalent strain
        const auto eps_vM = sqrt(2. * (eps_dev | eps_dev));
        // Compute and return Drucker-Prager equivalent strain
        return eps_vM + k * (eps | I2);
    }
} // namespace tfel::math::extensions
#endif /* LOISEAU_TFEL */
```

H   Procedure employed to fit the model

Model parameters are identified through a parametric study. The elastic parameters are set before the identification process. The other parameters are sampled using the Latin Hypercube Sampling method (McKay et al., 1979). The parameter space being sampled is

$$C_0 \in [10^{-6}, 10^{-4}], \qquad k \in [0.1, 4], \qquad \alpha \in [0.1, 10], \qquad S_1 \in [10^{-5}, 10^{-3}], \qquad S_2 \in [10^{-5}, 10^{-3}]. \tag{74}$$

Those intervals are the lower and upper bounds to fit the proposed model. Depending on the modeling choices, they have been refined during the fitting process (mainly to ensure the convergence of the non-linear solver). Also note that the parameters C_0, S_1, and S_2 are sampled with a logarithmic scale. Finally, this parameter space has been sampled with $2^{16} = 65\,536$ points, *i.e.* parameter sets.

Using the MTest utility from MFront, the reference loading cases (bitension, tension, and shear) are applied to a material point for each parameter set. The stress and damage responses predicted with the model are then compared to the results from the reference beam-particle simulations. The error is quantified between the stress and damage evolutions with

$$e_{\boldsymbol{\sigma}} = \frac{\sum_{k=1}^{N_t} \| \boldsymbol{\sigma}^k_{\text{model}} - \boldsymbol{\sigma}^k_{\text{ref}} \|}{\sum_{k=1}^{N_t} \| \boldsymbol{\sigma}^k_{\text{ref}} \|}, \qquad e_{\mathbf{D}} = \frac{\sum_{k=1}^{N_t} \| \mathbf{D}^k_{\text{model}} - \mathbf{D}^k_{\text{ref}} \|}{\sum_{k=1}^{N_t} \| \mathbf{D}^k_{\text{ref}} \|} \tag{75}$$

where $N_t = 100$ is the number of load steps, $\bullet^k$ is the tensor ($\boldsymbol{\sigma}$ or $\mathbf{D}$) at load step k. The set of parameters with the smallest errors are chosen as the best fitting results.

I   Extended abstract in French

I.1   Contexte général

L'un des principaux défis actuels est d'assurer une production et une utilisation durables de l'énergie et des matériaux. Ce défi rend nécessaire la recherche sur les matériaux, afin d'assurer leur utilisation durable dans les structures tout en garantissant qu'ils remplissent leur fonction au fil du temps. Cette thèse se concentre sur l'étude des matériaux quasi-fragiles, tels que le béton, les céramiques ou encore la glace. Ces matériaux sont largement utilisés dans divers domaines tels que les infrastructures, le transport et l'énergie. En particulier, le béton est le matériau le plus utilisé au monde. Selon le rapport de Chatham House, la production de ciment est responsable d'environ 8% des émissions mondiales de CO2 (Lehne & Preston, 2018). Il est donc nécessaire d'employer ces matériaux de manière plus efficace (par exemple, en réduisant les marges de sécurité dans la conception des structures) afin de réduire leur utilisation et l'impact de leur production.

Il est donc essentiel de comprendre comment un matériau se comporte au cours de son cycle de vie. Pour atteindre cet objectif, il faut décrire avec précision le comportement (complexe) des matériaux quasi-fragiles jusqu'à leur rupture. En particulier, quand il est soumis à diverses charges (mécaniques, thermiques, etc.), l'état du matériau peut changer et ainsi dégrader ses propriétés mécaniques. En fonction de ce changement, la capacité de la structure à remplir sa fonction peut être compromise, mettant potentiellement en danger des vies humaines ainsi l'équipement. La dégradation mécanique des matériaux quasi-fragiles, généralement due à la nucléation de microfissures, a une forte influence sur leur comportement mécanique. Elle entraîne notamment une perte de rigidité et, potentiellement, des variations des propriétés du matériau en fonction de son orientation. Une telle dégradation se produit lorsque le matériau est soumis à des chargements mécaniques élevées. La prise en compte de ce changement de comportement est de la plus haute importance pour réaliser des simulations précises et ainsi pouvoir faire un conception efficace des structures.

I.2   Approche scientifique

Cette thèse vise à modéliser la dégradation, c'est-à-dire la microfissuration, des matériaux quasi-fragiles. La première étape consiste à rassembler des données de référence sur le comportement des matériaux quasi-fragiles. Les données recueillies doivent ensuite être analysées afin d'identifier les différents phénomènes qui se produisent au cours de la dégradation. À partir d'un tel ensemble de données, un modèle mathématique de leur dégradation peut être développé. Cette dernière tâche est généralement divisée en deux sous-tâches : (1) modéliser comment la dégradation affecte le comportement du matériau, et (2) modéliser quand et comment la dégradation évolue lorsqu'une chargement mécanique est appliqué.

Pour formuler un modèle d'endommagement multiaxial, il faut d'abord recueillir des données sur la dégradation du matériau. Il s'agit de comprendre comment la dégradation évolue dans le temps et affecte le comportement du matériau sous différentes charges multiaxiales et non proportionnelles. Ce processus nécessite une mesure précise de l'évolution des propriétés élastiques effectives au cours de chaque chargement. En outre, chaque expérience

doit être répétée suffisamment pour obtenir un nombre de résultats statistiquement significatif. Cependant, il serait difficile, voire impossible, de mener une campagne expérimentale d'une telle ampleur. En effet, il faudrait réaliser des essais de caractérisation des matériaux très précis sur un nombre important d'échantillons, dont certains fortement endommagés. C'est pourquoi ce travail utilise les essais virtuels comme une approche alternative et complémentaire aux expériences. Les essais virtuels consistent à utiliser un modèle, estimé suffisamment précis, donnant réponse du matériau à une méso-échelle pour simuler et étudier son comportement macroscopique. Dans ce travail, le modèle à méso-échelle choisi est un modèle discret *beam-particle* qui fournit une représentation explicite de la microfissuration. En outre, il prend en compte de manière précise l'impact des microfissures sur le comportement macroscopique du matériau. Cependant, nous avons choisi de négliger l'effet de fermeture des fissures pour cette étude. Les résultats des essais virtuels en 2D serviront à constituer un ensemble de données de tenseurs d'élasticité effective bidimensionnels. Cet ensemble de données sera notre référence pour formuler le modèle d'endommagement multiaxial.

Cette thèse porte une attention particulière à l'analyse rigoureuse de l'anisotropie induite par la microfissuration. En mécanique de l'endommagement, ce phénomène est appelé anisotropie induite par l'endommagement (*damaged-induced anisotropy*). Pour étudier cette dernière, des notions mathématiques liées aux symétries des matériaux en 2D sont rappelées et utilisées. En particulier, la distance d'un tenseur d'élasticité aux différentes classes de symétrie sont utilisées pour justifier la nécessité de modèles d'endommagement anisotrope. La notion d'invariants et de covariants (une généralisation tensorielle des invariants) est également utilisée pour analyser les tenseurs sans référence à une base particulière. Après ces premières analyses, nous visons à formuler un modèle qui rend compte de la manière dont la microfissuration affecte le tenseur d'élasticité effectif en 2D. Nous nous appuyons sur une formule de reconstruction tensorielle (équivariante) pour les tenseurs d'élasticité afin de simplifier le processus de modélisation. Cette formule donne une expression du tenseur d'élasticité à partir de ses invariants et covariants (tensoriels), aussi appelés composantes harmoniques. La principale idée pour la formulation du modèle consiste à modéliser les composantes harmoniques en fonction de l'endommagement, puis à utiliser la formule de reconstruction pour obtenir le tenseur d'élasticité effectif comme une fonction de l'endommagement. Sur la base de la formule de reconstruction, des travaux antérieurs ont introduit une variable d'endommagement (tensorielle), un covariant du tenseur d'élasticité effectif, pour représenter l'état de dégradation du matériau. Elle a la particularité d'offrir des expressions explicites pour deux (sur quatre) des composantes harmoniques comme des fonctions de la variable d'endommagement. Les composantes harmoniques restantes sont modélisées sur la base de l'ensemble de données de référence. En particulier, une approche parsimonieuse et interprétable est employée pour formuler l'une des parties du modèle. Pour compléter le modèle, nous devons modéliser l'évolution de la dégradation, c'est-à-dire de l'endommagement, lorsqu'un chargement mécanique est appliqué au matériau. Tout d'abord, nous devons établir un critère permettant d'identifier le moment où l'endommagement se produit, sur la base des données issues de simulations discrètes. Ensuite, nous formulerons un modèle d'évolution préliminaire de l'endommagement pour décrire la façon dont la dégradation évolue au cours d'un chargement mécanique.

En résumé, cette étude propose d'utiliser une approche basée sur des essais virtuels pour formuler un modèle de d'endommagement anisotrope pour les matériaux quasi-fragiles. Les expériences virtuelles sont réalisées en simulant des éléments de surface à l'aide d'un modèle discret *beam-particle*. Les résultats de ces simulations, c'est-à-dire les évolutions des tenseurs d'élasticité effectifs des éléments de surface, sont stockées dans un ensemble de données. En analysant ces résultats, nous mettons en évidence la nécessité d'un modèle d'endommagement anisotrope pour décrire leur comportement. L'ensemble de données sert ensuite de référence pour la formulation du modèle d'endommagement anisotrope. Tout d'abord, l'impact de l'endommagement, *i.e.* micro-fissuration, sur le tenseur d'élasticité effectif est modélisé, ce qui conduit à la formulation du potentiel d'état. Ensuite, une loi d'évolution de l'endommagement (non standard) est proposée pour compléter le modèle. L'endommagement non-local est ensuite discuté pour introduire l'application du modèle à la simulation de structures.

I.3   Organisation de la thèse

Cette thèse est organisée en deux parties. La première partie, constituée des chapitres 1, 2 et 3, est principalement consacrée à l'analyse des travaux existants dans la littérature. Elle situe ce travail dans le contexte de la littérature existante, justifie la méthodologie de recherche et introduit les notions et les outils (existants) utilisés dans la deuxième partie. La seconde partie, constituée des chapitres 4, 5 et 6, est dédiée aux principales contributions de ce travail: la génération de l'ensemble de donnée de référence, la formulation du modèle d'état et la formulation d'une loi d'évolution préliminaire.

I.4   Principaux résultats et conclusions

Le chapitre 1 présente les observations expérimentales sur les matériaux quasi fragiles pour justifier leur étude et le besoin de les modéliser. Les résultats expérimentaux d'essais mécaniques sur des matériaux quasi fragiles montrent différents phénomènes : perte de rigidité, anisotropie induite par l'endommagement et effets de fermeture des fissures. Ces phénomènes sont tous expliqués par la nucléation et la croissance de microfissures. Pour modéliser les matériaux quasi-fragiles, on distingue deux types de modèles dans ce travail : les modèles discrets et les modèles continus. Les modèles discrets sont également subdivisés en trois sous-types : les modèles particulaires, les modèles treillis (*lattice*) et les modèles hybrides. Ils fournissent une représentation précise de la rupture des matériaux quasi fragiles en tenant compte explicitement de la microfissuration. Toutefois, leur coût de calcul limite leur utilisation pour modéliser des structures entières. Les modèles d'endommagement continus offrent une vue homogénéisée (à l'échelle macroscopique) des effets de la dégradation (à l'échelle mésoscopique). Ce point de vue homogénéisé permet, entre autre, de simuler des structure à moindre coût. Pour finir, ce chapitre présente aussi la formulation de modèle d'endommagement. Après avoir choisi une variable d'état pour décrire l'état du matériau, un modèle d'endommagement continu se compose de trois ingrédients principaux : un potentiel d'état, une fonction de critère d'endommagement et une loi d'évolution. Différents modèles d'endommagement issus de la littérature sont aussi présentés de ce chapitre.

L'objectif du chapitre 2 est de présenter les différents outils mathématiques utilisés dans la formulation du modèle. Dans un premier temps, des définitions fondamentales pour ce travail (tenseur d'élasticité, strate de symétrie, invariant, covariant, ...) ainsi que leurs interprétations sont données. Ensuite, la décomposition harmonique est introduite. Sur cette base, deux formules différentes de reconstruction du tenseur d'élasticité sont rappelées : une pour un tenseur d'élasticité génériques et une pour les tenseurs orthotropes. Ces décompositions serviront de base pour la formulation du modèle d'endommagement. D'autres outils mathématiques sont aussi introduits : les distances à l'isotropie et à l'orthotropie, ainsi qu'une borne supérieure de la distance à l'orthotropie. Ces distances permettent de vérifier dans quelle strate de symétrie se trouve un tenseur d'élasticité et sont utilisées dans les chapitres suivants pour la modélisation.

Une fois tous les outils fondamentaux présentés, l'étape suivante consiste à générer l'ensemble de données de référence pour la constitution du modèle. Cet ensemble de données doit contenir des évolutions du tenseur d'élasticité effectif d'éléments d'aire quasi-fragiles soumis à différent chargements mécaniques. Le chapitre 3 introduit le modèle discret *beam-particle* et montre comment obtenir les propriétés élastiques effectives d'éléments d'aire microfissurés dans le modèle discret. Après une présentation du modèle *beam-particle*, une brève introduction à l'homogénéisation est fournie. Sur cette base, une procédure de mesure des tenseurs d'élasticité effective d'éléments d'aire carrés, éventuellement micro-fissurés, est proposée. La procédure consiste à appliquer trois chargements élastiques in-dépendants, aussi appelés chargements de mesure, à l'élément d'aire. Différents choix de chargements de mesure (conditions aux limites cinématiquement uniformes, périodiques, ou statiquement uniformes) sont comparés et les conditions aux limites périodiques sont retenues. Après avoir comparé différentes méthodes de calcul des déformations et contraintes moyennes, la déformation moyenne est calculée à l'aide de la méthode de Bagi (1996) et la contrainte moyenne à l'aide de la méthode de Drescher and de Josselin de Jong (1972). En utilisant les déformations et les contraintes moyennes des trois charges de mesure, le tenseur d'élasticité effectif est calculé. Un algorithme et une illustration schématique d'une mesure du tenseur d'élasticité à partir du modèle discret sont proposés pour résumer la procédure en Section 3.5.

Le chapitre 4 a pour but de générer un ensemble de données de tenseurs d'élasticité effective et de l'analyser. En soumettant un élément d'aire à 21 chargements multiaxiaux (proportionnels et non proportionnels) et en appliquant la procédure de mesure proposé au chapitre précédent, un ensemble de 76 756 tenseurs d'élasticité effectifs a été constitué. Ces données nous serviront de référence dans les chapitres suivants. Après avoir illustré son contenu, nous avons montré que certaines erreurs de symétrisation dans la procédure de mesure ne sont pas négligeables, ce qui indique qu'un tenseur d'élasticité ne peut pas représenter exactement l'échantillon microfissuré. En particulier, un milieu de Cauchy n'est peut-être pas suffisant pour décrire le milieu micro-fissuré. Liées à ces erreurs, nous avons montré que certains tenseurs mesurés ont des valeurs propres négatives. Nous avons fait le choix de retirer ces tenseurs de l'ensemble de données pour la suite. Quelques incohérences sont également présentes dans l'évolution des tenseurs d'élasticité effective, car une minorité d'incréments sont définis positifs. Ces données ne sont pas filtrées mais nous imposerons une croissance de l'endommagement dans le modèle d'évolution de l'endommagement pour

garantir le respect du second principe. Le calcul de la distance des tenseurs à l'isotropie et à l'orthotropie fournit d'autres résultats essentiels. Tout d'abord, le tenseur d'élasticité effectif des éléments d'aire étudiés est isotrope quand ils ne sont pas micro-fissurés. Ensuite, la distance à l'isotropie devient significative pour une grande partie des tenseurs effectifs (endommagés). Ainsi, la plupart des tenseurs d'élasticité effectifs s'écartent de l'isotropie lorsque les microfissures apparaissent. Cela confirme que l'endommagement induit une anisotropie du comportement effectif. De plus, la plupart des tenseurs d'élasticité effective restent proches de l'orthotropie pendant le processus de dégradation. Cette observation justifie la nécessité d'une variable d'endommagement anisotrope (tensorielle), et plus précisément d'une variable orthotrope (tensorielle du second ordre). De plus, cela signifie que la reconstruction orthotropique par covariants, présentée dans la Section 2.2, peut être utilisée pour modéliser les tenseurs d'élasticité effectifs.

Le chapitre 5 vise à développer un modèle d'état tenant compte de l'endommagement anisotrope dans le matériau, c'est-à-dire un modèle du couplage entre l'endommagement anisotrope et l'élasticité effective. Pour ce faire, nous avons utilisé la reconstruction orthotrope du tenseur d'élasticité effectif (à partir de covariants) basée sur la décomposition harmonique pour faciliter la formulation. Ainsi, le problème de modélisation passe de la formulation de l'ensemble des composantes indépendantes du tenseur d'élasticité en fonction de l'endommagement à celle de ses composantes harmoniques (invariants et covariants). Tout d'abord, la variable d'endommagement est introduite pour représenter la microfissuration. Elle est basée sur le tenseur de dilatation, un covariant du tenseur d'élasticité effectif. La variable d'endommagement est alors elle-même un covariant du tenseur d'élasticité effectif. Ce choix de la variable d'endommagement nous permet de modéliser exactement deux composantes harmoniques (sur quatre) : le module de compressibilité κ et la partie déviatorique du tenseur de dilatation $\mathbf{d}'$. La suite de ce chapitre consiste alors à modéliser en fonction de l'endommagement les deux composantes harmoniques restantes: le module de cisaillement μ et la partie harmonique $\mathbf{H}$. En analysant l'ensemble de données, nous avons proposé un modèle pour le module de cisaillement μ effectif en fonction de l'endommagement. Ce modèle introduit un paramètre optionnel, le paramètre de couplage cisaillement-endommagement non linéaire m. Pour modéliser la partie harmonique, une analyse des données montrent que la partie harmonique peut-être modéliser en fonction de l'endommagement. Cependant, la relation entre les deux est complexes à determiner. Pour résoudre ce problème, nous avons choisit de représenter cette relation par un polynôme générique d'invariants de l'endommagement. Afin d'identifier (et filtrer) les nombreux paramètres de ce modèle, nous avons appliqué une régression parsimonieuse (*sparse regression*). Cette regression parsimonieuse permet d'automatiquement rendre nul les coefficients non-nécessaires au modèle. Après régression, le modèle proposé pour la partie harmonique introduit seulement un paramètre, le pré-facteur harmonique h. Avant de conclure ce chapitre, le modèle de tenseur d'élasticité effectif est évalué par comparaison avec l'ensemble de données. Il en ressort que le modèle proposé permet de prédire de manière satisfaisante les tenseurs d'élasticité effectifs de l'ensemble de données. Indirectement, ces résultats montrent qu'un tenseur d'endommagement du second ordre est suffisant pour représenter l'impact de la microfissuration sur l'élasticité effective pour l'ensemble de données considéré. La nécessité de prendre en compte l'anisotropie induite

par l'endommagement dans le modèle est également soulignée. En effet, on montre que la prédiction des contraintes (en connaissant la déformation et l'endommagement) par un modèle isotrope peut être très éloignée de la référence contrairement à la contrainte prédite avec le modèle anisotrope proposé.

Dans le chapitre 6, le modèle est complété en proposant une loi d'évolution (préliminaire) non-standard de l'endommagement. La première étape de la construction du modèle est l'analyse de l'initiation de la microfissuration dans les éléments d'aire. En particulier, une méthode efficace est proposée pour obtenir la surface d'élasticité de l'élément d'aire discret. En appliquant cette méthode, on détermine que la déformation équivalente dans le critère d'endommagement peut être modélisée par la déformation équivalente de Drucker-Prager. Ce résultat peut sembler surprenant, mais rappelons que le présent travail est consacré aux cas 2D. Ensuite, l'évolution de l'endommagement dans les éléments d'aire est analysée. En particulier, l'importance de la bi-axialité de l'endommagement est soulignée : même dans les cas de chargement uni-axial, l'endommagement sera bi-axial. Une loi d'évolution de l'endommagement non standard est ensuite proposée. Pour faciliter la limitation de l'endommagement, l'évolution est formulée sur une variable d'endommagement auxilaire. Cette technique permet de borner l'endommagement simplement et de faciliter la formulation du modèle d'évolution. Deux variables d'endommagement auxiliaires sont proposées. De plus, une fonction de consolidation, formulée comme une combinaison linéaire d'invariants de l'endommagement, est proposée. En indentifiant la loi d'évolution de l'endommagement à un cas de chargement en bitension, les deux choix de variables auxiliaires sont comparés. Le choix d'un changement de variable avec une dérivée non monotone permet de mieux modéliser l'évolution de l'endommagement pendant la phase de microfissuration diffuse. En effet, le taux d'endommagement des lois classiques est généralement haut en début d'endommagement puis décroit. La variable auxiliaire proposée dans ce travail permet d'avoir un taux d'endommagement d'abord faible (correspondant à la phase de microfissuration diffuse), puis qui augmente durant la coalescence et qui diminue pour que les endommagement principaux atteignent asymptotiquement 1. Cependant, la loi d'évolution non standard proposée dans ce travail doit encore être étendue, en particulier la direction d'endommagement **P**. Enfin, dans le but d'appliquer le modèle à des simulations structurelles, l'endommagement non local est abordé. Les modèles classiques, avec des interactions constantes, et les modèles plus récents, avec des interactions variables, sont présentés et discutés. L'application à la simulation de structures est laissée pour des travaux futurs.

Bibliography

Alejano, L. R., & Bobet, A. (2012). Drucker–prager criterion. *Rock Mechanics and Rock Engineering, 45*(6), 995–999. https://doi.org/10.1007/s00603-012-0278-2 (cit. on p. 25)

Andrieux, S., Bamberger, Y., & Marigo, J.-J. (1986). Model of microcracked material for concrete and rocks. *Journal de Mécanique Théorique et Appliquée, 5* (cit. on pp. 13, 20).

Angrand, L. (2016). *Modèle d'endommagement incrémental en temps pour la prévision de la durée de vie des composites tissés 3D en fatigue cyclique et en fatigue aléatoire* (Doctoral dissertation). Université Paris-Saclay. (Cit. on p. 21).

Antonelli, A., Desmorat, B., Kolev, B., & Desmorat, R. (2022). Distance to plane elasticity orthotropy by euler–lagrange method. *Comptes Rendus. Mécanique, 350*, 413–430. https://doi.org/10.5802/crmeca.122 (cit. on pp. 42, 43)

As'ad, F., Avery, P., & Farhat, C. (2022). A mechanics-informed artificial neural network approach in data-driven constitutive modeling. *International Journal for Numerical Methods in Engineering, 123*(12), 2738–2759. https://doi.org/10.1002/nme.6957 (cit. on p. 30)

Auffray, N., Kolev, B., & Petitot, M. (2014). On anisotropic polynomial relations for the elasticity tensor. *Journal of Elasticity, 115*(1), 77–103. https://doi.org/10.1007/s10659-013-9448-z (cit. on p. 34)

Azzi, P., Desmorat, R., Kolev, B., & Priziac, F. (2022). The distance to cubic symmetry class as a polynomial optimization problem. https://doi.org/10.48550/arXiv.2203.14562. (Cit. on p. 137)

Badel, P., Godard, V., & Leblond, J.-B. (2007). Application of some anisotropic damage model to the prediction of the failure of some complex industrial concrete structure. *International Journal of Solids and Structures, 44*(18), 5848–5874. https://doi.org/10.1016/j.ijsolstr.2007.02.001 (cit. on p. 23)

Bagi, K. (1996). Stress and strain in granular assemblies. *Mechanics of Materials, 22*(3), 165–177. https://doi.org/10.1016/0167-6636(95)00044-5 (cit. on pp. 55, 56, 63, 156)

Bagi, K. (2006). Analysis of microstructural strain tensors for granular assemblies. *International Journal of Solids and Structures, 43*(10), 3166–3184. https://doi.org/10.1016/j.ijsolstr.2005.07.016 (cit. on pp. 54, 57)

Bažant, Z. P. (1976). Instability, ductility, and size effect in strain-softening concrete. *Journal of the Engineering Mechanics Division, 102*(2), 331–344. https://doi.org/10.1061/JMCEA3.0002111 (cit. on p. 27)

Bažant, Z. P. (1984). Size effect in blunt fracture: Concrete, rock, metal. *Journal of Engineering Mechanics, 110*(4), 518–535. https://doi.org/10.1061/(ASCE)0733-9399(1984)110:4(518) (cit. on p. 7)

Bažant, Z. P., & Jirásek, M. (2002). Nonlocal integral formulations of plasticity and damage: Survey of progress. *Journal of Engineering Mechanics, 128*(11), 1119–1149. https://doi.org/10.1061/(ASCE)0733-9399(2002)128:11(1119) (cit. on p. 27)

Bažant, Z. P., & Planas, J. (2019). *Fracture and size effect in concrete and other quasibrittle materials.* Routledge. https://doi.org/10.1201/9780203756799. (Cit. on p. 7)

Bažant, Z. P., Tabbara, M. R., Kazemi, M. T., & Pijaudier-Cabot, G. (1990). Random particle model for fracture of aggregate or fiber composites. *Journal of Engineering Mechanics, 116*(8), 1686–1705. https://doi.org/10.1061/(ASCE)0733-9399(1990)116:8(1686) (cit. on p. 15)

Beetham, S., & Capecelatro, J. (2020). Formulating turbulence closures using sparse regression with embedded form invariance. *Physical Review Fluids, 5*(8), 084611. https://doi.org/10.1103/PhysRevFluids.5.084611 (cit. on p. 31)

Benallal, A., Billardon, R., & Geymonat, G. (1993). Bifurcation and localization in rate-independent materials. some general considerations. In Q. S. Nguyen (Ed.), *Bifurcation and stability of dissipative systems* (pp. 1–44). Springer. https://doi.org/10.1007/978-3-7091-2712-4_1. (Cit. on p. 27)

Benallal, A., Billardon, R., & Geymonat, G. (1989). Conditions de bifurcation à l'intérieur et aux frontière pour une classe de matériaux non-standards. (bifurcation conditions inside and at the boundary for a class of non-standard materials). *Comptes rendus de l'Académie des sciences. Série 2* (cit. on p. 27).

Benelfellah, A. (2013). *Contribution à la modélisation de l'anisotropie induite par endommagement d'un matériau agrégataire énergétique* (Doctoral dissertation). Université François Rabelais de Tours. (Cit. on p. 20).

Bernard, P. E., Moës, N., & Chevaugeon, N. (2012). Damage growth modeling using the thick level set (TLS) approach: Efficient discretization for quasi-static loadings. *Computer Methods in Applied Mechanics and Engineering, 233-236*, 11–27. https://doi.org/10.1016/j.cma.2012.02.020 (cit. on p. 29)

Berthaud, Y. (1991). Damage measurements in concrete via an ultrasonic technique. part i experiment. *Cement and Concrete Research, 21*(1), 73–82. https://doi.org/10.1016/0008-8846(91)90033-E (cit. on pp. 9, 10)

Blinowski, A., Ostrowska-Maciejewska, J., & Rychlewski, J. (1996). Two-dimensional hooke's tensors - isotropic decomposition, effective symmetry criteria. *Archives of Mechanics, 48*(2), 325–345. https://doi.org/10.24423/aom.1345 (cit. on p. 37)

Bolander, J. E., Eliáš, J., Cusatis, G., & Nagai, K. (2021). Discrete mechanical models of concrete fracture. *Engineering Fracture Mechanics, 257*, 108030. https://doi.org/10.1016/j.engfracmech.2021.108030 (cit. on p. 14)

Bonatti, C., & Mohr, D. (2022). On the importance of self-consistency in recurrent neural network models representing elasto-plastic solids. *Journal of the Mechanics and Physics of Solids, 158*, 104697. https://doi.org/10.1016/j.jmps.2021.104697 (cit. on pp. 30, 31)

Borré, G., & Maier, G. (1989). On linear versus nonlinear flow rules in strain localization analysis. *Meccanica, 24*(1), 36–41. https://doi.org/10.1007/BF01576001 (cit. on p. 27)

Bourdin, B., Francfort, G. A., & Marigo, J.-J. (2000). Numerical experiments in revisited brittle fracture. *Journal of the Mechanics and Physics of Solids, 48*(4), 797–826. https://doi.org/10.1016/S0022-5096(99)00028-9 (cit. on p. 29)

Bourdin, B., Francfort, G. A., & Marigo, J.-J. (2008). The variational approach to fracture. *Journal of Elasticity, 91*(1), 5–148. https://doi.org/10.1007/s10659-007-9107-3 (cit. on p. 29)

Brunton, S. L., Proctor, J. L., & Kutz, J. N. (2016). Discovering governing equations from data by sparse identification of nonlinear dynamical systems. *Proceedings of the National Academy of Sciences, 113*(15), 3932–3937. https://doi.org/10.1073/pnas.1517384113 (cit. on p. 30)

Capecchi, D., Ruta, G., & Trovalusci, P. (2010). From classical to voigt's molecular models in elasticity. *Archive for History of Exact Sciences, 64*(5), 525–559. https://doi.org/10.1007/s00407-010-0065-y (cit. on p. 14)

Carol, I., & Willam, K. (1996). Spurious energy dissipation/generation in stiffness recovery models for elastic degradation and damage. *International Journal of Solids and Structures, 33*(20), 2939–2957. https://doi.org/10.1016/0020-7683(95)00254-5 (cit. on p. 20)

Carrara, P., De Lorenzis, L., Stainier, L., & Ortiz, M. (2020). Data-driven fracture mechanics. *Computer Methods in Applied Mechanics and Engineering, 372*, 113390. https://doi.org/10.1016/j.cma.2020.113390 (cit. on p. 29)

Chaboche, J.-L. (1974). *Une loi différentielle d'endommagement de fatigue avec cumulation non linéaire*. Office Nationale d'Etudes et de Recherches Aérospatiales. (Cit. on p. 19).

Chaboche, J.-L. (1978). Description thermodynamique et phénoménologique de la viscoélasticité cyclique avec endommagement. *Description thermodynamique et phénoménologique de la viscoélasticité cyclique avec endommagement* (cit. on pp. 19, 22).

Chaboche, J.-L. (1979). Le concept de contrainte effective appliqué à l'élasticité et à la viscoplasticité en présence d'un endommagement anisotrope. *Col. Euromech, 115*, 737–760 (cit. on pp. 19, 21, 22).

Chaboche, J.-L. (1984). Anisotropic creep damage in the framework of continuum damage mechanics. *Nuclear Engineering and Design, 79*(3), 309–319. https://doi.org/10.1016/0029-5493(84)90046-3 (cit. on pp. 21, 22)

Chaboche, J.-L. (1992). Damage induced anisotropy: On the difficulties associated with the active/passive unilateral condition. *International Journal of Damage Mechanics, 1*(2), 148–171. https://doi.org/10.1177/105678959200100201 (cit. on p. 20)

Challamel, N., Picandet, V., & Pijaudier-Cabot, G. (2015). From discrete to nonlocal continuum damage mechanics: Analysis of a lattice system in bending using a continualized approach. *International Journal of Damage Mechanics, 24*(7), 983–1012. https://doi.org/10.1177/1056789514560913 (cit. on p. 31)

Challamel, N., Halm, D., & Dragon, A. (2006). On the non-conservativeness of a class of anisotropic damage models with unilateral effects. *Comptes Rendus Mécanique, 334*(7), 414–418. https://doi.org/10.1016/j.crme.2006.05.006 (cit. on p. 20)

Chevaugeon, N., & Moës, N. (2022). Lipschitz regularization for fracture: The lip-field approach. *Computer Methods in Applied Mechanics and Engineering, 402*, 115644. https://doi.org/10.1016/j.cma.2022.115644 (cit. on p. 29)

Chow, C. L., & Wang, J. (1987). An anisotropic theory of continuum damage mechanics for ductile fracture. *Engineering Fracture Mechanics, 27*(5), 547–558. https://doi.org/10.1016/0013-7944(87)90108-1 (cit. on pp. 19, 25)

Christoffersen, J., Mehrabadi, M. M., & Nemat-Nasser, S. (1981). A micromechanical description of granular material behavior. *Journal of Applied Mechanics, 48*(2), 339–344. https://doi.org/10.1115/1.3157619 (cit. on p. 63)

Cordebois, J.-P., & Sidoroff, F. (1980). Anisotropic damage in elasticity and plasticity. *Journal de mecanique theorique et appliquee*, 45–59 (cit. on p. 21).

Cordebois, J.-P., & Sidoroff, F. (1982). Damage induced elastic anisotropy. Dordrecht, Springer Netherlands. 761–774. https://doi.org/10.1007/978-94-009-6827-1_44. (Cit. on pp. 19, 21)

Cormery, F., & Welemane, H. (2010). A stress-based macroscopic approach for microcracks unilateral effect. *Computational Materials Science, 47*(3), 727–738. https://doi.org/10.1016/j.commatsci.2009.10.016 (cit. on pp. 20, 21, 98, 108)

Cormery, F., & Welemane, H. (2002). A critical review of some damage models with unilateral effect. *Mechanics Research Communications, 29*(5), 391–395. https://doi.org/10.1016/S0093-6413(02)00262-8 (cit. on p. 20)

Cundall, P. A., & Strack, O. D. L. (1979). A discrete numerical model for granular assemblies. *Géotechnique*, *29*(1), 47–65. https://doi.org/10.1680/geot.1979.29.1.47 (cit. on pp. 16, 17)

Curie, P. (1894). Sur la symétrie dans les phénomènes physiques, symétrie d'un champ électrique et d'un champ magnétique. *Journal de Physique Théorique et Appliquée*, *3*(1), 393–415. https://doi.org/10.1051/jphystap:018940030039300 (cit. on p. 33)

Cusatis, G., Mencarelli, A., Pelessone, D., & Baylot, J. (2011a). Lattice discrete particle model (LDPM) for failure behavior of concrete. II: Calibration and validation. *Cement and Concrete Composites*, *33*(9), 891–905. https://doi.org/10.1016/j.cemconcomp.2011.02.010 (cit. on p. 18)

Cusatis, G., Pelessone, D., & Mencarelli, A. (2011b). Lattice discrete particle model (LDPM) for failure behavior of concrete. i: Theory. *Cement and Concrete Composites*, *33*(9), 881–890. https://doi.org/10.1016/j.cemconcomp.2011.02.011 (cit. on p. 18)

D'Addetta, G. A., Kun, F., & Ramm, E. (2002). On the application of a discrete model to the fracture process of cohesive granular materials. *Granular Matter*, *4*(2), 77–90. https://doi.org/10.1007/s10035-002-0103-9 (cit. on pp. 16, 18, 46)

Davis, T. A. (2011). Algorithm 915, SuiteSparseQR: Multifrontal multithreaded rank-revealing sparse QR factorization. *ACM Transactions on Mathematical Software*, *38*(1), 8:1–8:22. https://doi.org/10.1145/2049662.2049670 (cit. on p. 51)

Delaplace, A. (2008). *Modélisation discrète appliquée au comportement des matériaux et des structures* (Mémoire d'habilitation à diriger des recherches). Ecole Normale Supérieure de Cachan. (Cit. on pp. 18, 31, 46, 48).

Delaunay, B. N. (1934). Sur la sphère vide. *Bulletin de l'Académie des Sciences de l'URSS. VII. Série*, *1934*(6), 793–800 (cit. on p. 47).

Desmorat, B., & Desmorat, R. (2015). Tensorial polar decomposition of 2d fourth-order tensors. *Comptes Rendus Mécanique*, *343*(9), 471–475. https://doi.org/10.1016/j.crme.2015.07.002 (cit. on pp. 39, 143)

Desmorat, B., & Desmorat, R. (2016). Second order tensorial framework for 2d medium with open and closed cracks. *European Journal of Mechanics - A/Solids*, *58*, 262–277. https://doi.org/10.1016/j.euromechsol.2016.02.004 (cit. on pp. 20–22, 89, 98, 136)

Desmorat, R., Gatuingt, F., & Jirásek, M. (2015). Nonlocal models with damage-dependent interactions motivated by internal time. *Engineering Fracture Mechanics*, *142*, 255–275. https://doi.org/10.1016/j.engfracmech.2015.06.015 (cit. on pp. 29, 132)

Desmorat, R., Ragueneau, F., & Pham, H. (2007). Continuum damage mechanics for hysteresis and fatigue of quasi-brittle materials and structures. *International Journal for Numerical and Analytical Methods in Geomechanics*, *31*(2), 307–329. https://doi.org/10.1002/nag.532 (cit. on p. 20)

Desmorat, R. (2016). Anisotropic damage modeling of concrete materials. *International Journal of Damage Mechanics, 25*(6), 818–852. https://doi.org/10.1177/1056789515606509 (cit. on pp. 20, 23, 26)

Desmorat, R., Desmorat, B., Olive, M., & Kolev, B. (2018). Micromechanics based framework with second-order damage tensors. *European Journal of Mechanics - A/Solids, 69*, 88–98. https://doi.org/10.1016/j.euromechsol.2017.11.014 (cit. on p. 22)

de Vree, J. H. P., Brekelmans, W. A. M., & van Gils, M. A. J. (1995). Comparison of nonlocal approaches in continuum damage mechanics. *Computers & Structures, 55*(4), 581–588. https://doi.org/10.1016/0045-7949(94)00501-S (cit. on pp. 24, 116)

Diner, Ç., Kochetov, M., & Slawinski, M. A. (2011). Identifying symmetry classes of elasticity tensors using monoclinic distance function. *Journal of Elasticity, 102*(2), 175–190. https://doi.org/10.1007/s10659-010-9272-7 (cit. on p. 41)

Dormieux, L., & Kondo, D. (2016). *Micromechanics of fracture and damage* (1st ed.). Wiley. (Cit. on pp. 21, 108).

Dragon, A., Cormery, F., Desoyer, T., & Halm, D. (1994). Localised failure analysis using damage models. International workshop on localisation and bifurcation theory for soils and rocks. 127–140. (Cit. on p. 23).

Drescher, A., & de Josselin de Jong, G. (1972). Photoelastic verification of a mechanical model for the flow of a granular material. *Journal of the Mechanics and Physics of Solids, 20*(5), 337–340. https://doi.org/10.1016/0022-5096(72)90029-4 (cit. on pp. 63, 156)

Drucker, D. C., & Prager, W. (1952). Soil mechanics and plastic analysis or limit design. *Quarterly of Applied Mathematics, 10*(2), 157–165. https://doi.org/10.1090/qam/48291 (cit. on p. 25)

Drummen, M. (2006). *DEM simulations and theory of the HCP* (M. Sc. Thesis). Dept. Chemical Engineering, Technological University of Delft. (Cit. on p. 54).

Durán, O., Kruyt, N. P., & Luding, S. (2010). Analysis of three-dimensional micro-mechanical strain formulations for granular materials: Evaluation of accuracy. *International Journal of Solids and Structures, 47*(2), 251–260. https://doi.org/10.1016/j.ijsolstr.2009.09.035 (cit. on p. 54)

Eggersmann, R., Kirchdoerfer, T., Reese, S., Stainier, L., & Ortiz, M. (2019). Model-free data-driven inelasticity. *Computer Methods in Applied Mechanics and Engineering, 350*, 81–99. https://doi.org/10.1016/j.cma.2019.02.016 (cit. on p. 29)

Eringen, A. C., & Edelen, D. G. B. (1972). On nonlocal elasticity. *International Journal of Engineering Science, 10*(3), 233–248. https://doi.org/10.1016/0020-7225(72)90039-0 (cit. on p. 28)

Fassin, M., Eggersmann, R., Wulfinghoff, S., & Reese, S. (2019). Gradient-extended anisotropic brittle damage modeling using a second order damage tensor – theory, implemen-

tation and numerical examples. *International Journal of Solids and Structures, 167*, 93–126. https://doi.org/10.1016/j.ijsolstr.2019.02.009 (cit. on p. 21)

Fichant, S., La Borderie, C., & Pijaudier-Cabot, G. (1999). Isotropic and anisotropic descriptions of damage in concrete structures. *Mechanics of Cohesive-frictional Materials, 4*(4), 339–359. https://doi.org/10.1002/(SICI)1099-1484(199907)4:4<339::AID-CFM65>3.0.CO;2-J (cit. on p. 20)

Flaschel, M., Kumar, S., & De Lorenzis, L. (2021). Unsupervised discovery of interpretable hyperelastic constitutive laws. *Computer Methods in Applied Mechanics and Engineering, 381*, 113852. https://doi.org/10.1016/j.cma.2021.113852 (cit. on p. 31)

Flaschel, M., Kumar, S., & De Lorenzis, L. (2023). Automated discovery of generalized standard material models with EUCLID. *Computer Methods in Applied Mechanics and Engineering, 405*, 115867. https://doi.org/10.1016/j.cma.2022.115867 (cit. on p. 31)

Forest, S., & Sab, K. (1998). Cosserat overall modeling of heterogeneous materials. *Mechanics Research Communications, 25*(4), 449–454. https://doi.org/10.1016/S0093-6413(98)00059-7 (cit. on p. 68)

Forte, S., & Vianello, M. (1996). Symmetry classes for elasticity tensors. *Journal of Elasticity, 43*(2), 81–108. https://doi.org/10.1007/BF00042505 (cit. on pp. 34, 35)

Francfort, G. A., & Marigo, J. .-. (1998). Revisiting brittle fracture as an energy minimization problem. *Journal of the Mechanics and Physics of Solids, 46*(8), 1319–1342. https://doi.org/10.1016/S0022-5096(98)00034-9 (cit. on p. 29)

François, M., Geymonat, G., & Berthaud, Y. (1998). Determination of the symmetries of an experimentally determined stiffness tensor: Application to acoustic measurements. *International Journal of Solids and Structures, 35*(31), 4091–4106. https://doi.org/10.1016/S0020-7683(97)00303-X (cit. on p. 41)

François, M. (1995). *Identification des symétries matérielles de matériaux anisotropes* (Doctoral dissertation). Université Pierre et Marie Curie - Paris VI. (Cit. on p. 41).

François, M. (2008). A new yield criterion for the concrete materials. *Comptes Rendus Mécanique, 336*(5), 417–421. https://doi.org/10.1016/j.crme.2008.01.010 (cit. on p. 25)

Gaines, B. R., Kim, J., & Zhou, H. (2018). Algorithms for fitting the constrained lasso. *Journal of Computational and Graphical Statistics, 27*(4), 861–871. https://doi.org/10.1080/10618600.2018.1473777 (cit. on p. 100)

Gazis, D. C., Tadjbakhsh, I., & Toupin, R. A. (1963). The elastic tensor of given symmetry nearest to an anisotropic elastic tensor. *Acta Crystallographica, 16*(9), 917–922. https://doi.org/10.1107/S0365110X63002449 (cit. on p. 41)

Geers, M. G. D., de Borst, R., Brekelmans, W. A. M., & Peerlings, R. H. J. (1998). Strain-based transient-gradient damage model for failure analyses. *Computer Methods in Applied Mechanics and Engineering, 160*(1), 133–153. https://doi.org/10.1016/S0045-7825(98)80011-X (cit. on p. 29)

Gerbaud, P.-W., Néron, D., & Ladevèze, P. (2022). Data-driven elasto-(visco)-plasticity involving hidden state variables. *Computer Methods in Applied Mechanics and Engineering, 402*, 115394. https://doi.org/10.1016/j.cma.2022.115394 (cit. on p. 30)

Germain, P., Nguyen, Q. S., & Suquet, P. (1983). Continuum thermodynamics. *Journal of Applied Mechanics, 50*(4), 1010–1020. https://doi.org/10.1115/1.3167184 (cit. on p. 20)

Giry, C., Dufour, F., & Mazars, J. (2011). Stress-based nonlocal damage model. *International Journal of Solids and Structures, 48*(25), 3431–3443. https://doi.org/10.1016/j.ijsolstr.2011.08.012 (cit. on pp. 29, 133)

Gitman, I. M., Askes, H., & Sluys, L. J. (2007). Representative volume: Existence and size determination. *Engineering Fracture Mechanics, 74*(16), 2518–2534. https://doi.org/10.1016/j.engfracmech.2006.12.021 (cit. on p. 53)

Goidescu, C., Welemane, H., Kondo, D., & Gruescu, C. (2013). Microcracks closure effects in initially orthotropic materials. *European Journal of Mechanics - A/Solids, 37*, 172–184. https://doi.org/10.1016/j.euromechsol.2012.06.001 (cit. on p. 20)

Grassl, P., & Jirásek, M. (2006). Damage-plastic model for concrete failure. *International Journal of Solids and Structures, 43*(22), 7166–7196. https://doi.org/10.1016/j.ijsolstr.2006.06.032 (cit. on pp. 19, 22)

Grassl, P., & Jirásek, M. (2010). Meso-scale approach to modelling the fracture process zone of concrete subjected to uniaxial tension. *International Journal of Solids and Structures, 47*(7), 957–968. https://doi.org/10.1016/j.ijsolstr.2009.12.010 (cit. on p. 18)

Grosse, C. U., Ohtsu, M., Aggelis, D. G., & Shiotani, T. (Eds.). (2022). *Acoustic emission testing: Basics for research – applications in engineering.* Springer International Publishing. https://doi.org/10.1007/978-3-030-67936-1. (Cit. on p. 12)

Guan, Y., Brunton, S. L., & Novosselov, I. (2021). Sparse nonlinear models of chaotic electroconvection. *Royal Society Open Science, 8*(8), 202367. https://doi.org/10.1098/rsos.202367 (cit. on p. 31)

Hadamard, J. (1903). *Leçons sur la propagation des ondes et les équations de l'hydrodynamique.* A. Hermann. (Cit. on p. 27).

Halm, D., & Dragon, A. (1996). A model of anisotropic damage by mesocrack growth; unilateral effect. *International Journal of Damage Mechanics, 5*(4), 384–402. https://doi.org/10.1177/105678959600500403 (cit. on pp. 20, 21, 23)

Halm, D., & Dragon, A. (1998). An anisotropic model of damage and frictional sliding for brittle materials. *European Journal of Mechanics - A/Solids, 17*(3), 439–460. https://doi.org/10.1016/S0997-7538(98)80054-5 (cit. on p. 20)

Halphen, B., & Son Nguyen, Q. (1975). Sur les matériaux standard généralisés. *Journal de Mécanique, 14*(1), 39–63 (cit. on pp. 20, 25, 26).

Helfer, T., Michel, B., Proix, J.-M., Salvo, M., Sercombe, J., & Casella, M. (2015). Introducing the open-source mfront code generator: Application to mechanical behaviours and

material knowledge management within the PLEIADES fuel element modelling platform. *Computers & Mathematics with Applications, 70*(5), 994–1023. https://doi.org/10.1016/j.camwa.2015.06.027 (cit. on p. 128)

Hérisson, B. (2018). *Endommagement discret et continu : application aux materiaux quasi-fragiles* (Doctoral dissertation). Université de Bretagne Sud. (Cit. on p. 31).

Herrmann, H. J., Hansen, A., & Roux, S. (1989). Fracture of disordered, elastic lattices in two dimensions. *Physical Review B, 39*(1), 637–648. https://doi.org/10.1103/PhysRevB.39.637 (cit. on p. 15)

Herrmann, H. J., & Roux, S. (Eds.)**. (1990)**. *Statistical models for the fracture of disordered media.* North-Holland. https://doi.org/10.1016/B978-0-444-88551-7.50001-X. (Cit. on p. 15)

Higham, N. J. (2008). *Functions of matrices.* Society for Industrial; Applied Mathematics. https://doi.org/10.1137/1.9780898717778. (Cit. on p. 126)

Hill, R. (1948). A variational principle of maximum plastic work in classical plasticity. *The Quarterly Journal of Mechanics and Applied Mathematics, 1*(1), 18–28. https://doi.org/10.1093/qjmam/1.1.18 (cit. on p. 19)

Hill, R. (1963). Elastic properties of reinforced solids: Some theoretical principles. *Journal of the Mechanics and Physics of Solids, 11*(5), 357–372. https://doi.org/10.1016/0022-5096(63)90036-X (cit. on p. 52)

Hill, R. (1967). The essential structure of constitutive laws for metal composites and poly-crystals. *Journal of the Mechanics and Physics of Solids, 15*(2), 79–95. https://doi.org/10.1016/0022-5096(67)90018-X (cit. on p. 19)

Horii, H., & Nemat-Nasser, S. (1983). Overall moduli of solids with microcracks: Load-induced anisotropy. *Journal of the Mechanics and Physics of Solids, 31*(2), 155–171. https://doi.org/10.1016/0022-5096(83)90048-0 (cit. on p. 20)

Hrennikoff, A. (1941). Solution of problems of elasticity by the framework method. *Journal of Applied Mechanics, 8*(4), A169–A175. https://doi.org/10.1115/1.4009129 (cit. on p. 15)

Hult, J. (1974). Creep in continua and structures In *Topics in applied continuum mechanics* (J. L. Zeman & F. Ziegler, Eds.). Vienna, Springer. 137–155. https://doi.org/10.1007/978-3-7091-4188-5_7. (Cit. on p. 19)

Ibañez, R., Borzacchiello, D., Aguado, J. V., Abisset-Chavanne, E., Cueto, E., Ladeveze, P., & Chinesta, F. (2017). Data-driven non-linear elasticity: Constitutive manifold construction and problem discretization. *Computational Mechanics, 60*(5), 813–826. https://doi.org/10.1007/s00466-017-1440-1 (cit. on pp. 29, 30)

Ibañez, R., Abisset-Chavanne, E., Aguado, J. V., Gonzalez, D., Cueto, E., & Chinesta, F. (2016). A manifold learning approach to data-driven computational elasticity and

inelasticity. *Archives of Computational Methods in Engineering, 25*(1), 47–57. https://doi.org/10.1007/s11831-016-9197-9 (cit. on p. 29)

Jason, L., Huerta, A., Pijaudier-Cabot, G., & Ghavamian, S. (2006). An elastic plastic damage formulation for concrete: Application to elementary tests and comparison with an isotropic damage model. *Computer Methods in Applied Mechanics and Engineering, 195*(52), 7077–7092. https://doi.org/10.1016/j.cma.2005.04.017 (cit. on p. 20)

Jefferson, A. D., & Mihai, I. C. (2015). The simulation of crack opening–closing and aggregate interlock behaviour in finite element concrete models. *International Journal for Numerical Methods in Engineering, 104*(1), 48–78. https://doi.org/10.1002/nme.4934 (cit. on p. 23)

Jirásek, M. (2002). Objective modeling of strain localization. *Revue Française de Génie Civil, 6*(6), 1119–1132. https://doi.org/10.1080/12795119.2002.9692735 (cit. on p. 27)

Jirásek, M. (2004). Non-local damage mechanics with application to concrete. *Revue Française de Génie Civil* (cit. on p. 27).

Jirásek, M. (2007). Mathematical analysis of strain localization. *Revue Européenne de Génie Civil, 11*(7), 977–991. https://doi.org/10.1080/17747120.2007.9692973 (cit. on p. 27)

Ju, J. W. (1989). On energy-based coupled elastoplastic damage theories: Constitutive modeling and computational aspects. *International Journal of Solids and Structures, 25*(7), 803–833. https://doi.org/10.1016/0020-7683(89)90015-2 (cit. on p. 19)

Kachanov, L. M. (1986). *Introduction to continuum damage mechanics* (Vol. 10). Springer Netherlands. https://doi.org/10.1007/978-94-017-1957-5. (Cit. on p. 18)

Kachanov, L. M. (1958). On creep rupture time. *Izv. Acad. Nauk SSSR, Otd. Techn. Nauk, 8*, 26–31 (cit. on pp. 18, 21).

Kachanov, M. (1980). Continuum model of medium with cracks. *Journal of the Engineering Mechanics Division, 106*(5), 1039–1051. https://doi.org/10.1061/JMCEA3.0002642 (cit. on p. 20)

Kachanov, M. (1992). Effective elastic properties of cracked solids: Critical review of some basic concepts. *Applied Mechanics Reviews, 45*(8), 304–335. https://doi.org/10.1115/1.3119761 (cit. on p. 94)

Kachanov, M. (1993). Elastic solids with many cracks and related problems. In J. W. Hutchinson & T. Y. Wu (Eds.), *Advances in applied mechanics* (pp. 259–445). Elsevier. (Cit. on pp. 21, 22, 108).

Kachanov, M. L. (1982). A microcrack model of rock inelasticity part i: Frictional sliding on microcracks. *Mechanics of Materials, 1*(1), 19–27. https://doi.org/10.1016/0167-6636(82)90021-7 (cit. on pp. 13, 20)

Kawai, T. (1978). New discrete models and their application to seismic response analysis of structures. *Nuclear Engineering and Design, 48*(1), 207–229. https://doi.org/10.1016/0029-5493(78)90217-0 (cit. on p. 16)

Kirchdoerfer, T., & Ortiz, M. (2016). Data-driven computational mechanics. *Computer Methods in Applied Mechanics and Engineering, 304*, 81–101. https://doi.org/10.1016/j.cma.2016.02.001 (cit. on pp. 29, 30)

Kirchdoerfer, T., & Ortiz, M. (2017). Data driven computing with noisy material data sets. *Computer Methods in Applied Mechanics and Engineering, 326*, 622–641. https://doi.org/10.1016/j.cma.2017.07.039 (cit. on p. 29)

Kolupaev, V. A. (2018). *Equivalent stress concept for limit state analysis* (Vol. 86). Springer International Publishing. https://doi.org/10.1007/978-3-319-73049-3. (Cit. on p. 25)

Krajcinovic, D. (1985). Continuous damage mechanics revisited: Basic concepts and definitions. *Journal of Applied Mechanics, 52*(4), 829–834. https://doi.org/10.1115/1.3169154 (cit. on p. 22)

Krajcinovic, D. (1996). *Damage mechanics.* Elsevier. (Cit. on p. 18).

Krajcinovic, D., & Lemaitre, J. (Eds.)**. (1987)**. *Continuum damage mechanics theory and application.* Springer. https://doi.org/10.1007/978-3-7091-2806-0. (Cit. on p. 18)

Krayani, A., Pijaudier-Cabot, G., & Dufour, F. (2009). Boundary effect on weight function in nonlocal damage model. *Engineering Fracture Mechanics, 76*(14), 2217–2231. https://doi.org/10.1016/j.engfracmech.2009.07.007 (cit. on p. 28)

Kupfer, H., Hilsdorf, H. K., & Rusch, H. (1969). Behavior of concrete under biaxial stresses. *Journal Proceedings, 66*(8), 656–666. https://doi.org/10.14359/7388 (cit. on pp. 10, 25)

Ladeveze, P., & Lemaitre, J. (1984). Damage effective stress in quasi-unilateral conditions. *The 16th International Cogress of Theoretical and Applied Mechanics, Lyngby, Denmark* (cit. on p. 20).

Ladevèze, P. (1983a). On an anisotropic damage theory. *Proc. CNRS Int. Coll, 351*, 355–363 (cit. on pp. 125, 126).

Ladevèze, P. (1983b). *Sur une théorie de l'endommagement anisotrope* (Rapport Interne No. 34). LMT Cachan. (Cit. on pp. 20, 22, 23, 25).

Ladevèze, P. (1995). Modelling and simulation of the mechanical behaviour of CMCs. *Ceram. Trans. Vol. 57*, 53–63 (cit. on pp. 22, 125, 126).

Ladevèze, P., Gerbaud, P.-W., & Néron, D. (2022). On a physics-compatible approach for data-driven computational mechanics. In F. Aldakheel, B. Hudobivnik, M. Soleimani, H. Wessels, C. Weißenfels, & M. Marino (Eds.), *Current trends and open problems in computational mechanics* (pp. 287–294). Springer International Publishing. https://doi.org/10.1007/978-3-030-87312-7_28. (Cit. on p. 30)

Ladevèze, P., Néron, D., & Gerbaud, P.-W. (2019). Data-driven computation for history-dependent materials. *Comptes Rendus Mécanique, 347*(11), 831–844. https://doi.org/10.1016/j.crme.2019.11.008 (cit. on pp. 29, 30)

Landis, E. N. (1999). Micro–macro fracture relationships and acoustic emissions in concrete. *Construction and Building Materials, 13*(1), 65–72. https://doi.org/10.1016/S0950-0618(99)00009-4 (cit. on pp. 12, 13)

Le Bellégo, C., Dubé, J.-F., Pijaudier-Cabot, G., & Gérard, B. (2003). Calibration of nonlocal damage model from size effect tests. *European Journal of Mechanics - A/Solids, 22*(1), 33–46. https://doi.org/10.1016/S0997-7538(02)01255-X (cit. on p. 27)

Leckie, F. A., & Hayhurst, D. R. (1974). Creep rupture of structures (J. F. Baker, Ed.). *Proceedings of the Royal Society of London. A. Mathematical and Physical Sciences, 340*(1622), 323–347. https://doi.org/10.1098/rspa.1974.0155 (cit. on p. 19)

Leckie, F. A., & Onat, E. T. (1981). Tensorial nature of damage measuring internal variables In *Physical non-linearities in structural analysis* (J. Hult & J. Lemaitre, Eds.). Berlin, Heidelberg, Springer. 140–155. https://doi.org/10.1007/978-3-642-81582-9_20. (Cit. on p. 21)

Lee, S.-K., Song, Y.-C., & Han, S.-H. (2004). Biaxial behavior of plain concrete of nuclear containment building. *Nuclear Engineering and Design, 227*(2), 143–153. https://doi.org/10.1016/j.nucengdes.2003.09.001 (cit. on pp. 10, 11)

Lehne, J., & Preston, F. (2018). *Making concrete change, innovation in low-carbon cement and concrete.* (Chatham House Report). Energy Enivronment and Resources Department: London, UK. (Cit. on pp. 1, 153).

Lemaitre, J., & Chaboche, J. L. (1975). A non-linear model of creep-fatigue damage cumulation and interaction In *Proc. IUTAM symp. of mechanics of visco-elastic media and bodies.* Gothenburg, Springer-Verlag. 1975. (Cit. on p. 19).

Lemaitre, J. (1971). *Evaluation of dissipation and damage in metals submitted to dynamic loading* (Technical). (Cit. on p. 19).

Lemaitre, J. (1984). How to use damage mechanics. *Nuclear Engineering and Design, 80*(2), 233–245. https://doi.org/10.1016/0029-5493(84)90169-9 (cit. on pp. 18, 21)

Lemaitre, J. (1985). A continuous damage mechanics model for ductile fracture. *Journal of Engineering Materials and Technology, 107*(1), 83–89. https://doi.org/10.1115/1.3225775 (cit. on p. 19)

Lemaitre, J. (1992). *A course on damage mechanics.* Springer-Verlag. https://doi.org/10.1007/978-3-662-02761-5. (Cit. on pp. 18, 108)

Lemaitre, J. (1996). *A course on damage mechanics.* Springer Berlin Heidelberg. https://doi.org/10.1007/978-3-642-18255-6. (Cit. on p. 18)

Lemaitre, J., & Chaboche, J.-L. (1985). *Mécanique des matériaux solides.* Dunod, english translation 1990 'Mechanics of Solid Materials' Cambridge University Press. (Cit. on pp. 21, 108).

Lemaitre, J., Chaboche, J.-L., Benallal, A., & Desmorat, R. (2009). *Mécanique des matériaux solides.* Dunod. (Cit. on pp. 19, 22).

Lemaitre, J., & Desmorat, R. (2005). *Engineering damage mechanics: Ductile, creep, fatigue and brittle failures.* Springer-Verlag. https://doi.org/10.1007/b138882. (Cit. on pp. 18, 20, 22)

Lemaitre, J., Desmorat, R., & Sauzay, M. (2000). Anisotropic damage law of evolution. *European Journal of Mechanics - A/Solids, 19*(2), 187–208. https://doi.org/10.1016/S0997-7538(00)00161-3 (cit. on pp. 20, 22)

Lemaitre, J., & Dufailly, J. (1977). Modélisation et identification de l'endommagement plastique des métaux. 3e congrès français de mécanique. Grenoble, France. (Cit. on p. 19).

Lemaitre, J., & Mazars, J. (1982). Application de la theorie de l'endommagement au comportement non lineaire et a la rupture du beton de structure. *Annales de l'Institut Technique du Bâtiment et des Travaux Publics,* (401) (cit. on p. 13).

Loiseau, F., Oliver-Leblond, C., Verbeke, T., & Desmorat, R. (2023a). Anisotropic damage state modeling based on harmonic decomposition and discrete simulation of fracture. *Engineering Fracture Mechanics,* 109669. https://doi.org/10.1016/j.engfracmech.2023.109669 (cit. on p. 109)

Loiseau, F., Oliver-Leblond, C., & Desmorat, R. (2023b). Dataset of 2d effective elasticity tensor from discrete simulations of quasi-brittle area elements. https://doi.org/10.57745/LYHM4W. (Cit. on pp. 76, 135)

Love, A. (1892). *A treatise on the mathematical theory of elasticity* (Vol. 1). (Cit. on p. 15).

Lubarda, V. A., & Krajcinovic, D. (1993). Damage tensors and the crack density distribution. *International Journal of Solids and Structures, 30*(20), 2859–2877. https://doi.org/10.1016/0020-7683(93)90158-4 (cit. on p. 22)

Lubliner, J., Oliver, J., Oller, S., & Oñate, E. (1989). A plastic-damage model for concrete. *International Journal of Solids and Structures, 25*(3), 299–326. https://doi.org/10.1016/0020-7683(89)90050-4 (cit. on pp. 19, 20)

Maji, A., & Shah, S. P. (1988). Process zone and acoustic-emission measurements in concrete. *Experimental Mechanics, 28*(1), 27–33. https://doi.org/10.1007/BF02328992 (cit. on p. 12)

Marconi, F. (2022). *Damage-fracture transition by an eikonal-based gradient-type formulation for damage (-plastic) models* (These de doctorat). université Paris-Saclay. (Cit. on p. 132).

Marigo, J.-J. (1981). Formulation d'une loi d'endommagement d'un matériau élastique. *C. R. Acad. Sci. Paris, 292,* 1309–1312 (cit. on p. 20).

Masi, F., & Stefanou, I. (2023). Evolution TANN and the identification of internal variables and evolution equations in solid mechanics. *Journal of the Mechanics and Physics of Solids, 174,* 105245. https://doi.org/10.1016/j.jmps.2023.105245 (cit. on p. 30)

Masi, F., Stefanou, I., Vannucci, P., & Maffi-Berthier, V. (2021). Thermodynamics-based artificial neural networks for constitutive modeling. *Journal of the Mechanics and Physics of Solids, 147,* 104277. https://doi.org/10.1016/j.jmps.2020.104277 (cit. on p. 30)

Masseron, B., Rastiello, G., & Desmorat, R. (2022). Analytical strain localization analysis of isotropic and anisotropic damage models for quasi-brittle materials. *International Journal of Solids and Structures, 254-255,* 111869. https://doi.org/10.1016/j.ijsolstr.2022.111869 (cit. on p. 27)

Mattiello, A., & Desmorat, R. (2021). Lode angle dependency due to anisotropic damage. *International Journal of Damage Mechanics, 30*(2), 214–259. https://doi.org/10.1177/1056789520948563 (cit. on pp. 25, 125)

Mazars, J., & Pijaudier-Cabot, G. (1989). Continuum damage theory—application to concrete. *Journal of Engineering Mechanics, 115*(2), 345–365. https://doi.org/10.1061/(ASCE)0733-9399(1989)115:2(345) (cit. on p. 19)

Mazars, J. (1984). *Application de la mécanique de l'endommagement au comportement non-linéaire et à la rupture du béton de structure* (Thèse de Doctorat d'État ès Sciences Physiques). Université Pierre et Marie Curie - Paris VI - Laboratoire de Mécanique et Technologie. (Cit. on pp. 13, 20, 22, 24, 108, 116).

Mazars, J. (1986). A description of micro- and macroscale damage of concrete structures. *Engineering Fracture Mechanics, 25*(5), 729–737. https://doi.org/10.1016/0013-7944(86)90036-6 (cit. on pp. 19, 125)

Mazars, J., & Berthaud, Y. (1989). Une technique expérimentale appliquée au béton pour créer un endommagement diffus et mettre en évidence son caractère unilatéral. *C. R. Acad. Sci., 308,* 579–584 (cit. on p. 8).

Mazars, J., Berthaud, Y., & Ramtani, S. (1990). The unilateral behaviour of damaged concrete. *Engineering Fracture Mechanics, 35*(4), 629–635. https://doi.org/10.1016/0013-7944(90)90145-7 (cit. on pp. 8, 9)

McKay, M. D., Beckman, R. J., & Conover, W. J. (1979). A comparison of three methods for selecting values of input variables in the analysis of output from a computer code. *Technometrics, 21*(2), 239–245. https://doi.org/10.2307/1268522 (cit. on p. 152)

Meguro, K., & Hakuno, M. (1989). Fracture analyses of concrete structures by the modified distinct element method. *Doboku Gakkai Ronbunshu, 1989*(410), 113–124. https://doi.org/10.2208/jscej.1989.410_113 (cit. on pp. 16, 17)

Meurer, A., Smith, C. P., Paprocki, M., Čertík, O., Kirpichev, S. B., Rocklin, M., Kumar, A., Ivanov, S., Moore, J. K., Singh, S., Rathnayake, T., Vig, S., Granger, B. E., Muller, R. P., Bonazzi, F., Gupta, H., Vats, S., Johansson, F., Pedregosa, F., ... Scopatz, A. (2017). SymPy: Symbolic computing in python. *PeerJ Computer Science, 3,* e103. https://doi.org/10.7717/peerj-cs.103 (cit. on p. 44)

Migliori, A., Sarrao, J. L., Visscher, W. M., Bell, T. M., Lei, M., Fisk, Z., & Leisure, R. G. (1993). Resonant ultrasound spectroscopic techniques for measurement of the elastic moduli of solids. *Physica B: Condensed Matter, 183*(1), 1–24. https://doi.org/10.1016/0921-4526(93)90048-B (cit. on p. 41)

Mindess, S. (1991). The fracture process zone in concrete. In S. P. Shah (Ed.), *Toughening mechanisms in quasi-brittle materials* (pp. 271–286). Springer Netherlands. https://doi.org/10.1007/978-94-011-3388-3_17. (Cit. on p. 12)

Misra, A., & Poorsolhjouy, P. (2015). Granular micromechanics model for damage and plasticity of cementitious materials based upon thermomechanics. *Mathematics and Mechanics of Solids.* https://doi.org/10.1177/1081286515576821 (cit. on p. 31)

Misra, A., & Singh, V. (2013). Micromechanical model for viscoelastic materials undergoing damage. *Continuum Mechanics and Thermodynamics, 25*(2), 343–358. https://doi.org/10.1007/s00161-012-0262-9 (cit. on p. 31)

Misra, A., & Singh, V. (2015). Thermomechanics-based nonlinear rate-dependent coupled damage-plasticity granular micromechanics model. *Continuum Mechanics and Thermodynamics, 27*(4), 787–817. https://doi.org/10.1007/s00161-014-0360-y (cit. on p. 31)

Moakher, M., & Norris, A. N. (2006). The closest elastic tensor of arbitrary symmetry to an elasticity tensor of lower symmetry. *Journal of Elasticity, 85*(3), 215–263. https://doi.org/10.1007/s10659-006-9082-0 (cit. on p. 41)

Moës, N., Stolz, C., Bernard, P.-E., & Chevaugeon, N. (2011). A level set based model for damage growth: The thick level set approach. *International Journal for Numerical Methods in Engineering, 86*(3), 358–380. https://doi.org/10.1002/nme.3069 (cit. on p. 29)

Moës, N., & Chevaugeon, N. (2021). Lipschitz regularization for softening material models: The lip-field approach. *Comptes Rendus. Mécanique, 349*(2), 415–434. https://doi.org/10.5802/crmeca.91 (cit. on p. 29)

Molnar, C. (2022). *Interpretable machine learning: A guide for making black box models explainable* (2nd ed.). (Cit. on p. 30).

Moukarzel, C., & Herrmann, H. J. (1992). A vectorizable random lattice. *Journal of Statistical Physics, 68*(5), 911–923. https://doi.org/10.1007/BF01048880 (cit. on p. 46)

Murakami, S. (1988). Mechanical modeling of material damage. *Journal of Applied Mechanics, 55*(2), 280–286. https://doi.org/10.1115/1.3173673 (cit. on p. 21)

Murakami, S., & Kamiya, K. (1997). Constitutive and damage evolution equations of elastic-brittle materials based on irreversible thermodynamics. *International Journal of Mechanical Sciences, 39*(4), 473–486. https://doi.org/10.1016/S0020-7403(97)87627-8 (cit. on p. 20)

Murakami, S., & Ohno, N. (1978). A constitutive equation of creep damage in pollicristalline metals In *IUTAM colloquium euromech.* (Cit. on p. 21).

Murakami, S. (2012). *Continuum damage mechanics* (Vol. 185). Springer Netherlands. https://doi.org/10.1007/978-94-007-2666-6. (Cit. on p. 18)

Nelissen, L. J. M. (1972). Biaxial testing of normal concrete. *HERON, 18 (1), 1972* (cit. on p. 10).

Nguyen, V. P., Lloberas-Valls, O., Stroeven, M., & Johannes Sluys, L. (2010). On the existence of representative volumes for softening quasi-brittle materials – a failure zone averaging scheme. *Computer Methods in Applied Mechanics and Engineering, 199*(45), 3028–3038. https://doi.org/10.1016/j.cma.2010.06.018 (cit. on p. 53)

Nguyen, V. P., Lloberas-Valls, O., Stroeven, M., & Sluys, L. J. (2011). Homogenization-based multiscale crack modelling: From micro-diffusive damage to macro-cracks. *Computer Methods in Applied Mechanics and Engineering, 200*(9), 1220–1236. https://doi.org/10.1016/j.cma.2010.10.013 (cit. on p. 53)

Nouailletas, O., La Borderie, C., Perlot-Bascoules, C., Rivard, P., & Balivy, G. (2015). Experimental study of crack closure on heterogeneous quasi-brittle material. *Journal of Engineering Mechanics - ASCE, 141*(11), 04015041. https://doi.org/10.1061/(ASCE)EM.1943-7889.0000928 (cit. on pp. 8, 9)

Ohtsu, M. (1996). The history and development of acoustic emission in concrete engineering. *Magazine of Concrete Research.* https://doi.org/10.1680/macr.1996.48.177.321 (cit. on p. 12)

Olive, M., Kolev, B., Desmorat, B., & Desmorat, R. (2017). Harmonic factorization and reconstruction of the elasticity tensor. *Journal of Elasticity, 132*(1), 67–101. https://doi.org/10.1007/s10659-017-9657-y (cit. on pp. 36, 39, 137)

Olive, M., Kolev, B., Desmorat, R., & Desmorat, B. (2022). Characterization of the symmetry class of an elasticity tensor using polynomial covariants. *Mathematics and Mechanics of Solids, 27*(1), 144–190. https://doi.org/10.1177/10812865211010885 (cit. on p. 39)

Oliver-Leblond, C. (2019). Discontinuous crack growth and toughening mechanisms in concrete: A numerical study based on the beam-particle approach. *Engineering Fracture Mechanics, 207*, 1–22. https://doi.org/10.1016/j.engfracmech.2018.11.050 (cit. on pp. 46, 49)

Oliver-Leblond, C., Desmorat, R., & Kolev, B. (2021). Continuous anisotropic damage as a twin modelling of discrete bi-dimensional fracture. *European Journal of Mechanics - A/Solids, 89*, 104285. https://doi.org/10.1016/j.euromechsol.2021.104285 (cit. on pp. 21, 31, 36, 39, 44, 65, 89, 92)

Ortiz, M. (1985). A constitutive theory for the inelastic behavior of concrete. *Mechanics of Materials, 4*(1), 67–93. https://doi.org/10.1016/0167-6636(85)90007-9 (cit. on p. 20)

Ottosen, N. S. (1977). A failure criterion for concrete. *Journal of the Engineering Mechanics Division, 103*(4), 527–535. https://doi.org/10.1061/JMCEA3.0002248 (cit. on p. 25)

Ouyang, C., Landis, E., & Shah, S. P. (1991). Damage assessment in concrete using quantitative acoustic emission. *Journal of Engineering Mechanics, 117*(11), 2681–2698. https://doi.org/10.1061/(ASCE)0733-9399(1991)117:11(2681) (cit. on p. 12)

Papa, E., & Taliercio, A. (1996). Anisotropic damage model for the multiaxial static and fatigue behaviour of plain concrete. *Engineering Fracture Mechanics, 55*(2), 163–179. https://doi.org/10.1016/0013-7944(96)00004-5 (cit. on p. 21)

Pathirage, M., Tong, D., Thierry, F., Cusatis, G., Grégoire, D., & Pijaudier-Cabot, G. (2023). Discrete modeling of concrete failure and size-effect. *Theoretical and Applied Fracture Mechanics, 124*, 103738. https://doi.org/10.1016/j.tafmec.2022.103738 (cit. on p. 18)

Peerlings, R. H. J., De Borst, R., Brekelmans, W. a. M., & De Vree, J. H. P. (1996). Gradient enhanced damage for quasi-brittle materials. *International Journal for Numerical Methods in Engineering, 39*(19), 3391–3403. https://doi.org/10.1002/(SICI)1097-0207(19961015)39:19<3391::AID-NME7>3.0.CO;2-D (cit. on pp. 28, 132)

Peerlings, R. H. J., Geers, M. G. D., de Borst, R., & Brekelmans, W. A. M. (2001). A critical comparison of nonlocal and gradient-enhanced softening continua. *International Journal of Solids and Structures, 38*(44), 7723–7746. https://doi.org/10.1016/S0020-7683(01)00087-7 (cit. on p. 28)

Pelissou, C., Baccou, J., Monerie, Y., & Perales, F. (2009). Determination of the size of the representative volume element for random quasi-brittle composites. *International Journal of Solids and Structures, 46*(14), 2842–2855. https://doi.org/10.1016/j.ijsolstr.2009.03.015 (cit. on p. 53)

Pensée, V., Kondo, D., & Dormieux, L. (2002). Micromechanical analysis of anisotropic damage in brittle materials. *Journal of Engineering Mechanics, 128*(8), 889–897. https://doi.org/10.1061/(ASCE)0733-9399(2002)128:8(889) (cit. on p. 20)

Pijaudier-Cabot, G., & Bažant, Z. P. (1987). Nonlocal damage theory. *Journal of Engineering Mechanics, 113*(10), 1512–1533. https://doi.org/10.1061/(ASCE)0733-9399(1987)113:10(1512) (cit. on pp. 27, 132)

Pijaudier-Cabot, G., & Grégoire, D. (2014). A review of non local continuum damage: Modelling of failure? *Networks and Heterogeneous Media, 9*(4), 575–597. https://doi.org/10.3934/nhm.2014.9.575 (cit. on p. 27)

Pijaudier-Cabot, G., Haidar, K., & Dubé, J.-F. (2004). Non-local damage model with evolving internal length. *International Journal for Numerical and Analytical Methods in Geomechanics, 28*(7), 633–652. https://doi.org/10.1002/nag.367 (cit. on p. 29)

Poh, L. H., & Sun, G. (2017). Localizing gradient damage model with decreasing interactions. *International Journal for Numerical Methods in Engineering, 110*(6), 503–522. https://doi.org/10.1002/nme.5364 (cit. on pp. 29, 133)

Poisson, S. D. (1828). Mémoire sur l'équilibre et le mouvement des corps élastiques In *Mémoires de l'académie des sciences de l'institut de france*. 357–570. (Cit. on p. 15).

Ponte Castañeda, P., & Willis, J. R. (1995). The effect of spatial distribution on the effective behavior of composite materials and cracked media. *Journal of the Mechanics and Physics of Solids, 43*(12), 1919–1951. https://doi.org/10.1016/0022-5096(95)00058-Q (cit. on p. 108)

Qu, J., & Cherkaoui, M. (2006). *Fundamentals of micromechanics of solids*. John Wiley & Sons, Inc. https://doi.org/10.1002/9780470117835. (Cit. on p. 52)

Rabotnov, Y. N. (1969). Creep problems in structural members (F. A. Leckie, Ed.). *North-Holland Publishing Company, Amsterdam*. https://doi.org/10.1115/1.3408479 (cit. on pp. 19, 21)

Ragueneau, F., Desmorat, R., & Gatuingt, F. (2008). Anisotropic damage modelling of biaxial behaviour and rupture of concrete structures. *Computers and Concrete, 5*(4), 417–434. https://doi.org/10.12989/cac.2008.5.4.417 (cit. on pp. 25, 116)

Ragueneau, F., Dominguez, N., & Ibrahimbegovic, A. (2006). Thermodynamic-based interface model for cohesive brittle materials: Application to bond slip in RC structures. *Computer Methods in Applied Mechanics and Engineering, 195*(52), 7249–7263. https://doi.org/10.1016/j.cma.2005.04.022 (cit. on p. 20)

Ramtani, S., Berthaud, Y., & Mazars, J. (1992). Orthotropic behavior of concrete with directional aspects: Modelling and experiments. *Nuclear Engineering and Design, 133*(1), 97–111. https://doi.org/10.1016/0029-5493(92)90094-C (cit. on pp. 21, 22, 26)

Rastiello, G., Giry, C., Gatuingt, F., & Desmorat, R. (2018). From diffuse damage to strain localization from an eikonal non-local (ENL) continuum damage model with evolving internal length. *Computer Methods in Applied Mechanics and Engineering, 331*, 650–674. https://doi.org/10.1016/j.cma.2017.12.006 (cit. on pp. 28, 29, 132)

Reese, S. (2003). Meso-macro modelling of fibre-reinforced rubber-like composites exhibiting large elastoplastic deformation. *International Journal of Solids and Structures, 40*(4), 951–980. https://doi.org/10.1016/S0020-7683(02)00602-9 (cit. on p. 45)

Reinhardt, H. W., & Cornelissen, H. A. W. (1984). Post-peak cyclic behaviour of concrete in uniaxial tensile and alternating tensile and compressive loading. *Cement and Concrete Research, 14*(2), 263–270. https://doi.org/10.1016/0008-8846(84)90113-3 (cit. on pp. 8, 9)

Reinhardt, H. W., Cornelissen, H. A. W., & Hordijk, D. A. (1986). Tensile tests and failure analysis of concrete. *Journal of Structural Engineering, 112*(11), 2462–2477. https://doi.org/10.1061/(ASCE)0733-9445(1986)112:11(2462) (cit. on pp. 8, 9)

Ribeiro Nogueira, B., Rastiello, G., Giry, C., Gatuingt, F., & Callari, C. (2023). Differential geometry-based thermodynamics derivation of isotropic and anisotropic eikonal

non-local gradient damage models using a micromorphic media framework. (Cit. on p. 132).

Richard, B., & Ragueneau, F. (2013). Continuum damage mechanics based model for quasi brittle materials subjected to cyclic loadings: Formulation, numerical implementation and applications. *Engineering Fracture Mechanics, 98,* 383–406. https://doi.org/10.1016/j.engfracmech.2012.11.013 (cit. on pp. 20, 22)

Richard, B., Ragueneau, F., Cremona, C., & Adelaide, L. (2010). Isotropic continuum damage mechanics for concrete under cyclic loading: Stiffness recovery, inelastic strains and frictional sliding. *Engineering Fracture Mechanics, 77*(8), 1203–1223. https://doi.org/10.1016/j.engfracmech.2010.02.010 (cit. on p. 20)

Rima, A. (2021). *Étude du comportement des ancrages chevillés dans les ouvrages de génie civil des installations nucléaires françaises* (Doctoral dissertation). Université Paris-Saclay. (Cit. on p. 48).

Rinaldi, A. (2013). Bottom-up modeling of damage in heterogeneous quasi-brittle solids. *Continuum Mechanics and Thermodynamics, 25*(2), 359–373. https://doi.org/10.1007/s00161-012-0265-6 (cit. on pp. 31, 45)

Rinaldi, A., & Lai, Y.-C. (2007). Statistical damage theory of 2d lattices: Energetics and physical foundations of damage parameter. *International Journal of Plasticity, 23*(10), 1796–1825. https://doi.org/10.1016/j.ijplas.2007.03.005 (cit. on pp. 31, 45)

Rossi, P., Robert, J. L., Gervais, J. P., & Bruhat, D. (1990). The use of acoustic emission in fracture mechanics applied to concrete. *Engineering Fracture Mechanics, 35*(4), 751–763. https://doi.org/10.1016/0013-7944(90)90158-D (cit. on p. 12)

Rothenburg, L., & Selvadurai, A. P. S. (1981). A micromechanical definition of the cauchy stress tensor for particulate media. *Mechanics of structured media,* 469–486 (cit. on p. 63).

Roux, J., Hosten, B., Castagnede, B., & Deschamps, M. (1985). Caractérisation mécanique des solides par spectro-interférométrie ultrasonore. *Revue de Physique Appliquée, 20*(6), 351–358. https://doi.org/10.1051/rphysap:01985002006035100 (cit. on p. 41)

Roux, S., & Guyon, E. (1985). Mechanical percolation : A small beam lattice study. *Journal de Physique Lettres, 46*(21), 999–1004. https://doi.org/10.1051/jphyslet:019850046021099900 (cit. on p. 15)

Rudnicki, J. W., & Rice, J. R. (1975). Conditions for the localization of deformation in pressure-sensitive dilatant materials. *Journal of the Mechanics and Physics of Solids, 23*(6), 371–394. https://doi.org/10.1016/0022-5096(75)90001-0 (cit. on p. 27)

Saanouni, K., Forster, C., & Hatira, F. B. (1994). On the anelastic flow with damage. *International Journal of Damage Mechanics, 3*(2), 140–169. https://doi.org/10.1177/105678959400300203 (cit. on p. 19)

Saliba, J., Matallah, M., Loukili, A., Regoin, J. P., Grégoire, D., Verdon, L., & Pijaudier-Cabot, G. (2016). Experimental and numerical analysis of crack evolution in concrete through acoustic emission technique and mesoscale modelling. *Engineering Fracture Mechanics, 167*, 123–137. https://doi.org/10.1016/j.engfracmech.2016.03.044 (cit. on p. 12)

Schlangen, E., & van Mier, J. G. M. (1992). Simple lattice model for numerical simulation of fracture of concrete materials and structures. *Materials and Structures, 25*(9), 534–542. https://doi.org/10.1007/BF02472449 (cit. on pp. 15, 16)

Schouten, J. A. (1989). *Tensor analysis for physicists* (2nd ed.). Dover Publications. (Cit. on p. 37).

Shahin, G., Herbold, E. B., Hall, S. A., & Hurley, R. C. (2022). Quantifying the hierarchy of structural and mechanical length scales in granular systems. *Extreme Mechanics Letters, 51*, 101590. https://doi.org/10.1016/j.eml.2021.101590 (cit. on p. 53)

Simo, J. C., & Ju, J. W. (1987). Strain- and stress-based continuum damage models—i. formulation. *International Journal of Solids and Structures, 23*(7), 821–840. https://doi.org/10.1016/0020-7683(87)90083-7 (cit. on p. 19)

Simone, A., Wells, G. N., & Sluys, L. J. (2003). From continuous to discontinuous failure in a gradient-enhanced continuum damage model. *Computer Methods in Applied Mechanics and Engineering, 192*(41), 4581–4607. https://doi.org/10.1016/S0045-7825(03)00428-6 (cit. on p. 29)

Singh, V. (2014). Nonlinear rate-dependent material model with damage and plasticity from granular micromechanics approach (cit. on p. 31).

Spencer, A. J. M. (1970). A note on the decomposition of tensors into traceless symmetric tensors. *International Journal of Engineering Science, 8*(6), 475–481. https://doi.org/10.1016/0020-7225(70)90024-8 (cit. on pp. 37, 38)

Stolz, C. (2019). A new approach of graded damage modelling. *Mathematics and Mechanics of Solids, 24*(6), 1922–1934. https://doi.org/10.1177/1081286518810068 (cit. on p. 29)

Stroeven, M., Askes, H., & Sluys, L. J. (2004). Numerical determination of representative volumes for granular materials. *Computer Methods in Applied Mechanics and Engineering, 193*(30), 3221–3238. https://doi.org/10.1016/j.cma.2003.09.023 (cit. on p. 53)

Taurines, J., Kolev, B., Desmorat, R., & Hubert, O. (2023). Modeling of the morphic effect using a vanishing 2nd order magneto-elastic energy. *Journal of Magnetism and Magnetic Materials, 570*, 170471. https://doi.org/10.1016/j.jmmm.2023.170471 (cit. on p. 137)

Taurines, J., Olive, M., Desmorat, R., Hubert, O., & Kolev, B. (2022). Integrity bases for cubic nonlinear magnetostriction. *Journal of Magnetism and Magnetic Materials, 546*, 167885. https://doi.org/10.1016/j.jmmm.2021.167885 (cit. on p. 137)

Terrien, M. (1980). Emission acoustique et comportement mécanique post-critique d'un béton sollicité en traction. *Bulletin de liaison des laboratoires des ponts et chaussees, 1980*(105), 65–71 (cit. on pp. 8, 9, 12).

Thierry, F. (2021). *Modélisation de la localisation des déformations dans les milieux adoucissants par une approche eikonale* (Doctoral dissertation). Université Paris-Saclay. (Cit. on p. 132).

Tian, W., Qi, L., Chao, X., Liang, J., & Fu, M. (2019). Periodic boundary condition and its numerical implementation algorithm for the evaluation of effective mechanical properties of the composites with complicated micro-structures. *Composites Part B: Engineering, 162*, 1–10. https://doi.org/10.1016/j.compositesb.2018.10.053 (cit. on p. 53)

Tibshirani, R. (1996). Regression shrinkage and selection via the lasso. *Journal of the Royal Statistical Society. Series B (Methodological), 58*(1), 267–288 (cit. on pp. 30, 100).

Vakulenko, A. A., & Kachanov, M. (1971). Continuum theory of medium with cracks. *Mekhanika tverdogo tela, 4*, 159–166 (cit. on p. 21).

Valoroso, N., & Stolz, C. (2022). Graded damage in quasi-brittle solids. *International Journal for Numerical Methods in Engineering, 123*(11), 2467–2498. https://doi.org/10.1002/nme.6947 (cit. on p. 29)

Vandoren, B., & Simone, A. (2018). Modeling and simulation of quasi-brittle failure with continuous anisotropic stress-based gradient-enhanced damage models. *Computer Methods in Applied Mechanics and Engineering, 332*, 644–685. https://doi.org/10.1016/j.cma.2017.12.027 (cit. on p. 133)

Vannucci, P. (2002). A special planar orthotropic material. *Journal of elasticity and the physical science of solids, 67*(2), 81–96. https://doi.org/10.1023/A:1023949729395 (cit. on pp. 41, 101)

Vannucci, P. (2005). Plane anisotropy by the polar method*. *Meccanica, 40*(4), 437–454. https://doi.org/10.1007/s11012-005-2132-z (cit. on pp. 39, 101, 143)

Vassaux, M., Oliver-Leblond, C., Richard, B., & Ragueneau, F. (2016). Beam-particle approach to model cracking and energy dissipation in concrete: Identification strategy and validation. *Cement and Concrete Composites, 70*, 1–14. https://doi.org/10.1016/j.cemconcomp.2016.03.011 (cit. on pp. 18, 46, 48, 49)

Vassaux, M. (2015). *Comportement mécanique des matériaux quasi-fragiles sous sollicitations cycliques : de l'expérimentation numérique au calcul de structures.* (Doctoral dissertation). École normale supérieure de Cachan - ENS Cachan. (Cit. on p. 46).

Verchery, G. (1982). Les invariants des tenseurs d'ordre 4 du type de l'élasticité In *Mechanical Behavior of Anisotropic Solids / Comportment Mécanique des Solides Anisotropes* (J.-P. Boehler, Ed.). Dordrecht, Springer Netherlands. 93–104. https://doi.org/10.1007/978-94-009-6827-1_7. (Cit. on pp. 39, 143)

Vianello, M. (1997). An integrity basis for plane elasticity tensors. *Archives of Mechanics, 49*(1), 197–208. https://doi.org/10.24423/aom.1401 (cit. on pp. 35, 37–42)

Voigt, W. (1887). *Theoretische studien über die elasticitätsverhältnisse der krystalle*. Dieterich. (Cit. on p. 15).

Walsh, J. B. (1965a). The effect of cracks on the compressibility of rock. *Journal of Geophysical Research (1896-1977), 70*(2), 381–389. https://doi.org/10.1029/JZ070i002p00381 (cit. on p. 20)

Walsh, J. B. (1965b). The effect of cracks on the uniaxial elastic compression of rocks. *Journal of Geophysical Research (1896-1977), 70*(2), 399–411. https://doi.org/10.1029/JZ070i002p00399 (cit. on p. 20)

Wang, Y., Wagner, N., & Rondinelli, J. M. (2019). Symbolic regression in materials science. *MRS Communications, 9*(3), 793–805. https://doi.org/10.1557/mrc.2019.85 (cit. on p. 30)

Willam, K., Pramono, E., & Sture, S. (1989). Fundamental issues of smeared crack models In *Fracture of concrete and rock* (S. P. Shah & S. E. Swartz, Eds.). New York, NY, Springer. 142–157. https://doi.org/10.1007/978-1-4612-3578-1_15. (Cit. on pp. 21, 75)

Wriggers, P., & Moftah, S. O. (2006). Mesoscale models for concrete: Homogenisation and damage behaviour. *Finite Elements in Analysis and Design, 42*(7), 623–636. https://doi.org/10.1016/j.finel.2005.11.008 (cit. on p. 45)

Yvonnet, J., He, Q.-C., & Li, P. (2022). A data-driven harmonic approach to constructing anisotropic damage models with a minimum number of internal variables. *Journal of the Mechanics and Physics of Solids, 162*, 104828. https://doi.org/10.1016/j.jmps.2022.104828 (cit. on p. 31)

Yvonnet, J., He, Q.-C., & Li, P. (2023). Reducing internal variables and improving efficiency in data-driven modelling of anisotropic damage from RVE simulations. *Computational Mechanics, 72*(1), 37–55. https://doi.org/10.1007/s00466-023-02326-7 (cit. on p. 31)

Zafati, E., & Richard, B. (2019). Anisotropic continuum damage constitutive model to describe the cyclic response of quasi-brittle materials: The regularized unilateral effect. *International Journal of Solids and Structures, 162*, 164–180. https://doi.org/10.1016/j.ijsolstr.2018.12.009 (cit. on p. 23)

Zanna, L., & Bolton, T. (2020). Data-driven equation discovery of ocean mesoscale closures. *Geophysical Research Letters, 47*(17), e2020GL088376. https://doi.org/10.1029/2020GL088376 (cit. on p. 31)